Ali Edalat Behbahani

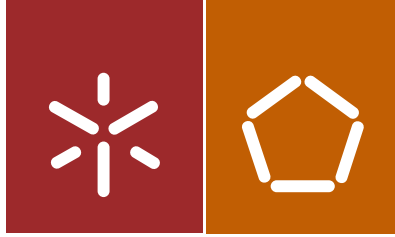Constitutive Models to Simulate Failure of
Structures Made by Cement Based Materials

Ali Edalat Behbahani   Constitutive Models to Simulate Failure of
Structures Made by Cement Based Materials

UMinho | 2017

janeiro de 2017

Universidade do Minho
Escola de Engenharia

Ali Edalat Behbahani

Constitutive Models to Simulate Failure of
Structures Made by Cement Based Materials

janeiro de 2017

STATEMENT OF INTEGRITY

I hereby declare having conducted my thesis with integrity. I confirm that I have not used plagiarism or any form of falsification of results in the process of the thesis elaboration.
I further declare that I have fully acknowledged the Code of Ethical Conduct of the University of Minho.

University of Minho, _____

Full name: _Ali Edelaty Behbahani_____

Signature: _____

iii

Dedicated To:

My family

Without their help, this work would not be possible.

ACKNOWLEDEMENTS

Ali found love of his life, Faranak, at University of Minho. Thank you, Faranak, for all the unconditional supports and sacrifices that you made.

Most importantly, I thank God for all His blessing to live this unmemorable experience.

Ali Edalat Behbahani

September 2016

ABSTRACT

Nonlinear Finite Element Analysis (NFEA) has been widely adopted as an effective and reliable method to analyze reinforced concrete (RC) structures subjected to various loading scenarios. Amongst many key factors that affect the reliability of a NFEA tool used for analysing RC structures, the selected constitutive model still remains the foremost challenging task due to the complexity of concrete behaviour associated to the cracking in tension and crushing in compression. The present work proposes a new constitutive model for cement based materials, allowing the possibility of simulating the complex functioning of concrete under both tension and compression. The model proposes a unified approach combining a multidirectional fixed smeared crack model to simulate the crack initiation and propagation with a plastic-damage model to account for the inelastic compressive behaviour of concrete between cracks. The smeared cracking model considers the possibility of forming several cracks in the same integration point, whose orientations, conditioned by an adopted criterion, are however preserved constant during the cracking process. The crack initiation is governed by the Rankine failure criterion, whereas the crack propagation (crack opening process) is simulated by a trilinear (or a quadrilinear) softening diagram. Two approaches are available to simulate the fracture mode II: one based on the concept of shear retention factor, and the other one on a shear softening diagram that requires some information about the fracture mode II propagation. The plasticity model is defined by four entities: yield function (yield surface); flow rule; evolution law for the hardening variable; and condition for defining loading–unloading process. Evolution of the yield surface during the plastic flow is governed by a single hardening parameter for compression. The plasticity part is responsible for simulating irreversible strains and volumetric strain in compression, whereas the strain softening and stiffness degradation of the material under compression are simulated by a strain based isotropic damage model. In this damage approach the state of damage in concrete under compression is equally distributed in all directions, and can be represented by a scalar damage parameter. Calculation of the scalar damage parameter is an explicit operation as this parameter is driven by the plastic hardening parameter.

Two versions of the model are developed, one dedicated to concrete structures subjected to plane stress fields, and the second for being applied to concrete structures submitted to three dimensional stress states. Both versions of the model are implemented into FEMIX 4.0 computer program. To appraise the performance of the model and to evidence the interaction between cracking and plasticity-damage parts of the model, some numerical tests at material level are executed, and the obtained results are discussed. The model appraisal at the structural level is also considered. The set of experimental tests simulated in this thesis covers a wide range of specimens regarding geometry, concrete type, loading configurations, and reinforcement conditions, in order to demonstrate the robustness of the developed model. These structures are of particular interest for the assessment of the reliability of the model, since in these examples the failure mechanism involved simultaneous occurrence of cracking and inelastic deformation in compression. The predictive performance of the model in terms of load carrying capacity, ductility, crack pattern, plastic zones, and failure modes is obtained by comparing the results of the numerical simulations and the available experimental data.

Keywords: finite element analysis; plastic-damage multidirectional fixed smeared crack model; compressive nonlinearity; cracked concrete; RC structures; cement based materials.

RESUMO

O método dos elementos finitos (MEF) tem-se revelado eficaz na análise não linear de estruturas de betão armado submetidas a diferentes tipos de carregamentos. De entre os muitos fatores que podem afetar a fiabilidade de uma ferramenta capaz de efetuar uma análise não linear usando o MEF, o modelo constitutivo selecionado ainda continua a ser o desafio mais importante, nomeadamente devido à complexidade do comportamento do betão associado à fendilhação quando sujeito a tração e ao esmagamento em compressão.

O presente trabalho propõe um novo modelo constitutivo, capaz de simular o comportamento complexo de materiais de matriz cimentícia quando sujeitos a esforços de tração e de compressão. O modelo propõe uma abordagem unificada, combinando um modelo de múltiplas fendas fixas distribuídas que permite simular o início de fendilhação e a sua propagação com um modelo de dano e plasticidade para simular o comportamento inelástico do betão entre fendas. O modelo de fendilhação permite a formação de várias fendas por ponto de integração, cuja orientação é condicionada por um determinado critério e preservada constante durante o processo de fendilhação. A abertura de fenda é condicionada pelo critério de Rankine, sendo o seu desenvolvimento simulado por intermédio de um diagrama de amolecimento trilinear ou quadrilinear. Duas abordagens estão disponíveis para simular o modo II de fratura: uma baseada no conceito de fator de retenção ao corte, e o outro utilizando um diagrama de amolecimento definido com base nos parâmetros do modo II de fractura.

O modelo de plasticidade é definido: pela função de cedência (superfície de cedência); lei de escoamento plástico; lei de endurecimento; condição para a definição do processo de carga e descarga. A evolução da superfície de cedência durante o escoamento plástico é governada por um único parâmetro de endurecimento. A parte da plasticidade é responsável por simular as deformações irreversíveis e a deformação volumétrica em compressão, enquanto o amolecimento e a degradação da rigidez do material sob compressão são simulados por um modelo de dano isotrópico. Nesta abordagem, o estado de dano no betão sob compressão é igualmente distribuído em todas as direções, e pode ser representado por um escalar denominado parâmetro de dano.

O modelo proposto é desenvolvido numa primeira fase para estados planos de tensão e posteriormente generalizado para estados de tensão tridimensionais. Estas duas versões do modelo foram integradas no código computacional denominado FEMIX 4.0. De forma a evidenciar as partes do modelo que têm em conta a simulação da propagação da fendilhação, do dano e da plasticidade, bem como da sua interação, são executados alguns testes numéricos focados no comportamento do material, sendo os seus resultados discutidos.

Os ensaios experimentais escolhidos para avaliar a robustez do modelo a nível estrutural abrangem uma ampla gama de elementos no que respeita a geometria, tipo de betão, configurações de carga e de reforço. Estas estruturas são de particular interesse para a avaliação da fiabilidade do modelo, uma vez que nestes exemplos ocorrem simultaneamente fendilhação e deformação plástica em compressão. O desempenho do modelo em termos de previsão da capacidade de carga, da ductilidade, do padrão de fendilhação, das zonas plásticas e dos modos de rutura é obtido comparando os resultados das simulações numéricas com os dos ensaios experimentais disponíveis.

CONTENTS

LIST OF FIGURES

CHAPTER 3 – TWO DIMENSIONAL PLASTIC-DAMAGE MULTIDIRECTIONAL FIXED SMEARED CRACK MODEL

CHAPTER 5 – THREE DIMENSIONAL PDSC MODEL: FORMULATION AND APPLICATION IN STRUCTURAL ANALYSIS

LIST OF TABLES

CHAPTER 5 – THREE DIMENSIONAL PDSC MODEL: FORMULATION AND APPLICATION IN STRUCTURAL ANALYSIS

ANNEX B

LIST OF SYMBOLS USED IN THE PORPOSED CONSTITUTIVE MODELS

$\bar{\underline{\sigma}}$ effective stress vector at global coordinate system

$\underline{\sigma}$ nominal stress vector at global coordinate system

$\underline{D}^e$ linear elastic constitutive matrix

$\bar{\underline{\sigma}}^+$ the positive component, corresponding to tensile state of stress, of stress vector $\bar{\underline{\sigma}}$

$\bar{\underline{\sigma}}^-$ the negative component, corresponding to compressive state of stress, of stress vector $\bar{\underline{\sigma}}$

$\bar{\sigma}^i$ ith principle stress extracted from the vector $\bar{\underline{\sigma}}$

$\underline{P}^i$ the normalized eigenvector associated with the ith principle stress $\bar{\sigma}^i$

$\Delta\underline{\varepsilon}^{cr}$ incremental crack strain vector

$\Delta\underline{\varepsilon}^{co}$ incremental concrete strain vector

$\Delta\underline{\varepsilon}$ incremental total strain vector

$\Delta\underline{\varepsilon}^p$ incremental plastic strain vector

θ_i orientation corresponding to the i-th crack

IP integration point

$\Delta\underline{\varepsilon}^{cr}_\ell$ incremental crack strain vector at crack coordinate system

$\Delta\underline{\sigma}^{cr}_\ell$ incremental stress vector at crack coordinate system

σ^{cr}_n normal components of the local crack stress vector

τ^{cr}_t shear components of the local crack stress vector

ε^{cr}_n normal components of the local crack strain vector

γ_t^{cr}	shear components of the local crack strain vector
$\underline{T}^{cr}$	transformation matrix from the coordinate system of the finite element to the local crack coordinate system
$\underline{D}^{cr}$	crack constitutive matrix
D_n^{cr}	the stiffness modulus correspondent to the fracture mode I
D_t^{cr}	the stiffness modulus correspondent to the fracture mode II
E	modulus of elasticity
v	Poisson's coefficient
α_i	normalized stress parameters (i=1, 2) in trilinear diagram
β	shear retention factor
ξ_i	normalized strain parameter (i =1, 2) in trilinear diagram
f_c	compressive strength of concrete
f_{ct}	tensile strength of concrete
G_c	elastic shear modulus
G_f^I	mode I fracture energy
$G_{f,s}$	mode II fracture energy
$G_{f,c}$	compressive fracture energy
l_b	crack bandwidth
l_c	Compressive characteristic length which was assumed identical to the crack bandwidth
$\varepsilon_{n,u}^{cr}$	ultimate crack normal strain
P_1	parameter that defines the amount of the decrease of β upon increasing ε_n^{cr}
$\gamma_{t,p}^{cr}$	peak crack shear strain
$\tau_{t,p}^{cr}$	peak crack shear stress
$\gamma_{t,u}^{cr}$	ultimate crack shear strain

$\bar{I}_1$	first invariant of the effective stress tensor
$\bar{J}_2$	second invariant of the deviatoric effective stress tensor
$\bar{J}_3$	third invariant of deviatoric eddective stress tensor
$\bar{\theta}$	angle of similarity
$\bar{\xi}$	hydrostatic stress invariant
$\bar{\rho}$	deviatoric stress invariants
a, b, c	parameters of Willam-Warnke yield surface depending to state of stress
$\bar{\sigma}_c$	hardening function of the plasticity model
ε_{c1}	strain at compression peak stress
$f(\underline{\bar{\sigma}}, \bar{\sigma}_c)$	yield function
$\tilde{\epsilon}_c$	compressive hardening variable
$\Delta\lambda$	plastic multiplier
$\tilde{\epsilon}_{c1}$	accumulated plastic strain at uniaxial compressive peak stress
f_{c0}	uniaxial compressive stress at plastic threshold
α_0	material constant to define the beginning of the nonlinear behaviour in uniaxial compressive stress-strain test
d_c	scalar describing the amount compressive damage
$\tilde{\epsilon}_d$	internal damage variable for compression
a_c	non-dimensional parameter of damage
$\varepsilon_{sy}, \varepsilon_{sh}, \varepsilon_{su}$	three strain points at the steel constitutive law
$\sigma_{sy}, \sigma_{sh}, \sigma_{su}$	three stress points at the steel constitutive law
P	parameter that defines the shape of the last branch of the steel stress-strain curve

E_{sy} unloading-reloading slop for the steel constitutive law

CHPATER 1

INTRODUCTION

1.1 MOTIVATION

Concrete is known as one of the most widely used construction material in civil engineering. The main advantages of concrete are: high workability and formability that allows its application to various structural elements in buildings, bridges, dams, etc; high durability in severe environmental condition; it is a relatively cheap material with a few maintenance requirements; fire resistance of reinforced concrete (RC) structures, since concrete bulk limits the elevation of temperature in the reinforcement rebars. However, concrete exhibits highly nonlinear behaviour by increasing deformation, with dissymmetric responses in tension and in compression (i.e. concrete has relatively low tensile strength when compared to its compressive strength).

Since the advent of concrete, the analysis and design of concrete structures have been objective of many researchers and designers. The development of computer oriented FEM (finite element method) based numerical models for two- and three- dimensional structural analysis contributed much to the possibility of calculating nowadays concrete structures with complex/arbitrary geometry. Analysis of structural engineering problems by FEM is based on solution of a set of equilibrium equations between the internal forces (those supported by the consitituent materials of the structure) and the external ones (combination of load cases). To determine with appropriate accuracy the internal forces,

the FEM-based approach must take into consideration the strain/stress limits capable of supporting by the materials. The physical/mathematical representation of these limits simulates the behaviour of a material, and is generally designated by the "material constitutive model". Many constitutive models, from simple to sophisticated, have been developed for material nonlinear analysis of RC structures. However, during the course of these developments, modelling of concrete structures has always proven to be a challenge, particularly due to the complexity of concrete behaviour. Concrete exhibits highly nonlinear behaviour by increasing deformation, with dissymmetric responses in tension and in compression. Experimental tests demonstrate that concrete behaviour in tension is brittle, and after cracking initiation it develops a softening behaviour with a decay of tensile capacity with the widening of the cracks. This crack opening process is followed by a decrease of crack shear stress transfer due to the deterioration of aggregate interlock. Concrete in compression also exhibits a pronounced nonlinear behaviour with an inelastic irreversible deformation. In the pre-peak stage of concrete response in uniaxial compression, a nonlinear stage is observed, whose amplitude depends of the concrete strength class, followed by a softening stage where brittleness is also dependent of the strength class. The complexity of concrete behaviour increases when submitted to multiaxial stress field that is the current situation of the major RC structures. For a realistic Nonlinear Finite Element Analysis (NFEA) of RC structures, constitutive models are required to adequately describe these complex behaviours of concrete.

One possible theoretical framework to develop a constitutive model capable of simulating both dissymmetric responses of concrete under tension and compression, is coupling a fracture approach to the plasticity theory. In this class of models, the theory of plasticity is used to deal with the elastoplastic behaviour of material under compression, whereas various fracture theories can be used to simulate the cracking behaviour (de Borst, 1986; Cervenka and Papanikolaou, 2008). However, numerical difficulties may occur with this class of models when applied to simulate structures whose failure is governed, simultaneously, by cracking and inelastic behaviour in compression (Feenstra, 1993; Cervenka and Papanikolaou, 2008). The problem is that in this kind of simulations both fracture and plasticity parts of the model might be active over a large region of the simulated structure, therefore several types of nonlinearities are occurring simultaneously.

1.2 SCOPES AND OBJECTIVES

The primary aim in this thesis is the development of two- and three- dimensional constitutive models based on the combination of fracture and plasticity theories, to perform material nonlinear analysis of structures made by cement based materials. So, the main objectives of the research carried out in the scope of this thesis are:

- Develop a robust constitutive model able to be used in relatively large scale structures whose failure is governed by cracking and inelastic behaviour in compression.

- Develop a constitutive model that is stable and numerically effective in the entire loading regime until failure.

- Integrate the proposed model into FEMIX FEM based computer program (Sena-Cruz et al., 2007), and assess its predictive performance, at both material and structural levels, by considering available experimental data. The developed model should be able to predict with good accuracy the load carrying capacity, ductility, crack pattern, plastic (compressive) zone, and failure modes of structures subjected to different loading paths.

- Validate the model by choosing a set of experimental tests that should cover a wide range of geometry of specimens, concrete type, loading configurations, and reinforcement conditions in order to demonstrate the robustness of the developed model.

- Perform an extensive parametric study to demonstrate the sensitivity of the simulations to the values adopted for the model parameters.

- Compare the results obtained by the proposed model with those obtained by the already existing constitutive approaches available in FEMIX computer program. Advantages of the proposed model over the already existing ones should be critically commented.

1.3 OUTLINE OF THESIS

The present thesis is divided into six chapters. The introduction represented in this chapter, chapter 1, defines the motivation and the objectives of the present doctoral study.

Chapter 2 is dedicated to review the most important mechanical/material behavior of concrete under different loading states. A review of several theories frequently used to

model these mechanical behaviours of concrete is also presented. The theoretical framework for the proposed model, developed in the next chapters, is selected based on the discussions made in chapter 2.

In chapter 3, a two dimensional (2D) constitutive model, called herein as plastic-damage multidirectional fixed smeared crack (PDSC) model, is developed. The description of the model is made at the domain of an integration point (IP) of a plane stress finite element. The proposed model is based on the combination of an already existing multidirectional fixed smeared crack model (Sena-Cruz, 2004; Ventura-Gouveia, 2011) to simulate crack initiation and propagation, and a numerical strategy that combines plasticity and damage theories to simulate the inelastic behaviour of material between cracks. All the theoretical aspects related to the fracture, plasticity, and damage components of the model are described in detail. This chapter establishes the system of nonlinear equations that should be solved to update the local variables of the PDSC model at a generic load increment of the incremental/iterative Newton–Raphson algorithm generally adopted in FEM-based material nonlinear analysis. A special attention is dedicated in this chapter to the algorithm when both smeared cracking and plastic-damage parts of the model are simultaneously active in an IP. In this chapter the numerical model is appraised at the material level using several single element tests.

Chapter 4 is dedicated to the application of the 2D PDSC model in the analysis of concrete and RC structures. The set of experimental tests simulated in this chapter covers a wide range of geometry of specimens, concrete type, loading configurations, and reinforcement conditions in order to show the robustness of the developed model. These simulated examples are of particular interest for the assessment of the reliability of the proposed model, since in these examples the failure mechanism involved simultaneous occurrence of cracking and inelastic deformation in compression. In this chapter the predictive performance of the PDSC model is also compared with another constitutive model, available in FEMIX computer, which includes the same multidirectional fixed smeared crack to account for cracking, but considers the linear elastic behaviour for the material under compressive deformations. The two models are critically compared to demonstrate the advantages of the PDSC model in the simulation of this type of tests.

Chapter 5 proposes a new three dimensional (3D) constitutive model for cement based materials, based in the generalization of the 2D plastic-damage multidirectional fixed

smeared crack model. The principal theoretical aspects of the model, called herein as 3D PDSC model, are described. In this chapter the 3D PDSC model is validated in both material and structural levels. A wide range of experimental tests from literature, including RC column under combined axial and flexural loading condition, RC beams made by different concrete strength classes, and RC walls subjected to torsion, are simulated to highlight the capability of the model to predict with good accuracy the deformation and cracking behaviour of these types of structures.

Finally, Chapter 6 gives the conclusions of this research, as well as some suggestions for future researches. Fig. 1.1 represents an overview over the structure of the present thesis.
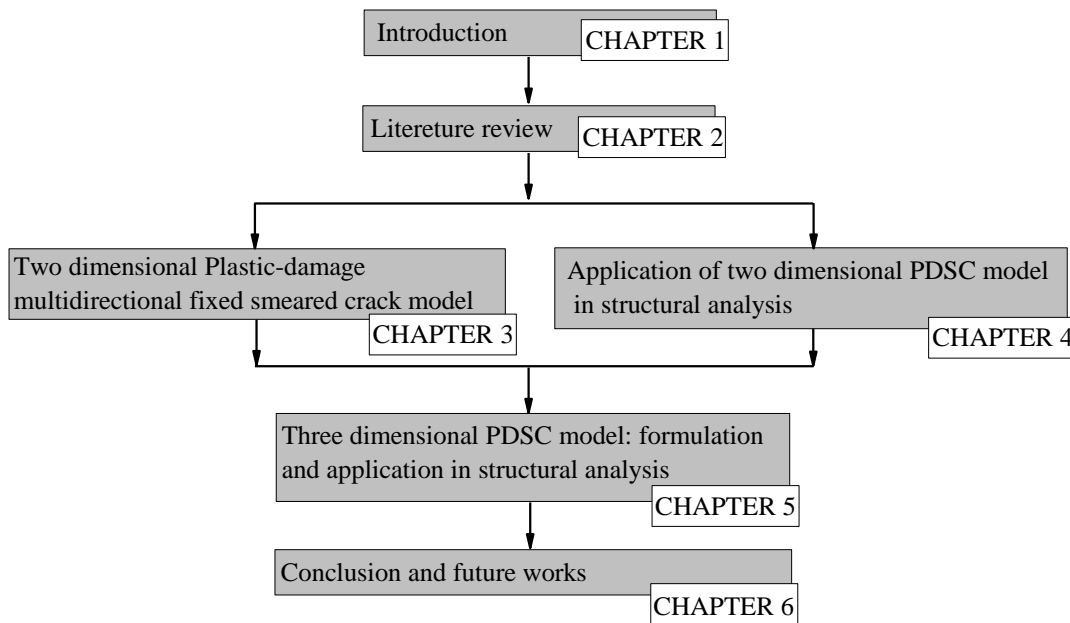
Fig. 1.1 - Structure of the thesis.

CHAPTER 2

LITERATURE REVIEW

2.1 INTRODUCTION

During the last decades several constitutive models have been developed in an attempt of capturing the quite sophisticated behaviour of concrete when submitted to multi-stress fields. To simulate the complex functioning of the structures made by this material, those constitutive models are in general implemented in computer programs based on the Finite Element Method (FEM) (Hillerborg et al., 1976; Bazant and Oh, 1983; Lubliner et al., 1989; Moës and Belytschko, 2002). Getting reliable FEM-based simulations is still a challenge due to the high complexity of concrete behaviour, mainly its brittle nature. Thereby, the section 2.2 is dedicated to review the most important mechanical/material behavior of concrete under different loading states. Later, section 2.3 reviews several theories frequently used to model these mechanical behaviours of concrete, while section 2.4 is dedicated to briefly present the formulations of some of these theories. Then, as a conclusion, the theoretical framework for the proposed model, that is developed in the next chapters, is selected based on the discussions made in sections 2.3 and 2.4.

2.2 MECHANICAL BEHAVIOUR OF CONCRETE

Concrete exhibits highly nonlinear behaviour by increasing deformation, with dissymmetric responses in tension and in compression. In this section the main

mechanical behavioural aspects of concrete under tension and compression are reviewed based on experimental observations.

2.2.1 Concrete behaviour under compression

Concrete in compression exhibits a pronounced nonlinear behaviour. Fig. 2.1 identifies the three consecutive load-deformation stages that can be identified in concrete under uniaxial compressive load, based on initiation and propagation of cracks (Shah et al., 1995):

Stage I - below ≈30% of the peak stress. The formation of internal cracks at this stage is negligible, and the stress-strain response of the material may be assumed as linear. The amplitude of stage I increases with the concrete compressive strength;

Stage II - between ≈30% and ≈100% of the peak stress. At the beginning of this stage the internal cracks initiate and propagate at the interface zone, and new micro-cracks develop. Around 60% of the peak stress, the micro-cracks at the cementitious matrix start to develop randomly over volume of the material. At approximately 80% up to 100% of the peak stress, all the small internal cracks become unstable and start to localize into major cracks. The amplitude of stage II decreases with the concrete compressive strength;

Stage III - after peak load. At this stage the major cracks continuously propagate, although the applied load is decreasing.
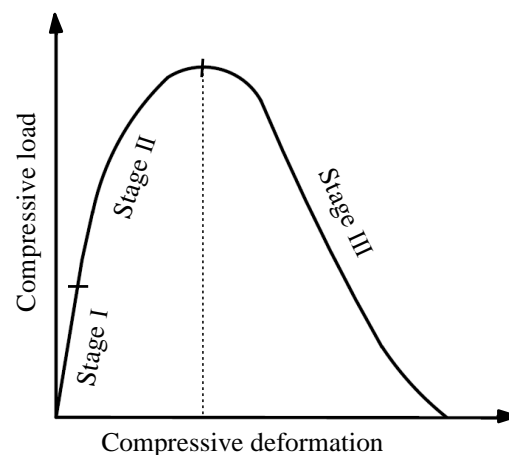
Fig. 2.1 – Load-deformation behaviour of the cement based materials under uniaxial compression (Shah et al., 1995).

Uniaxial compressive strength of concrete, f_c, typically ranges from 15 MPa to 120 MPa. A concrete with the compressive strength less than 55 MPa is usually referred as normal strength concrete, while to the one considered of high strength has a compressive strength higher than 55 MPa. The value of axial strain at (uniaxial) compressive strength, ε_{c1}, increases with the compressive strength (see Fig. 2.2). The value of ε_{c1} typically ranges from 1.8 ‰ and 3.0 ‰ (CEB-FIP Model Code 2010).
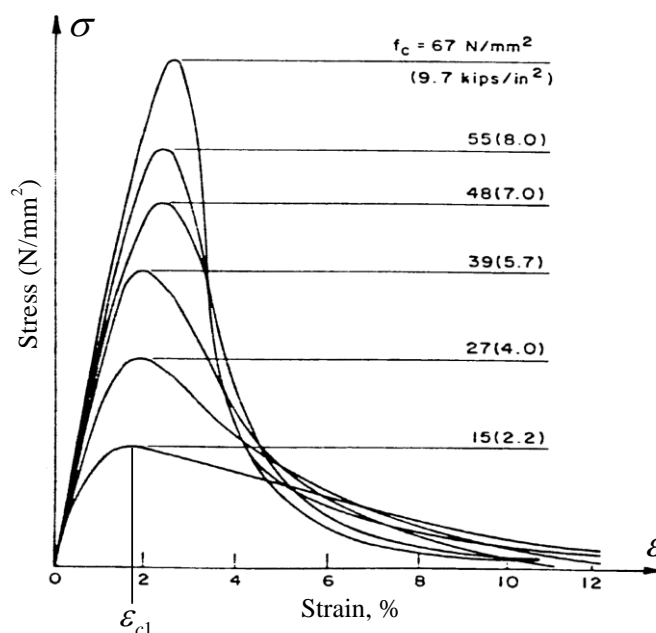
Fig. 2.2 – Uniaxial compressive stress-strain curves for the
concrete in different strength (Wischers, 1978).

Concrete in uniaxial compression also exhibits pronounced volumetric strain. Results of a test executed by van Mier (1984) are represented in Fig. 2.3 to show the variation of volumetric strain (ε_{vol}) in uniaxial compressive test. As can be seen in Fig. 2.3b, near the peak load the volumetric strain changes its sign to positive which means that the volume of sample increases (volumetric expansion). The volumetric expansion, also referred as dilatancy, has a significant effect on the behavior of plain and reinforced concrete structures in multiaxial stress states (Lee and Fenves, 1998), and should be properly considered in the development of a concrete constitutive model.

(a) (b)
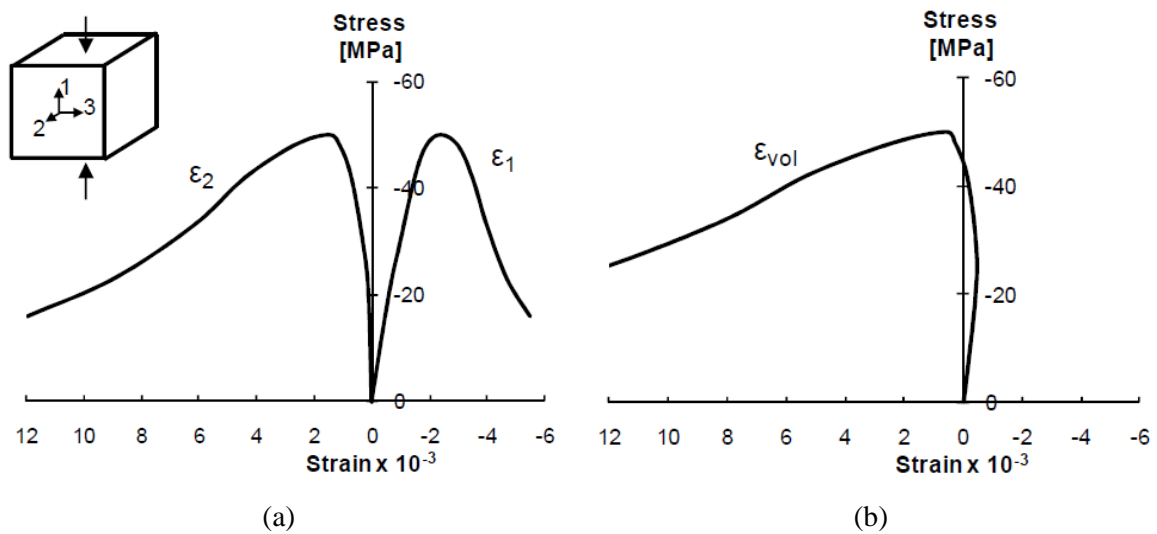
Fig. 2.3 – Behaviour of concrete under uniaxial compression test (van Mier, 1984): (a) axial stress-strain response, (b) axial stress-volumetric strain (ε_{vol}) response.

Fig. 2.4 demonstrates, as an example, the behavior of a concrete subjected to cyclic uniaxial compressive loading. It can be observed that by increasing deformation, the initial elastic stiffness (of intact material) gradually decreases, which is due to the cracking process (developed at Stage II and Stage III of the load-deformation response of concrete under uniaxial compression, see Fig. 2.1). As unloading occurs, irreversible plastic strains develop in concrete, which is due to the presence of aggregates in the crack faces and the damage in the aggregates-paste interfaces (the openings of the cracks are partially irreversible).
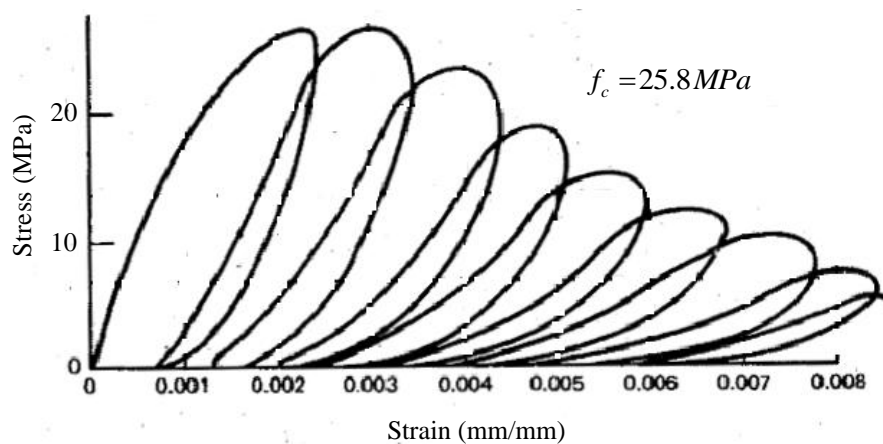
Fig. 2.4 – Stress-strain behaviour of concrete under cyclic uniaxial compression test (Sinha et al., 1964).

2.2.2 Concrete behaviour under tension

According to the principles of nonlinear fracture mechanics of cement based materials, three different types of fracture modes can be identified: crack opening mode (fracture mode I); shearing mode (fracture mode II – in-plane shear); tearing mode (fracture mode III – out-of-plane shear). Fig. 2.5 shows schematically these fracture modes. Fracture mode I is one of the most common failure modes in cement based materials, since it occurs in uniaxial, splitting and bending tensile failure. In Fracture mode II, the displacement of crack surfaces is in the plain of the crack and perpendicular to the leading edge of the crack. The tearing mode is not so common like the previous failures modes, and occurs in massive structures where 3D stress field can be developed (Ayatollahi and Aliha, 2005), or in slab or shell type structures where punching failure mode is a concern (Ventura-Gouveira, 2011, Teixeira et al., 2015).
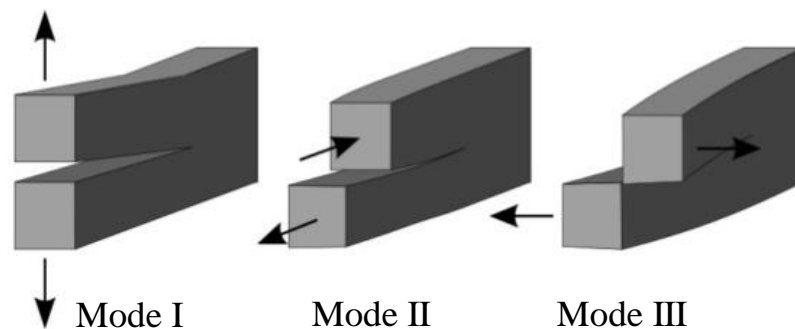
Fig. 2.5- Basic fracture modes (Wang, 1996).

Uniaxial tensile test is frequently executed to define the fracture Mode I related properties of cement based materials. Experimental tests demonstrate that the concrete response in uniaxial tension is almost linear elastic up to attain its tensile strength, f_{ct}, (assumed as being the crack initiation), and after cracking initiation develops a softening behaviour with a decay of tensile capacity with the widening of the cracking process. Concrete has low tensile strength, f_{ct}, when compared to its compressive strength, resulting in the appearance of cracks at relatively low stress level. The ratio between the uniaxial tensile and compressive strength of concrete, f_{ct}/f_c, is reported in literature by values usually in the range 0.05 to 0.1 (Hugues and Chapman, 1966). Beside, by increasing crack opening

the unloading-reloading stiffness of concrete gradually decreases, see Fig. 2.6 (Reinhardt, 1984).
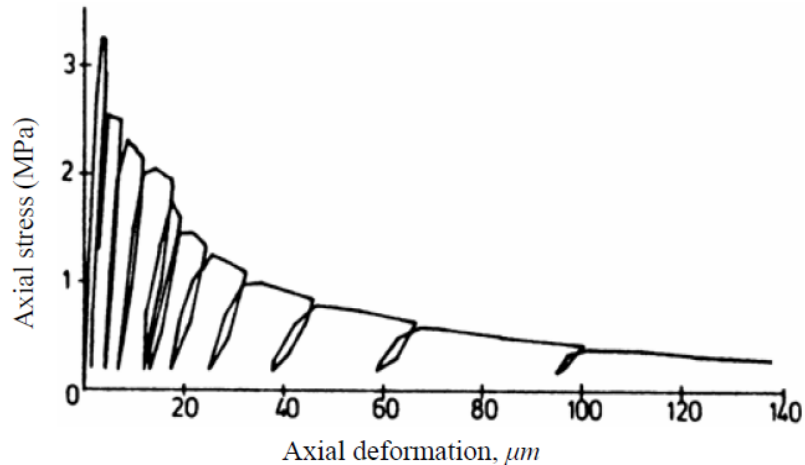
Fig. 2.6 – Cyclic uniaxial tensile loading test (Reinhardt, 1984).

In a tensile cyclic test the permanent tensile deformation developed in each unloading is caused by the occurrence of some sliding during the opening process due to the granular nature of concrete and non-homogeneous geometry of aggregates and their distribution.

Mechanical behavior of concretes under the fracture mode II is generally evaluated using a shear test suggested by JSCE-G 553-1999 (or the ones suggested by some researchers, such as: Petrova and Sadowski 2012, Xu and Reinhardt 2005, Sagaseta and Vollum 2011, etc). In general, plain concrete represent a brittle shear behavior after forming a crack (Hisabe et al., 2006). The aggregate interlock and friction at the crack faces are known as the responsible for transferring shear stresses across the crack (Kim et al. 2010). Application of fibers as shear reinforcement is pronounced recently to avoid the brittle failures of unreinforced concrete. As concrete matrix is combined with fibers randomly distributed over volume of concrete at relatively small spacing, the resulting composite exhibits uniform resistance in all the directions and alters brittle material in to ductile one (Rao and Rao, 2009). This increase in ductility is due to successive pull-out of the fiber, which consumes large amounts of energy. These advantages are dependant mainly to the type and volume of fiber added to the matrix.

Axial stress (MPa)
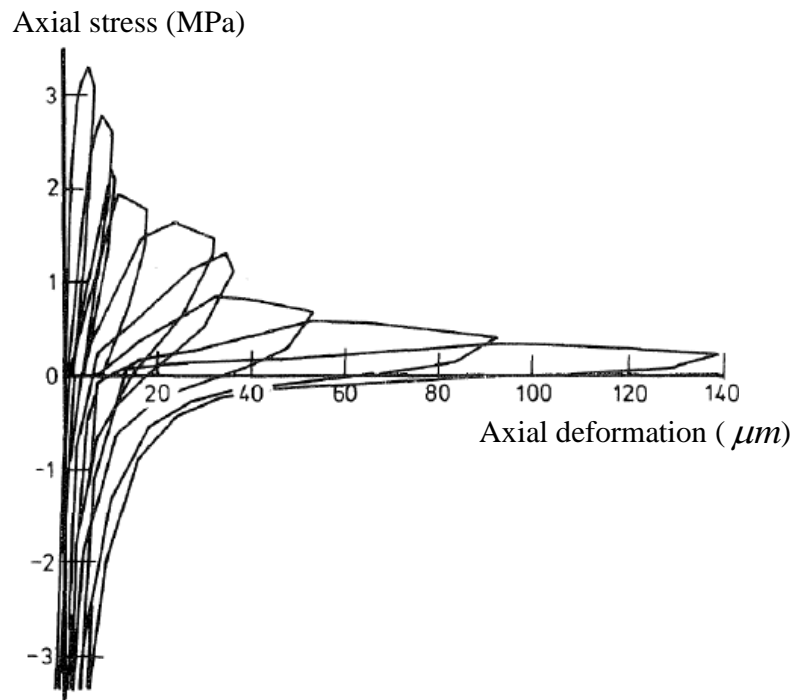
Fig. 2.7 – Cyclic uniaxial tensile-compressive loading test (Reinhardt, 1984).

Typical behaviour of concrete under cyclic uniaxial tension-compression test is shown in Fig. 2.7 (Reinhardt, 1984). According to this figure, as the unloading from tension to compression occurs, i.e., as the tensile cracks are completely closed and the state of stress is changed to compression, the material almost attains its original compressive stiffness. This phenomenon is called unilateral effect. In fact according to this experimental observation, the stiffness of stress-strain response in compression is marginally affected by the already existing tensile cracks, since these cracks (tensile cracks) are almost orthogonal to the cracks developed in compression.

2.3 REVIEW OF THE THEORIES FREQUENTLY USED FOR MODELLING THE MECHANICAL BEHAVIOUR OF CONCRETE

Mechanical behaviour of concrete was briefly introduced in section 2.2 based on the experimental observations. Concrete behaviour in tension and compression is dissymmetric and exhibits nonlinear phenomena like strain softening, stiffness degradation, volumetric expansion. Many theories can be found in literature to capture these concrete behaviours. The plasticity, continuum damage mechanics (CDM), combination of plasticity and CDM, smeared cracking approach, microplane theory,

discrete interface approach, and generalised finite element method are common theories for modelling the nonlinear behaviour of concrete. These models can be categorized into two different approaches in respect to their strategies to simulate the failure process of the materials: the continuum and the discrete modelling (discrete crack) approaches.

The models based on discrete approach simulate the cracking by introducing a geometric discontinuity in the domain. For instance, in the discrete interface approach (DIA) cracks are introduced by explicitly modeling the discontinuity using zero thickness finite elements, whereas the surrounding bulk is discretized by regular finite elements (e.g. Ortiz and Pandolfi, 1999; Tijssens et al., 2000). Discrete interface approach was initially applied to simulate discontinuities in rock mechanics, and later this approach was extended to simulate fracture mode I (Rots, 1988; Schellekens and de Borst, 1993), fracture mode II (Schellekens, 1990) in brittle materials like concrete. Further applications of discrete interface approach can be found in modelling delamination and fracture in multi-layered composites (Alfano et al., 2001; Seguarado and LLorca, 2004), masonry structures (Thanoon et al., 2008; Ghiasi et al., 2012), soil-structure interaction (Coutinho et al., 2003; Cerfontaine et al., 2015), and bond between concrete and reinforcement (Kaliakin and Li, 1995; Sena-Cruz, 2004; Wu and Gilbert, 2009; Hawileh, 2012). Drawback of the discrete interface approach is that the failure zone should be predefined before the analysis. Adoption of the discrete interface approach for capturing arbitrary crack initiation and propagation requires sophisticated automated mesh regeneration techniques to adjust side the finite element mesh to the propagated crack surface (Camacho and Ortiz, 1996; May et al., 2016). An interesting discrete crack model which allows for capturing arbitrary crack initiation and propagation is the generalised finite element method, GFEM (e.g. Wells and Sluys, 2001). This approach incorporates in the shape function of the finite element the displacement discontinuity that represents the occurrence of a crack.

In contrast, the models based on the continuum approach maintain the notion of continuity of displacement field, and interpret the failure zone by a stress-strain relationship. The basic idea of continuum approach is that a large number of small cracks usually develop in concrete mainly due to its heterogeneity, but only at the later

deformation stage of structures these cracks joint and form the critical cracks (dominant crack at the failure stage) (de Borst et al., 2004; Simone, 2007).

The smeared cracking approach is the most popular continuum approach to simulate concrete cracking. The models based on a smeared crack approach assume that the local displacement discontinuities at cracks are assumed distributed over a certain length used to transform crack width/sliding in a strain concept, also assumed to represent the length zone of the fracture process. This length dimension is related to the finite element characteristics in order to assure that the results are independent of the adopted finite element mesh refinement (Oliver, 1989; de Borst et al., 2004; Oliver, et al., 2008), preserving the fracture energy as a material property (de Borst et al., 2004). In the smeared crack models the cracks are allowed to form in any directions (according to the rules adopted for cracking formation), by preserving the topology of the finite element mesh during the cracking process. However, these models cannot predict the precise localization and propagation of the discrete cracks, especially the crack opening, since the assumption of continuity of displacement field does not reflect the nature of displacement discontinuities at the cracks. However, for simulating relatively large concrete structures, mainly those with reinforcement that assures the formation of relatively high number of cracks, the smeared cracking approach is very convenient, since modelling the cracking process is almost resumed to the adoption of a proper constitutive model.

The models based on the smeared crack approach can be categorized into two main groups: fixed and rotating crack models. When the maximum principal tensile stress in an integration point attains the concrete tensile strength for the first time, a crack is formed and a local *ns*-coordinate system (where *n* and *s*-axes represent the direction normal and tangential to crack, respectively) can be assumed for the crack. In fixed crack approach, the direction of *n*-axis is assumed to be fixed for the rest of analysis. This permanent allocation of the local crack coordinate system is the main characteristic of fixed smeared crack approach. After the crack initiation, the orientation and the values of the principal stresses may change during subsequent loading, due to the shear stress transfer between the faces of the crack (Rots and de Borst, 1987; Sena-Cruz, 2004). In this case, the local *ns*-coordinate system does not remain coincident with the directions of the actual principal stresses. In the multidirectional fixed smeared crack models, another set of

smeared cracks is allowed to propagate if the following two criteria are met simultaneously (de Borst and Nauta, 1985; Sena-Cruz, 2004): (*i*) the calculated maximum principal stress attains the tensile strength; (*ii*) the angle between the direction of the existing cracks and newly calculated maximum principal stress exceeds a predefined threshold angle. In the rotating crack approach the direction of principal stresses are calculated for every load increment, and then based on the orientations of principal stresses, the direction of crack keeps rotating in order to assure coaxiality between principal stresses and strains.

It is to be noted that the material behaviour in the direction normal to the crack plane (crack opening response) and the behaviour in the direction tangential to the crack plane (shear sliding response) can be simulated by different damage evolution laws. In the models based on the smeared crack approach the concept of shear retention factor (Suidan and Schnobrich, 1973) or a local strain-softening law (crack shear stress-shear strain softening law) (Rots and de Borst, 1987; Suryanto et al., 2010; Ventura-Gouveia, 2011) are the strategies usually adopted to simulate the shear sliding process for cracked oncrete.

The models based on the microplane theory, CDM, and plasticity theory, lie in the category of the continuum approach. In the microplane model, the constitutive equation is integrated based on volumetric, deviatoric, and tangential microscopic stress and strain components on the planes of any orientation, called microplanes, composing a spherical surface. Various characteristic behaviour of concrete can be adequately described using the microplane theory (Bazant et al., 2000; Cervenka et al., 2005; Kozar and Ozbolt, 2010). The main shortcoming of the models based on the microplane theory is that computational cost and storage requirements are high, since this class of models deal with the stress components acting on all the microplanes.

The plasticity theory has been widely used for modelling concrete behaviour subjected to multiaxial stress field (Park and Kim, 2005; Papanikolaou and Kappos, 2007; Pereira, 2012; Zhang and Li, 2012; Carrazedo et al., 2013; Poltronieri et al., 2014). The plasticity theory adopts the split of strain field into the elastic (reversible) and plastic (irreversible) parts that realistically represents the experimentally observed inelastic deformation of concrete. Plasticity models are defined by four entities: yield function; hardening law;

flow rule; and conditions describing loading-unloading paths. The yield surface is derived from a failure criterion that defines the strength capacity of a material when submitted to a generic stress field. The hardening law defines the evolution of the yield surface during the plastic flow. The flow rule defines size and direction of the increment of plastic deformation.

The models based on the plasticity alone fail to address the damage process due to crack initiation and propagation, therefore the experimentally observed stiffness degradation of the material is not captured accurately by using exclusively the plasticity theory (Gernay, 2012; Carrazedo et al., 2013; Omidi et al., 2013). In fact, the recent numerical models complement the plasticity theory with other approaches that provide a better interpretation of concrete behaviour in tension. Combining the plasticity theory with CDM (Grassl and Jirasek, 2006; Wu et al., 2006; Taqieddin et al., 2012; Grassl et al., 2013; Gernay et al., 2013; Omidi and Lotfi, 2013), and with the nonlinear fracture mechanics (de Borst, 1986; Cervenka and Papanikolaou, 2008) are alternatives that have been explored.

The theoretical framework of the CDM is based on the gradual reduction of the elastic stiffness. The damage is defined as the loss of strength and stiffness of the material when subjected to a certain loading process. There are several possibilities of how the state of damage can be represented by a model. The isotropic (scalar) damage models assume a state of damage is equally distributed in all directions by means of a scalar measure. As stated before, concrete materials exhibit different responses (damage mechanisms) in tension and compression. Some isotropic damage models accounted for both the damage mechanisms in tension and compression using a single damage variable (Lee and Fenves, 1998; Willam et al., 2001; Ferrara and di Prisco, 2001; Nechnech et al., 2002; Luccioni and Rougier, 2005; Jason et al., 2006; Grassl and Jirásek, 2006). The other isotropic damage models account for different responses of concrete under various loadings using multiple hardening scalar damage variables (Mazars and Pijaudier-Cabot, 1989; Faria et al, 1998; Willam et al., 2003; Jirásek, 2004; Marfia et al., 2004; Tao and Phillips, 2005). However, it was argued that isotropic damage models (with single or multiple damage variables) cannot simulate anosotropic damage effects, i.e. different cracking in different directions, in concrete. This shortcoming is eliminated in the anisotropic damage models

that consider a damage tensor to account for micro-cracking (damage) in different directions, but the adoption of this approach is limited due to the high level of sophistication, especially when it is combined with the other theories, like plasticity (Meschke et al., 1998; Hansen et al., 2001; Carol et al., 2001; Cicekli et al., 2007).

Drawback of the models based on CDM is that these models are not suitable for simulating the irreversible (plastic) deformations and inelastic volumetric expansion in compression (Abu Al-Rub and Kim, 2010; Omidi and Lotfi, 2013). At nonlinear stage of stress–strain response of a concrete like material, neglecting the irreversible deformations according to a pure damage model would result in an artificial increase of damage (a secant branch is assumed in this approach to simulate unloading phase), see Fig. 2.8. Neglecting damage effects in a pure plasticity model would result in maintaining initial elastic stiffness (stiffness of intact material) by increasing deformation (i.e. at any given point of the stress-strain response the slope of the unloading branch is the same as initial elastic stiffness). Therefore plasticity and damage theories can be merged in an attempt of constituting reliable approaches capable of simulating the strength and stiffness degradation and occurrence of irreversible deformations.
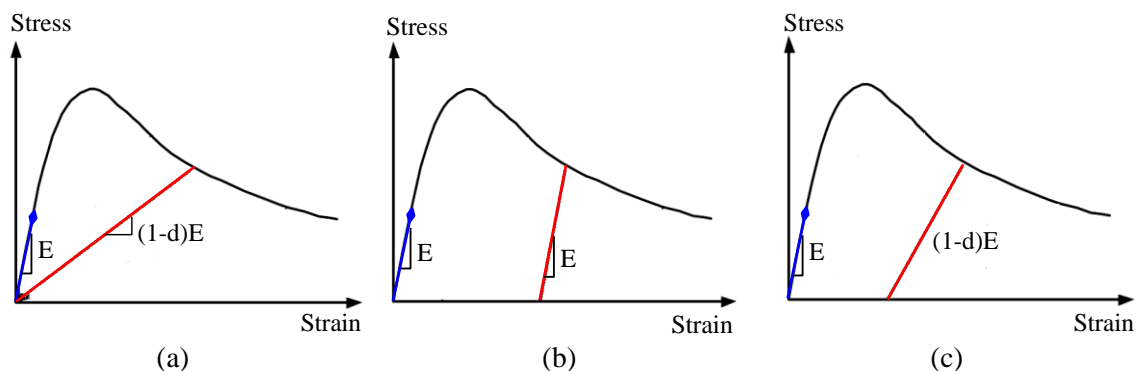
Fig. 2.8 – Schematic unloading responses according to three approaches (Jason et al., 2006): (a) damage model, (b) plasticity model, (c) plastic-damage model (Note: in this figure the parameter E is the initial elastic stiffness, and the parameter d is an scalar representing the state of damage in the material).

One popular class of plastic-damage models incorporate the plasticity approach formulated in effective stress space (Ju, 1989; Mazars and Pijaudier-Cabot, 1989; Lee and Fenves, 1998; Jefferson, 2003; Voyiadjis and Kattan, 2006; Jason et al., 2006; Voyiadjis

et al., 2008), while another group relies on the plasticity part formulated in nominal stress space (Lubliner et al., 1989; Krätzig and Pölling, 2004). Effective stress is the stress acting on undamaged configuration of the material, while the nominal stress is defined as the stress acting on damaged configuration of the material. In the models which the plasticity is formulated in the effective stress space, the plasticity part is responsible to simulate irreversible deformations, while the damage part account for stiffness degradation of the materials. The advantage of this approach is that the stiffness degradation is decoupled from the plastic deformation in the computation process. It was demonstrated by Grassl and Jirásek (2006) local uniqueness condition (i.e. the condition that for any prescribed displacement there is a unique response for stress and internal variables) is guaranteed for the plastic-damage models with the plasticity part formulated in effective stress space, while for the other group (the plastic-damage models with the plasticity part formulated in nominal stress space) local uniqueness requires severe restriction. Besides, it was demonstrated by some authors that the plastic-damage models with the plasticity part formulated in effective stress space are more stable and numerically efficient in comparison to those with the plasticity part formulated in nominal stress space (Taqieddin, 2008; Gernay, 2012; Omidi and Lotfi, 2013).

2.4 BASICS OF THE CONSTITUTIVE MODELS FREQUENTLY USED FOR CONCRETE

Several theories frequently used to model the mechanical behaviour of concrete were reviewed in section 2.3. In the current section, the basic formulations of some of them, namely discrete interface approach, generalized finite element method, fixed smeared crack approach, and plasticity theory are presented.

2.4.1 Discrete interface approach (DIA)

Consider a body Ω with the boundary Γ which contains a discontinuity surface Γ_d separating the body into two subregions Ω^+, and Ω^- (see Fig. 2.9). The body containing the discontinuity is designated hereafter as $\Omega \backslash \Gamma_d$.
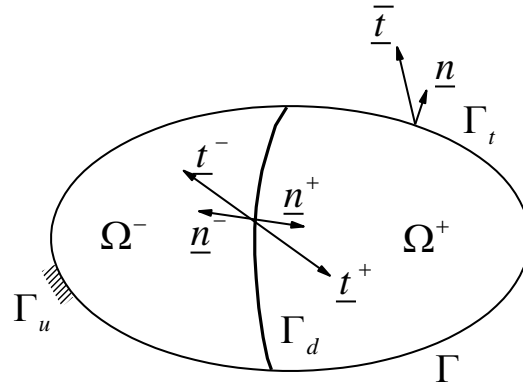
Fig. 2.9 – Domain Ω crossed by a discontinuity Γ_d (Wells and Sluys, 2001).

The load applied to $\Omega \backslash \Gamma_d$ consist of body forces $\overline{\underline{b}}$, and natural[1] boundary conditions $\overline{\underline{t}}$. The natural boundary conditions are distributed over the external bonndary Γ_t . The essential boundary conditions are applied on the remaining part of the boundary, Γ_u , in a way that $\Gamma_t \bigcup \Gamma_u = \Gamma$ and $\Gamma_t \bigcap \Gamma_u = \varnothing$. The vector $\underline{n}$ is normal to the boundary surface pointing outward the body, while $\underline{n}^+$ is the vector normal to Γ_d pointing inward the region Ω^+.

The displacement field for each point in the domain Ω, $\underline{u}$, can be decomposed into two parts: a regular (continuum) displacement field, $\hat{\underline{u}}$, and enhanced displacement field $\tilde{\underline{u}}$ induced by the jumps at the discontinuity Γ_d, such that:

$$\underline{u} = \begin{cases} \hat{\underline{u}} + \tilde{\underline{u}}^+ & in\ \Omega^+ \\ \hat{\underline{u}} + \tilde{\underline{u}}^- & in\ \Omega^- \end{cases} \tag{2.1}$$

Following the principle work for the continuum body with a discontinuity, shown in Fig. 2.9, the following variational formulation can be written (Malvern, 1969; Dias-da-Costa 2010):

$$-\int_{\Omega \backslash \Gamma_d} (\nabla^s \delta \underline{u}) : \underline{\sigma} d\Omega - \int_{\Gamma_d} (\delta \underline{u}^+ - \delta \underline{u}^-).\underline{t}^+ d\Gamma + \int_{\Omega \backslash \Gamma_d} \delta \underline{u}.\overline{\underline{b}}\ d\Omega + \int_{\Gamma t} \delta \underline{u}.\overline{\underline{t}}\ d\Gamma = 0 \tag{2.2}$$

---

[1] *If a condition involves the applied loads, it is natural. A condition is essential if it directly involves the nodal freedom, such as displacement or rotaion.*

where $(.)^s$ implies symmetric part of $(.)$, $(.)^+$ and $(.)^-$ denote the quantity $(.)$ at the Ω^+ and Ω^- side of the discontinuity, respectively, and $\nabla(.)$ implies gradient of $(.)$, and $\delta(.)$ means virtual variation of $(.)$.

The variational formulations of the DIA and GFEM are derived based on Eq. (2.2). In this equation the term $\int_{\Omega\backslash\Gamma_d}(\nabla^s\delta\underline{u}):\underline{\sigma}d\Omega$ is the internal work, and the term $\int_{\Omega\backslash\Gamma_d}\delta\underline{u}.\overline{\underline{b}}\,d\Omega+\int_{\Gamma_t}\delta\underline{u}.\overline{\underline{t}}\,d\Gamma$ is the external work, which both are the regular terms adopted in a continuum finite element approach. The term $\int_{\Gamma_d}(\delta\underline{u}^+-\delta\underline{u}^-).\underline{t}^+d\Gamma$ is the work produced at the discontinuity.

In DIA the discontinuity is modelled explicitly by adopting zero thickness finite elements, while the surrounding domain is modelled by regular finite elements. For this approach the Eq. (2.2) can be written separately for the domains $\Omega\backslash\Gamma_d$ and Γ_d according to the following form (Dias-da-Costa 2010):

$$\int_{\Omega\backslash\Gamma_d}(\nabla^s\delta\underline{u}):\underline{\sigma}d\Omega=\int_{\Omega\backslash\Gamma_d}\delta\underline{u}.\overline{\underline{b}}\,d\Omega+\int_{\Gamma_t}\delta\underline{u}.\overline{\underline{t}}\,d\Gamma \tag{2.3a}$$

$$\int_{\Gamma_d}(\delta\underline{u}^+-\delta\underline{u}^-).\underline{t}^+d\Gamma=\int_{\Gamma_d}\delta\underline{u}.\overline{\underline{t}}\,d\Gamma \tag{2.3b}$$

Eq. (2.3a) can be assumed as the application of usual virtual work principle to the domain $\Omega\backslash\Gamma_d$. Eq. (2.3b) corresponds to virtual work principle applied to the domain of the discontinuity Γ_d, and the procedure used to discretize this equation is addressed in this section.

Consider the interface finite elements with n pairs of nodes as shown in Fig. 2.10. The displacement field for each interface finite element can be approximated as following:

$$\delta\underline{u}^+-\delta\underline{u}^-=[\![\underline{u}]\!]=\underline{N}\,\underline{W} \tag{2.4}$$
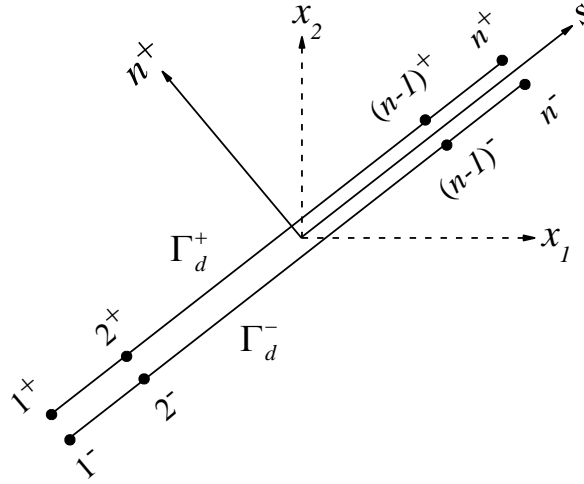
Fig. 2.10 – Zero thickness interface elements with *n* pars of nodes with indication of local (*s*, *n*) and global (*x₁*, *x₂*) coordinate systems (Malvern, 1969; Dias-da-Costa 2010).

Eq. (2.4) in incremental form can be written as:

$$d[\![\underline{u}]\!] = \underline{N}\, d\underline{W} \tag{2.5}$$

The matrix $\underline{N}$ includes the interpolation functions of *n* pairs of nodes, such that:

$$\underline{N} = \begin{bmatrix} \underline{N}^1 & 0 & ... & \underline{N}^n & 0 \\ 0 & \underline{N}^1 & ... & 0 & \underline{N}^n \end{bmatrix} \tag{2.6}$$

The term $d\underline{W}$ is obtained by computing the difference between the incremental displacements of each pairs of nodes at the domains Γ_d^+ and Γ_d^-:

$$d\underline{W} = \underline{L}\, d\underline{a} \tag{2.7}$$

where $\underline{L}$ is a ($2n \times 4n$) matrix defined as:

$$\underline{L} = \begin{bmatrix} 1 & 0 & -1 & 0 & ... & 0 & 0 & 0 & 0 \\ 0 & 1 & 0 & -1 & ... & 0 & 0 & 0 & 0 \\ ... & ... & ... & ... & ... & ... & ... & ... & ... \\ 0 & 0 & 0 & 0 & ... & 1 & 0 & -1 & 0 \\ 0 & 0 & 0 & 0 & ... & 0 & 1 & 0 & -1 \end{bmatrix} \tag{2.8}$$

and the term $d\underline{a}$ includes incremental displacements of the nodes 1 to n, as the following:

$$d\underline{a}^T = \begin{bmatrix} d\underline{a}_{1^+}^T & d\underline{a}_{1^-}^T & ... & d\underline{a}_{n^+}^T & d\underline{a}_{n^-}^T \end{bmatrix} \tag{2.9}$$

where $(.)^T$ implies transpose of $(.)$.

The constitutive equations at the discontinuity can be represented by the following traction-relative displacement at discontinuity (jump) relationship:

$$d\underline{t} = \underline{D}_d \, d[\![\underline{u}]\!] = \underline{D}_d \, \underline{N} \, d\underline{W} \tag{2.10}$$

where $\underline{D}_d$ is the constitutive matrix of the discontinuity, and it can be represented as:

$$\underline{D}_d = \begin{bmatrix} D_n & 0 \\ 0 & D_t \end{bmatrix} \tag{2.11}$$

where D_n, and D_t represent, respectively, the normal and tangential stiffness modulus.

Substituting Eq. (2.5) and Eq. (2.10) into Eq. (2.3b), and taking to account $\underline{B} = \underline{N}\,\underline{L}$, yields:

$$\underline{K}_{aa} \, d\underline{a} = d\underline{f} \tag{2.12}$$

In Eq. (2.12), $d\underline{f}$, is the vector of external loads and $\underline{K}_{aa}$ is the stiffness matrix obtained as:

$$K_{aa} = \int_{\Gamma_d} B^T \, \underline{D}_d \, B \, d\Gamma \tag{2.13}$$

2.4.2 Generalized finite element method (GFEM)

As discussed before, in the DIA the discontinuity is explicitly modelled using interface finite elements, so the discontinuity can only propagate along the interface finite elements. In GFEM the discontinuity is implicitly modelled using the element own shape function, not the shape function of interface finite elements (Dias-da-Costa 2010). Consider an element before the formation of a crack discontinuity. The element has the nodal displacements of $\underline{\hat{a}}$, which is the regular displacement adopted in a continuum finite element approach. As the element is crossed by a discontinuity, GFEM incorporate the nodal enrichment techniques by adding an additional nodal displacements ($\underline{\tilde{a}}$) to each node of the element (in the GFEM the nodes at the edge containing the tip are not enriched (Wells and Sluys, 2001)). Then the displacement field can be represented such that:

$$\underline{u} = \underline{\hat{u}} + H_{\Gamma d} \, \underline{\tilde{u}} \tag{2.14}$$

$$H_{\Gamma d} = \begin{cases} 1 & in \ \Omega^+ \\ 0 & otherwise \end{cases} \tag{2.15}$$

The term $H_{\Gamma d} = 1$ (which appears in Eq. (2.15)) for the domain Ω^+, implies the jump of displacement in discontinuity is entirely transmitted to the domain Ω^+ (see Fig. 2.11).

The displacement at discontinuity can be written as the following:

$$(\underline{u}^+ - \underline{u}^-)_{|\Gamma_d} = (\underline{\tilde{u}}^+ - \underline{\tilde{u}}^-)_{|\Gamma_d} = [\![\underline{u}]\!] = \underline{\tilde{u}}_{|\Gamma_d} \tag{2.16}$$
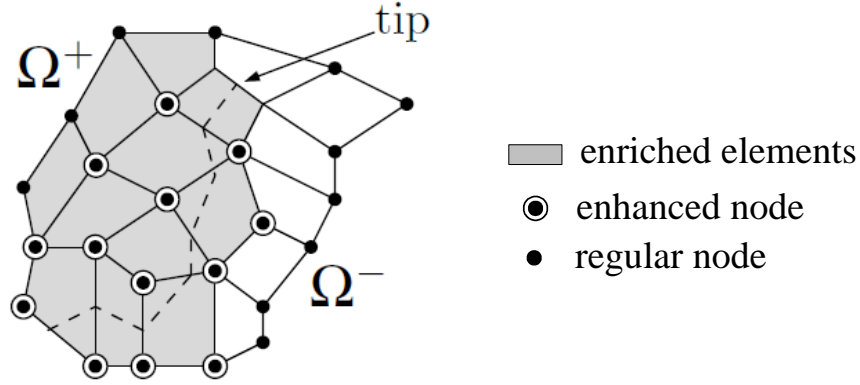
Fig. 2.11 – Propagation of discontinuity in GFEM (Dias-da-Costa 2010).

To obtain the variational formulation of GFEM, the term $\delta[\![\underline{u}]\!] = (\delta\underline{u}^+ - \delta\underline{u}^-)$ (see Eq. (2.16)) is inserted into Eq. (2.2), such that:

$$-\int_{\Omega\backslash\Gamma_d} (\nabla^s \delta\underline{u}) : \underline{\sigma} d\Omega - \int_{\Gamma_d} \delta[\![\underline{u}]\!].\underline{t}^+ d\Gamma + \int_{\Omega\backslash\Gamma_d} \delta\underline{u}.\overline{\underline{b}}\, d\Omega + \int_{\Gamma_t} \delta\underline{u}.\overline{\underline{t}}\, d\Gamma = 0 \qquad (2.17)$$

Similar to Eq. (2.14), the virtual displacements $\delta\underline{u}$ are decomposed into regular end enhanced parts, as the following:

$$\delta\underline{u} = \delta\hat{\underline{u}} + H_{\Gamma_d}\, \delta\tilde{\underline{u}} \qquad (2.18)$$

By inserting Eq. (2.18) into Eq. (2.17) and considering: i) $\delta\tilde{\underline{u}} = 0$; and ii) $\delta\hat{\underline{u}} = 0$, the variational formulation of GFEM in the final form can be written as (Dias-da-Costa 2010):

$$\int_{\Omega\backslash\Gamma_d} (\nabla^s \delta\hat{\underline{u}}) : \underline{\sigma} d\Omega = \int_{\Omega\backslash\Gamma_d} \delta\hat{\underline{u}}.\overline{\underline{b}}\, d\Omega + \int_{\Gamma_t} \delta\hat{\underline{u}}.\overline{\underline{t}}\, d\Gamma \qquad (2.19a)$$

$$\int_{\Omega^+} (\nabla^s \delta\tilde{\underline{u}}) : \underline{\sigma} d\Omega + \int_{\Gamma_d} \delta[\![\underline{u}]\!].\underline{t}^+ d\Gamma = \int_{\Omega^+} \delta\tilde{\underline{u}}.\overline{\underline{b}}\, d\Omega + \int_{\Gamma_{t^+}} \delta\tilde{\underline{u}}.\overline{\underline{t}}\, d\Gamma \qquad (2.19b)$$

The displacement field ($\underline{u}$) in Eq. (2.19a) and Eq. (2.19b) can be approximated as:

$$\underline{u} = \underline{N}\,(\hat{\underline{a}} + H_{\Gamma d}\,\tilde{\underline{a}}) \qquad in\ \Omega \backslash \Gamma_d \tag{2.20}$$

The displacement at discontinuity can be written as the following:

$$(\underline{u}^+ - \underline{u}^-)_{|\Gamma_d} = (\tilde{\underline{u}}^+ - \tilde{\underline{u}}^-)_{|\Gamma_d} = [\![\underline{u}]\!] = \underline{N}\,\tilde{\underline{a}} \tag{2.21}$$

where $\underline{N}$ is the matrix of element shape function evaluated at Γ_d.

The strain field can be represented as:

$$\underline{\varepsilon}^e = \underline{LN}\,\underline{a} = \underline{B}(\hat{\underline{a}} + H_{\Gamma d}\,\tilde{\underline{a}}) \qquad in\ \Omega \backslash \Gamma_d \tag{2.22}$$

The incremental stress and incremental traction are computed by the following equations:

$$d\sigma = \underline{D}\,B(d\hat{a} + H_{\Gamma d}\,d\tilde{a}) \qquad in\ \Omega \backslash \Gamma_d \tag{2.23}$$

$$d\underline{t} = \underline{T}_{el}\,d[\![\underline{u}]\!] = \underline{T}_{el}\,\underline{N}\,\underline{L}\,d\tilde{\underline{a}} \qquad at\ \Gamma_d \tag{2.24}$$

being $\underline{D}$ the constitutive matrix of the material.

By inserting Eqs. (2.20) to (2.24) the variational formulation of GFEM (Eq. (2.19a), and Eq. (2.19b)) can be discretized as:

$$\underline{K}_{\hat{a}\hat{a}}\,d\hat{\underline{a}} + \underline{K}_{\hat{a}\tilde{a}}\,d\tilde{\underline{a}} = d\hat{\underline{f}} \tag{2.25}$$

$$\underline{K}_{\tilde{a}\hat{a}}\,d\hat{\underline{a}} + (\underline{K}_{\tilde{a}\tilde{a}} + \underline{K}_d)d\tilde{\underline{a}} = d\tilde{\underline{f}} \tag{2.26}$$

where the stiffness matrixes $\underline{K}_{\hat{a}\hat{a}}$, $\underline{K}_{\hat{a}\tilde{a}}$, $\underline{K}_{\tilde{a}\hat{a}}$, $\underline{K}_{\tilde{a}\tilde{a}}$, $\underline{K}_d$ are given by:

$$\underline{K}_{\hat{a}\hat{a}} = \int_{\Omega \backslash \Gamma_d} \underline{B}^T\,\underline{D}\,\underline{B}\,d\Omega \tag{2.27}$$

$$\underline{K}_{\hat{a}\tilde{a}} = \int_{\Omega^+} \underline{B}^T\,\underline{D}\,\underline{B}\,d\Omega; \quad \underline{K}_{\tilde{a}\tilde{a}} = \underline{K}_{\tilde{a}\hat{a}} = \underline{K}_{\hat{a}\tilde{a}}^T \tag{2.28}$$

$$\underline{K}_d = \int_{\Gamma_d} \underline{N}^T \, \underline{D}_d \, \underline{N} \, d\Gamma \tag{2.29}$$

and the force vectors $d\hat{\underline{f}}$ and $d\tilde{\underline{f}}$ are defined as:

$$d\hat{\underline{f}} = \int_{\Omega \backslash \Gamma_d} \underline{N}^T \, d\overline{\underline{b}} \, d\Omega + \int_{\Gamma_t} \underline{N}^T \, d\overline{\underline{t}} \, d\Gamma \tag{2.30}$$

$$d\tilde{\underline{f}} = \int_{\Omega^+} \underline{N}^T \, d\overline{\underline{b}} \, d\Omega + \int_{\Gamma_t^+} \underline{N}^T \, d\overline{\underline{t}} \, d\Gamma \tag{2.31}$$

2.4.3 Fixed smeared crack approach

This section represents the fundamental theoretical aspects of the non-orthogonal fixed smeared crack approach, considering the presentation is restricted to plane stress state, and at the domain of an IP. In the smeared crack approach, total strain increment, $\Delta \underline{\varepsilon}$, can be decomposed into an incremental crack strain component, $\Delta \underline{\varepsilon}^{cr}$, and an incremental concrete strain component, $\Delta \underline{\varepsilon}^{co}$, as proposed by de Borst and Nauta (1985), $\Delta \underline{\varepsilon} = \Delta \underline{\varepsilon}^{co} + \Delta \underline{\varepsilon}^{cr}$. The $\Delta \underline{\varepsilon}^{cr}$ is obtained from the incremental local crack strain vector, $\Delta \underline{\varepsilon}_\ell^{cr}$, as the followings:

$$\Delta \underline{\varepsilon}^{cr} = \left[\underline{T}^{cr} \right]^T \Delta \underline{\varepsilon}_\ell^{cr} \tag{2.32}$$

Assuming m cracks can be formed in a generic IP, the incremental local crack strain ($\Delta \underline{\varepsilon}_\ell^{cr}$) is given:

$$\Delta \underline{\varepsilon}_\ell^{cr} = \left[\Delta \varepsilon_{n,1}^{cr} \; \Delta \gamma_{t,1}^{cr} \dots \Delta \varepsilon_{n,i}^{cr} \; \Delta \gamma_{t,i}^{cr} \dots \Delta \varepsilon_{n,m}^{cr} \; \Delta \gamma_{t,m}^{cr} \right]^T \tag{2.33}$$

being $\Delta \varepsilon_n^{cr}$, $\Delta \gamma_t^{cr}$ normal and tangential crack strain components of the m cracks. $\underline{T}^{cr}$ is the matrix that transforms the stress components from the coordinate system of the finite element to the local coordinate system of each crack (a subscript ℓ is used to identify entities in the local crack coordinate system). If m cracks occur at an IP:

$$\underline{T}^{cr} = \left[\underline{T}_1^{cr} \cdots \underline{T}_i^{cr} \cdots \underline{T}_m^{cr} \right]^T \tag{2.34}$$

The constitutive equation at the crack coordinate system has the following form:

$$\Delta \underline{\sigma}_\ell^{cr} = \underline{D}^{cr} \Delta \underline{\varepsilon}_\ell^{cr} \tag{2.35}$$

where $\Delta \underline{\sigma}_\ell^{cr}$ is the vector of the incremental crack stress in the crack coordinate system with the contribution of normal, $\Delta \sigma_n^{cr}$, and tangential components, $\Delta \tau_t^{cr}$. For m crack, $\Delta \underline{\sigma}_\ell^{cr}$ can be obtained as:

$$\Delta \underline{\sigma}_\ell^{cr} = \left[\Delta \sigma_{n,1}^{cr} \; \Delta \tau_{t,1}^{cr} \cdots \Delta \sigma_{n,i}^{cr} \; \Delta \tau_{t,i}^{cr} \cdots \Delta \sigma_{n,m}^{cr} \; \Delta \tau_{t,m}^{cr} \right]^T \tag{2.36}$$

where $\underline{D}^{cr}$ is the matrix that includes the constitutive law of the m active cracks (de Borst and Nauta, 1985; Rots and de Borst, 1987).

The following relation is hold between the increment of global stress, $\Delta \underline{\sigma}$, and increment of stress at local crack coordinate system:

$$\Delta \underline{\sigma}_\ell^{cr} = \underline{T}^{cr} \Delta \underline{\sigma} \tag{2.37}$$

The constitutive equation for the elastic-cracked material is given by:

$$\Delta \underline{\sigma} = \underline{D}^e \, \Delta \underline{\varepsilon}^{co} \tag{2.38}$$

Including Eq. (2.32), Eq. (2.35) and Eq. (2.38) into Eq. (2.37) and taking to account $\Delta \underline{\varepsilon}^{co} = \Delta \underline{\varepsilon} - \Delta \underline{\varepsilon}^{cr}$, yields:

$$\Delta \underline{\varepsilon}_\ell^{cr} = \left(\underline{D}^{cr} + \underline{T}^{cr} \underline{D}^e \left[\underline{T}^{cr} \right]^T \right)^{-1} \underline{T}^{cr} \underline{D}^e \Delta \underline{\varepsilon} \tag{2.39}$$

Substituting Eq. (2.39) into Eq. (2.38) and taking into account that $\Delta \underline{\varepsilon}^{co} = \Delta \underline{\varepsilon} - \Delta \underline{\varepsilon}^{cr}$, and $\Delta \underline{\varepsilon}^{cr} = \left[\underline{T}^{cr} \right]^{T} \Delta \underline{\varepsilon}_{\ell}^{cr}$, gives, after some arrangements (Borst and Nauta, 1985):

$$\Delta \underline{\sigma} = \underline{D}^{crco} \Delta \underline{\varepsilon} = \left(\underline{D}^{e} - \underline{D}^{e} \left[\underline{T}^{cr} \right]^{T} \left(\underline{D}^{cr} + \underline{T}^{cr} \underline{D}^{e} \left[\underline{T}^{cr} \right]^{T} \right)^{-1} \underline{T}^{cr} \underline{D}^{e} \right) \Delta \underline{\varepsilon} \qquad (2.40)$$

Eq. (2.40) represents the constitutive relation for the cracked concrete.

2.4.4 Plasticity approach

The classical plasticity theory emerged through the study of the behavior of metal materials in the late nineteen century. Nowadays many constitutive models for simulating mechanical behaviour of concrete are based in this theory (e.g. Poltronieri et al., 2014; Xenos and Grassl, 2016; Zhang et al., 2016; Lu et al., 2016). In the plasticity approach the total strain increment, $\Delta \underline{\varepsilon}$, is decomposed into an incremental plastic strain component, $\Delta \underline{\varepsilon}^{p}$, and an incremental elastic strain component, $\Delta \underline{\varepsilon}^{e}$, $\Delta \underline{\varepsilon} = \Delta \underline{\varepsilon}^{e} + \Delta \underline{\varepsilon}^{p}$. The incremental elastic strain vector is related to the incremental stress vector, $\Delta \underline{\sigma}$, according to the following constitutive equation:

$$\Delta \underline{\sigma} = \underline{D}^{e} (\Delta \underline{\varepsilon} - \Delta \underline{\varepsilon}^{p}) \qquad (2.41)$$

In general, a plasticity model needs to be defined by four components:

1) *Yield function*: the yield function, also known as yield surfaces or loading surfaces, is derived from a failure criterion. The strength capacity of a material when submitted to a generic stress field can be represented by a failure criterion. The yield function is a scalar function which represents a surface in a stress space coordinate system. The yield function is used in a plasticity model to identify the permissible stress states from non-permissible ones. If the current state of stress is inside the yield surface, the deformation is purely elastic. The plastic deformation (plastic flow) can only occur if the stress point is on the yield surface. Stress states

outside the yield surface are not possible in this concept. During the plastic flow, size and shape of the yield surfaces can be changed by means of at least one internal variable, called here hardening variables, $\tilde{\epsilon}$. In general, a yield function, f, has the following form:

$$f\left(\underline{\sigma}_{ij}, \tilde{\epsilon}\right) = 0 \tag{2.42}$$

Where $\underline{\sigma}_{ij,(i,j=1,2,3)}$ is the stress tensor which is defined in Cartesian coordinate system as:

$$\underline{\sigma}_{ij} = \begin{bmatrix} \sigma_x & \tau_{xy} & \tau_{xz} \\ \tau_{xy} & \sigma_y & \tau_{yz} \\ \tau_{xz} & \tau_{yz} & \sigma_z \end{bmatrix} \tag{2.43}$$

2) *Flow rule*; The following equation represent a generic flow rule:

$$\Delta\underline{\varepsilon}^p = \Delta\lambda \frac{\partial g}{\partial \underline{\sigma}_{ij}} \tag{2.44}$$

where g is a scalar function, called plastic potential function, $\Delta\lambda$ is the non-negative plastic multiplier.

The flow rule, represented in Eq. (2.44), defines the magnitude ($\Delta\lambda$) and the direction ($\partial g / \partial \underline{\sigma}_{ij}$) of the increment of plastic strains ($\Delta\underline{\varepsilon}^p$) developed during the plastic flow.

3) *Evolution law for the hardening variable*: the state of hardening parameter, $\tilde{\epsilon}$, during the plastic flow is changed according to an evolution law of the hardening variable. An evolution law, in general, has the following form (Grassl and Jirasek, 2006):

$$\Delta\tilde{\epsilon} = \Delta\lambda\, k_p(\underline{\sigma}_{ij}, \tilde{\epsilon}) \tag{2.45}$$

where k_p an scalar function depending on the state of stress and hardening variable (i.e. $k_p(\underline{\sigma}_{ij}, \tilde{\epsilon})$).

4) *Conditions describing loading-unloading paths*:   at any stage of loading-unloading process the following conditions, Kuhn–Tucker conditions, must be satisfied:

$$\Delta\lambda \geq 0, \quad f(\underline{\sigma}_{ij}, \tilde{\epsilon}) \leq 0, \quad \Delta\lambda\, f(\underline{\sigma}_{ij}, \tilde{\epsilon}) = 0 \tag{2.46}$$

The first condition indicates the plastic multiplier is always non-negative. The second condition implies the stress state must be inside or on the yield surface, whereas the last condition ensures the stress state during the plastic flow is on the yield surface.

In three dimensional problems, the state of stress is defined by six independent components of the stress tensor ($\underline{\sigma}_{ij}$), see Eq. (2.43). For isotropic materials, the values of the three principle stresses ($\underline{\sigma}_1, \underline{\sigma}_2, \underline{\sigma}_3$) are sufficient to describe the state of stress, since in this case the orientation of principle stresses is immaterial (Chen and Han, 1988; Dunne and Petrinic, 2005). The principle stresses for the stress tensor $\underline{\sigma}_{ij}$, represented in Eq. (2.43), are roots of the following characteristic equation:

$$\sigma^3 - I_1\,\sigma^2 + I_2\,\sigma - I_3 = 0 \tag{2.47}$$

where $\underline{\sigma}$ represents the three roots, and I_1, I_2, I_3 are the constants known as first, second and third invariants of hydrostatic stresses, respectively. These constants are defined as:

$$I_1 = \sigma_x + \sigma_y + \sigma_z \tag{2.48}$$

$$I_2 = (\sigma_x\sigma_y + \sigma_y\sigma_z + \sigma_z\sigma_x) - \tau_{xy}^2 - \tau_{yz}^2 - \tau_{zx}^2 \tag{2.49}$$

$$I_3 = \left| \sigma_{ij} \right| = \begin{vmatrix} \sigma_x & \tau_{xy} & \tau_{xz} \\ \tau_{xy} & \sigma_y & \tau_{yz} \\ \tau_{xz} & \tau_{yz} & \sigma_z \end{vmatrix} \qquad (2.50)$$

So the yield function represented in Eq. (2.42) can be represented as a function of the principle stresses:

$$f\left(\sigma_1, \sigma_2, \sigma_3, \tilde{\epsilon} \right) = 0 \qquad (2.51)$$

The three principal stresses, as well as most other stress invariants, can be represented in terms of the combination of the three stress invariants: the first invariants of hydrostatic stresses (I_1); second invariant of the deviatoric stress (J_2); and third invariant of the deviatoric stress (J_3). The invariants J_2, J_3 are defined as:

$$J_2 = (1/3)\left(\sigma_x^2 + \sigma_y^2 + \sigma_z^2 - \sigma_x\sigma_y - \sigma_x\sigma_z - \sigma_y\sigma_z + 3\tau_{yz}^2 + 3\tau_{xz}^2 + +3\tau_{xy}^2 \right) \qquad (2.52)$$

$$J_3 = (2/27)(\sigma_x^3 + \sigma_y^3 + \sigma_z^3) - (1/9)(\sigma_x^2\sigma_y + \sigma_x^2\sigma_z + \sigma_y^2\sigma_x + \sigma_y^2\sigma_z + \sigma_z^2\sigma_x + \sigma_z^2\sigma_y) \qquad (2.53)$$
$$+ (4/9)\sigma_x\sigma_z\sigma_y - (2/3)(\sigma_x\tau_{yz}^2 + \sigma_y\tau_{xz}^2 + \sigma_z\tau_{xy}^2) + (1/3)(\sigma_x\tau_{xy}^2 + \sigma_x\tau_{xz}^2 +$$
$$+ \sigma_y\tau_{xy}^2 + \sigma_y\tau_{yz}^2 + \sigma_z\tau_{xz}^2 + \sigma_z\tau_{yz}^2) + 2\tau_{yz}\tau_{xz}\tau_{xy}$$

Thus, Eq. (2.51) is replaced by the following expression:

$$f(I_1, J_2, J_3, \tilde{\epsilon}) = 0 \qquad (2.54)$$

The geometrical and physical interpretation of the invariants I_1, J_2, J_3 are described in detail in Annex A.

Including Eq. (2.44) into Eq. (2.41) the constitutive equation of the material under plastic deformations is obtained:

$$\Delta\underline{\sigma} = \underline{D}^e \, (\Delta\underline{\varepsilon} - \Delta\lambda \, \frac{\partial g}{\partial \underline{\sigma}_{ij}}) \tag{2.55}$$

The system of equations for the plasticity model includes the Eqs. (2.45), (2.54), and (2.55) that should be solved for set of the unknowns that are components of the stress tensor, and the plasticity internal variables, $\Delta\lambda$ and $\tilde{\epsilon}$.

2.5 CONCLUSIONS

Based on the literature review presented in this chapter, the following decisions are made for the development of a new constitutive model described in the next chapters:

- The model adopts a multidirectional fixed smeared cracking approach to account for crack opening and shear sliding process of concrete. It was discussed in this chapter that the models based on the smeared cracking approach are less precise on prediction of localization and propagation of the discrete cracks, but they are more appropriate for simulating relatively large concrete structures, mainly those with reinforcement that assure the formation of relatively high number of cracks. Besides, it is of special interest to use the proposed model for simulating structures made of steel fiber cement based materials. Since this type of materials assures formation of diffuse crack patterns, due to reinforcing mechanisms of fibers bridging the cracks, thus a smeared crack model can be practically more appropriate when compared to a model based on discrete crack approach.

- The proposed model simulates the inelastic compressive behaviour of material between cracks, by a numerical strategy that combines plasticity and damage theories. As it was argued in literature review, the models based on plasticity or damage theories alone are not able to describe some important mechanical behaviour of concrete (see section 2.3). So, in the proposed model, plasticity and damage theories are being merged in an attempt of constituting reliable approaches capable of simulating the strength and stiffness degradation and occurrence of irreversible deformations of concrete in compression.

Combination of the plasticity and damage theories is assured by considering that the plastic flow occurs in undamaged (with respect to compression) material, together with the strain based damage approach assuming state of damage equally distributed in all the material directions (isotropic damage). This type of coupling between the damage and plasticity was noticed robust and numerically efficient by many authors (as discussed in section 2.3). The isotropic damage approach is considered for the proposed model because of its convenience and applicability in structural analysis.

CHAPTER 3

TWO DIMENSIONAL PLASTIC-DAMAGE MULTIDIRECTIONAL FIXED SMEARED CRACK MODEL

3.1 INTRODUCTION

In this chapter the development of an efficient model capable of simulating the nonlinearities of cement based materials, like concrete, subjected to several loading paths is presented. For this purpose a brief description of an already existing multidirectional fixed smeared crack (SC) model is made (Sena-Cruz, 2004; Ventura- Gouveia, 2011). Then, a plasticity-damage model is proposed to consider the inelastic compressive deformation of material between the cracks, and its coupling with the SC is described. The predictive performance of the developed model is validated at the material level by simulating the stress-strain histories of a single element with one integration point (IP), loaded under some different scenarios. The model appraisal at the structural level is assessed in the next chapter.

3.2 MULTIDIRECTIONAL FIXED SMEARED CRACK MODEL (SC MODEL)

In the present section the SC model is briefly discussed and its presentation is restricted to plane stress state and at the domain of an IP. In this approach modelling cracked materials is based on the decomposition of the total incremental strain vector into an incremental crack strain vector ($\Delta\underline{\varepsilon}^{cr}$) and an incremental concrete strain vector ($\Delta\underline{\varepsilon}^{co}$), as earlier discussed in section 2.4.3. For the present stage of the model description, it is assumed that material between cracks develops linear elastic behaviour, therefore the $\Delta\underline{\varepsilon}^{co}$ is the incremental elastic strain vector ($\Delta\underline{\varepsilon}^{co} = \Delta\underline{\varepsilon}^{e}$). To simulate the plastic response of material in compression, the $\Delta\underline{\varepsilon}^{co}$ should also include the plastic part of the material deformation, $\Delta\underline{\varepsilon}^{co} = \Delta\underline{\varepsilon}^{e} + \Delta\underline{\varepsilon}^{p}$, which will be discussed in the next section.

The constitutive law for the elastic-cracked material can be, therefore, written as:

$$\Delta\overline{\underline{\sigma}} = \underline{D}^{e}\,(\Delta\underline{\varepsilon} - \Delta\underline{\varepsilon}^{cr}) \tag{3.1}$$

being $\Delta\overline{\underline{\sigma}} = \{\Delta\overline{\sigma}_1, \Delta\overline{\sigma}_2, \Delta\overline{\tau}_{12}\}$ the incremental stress vector induced into the material due to $\Delta\underline{\varepsilon} = \{\Delta\varepsilon_1, \Delta\varepsilon_2, \Delta\gamma_{12}\}$ and considering the constitutive matrix of the intact material, $\underline{D}^{e}$.

The $\Delta\underline{\varepsilon}^{cr}$ is obtained from the incremental local crack strain vector, $\Delta\underline{\varepsilon}^{cr}_{\ell}$, and the transformation matrix $\underline{T}^{cr}$ according to Eq. (2.32).

The vector $\Delta\underline{\varepsilon}^{cr}_{\ell}$ includes normal ($\Delta\varepsilon_n^{cr}$) and tangential ($\Delta\gamma_t^{cr}$) crack strain components of the *m* cracks that can be formed in an IP (see Eq. (2.33)). The transformation matrix of generic *i*th crack, $\underline{T}^{cr}_i$, is obtained by having orientation of the *i*th crack, θ_i, that is the angle between x_1 axis and the vector perpendicular to the *i*th crack (Sena-Cruz, 2004).

At the crack zone (damage material) of an IP, the opening and sliding process is governed by the crack constitutive relationship introduced in Eq. (2.35), (i.e. $\Delta\underline{\sigma}^{cr}_{\ell} = \underline{D}^{cr}\Delta\underline{\varepsilon}^{cr}_{\ell}$).

As defined in section 2.4.3, $\Delta\underline{\sigma}^{cr}_{\ell}$ is the vector of the incremental crack stress in the crack coordinate system with the contribution of normal, $\Delta\sigma_n^{cr}$, and tangential components,

$\Delta\tau_t^{cr}$, of the *m* cracks that can be formed in an IP (see Eq. (2.36)). Accordingly the constitutive law of *i*th generic crack, $\underline{D}_i^{cr}$, is given:

$$\underline{D}_i^{cr} = \begin{bmatrix} D_n^{cr} & 0 \\ 0 & D_t^{cr} \end{bmatrix} \tag{3.2}$$

where D_n^{cr} and D_t^{cr} represent, respectively, the stiffening/softening modulus corresponding to fracture mode I (normal), and fracture mode II (shear), of the *i*th crack.

At the IP the equilibrium condition is assured by imposing the Eq. (2.37), (i.e. $\Delta\underline{\sigma}_\ell^{cr} = \underline{T}^{cr}\Delta\underline{\bar{\sigma}}$).

In the course of the implementation of the constitutive model, it is assumed that at a certain loading step, *n*, the stress and strain quantities are known, and the local crack variables are updated as well. At the onset of the next loading step, *n+1*, Eq. (2.37) must be accomplished:

$$\underline{\sigma}_{\ell,n+1}^{cr} = \underline{T}_{n+1}^{cr}\ \underline{\bar{\sigma}}_{n+1} \tag{3.3}$$

Including Eqs. (3.1), (2.32) and (2.35) into Eq. (3.3), and taking into account that $\underline{\sigma}_{\ell,n+1}^{cr} = \underline{\sigma}_{\ell,n}^{cr} + \Delta\underline{\sigma}_{\ell,n+1}^{cr}$ and $\underline{\bar{\sigma}}_{n+1} = \underline{\bar{\sigma}}_n + \Delta\underline{\bar{\sigma}}_{n+1}$, yields, after some arrangements, in:

$$\underline{\sigma}_{\ell,n}^{cr} + \underline{D}_{n+1}^{cr}\Delta\underline{\varepsilon}_{\ell,n+1}^{cr} - \underline{T}_{n+1}^{cr}\underline{\bar{\sigma}}_n - \underline{T}_{n+1}^{cr}\underline{D}^e\ \Delta\underline{\varepsilon}_{n+1} + \underline{T}_{n+1}^{cr}\underline{D}^e\left[\underline{T}_{n+1}^{cr}\right]^T \Delta\underline{\varepsilon}_{\ell,n+1}^{cr} = \underline{0} \tag{3.4}$$

From the load step *n* to *n+1*, the the total strain increment ($\Delta\underline{\varepsilon}_{n+1}$) is already calculated by the main FEM iterative solving algorithm. Afterward the Newton-Raphson method is used to solve the Eq. (3.4), the system of nonlinear equations, where the unknowns are the components of $\Delta\underline{\varepsilon}_{\ell,n+1}^{cr}$. After obtaining $\Delta\underline{\varepsilon}_{\ell,n+1}^{cr}$, the $\Delta\underline{\varepsilon}_{n+1}^{cr}$ and $\Delta\underline{\sigma}_{\ell,n+1}^{cr}$ are determined from Eqs. (2.32) and (2.35), respectively, and finally $\Delta\underline{\bar{\sigma}}_{n+1}$ is calculated from Eq. (3.1).

The crack initiation is governed by the Rankine failure criterion that assumes that a crack occurs when the maximum principal tensile stress in a IP attains the concrete tensile strength, f_{ct}, under an assumed tolerance. After crack initiation, the relationship between the normal stress and the normal strain in the crack coordinate system, i.e. $\sigma_n^{cr} - \varepsilon_n^{cr}$, is simulated via the trilinear (Sena-Cruz, 2004) or the quadrilinear (Salehian and Barros, 2015) diagrams represented in Fig. 3.1. Normalized strain, ξ_i (for trilinear i=1,2; for quadrilinear i=1,2,3), and stress, α_i (for trilinear i=1,2; for quadrilinear i=1,2,3), parameters are used to define the transition points between linear segments, being G_f^I the fracture energy mode I, while l_b is the characteristic length (crack bandwidth) used to assure that the results of a material nonlinear analysis is not dependent of the refinement of the finite element mesh.
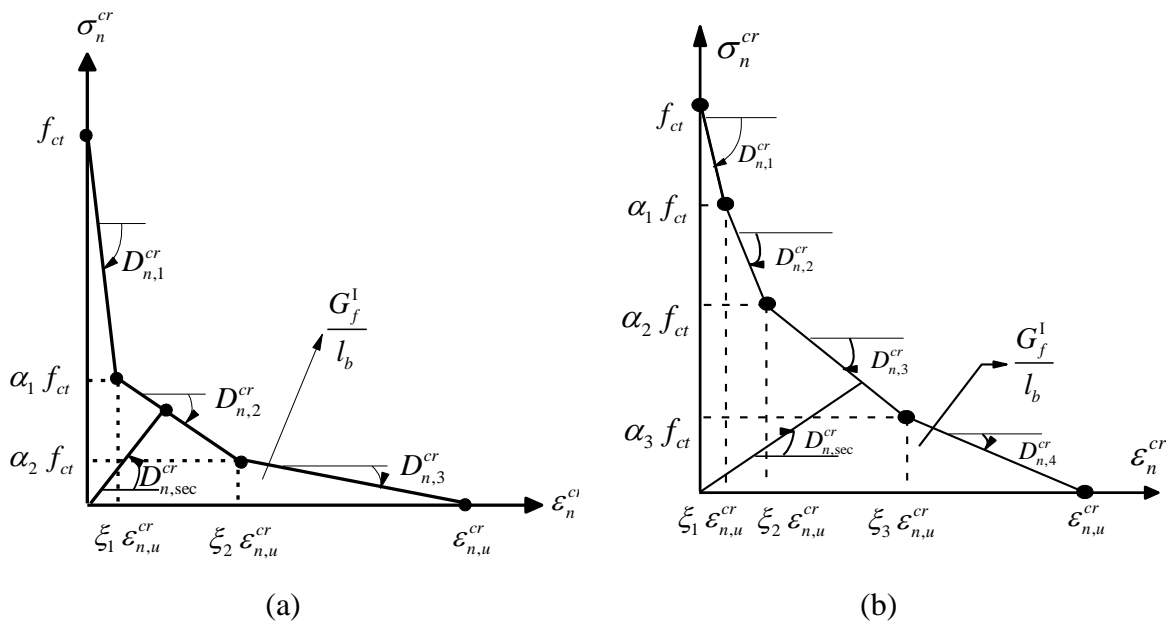
Fig. 3.1 – Diagrams for modelling the fracture mode I at the crack coordinate system: (a) trilinear diagram (Sena-Cruz, 2004), (b) quadrilinear diagram (Salehian and Barros, 2015).

The model considers shear behaviour of the cracked concrete according to two methods:

1) using an incremental crack shear stress shear strain approach based on a shear retention factor, β. According to this approach the fracture mode II modulus, D_t^{cr}, is simulated as:

$$D_t^{cr} = \frac{\beta}{1-\beta} G_c \tag{3.5}$$

where G_c is the concrete elastic shear modulus, while the shear retention factor, β, can be a constant value or, alternatively, as a function of current crack normal strain, ε_n^{cr}, and of ultimate crack normal strain, $\varepsilon_{n,u}^{cr}$, such as:

$$\beta = \left(1 - \frac{\varepsilon_n^{cr}}{\varepsilon_{n,u}^{cr}}\right)^{P_1} \tag{3.6}$$

being the exponent P_1 a parameter that defines the decrease rate of β with increasing ε_n^{cr}.

2) adopting a $\tau_t^{cr} - \gamma_t^{cr}$ softening law to simulate more correctly the shear stress transfer during the crack opening process, which allows better predictions in terms of load carrying capacity, deformability, and crack pattern of RC elements failing in shear (Ventura-Gouveia, 2011). The adopted shear softening law is represented in Fig. 3.2, and can be formulated by the following equation (Ventura-Gouveia, 2011):

$$\tau_t^{cr} = \begin{cases} D_{t,1}^{cr} \gamma_t^{cr} & 0 < \gamma_t^{cr} \le \gamma_{t,p}^{cr} \\ \tau_{t,p}^{cr} - \dfrac{\tau_{t,p}^{cr}}{\gamma_{t,u}^{cr} - \gamma_{t,p}^{cr}}\left(\gamma_t^{cr} - \gamma_{t,p}^{cr}\right) & \gamma_{t,p}^{cr} < \gamma_t^{cr} \le \gamma_{t,u}^{cr} \\ 0 & \gamma_t^{cr} > \gamma_{t,u}^{cr} \end{cases} \tag{3.7}$$

where $\tau_{t,p}^{cr}$ is the crack shear strength (shear stress at peak), $\gamma_{t,p}^{cr} = \tau_{t,p}^{cr}/D_{t,1}^{cr}$ is the crack shear strain at peak, and $\gamma_{t,u}^{cr}$ is the ultimate crack shear strain:

$$\gamma_{t,u}^{cr} = \frac{2G_{f,s}}{\tau_{t,p}^{cr} l_b}$$

(3.8)

being $G_{f,s}$ the fracture energy corresponding to fracture mode II, and l_b the crack bandwidth that is assumed to be equal to the one adopted to simulate the fracture mode I. Since no dedicated research is available on the process of determining the crack bandwidth parameter that bridges crack shear slide with shear deformation in the smeared shear crack band, it was decided to adopt the same strategy for the crack bandwidth regardless the type of fracture process. This decision has, at least, the advantage of assuring the same results regardless the mesh refinement, which is not assured when using the concept of shear retention factor in structures failing in shear. The inclination of the hardening branch of diagram, $D_{t,1}^{cr}$ (see Fig. 3.2), is introduced according to (3.5) where β is set as a constant value in the range $]0,1[$. More details corresponding to the crack shear softening diagram can be found elsewhere (Ventura-Gouveia, 2011).
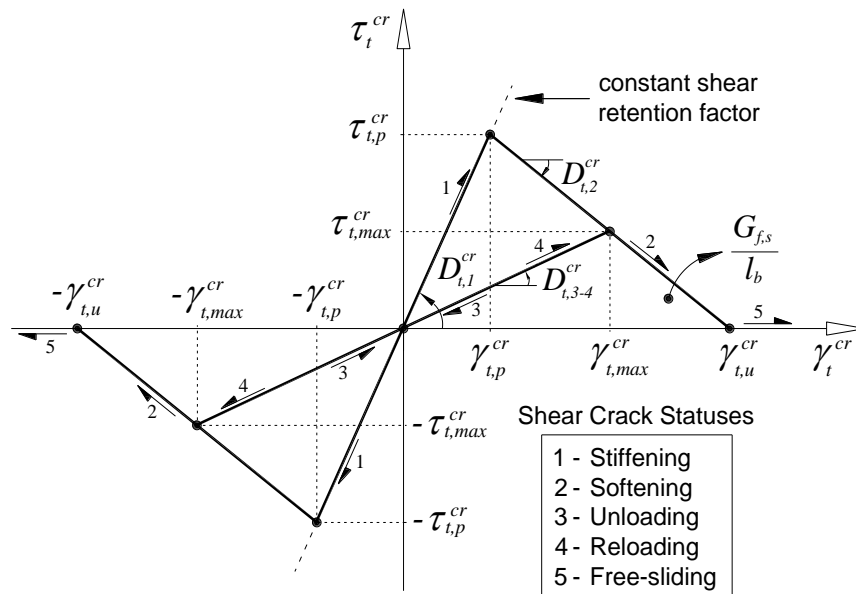
Fig. 3.2 – Diagram for modelling the fracture mode II at the crack coordinate system (Ventura-Gouveia, 2011).

Fig. 3.3 represents a schematic representation of the crack shear stress-shear strain diagram for the incremental approach based on shear retention factor (Eq. (3.5) and Eq.

(3.6)). It is verified that with the increase of γ_t^{cr} the crack shear modulus, D_t^{cr}, decreases but the crack shear stress, τ_t^{cr}, increases up to attain a maximum that depends on the parameters considered for the Eq. (3.6). This value can be much higher than the concrete shear strength according to available experimental data and design guidelines.
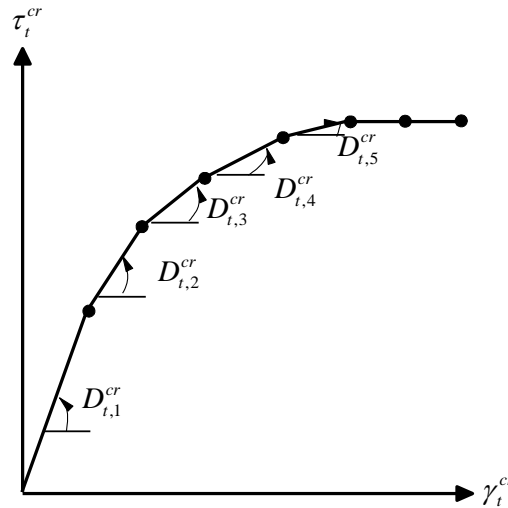
Fig. 3.3 – Relation between crack shear stress and crack shear strain for the incremental approach based on a shear retention factor (Barros et al., 2011).

For RC elements failing in bending the maximum value of γ_t^{cr} is relatively small, therefore simulating shear stress degradation with the evolution of γ_t^{cr} has not relevant impact of the predictive performance of the simulations. However, in RC structures failing in shear, the adoption of a constitutive law capable of simulating the crack shear stress degradation, as the one adopted in the present work, is fundamental for the predictive performance. The computing time consuming and the convergence stability of the incremental and iterative procedure of the model when adopting softening diagrams for simulating all the fracture processes are, however, increased, therefore shear softening approach is only recommended when shear is the governing failure mode.

3.3 PLASTIC-DAMAGE MULTIDIRECTIONAL FIXED SMEARED CRACK MODEL (PDSC MODEL)

The SC model described in the section 3.2 is now extended in order to simulate the inelastic behaviour of cement based materials in a compression-compression and

compression-tension stress fields. For this purpose a plastic-damage approach is coupled with the SC model, deriving a model herein designated as plastic-damage multidirectional fixed smeared crack (PDSC) model, which is capable of simulating the nonlinear behaviour of cement based materials due to both cracking and inelastic deformation in compression.

3.3.1 Damage concept in the context of plastic-damage model

To demonstrate the process of damage evolution in compression when an isotropic damage model is applied to simulate strength and stiffness degradation in compression, a simple bar loaded in compression is presented. This problem is similar to the case of the bar under tension proposed by Kachonov (1958). Consider a bar made by cement based materials and exposed to a certain level of damage due to uniaxial compressive force, N, as illustrated in Fig. 3.4a (Abu Al-Rub and Kim, 2010). The total cross-sectional area of the bar in damaged, nominal, status is denoted by A, then the stress developed on this area is defined as $\sigma = N/A$, herein designated as nominal stress. Due to the thermo-hygrometric effects during the curing process of cement based materials, voids and micro-cracks are formed even before these materials have been loaded by external loads (Pereira, 2012). However, the impact of these "defects" in terms of stiffness and strength of the material can be neglected, and the degeneration of the micro- into meso- and macro cracks is generally a gradual damage process depending on the evolution of the external loading conditions. Let's assume the variable A^D represents the area corresponding to these defects (meso- and macro cracks) (Fig. 3.4b). According to the principle of isotropic damage approach, a scalar measure, d_c, is defined to represent this damage level in total cross-sectional area (A), such that:

$$d_c = \frac{A_D}{A}$$

(3.9)

that can take values from 0 to 1. The state $d_c = 0$ implies the area of A is intact, while $d_c = 1$ denotes the area of A is completely damaged.

(a) the bar under compression   (b) Nominal (damaded) configuration

(c) Effective (undamaded) configuration
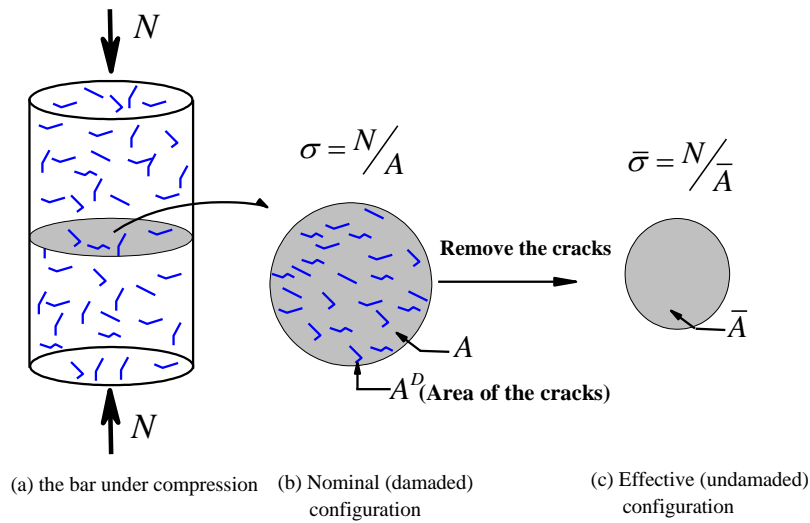
Fig. 3.4 – One dimensional representation of the effective and nominal stresses (Abu Al-Rub and Kim, 2010).

A fictitious undamaged, effective, area of $\bar{A}$, is defined by removing all the damage regions from the area of A ($\bar{A} = A - A_D = (1 - d_c)A$), then the uniaxial stress developed on the area $\bar{A}$, $\bar{\sigma} = N/\bar{A}$, is denoted as effective stress (Fig. 3.4c). Since the applied force on both damaged and undamaged areas is N, then the following relation holds between the uniaxial stress at damaged (nominal), σ, and undamaged (effective), $\bar{\sigma}$, configurations:

$$\sigma = (1 - d_c)\bar{\sigma} \tag{3.10}$$

By extending this concept for a multidimensional stress field, the relation between the nominal stress vector ($\underline{\sigma}$), and the effective stress vector ($\underline{\bar{\sigma}}$) for isotropic damage models can be expressed as:

$$\underline{\sigma} = (1 - d_c)\underline{\bar{\sigma}} \tag{3.11}$$

The present study adopts a stress based plasticity model formulated in effective stress space in combination with an isotropic damage model. The resultant plastic-damage approach is meant to utilize for modelling inelastic deformation of material under compression.
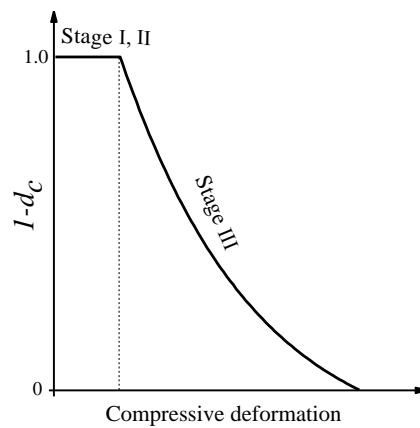
Fig. 3.5 – Schematic representation of damage evolution in the proposed model.

An important assumption of the proposed plastic-damage model is to define the stage that damage initiation takes place. In this study the damage threshold was assumed based on the phenomenological interpretation of the behaviour of current concrete under compressive loading. In section 2.2.1 the three distinct consecutive stages (stage I, stage II, and stage III) of cracking that can be identified in concrete under uniaxial compressive load were introduced. In this study damage initiation is assumed to be related to development of the major cracks formed after the peak load (i.e. stage III). Then evolution of the damage through the stage II is considered to be null (d_c=0), and nonlinear behaviour of the current concrete in this stage is reproduced by only a plasticity model. At the stage III the plasticity model is responsible for simulating irreversible plastic deformation and inelastic volumetric expansion of the material whereas the isotropic damage model deals with strength and stiffness degradation of the material due to formation of the major cracks. Fig. 3.5 demonstrates the schematic representation of the damage evolution at the proposed plastic-damage model for the three stages of cracking in uniaxial compression.

It is noted the statement of "damage" in the text intends to simulate the inelastic behaviour of concrete in compression by using a plastic-damage model, while cracking formation and propagation is simulated by a SC model. Therefore, if concrete is cracked and concrete between cracks experience inelastic deformation in compression, both models are coupled.

3.3.2 Constitutive relationship for PDSC model

For modelling of a cracked member with material between cracks in compression, the term $\Delta\underline{\varepsilon}^{co}$ is further decomposed into its elastic, $\Delta\underline{\varepsilon}^{e}$, and plastic parts, $\Delta\underline{\varepsilon}^{p}$, ($\Delta\underline{\varepsilon}^{co} = \Delta\underline{\varepsilon}^{e} + \Delta\underline{\varepsilon}^{p}$), thereby the incremental constitutive relation for the PDSC model is given by:

$$\Delta\underline{\bar{\sigma}} = \underline{D}^{e}(\Delta\underline{\varepsilon} - \Delta\underline{\varepsilon}^{p} - \Delta\underline{\varepsilon}^{cr}) \tag{3.12}$$

where the incremental crack strain vector, $\Delta\underline{\varepsilon}^{cr}$, is evaluated by the SC model described in section 3.2. A stress based plasticity model formulated in effective stress space, i.e. without considering damage, is responsible for the evaluation of $\Delta\underline{\varepsilon}^{p}$. The plasticity model assumes that plastic flow occurs on the undamaged material between the damaged regions formed during the strain softening compression stage of the material. Then the effective stress state obtained according to Eq. (3.12) needs to be mapped into nominal stress space according to the principle of CDM. This mapping process should distinguish the tensile from the compressive stress components, since the damage is only applied to these last ones. Ortiz (1985) proposed the split of the effective stress vector, $\underline{\bar{\sigma}}$, into positive (tensile) and negative (compressive) components to adopt different scalar damage variables for tension and compression. Such operation is given by:

$$\underline{\bar{\sigma}} = \underline{\bar{\sigma}}^{+} + \underline{\bar{\sigma}}^{-} , \qquad \underline{\bar{\sigma}}^{+} = \sum_{i}\langle\bar{\sigma}^{i}\rangle\underline{P}^{i}\otimes\underline{P}^{i} \tag{3.13}$$

where $\underline{\bar{\sigma}}^{+}$ and $\underline{\bar{\sigma}}^{-}$ are the positive and the negative parts of the effective stress vector, respectively, and $\bar{\sigma}^{i}$ is the ith principal stress extracted from vector $\underline{\bar{\sigma}}$, and $\underline{P}^{i}$ is the normalized eigenvector associated with the ith principal stress ($\bar{\sigma}^{i}$). The symbol $\langle.\rangle$ denotes Macaulay bracket function operating as $\langle x\rangle = (x+|x|)/2$.

The compressive damage scalar, d_c, must affect only the negative part of the effective stress vector, i.e. $\underline{\bar{\sigma}}^-$, therefore a similar approach to Eq. (3.11) gives the nominal stress vector, such as:

$$\underline{\sigma} = \underline{\bar{\sigma}}^+ + (1 - d_c)\underline{\bar{\sigma}}^-$$

(3.14)

3.3.3 – Plasticity model in effective stress space

The plastic strain vector, $\Delta\underline{\varepsilon}^p$, is evaluated by a time-independent plasticity model that is defined by four entities: yield function (yield surface); flow rule; evolution law for the hardening variable; and condition for defining loading-unloading process. In this study the yield function, *f*, was derived from the five-parameter Willam and Warnke (W-W) failure criterion (Willam and Warnke, 1974) (the details of this process are in the Annex B), which shows a good ability to represent the experimental results of cement based materials (Willam and Warnke, 1974; Swaddiwudhipong and Seow, 2006), and also satisfies all the requirements of being smooth, convex, pressure dependent, and curved in the meridian plane. The equation of this yield function is:

$$f\left(\underline{\bar{\sigma}};\, \bar{\sigma}_c(\tilde{\epsilon}_c)\right) = \left[\left(\frac{\bar{I}_1}{\sqrt{3}\,c} - \frac{\sqrt{2}\,b}{c}\sqrt{\bar{J}_2}\right)\bar{\sigma}_c(\tilde{\epsilon}_c) - \frac{2a}{c}\bar{J}_2\right]^{1/2} - \bar{\sigma}_c(\tilde{\epsilon}_c) = 0$$

(3.15)

where $\bar{I}_1$ is the first invariant of the effective stress tensor, $\bar{J}_2$ is the second invariant of the deviatoric effective stress tensor (see Eq. (2.48) and Eq. (2.52), respectively). The variables *a*, *b* and *c* are the scalars used to interpolate the current yield meridian between the tensile and compressive meridians, as described in detail in the Annex B.

The term $\bar{\sigma}_c(\tilde{\epsilon}_c)$, which appears in Eq. (3.15), is the hardening function depending on the hardening parameter $(\tilde{\epsilon}_c)$. The hardening parameter is a scalar measure used to characterize the plastic state of the material under compressive stress field. Therefore $\tilde{\epsilon}_c$ is an indicator of the degree of inelastic deformation the material has experienced during the loading history. The evolution of the yield surface during the plastic flow is governed

by $\tilde{\epsilon}_c$. As long as $\tilde{\epsilon}_c$ is null, no inelastic deformation occurred, and $f(\overline{\underline{\sigma}}; \overline{\sigma}_c(\tilde{\epsilon}_c = 0)) = 0$ corresponds to the initial yield surface.

When the effective stress state reaches to the yield surface at generic stage (*i*) of yielding process, $f_i \geq 0$, plastic strains are developed, being its increment evaluated by a flow rule:

$$\Delta\underline{\varepsilon}^p = \Delta\lambda \frac{\partial g}{\partial \overline{\underline{\sigma}}} \tag{3.16}$$

where g is a scalar function, called plastic potential function, and $\Delta\lambda$ is the non-negative plastic multiplier. In the present version of the model, $g = f$ was assumed (Dunne and Petrinic, 2005).

The state of hardening parameter, $\tilde{\epsilon}_c$, during the plastic flow is changed according to the following evolution law (Ristinmaa et al., 2007):

$$\Delta\tilde{\epsilon}_c = -\Delta\lambda \frac{\partial f}{\partial \overline{\sigma}_c} \tag{3.17}$$

The yield function (f) and plastic multiplier ($\Delta\lambda$) at any stage of loading and unloading paths are constrained to follows Kuhn-Tucker conditions:

$$\Delta\lambda \geq 0, \quad f(\overline{\underline{\sigma}}, \tilde{\epsilon}_c) \leq 0, \quad \Delta\lambda\, f(\overline{\underline{\sigma}}, \tilde{\epsilon}_c) = 0 \tag{3.18}$$

3.3.3.1 Hardening law

Compressive behaviour of the material in effective stress space is governed by the uniaxial hardening law of $\overline{\sigma}_c - \tilde{\epsilon}_c$ (Fig. 3.6a). The term $\overline{\sigma}_c$ is the uniaxial compressive stress in effective stress space, and the hardening parameter ($\tilde{\epsilon}_c$) is an equivalent plastic strain measure that is proportional to the plastic strain ($\underline{\varepsilon}^p$) developed in the material.

Hardening parameter corresponding to total axial strain at compression peak stress ($\tilde{\epsilon}_{c1}$) is obtained such that:

$$\tilde{\epsilon}_{c1} = \varepsilon_{c1} - f_c / E \tag{3.19}$$

being ε_{c1} the total strain at compression peak stress, and f_c the compressive strength.

In this study it is assumed that the compressive damage, d_c, is initiated at the plastic deformation corresponding to $\tilde{\epsilon}_{c1}$, i.e. if $\tilde{\epsilon}_c \leq \tilde{\epsilon}_{c1}$, then d_c =0 (Fig. 3.6b). According to this assumption, the effective and nominal responses are identical for the domain of $\tilde{\epsilon}_c \leq \tilde{\epsilon}_{c1}$ (Eq. (3.15) assuming d_c =0). Then $\bar{\sigma}_c - \tilde{\epsilon}_c$ for the domain of $\tilde{\epsilon}_c \leq \tilde{\epsilon}_{c1}$ can be directly obtained by experimental uniaxial stress-strain curves, which are in the nominal stress space, such relation was adopted according to the following equation:

$$\bar{\sigma}_c = E \left[\varepsilon_{c1} + E/(2\kappa) - \tilde{\epsilon}_c + \lambda \right] \tag{3.20}$$

where:

$$\kappa = f_c (\alpha_0 - 1) / \left[(f_{c0}/E)^2 - 2\alpha_0 f_c / E \varepsilon_{c1} + (\varepsilon_{c1})^2 \right] \tag{3.21}$$

$$\lambda = \left[E/\kappa (\varepsilon_{c1} - f_c/E - \tilde{\epsilon}_c) + (E/(2\kappa))^2 \right]^{1/2} \tag{3.22}$$

where f_{c0} is the uniaxial compressive strength at plastic threshold, i.e. $f_{c0} = \bar{\sigma}_c (\tilde{\epsilon}_c = 0) = \alpha_0 f_c$, and α_0 is a material constant to define the beginning of the nonlinear behaviour in uniaxial compressive stress-strain test.

For $\tilde{\epsilon}_c > \tilde{\epsilon}_{c1}$, the damage takes place ($d_c > 0$), then the effective stresses cannot be determined by direct identifications from relevant uniaxial compressive stress-strain tests (Gernay et al., 2013; Abu Al-Rub and Kim, 2010). For this domain ($\tilde{\epsilon}_c > \tilde{\epsilon}_{c1}$) and in order to reduce the number of parameters required in the plasticity model, a perfectly-plastic behaviour is assumed for the $\bar{\sigma}_c - \tilde{\epsilon}_c$ law, with an effective stress capacity equal to the

compressive strength of the material, $\bar{\sigma}_c(\tilde{\epsilon}_c) = f_c$. Fig. 3.6a represents the above described hardening law ($\bar{\sigma}_c - \tilde{\epsilon}_c$). In Annex C, the adopted $\bar{\sigma}_c - \tilde{\epsilon}_c$ law for the domain $\tilde{\epsilon}_c > \tilde{\epsilon}_{c1}$ is replaced by a more elaborated equation, and the resultant response of the proposed model in cyclic uniaxial compressive test is discussed.

(a)

(b)

(c)
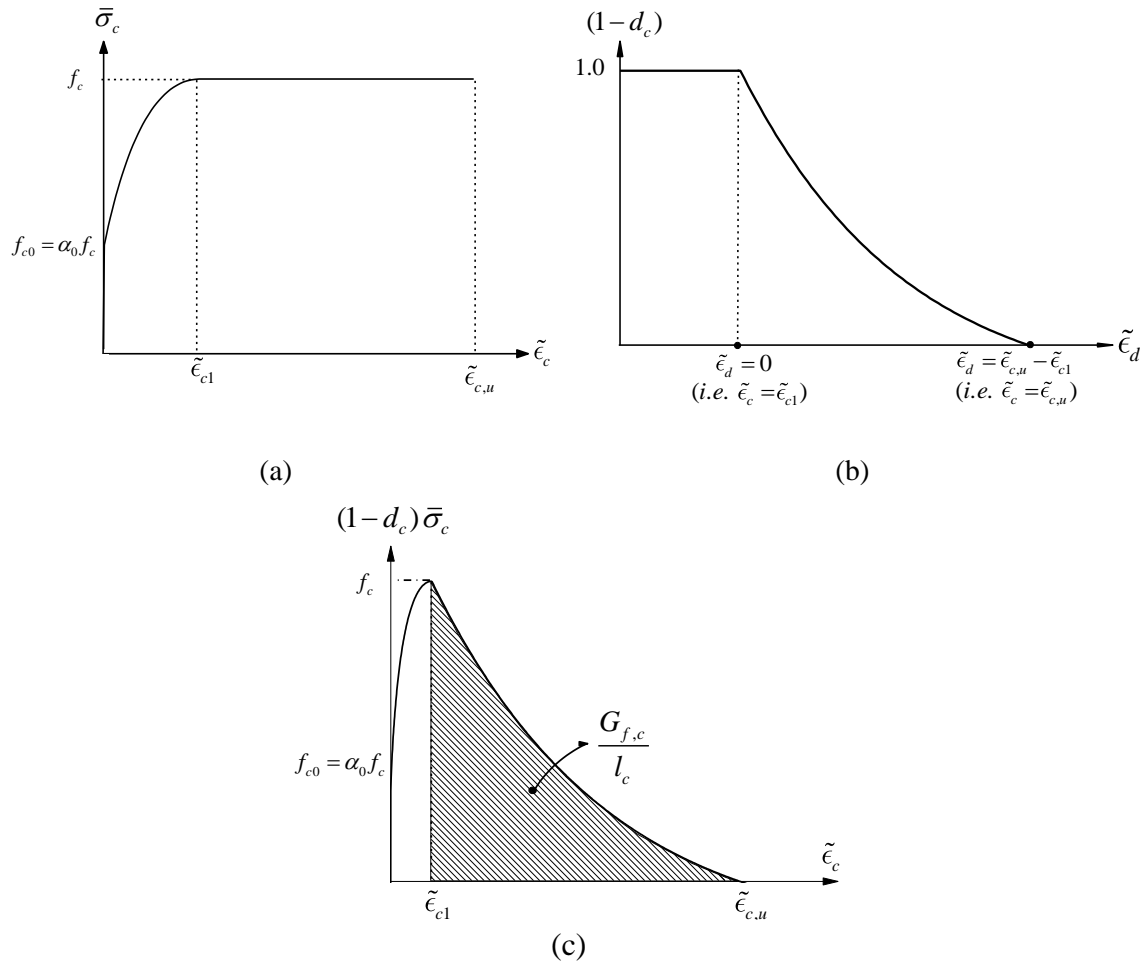
Fig. 3.6 – Diagrams for modelling the concrete compression behaviour: (a) the $\bar{\sigma}_c - \tilde{\epsilon}_c$ relation used in the plasticity model; (b) the $(1-d_c) - \tilde{\epsilon}_d$ relation adopted in the isotropic damage model; (c) the $(1-d_c)\bar{\sigma}_c - \tilde{\epsilon}_c$ diagram for compression with indication of the compressive fracture energy, $G_{f,c}$.

3.3.3.2 System of nonlinear equations

Assuming the material is in uncracked stage, or eventually the former active cracks are completely closed, then the incremental crack strain is null, $\Delta\underline{\varepsilon}^{cr} = \underline{0}$, and the constitutive law of PDSC model, Eq. (3.12), is reduced to:

$$\Delta \overline{\underline{\sigma}} = \underline{D}^e \, (\Delta \underline{\varepsilon} - \Delta \underline{\varepsilon}^p)$$
(3.23)

It is assumed that at a certain loading step of the incremental/iterative Newton-Raphson algorithm generally used for solving the equilibrium of the structure, n, the stress and strain quantities and the local variables of the plasticity ($\Delta \lambda_n$ and $\tilde{\epsilon}_{c,n}$) are known at all IPs. At the next loading step ($n+1$) the increment of total strain vector ($\Delta \underline{\varepsilon}_{n+1}$) is calculated by the main FEM iterative solving algorithm, and the problem is to update the effective stress vector ($\overline{\underline{\sigma}}_{n+1}$), the increment of plastic strain vector ($\Delta \underline{\varepsilon}_{n+1}^p$) and the local variables of the plasticity ($\Delta \lambda_{n+1}$ and $\tilde{\epsilon}_{c,n+1}$), in a way that is consistent with the constitutive law.

A mathematical basis scheme called return-mapping algorithm (Simo and Hughes, 1998) is used to calculate these unknowns within a generic loading step ($n+1$). The return-mapping algorithm is strain driven and basically consists of two steps: calculation of the elastic trial stress, elastic-predictor step, and mapping back to the proper yield surface using a local iterative process, plastic-corrector step. In the first approximation (elastic-predictor step), the effective stress vector ($\overline{\underline{\sigma}}_{n+1}^{trial}$) is calculated assuming null value for the plastic strain increment (the total strain increment is assumed to be elastic, $\Delta \underline{\varepsilon}_{n+1}^e = \Delta \underline{\varepsilon}_{n+1}$). In this step null plastic multiplier is assumed ($\Delta \lambda_{n+1} = 0$) and hardening parameter has the value corresponding to the previous loading step (n). The conditions at the elastic-predictor step can be written as:

$$\Delta \underline{\varepsilon}_{n+1}^{p,trial} = \underline{0}; \ \Delta \lambda_{n+1}^{trial} = 0$$
$$\Delta \overline{\underline{\sigma}}_{n+1}^{trial} = \underline{D}^e \, (\Delta \underline{\varepsilon}_{n+1} - \Delta \underline{\varepsilon}_{n+1}^{p,trial}) = \underline{D}^e \, \Delta \underline{\varepsilon}_{n+1}$$
$$\overline{\underline{\sigma}}_{n+1}^{trial} = \overline{\underline{\sigma}}_n + \Delta \overline{\underline{\sigma}}_{n+1}^{trial}$$
$$\underline{\varepsilon}_{n+1}^{p,trial} = \underline{\varepsilon}_n^p; \ \tilde{\epsilon}_{c,n+1}^{trial} = \tilde{\epsilon}_{c,n}$$
$$\overline{\sigma}_{c,n+1}^{trial} = \overline{\sigma}_{c,n}$$
(3.24)

Substitution of Eq. (3.24) into Eq. (3.15), gives the yield surface in trial state as:

$$f_{n+1}^{trial} = f_{n+1}^{trial}(\overline{\underline{\sigma}}_{n+1}^{trial}, \overline{\sigma}_{c,n+1}^{trial}) \tag{3.25}$$

Then behaviour of the material remains elastic if:

$$f_{n+1}^{trial}(\overline{\underline{\sigma}}_{n+1}^{trial}, \overline{\sigma}_{c,n+1}^{trial}) < 0 \tag{3.26}$$

In this case ($f_{n+1}^{trial} < 0$), it can be seen that the Kuhn-Tucker conditions are satisfied ($f_{n+1}^{trial}(\overline{\underline{\sigma}}_{n+1}^{trial}, \overline{\sigma}_{c,n+1}^{trial}) < 0$ and $\Delta\lambda_{n+1}^{trial} = 0$), implying that the trial state of stress ($\overline{\underline{\sigma}}_{n+1}^{trial}$) is acceptable. The updated variables at the load step *n+1* are given as:

$$\overline{\underline{\sigma}}_{n+1} = \overline{\underline{\sigma}}_{n+1}^{trial} \; ; \; \underline{\varepsilon}_{n+1}^{p} = \underline{\varepsilon}_{n}^{p} \; ; \; \tilde{\epsilon}_{c,n+1} = \tilde{\epsilon}_{c,n} \tag{3.27}$$

Otherwise, if $f_{n+1}^{trial}(\overline{\underline{\sigma}}_{n+1}^{trial}, \overline{\sigma}_{c,n+1}^{trial}) \geq 0$, the material enters into elasto-plastic behaviour (plastic flow occurs). In this case ($f_{n+1}^{trial} \geq 0$), the effective stress vector, at the load step n+1, should be corrected by applying a plastic-corrector step such that:

$$\begin{aligned} \overline{\underline{\sigma}}_{n+1} &= \overline{\underline{\sigma}}_{n} + \underline{D}^{e}(\Delta\underline{\varepsilon}_{n+1} - \Delta\underline{\varepsilon}_{n+1}^{p}) = \\ &(\overline{\underline{\sigma}}_{n} + \underline{D}^{e}\Delta\underline{\varepsilon}_{n+1}) - \underline{D}^{e}\Delta\underline{\varepsilon}_{n+1}^{p} = \underbrace{\overline{\underline{\sigma}}_{n+1}^{trial}}_{elastic\ predictor} - \underbrace{\underline{D}^{e}\Delta\underline{\varepsilon}_{n+1}^{p}}_{Plastic\ corrector} \end{aligned} \tag{3.28}$$

Including Eq. (3.16) in Eq. (3.38), yields:

$$\overline{\underline{\sigma}}_{n+1} = \underbrace{\overline{\underline{\sigma}}_{n+1}^{trial}}_{elastic\ predictor} - \underbrace{\Delta\lambda_{n+1}\underline{D}^{e}(\partial f_{n+1}/\partial\overline{\underline{\sigma}}_{n+1})}_{Plastic\ corrector} \tag{3.29}$$

The hardening variable at the loading step *n+1* should be updated according to the following equations:

$$\Delta\tilde{\epsilon}_{c,n+1} = -\Delta\lambda_{n+1}\frac{\partial f_{n+1}}{\partial\overline{\sigma}_{c,n+1}} \tag{3.30}$$

$$\tilde{\epsilon}_{c,n+1} = \tilde{\epsilon}_{c,n} + \Delta\tilde{\epsilon}_{c,n+1} \tag{3.31}$$

The system of equations for the proposed plasticity model includes the Eqs. (3.15), (3.29), (3.31) which can be rewritten in the form:

$$\underline{f}_{1,n+1} = \left(\underline{D}^e\right)^{-1}(\overline{\underline{\sigma}}_{n+1} - \overline{\underline{\sigma}}_{n+1}^{trial}) + \Delta\lambda_{n+1} \frac{\partial f_{n+1}}{\partial\overline{\underline{\sigma}}_{n+1}} = \underline{0} \tag{3.32a}$$

$$f_{2,n+1} = -\tilde{\epsilon}_{c,n+1} + \tilde{\epsilon}_c - \Delta\lambda_{n+1} \frac{\partial f_{n+1}}{\partial\overline{\sigma}_{c,n+1}} = 0 \tag{3.32b}$$

$$f_{3,n+1} = f_{n+1}\left(\overline{\underline{\sigma}}_{n+1}, \overline{\sigma}_{c,n+1}\right) = 0 \tag{3.32c}$$

The unknowns of the system of equations are the components of effective stress vector, $\overline{\underline{\sigma}}_{n+1}$, and the plasticity internal variables, $\Delta\lambda_{n+1}$ and $\tilde{\epsilon}_{c,n+1}$. An iterative local Newton-Raphson method is used to solve this system of equations, according to the following equation:

$$J_{n+1}^{(k)} \begin{bmatrix} d\overline{\underline{\sigma}}_{n+1}^{(k+1)} \\ d\tilde{\epsilon}_{c,n+1}^{(k+1)} \\ d\lambda_{n+1}^{(k+1)} \end{bmatrix} = \begin{bmatrix} -\underline{r}_{1,n+1}^{(k)} \\ -r_{2,n+1}^{(k)} \\ -r_{3,n+1}^{(k)} \end{bmatrix} \tag{3.33}$$

Within this procedure the objective is to minimize the residues vector, $\begin{bmatrix} -\underline{r}_{1,n+1}^{(k)} & -r_{2,n+1}^{(k)} & -r_{3,n+1}^{(k)} \end{bmatrix}^T$, to be less than an assumed tolerance. The variable k denotes the iteration required to minimize the residues vector. For this system of equations the residues $\underline{r}_{1,n+1}^{(k)}$, $r_{2,n+1}^{(k)}$, $r_{3,n+1}^{(k)}$ are given as:

$$\underline{r}_{1,n+1}^{(k)} = \left(\underline{D}^e\right)^{-1}(\overline{\underline{\sigma}}_{n+1}^{(k)} - \overline{\underline{\sigma}}_{n+1}^{trial}) + \Delta\lambda_{n+1}^{(k)} \frac{\partial f_{n+1}^{(k)}}{\partial\overline{\underline{\sigma}}_{n+1}^{(k)}}$$

$$r_{2,n+1}^{(k)} = -\tilde{\epsilon}_{c,n+1}^{(k)} + \tilde{\epsilon}_{c,n} - \Delta\lambda_{n+1}^{(k)} \frac{\partial f_{n+1}^{(k)}}{\partial\overline{\sigma}_{c,n+1}^{(k)}} \tag{3.34}$$

$$r_{3,n+1}^{(k)} = f_{n+1}^{(k)}\left(\overline{\underline{\sigma}}_{n+1}^{(k)}, \overline{\sigma}_{c,n+1}^{(k)}\right)$$

The Jacobian matrix ($J_{n+1}^{(k)}$) used in the iterative local Newton-Raphson method is given:

$$
J_{n+1}^{(k)} = \begin{bmatrix}
\dfrac{\partial f_{1,n+1}}{\partial \underline{\bar{\sigma}}_{n+1}} & \dfrac{\partial f_{1,n+1}}{\partial \tilde{\epsilon}_{c,n+1}} & \dfrac{\partial f_{1,n+1}}{\partial \lambda_{n+1}} \\[2ex]
\dfrac{\partial \underline{f}_{2,n+1}}{\partial \underline{\bar{\sigma}}_{n+1}} & \dfrac{\partial \underline{f}_{2,n+1}}{\partial \tilde{\epsilon}_{c,n+1}} & \dfrac{\partial \underline{f}_{2,n+1}}{\partial \lambda_{n+1}} \\[2ex]
\dfrac{\partial f_{3,n+1}}{\partial \underline{\bar{\sigma}}_{n+1}} & \dfrac{\partial f_{3,n+1}}{\partial \tilde{\epsilon}_{c,n+1}} & \dfrac{\partial f_{3,n+1}}{\partial \lambda_{n+1}}
\end{bmatrix}^{(k)}
\tag{3.35}
$$

where the components of the Jacobian matrix are as follows:

$$
\frac{\partial \underline{f}_{1,n+1}}{\partial \underline{\bar{\sigma}}_{n+1}} = \left(\underline{D}^e \right)^{-1} + \Delta\lambda_{n+1} \frac{\partial^2 f_{n+1}}{\left(\partial \underline{\bar{\sigma}}_{n+1} \right)^2}
$$

$$
\frac{\partial \underline{f}_{1,n+1}}{\partial \tilde{\epsilon}_{c,n+1}} = \Delta\lambda_{n+1} \frac{\partial^2 f_{n+1}}{\partial \underline{\bar{\sigma}}_{n+1} \partial \bar{\sigma}_{c,n+1}} \frac{\partial \bar{\sigma}_{c,n+1}}{\partial \tilde{\epsilon}_{c,n+1}}
\tag{3.36}
$$

$$
\frac{\partial \underline{f}_{1,n+1}}{\partial \lambda_{n+1}} = \frac{\partial f_{n+1}}{\partial \underline{\bar{\sigma}}_{n+1}}
$$

$$
\frac{\partial f_{2,n+1}}{\partial \underline{\bar{\sigma}}_{n+1}} = -\Delta\lambda_{n+1} \frac{\partial^2 f_{n+1}}{\partial \bar{\sigma}_{c,n+1} \partial \underline{\bar{\sigma}}_{n+1}}
$$

$$
\frac{\partial f_{2,n+1}}{\partial \tilde{\epsilon}_{c,n+1}} = -1 - \Delta\lambda_{n+1} \frac{\partial^2 f_{n+1}}{\left(\partial \bar{\sigma}_{c,n+1} \right)^2} \frac{\partial \bar{\sigma}_{c,n+1}}{\partial \tilde{\epsilon}_{c,n+1}}
\tag{3.37}
$$

$$
\frac{\partial f_{2,n+1}}{\partial \lambda_{n+1}} = - \frac{\partial f_{n+1}}{\partial \bar{\sigma}_{c,n+1}}
$$

$$
\frac{\partial f_{3,n+1}}{\partial \underline{\bar{\sigma}}_{n+1}} = \frac{\partial f_{n+1}}{\partial \underline{\bar{\sigma}}_{n+1}}
$$

$$
\frac{\partial f_{3,n+1}}{\partial \tilde{\epsilon}_{c,n+1}} = \frac{\partial f_{n+1}}{\partial \bar{\sigma}_{c,n+1}} \frac{\partial \bar{\sigma}_{c,n+1}}{\partial \tilde{\epsilon}_{c,n+1}}
\tag{3.38}
$$

$$
\frac{\partial f_{3,n+1}}{\partial \lambda_{n+1}} = 0
$$

The implementation of Eq. (3.35) requires other derivatives which are exposed in details in Annex D. These derivatives are: first and second order derivatives of the yield function respect to components of the effective stress vector (i.e. $\partial f / \partial \underline{\bar{\sigma}}$, $\partial^2 f / (\partial \underline{\bar{\sigma}})^2$); first and second order derivatives of the yield function respect to the hardening function ($\partial f / \partial \bar{\sigma}_c$, $\partial^2 f / (\partial \bar{\sigma}_c)^2$); the second order derivative of the yield function respect to the stress, and respect to the hardening function ($\partial^2 f / (\partial \underline{\bar{\sigma}} \partial \bar{\sigma}_c)$).

Once the convergence is obtained through the certain number of iteration (k), i.e. the residues $\underline{r}^{(k)}_{1,n+1}$, $r^{(k)}_{2,n+1}$, $r^{(k)}_{3,n+1}$ are less than an assumed tolerance, the unknowns can be obtained by summation of the increments calculated in each iteration ($i=1$ to k):

$$\underline{\bar{\sigma}}^{(k)}_{n+1} = \underline{\bar{\sigma}}_n + \sum_{i=1}^{k} d\underline{\bar{\sigma}}^{(i)}_{n+1}$$

$$\tilde{\epsilon}^{(k)}_{c,n+1} = \tilde{\epsilon}_{c,n} + \sum_{i=1}^{k} d\tilde{\epsilon}^{(i)}_{c,n+1} \qquad (3.39)$$

$$\Delta\lambda^{(k)}_{n+1} = \sum_{i=1}^{k} d\lambda^{(i)}_{n+1}$$

3.3.4 – Coupling the plasticity and the SC models

In this section the plasticity model, formulated in effective stress space, and the multidirectional smeared crack (SC) model are combined within an integrated approach in order to be capable of evaluating $\Delta\underline{\varepsilon}^{cr}$ and $\Delta\underline{\varepsilon}^{p}$ simultaneously at a generic IP. For a loading path the computation of the unknowns, which are the effective stress state and the local variables of the plasticity and cracking models, follows an iterative process similar to the return-mapping algorithm indicated in 3.3.3.2.

In the first approximation of the unknowns (elastic-predictor step), values of effective stress vector, i.e. trial stress ($\underline{\bar{\sigma}}^{trial}_{n+1}$), and incremental crack strain vector ($\Delta\underline{\varepsilon}^{cr,trial}_{n+1}$), and the local crack variables are calculated by only the SC model assuming the elastic behaviour for the material under compressive deformations. In this step null plastic multiplier is assumed ($\Delta\lambda^{trial}_{n+1} = 0$) and hardening parameter has the value corresponding

to the previous loading step (n). The conditions at the elastic-predictor step can be written as:

$$\Delta\underline{\varepsilon}_{n+1}^{p,trial} = \underline{0} \; ; \; \Delta\lambda_{n+1}^{trial} = 0 \; ; \; \underline{\varepsilon}_{n+1}^{p,trial} = \underline{\varepsilon}_{n}^{p}$$

$$\Delta\underline{\bar{\sigma}}_{n+1}^{trial} = \underline{D}^{e}(\Delta\underline{\varepsilon}_{n+1} - \Delta\underline{\varepsilon}_{n+1}^{cr,trial})$$

$$\bar{\underline{\sigma}}_{n+1}^{trial} = \bar{\underline{\sigma}}_{n} + \Delta\bar{\underline{\sigma}}_{n+1}^{trial}$$

$$\tilde{\epsilon}_{c,n+1}^{trial} = \tilde{\epsilon}_{c,n} \; ; \; \bar{\sigma}_{c,n+1}^{trial} = \bar{\sigma}_{c,n} \tag{3.40}$$

The value of yield function at the trial state, $f_{n+1}^{trial}(\underline{\bar{\sigma}}_{n+1}^{trial}, \bar{\sigma}_{c,n+1}^{trial})$, is calculated next. Behaviour of the material remains elastic-cracked if $f_{n+1}^{trial} < 0$, while for $f_{n+1}^{trial} \geq 0$, material enters into elasto-plastic-cracked behaviours and the state of effective stress needs to be corrected by determining the plastic part of strain increment ($\Delta\underline{\varepsilon}_{n+1}^{p}$), (plastic-corrector step).

As indicated in section 3.1, the equilibrium condition for a cracked IP is assured when:

$$\underline{\sigma}_{\ell,n}^{cr} + \underline{D}_{n+1}^{cr}\Delta\underline{\varepsilon}_{\ell,n+1}^{cr} = \left[\underline{T}_{n+1}^{cr}\right]\left(\bar{\underline{\sigma}}_{n} + \Delta\bar{\underline{\sigma}}_{n+1}\right) \tag{3.41}$$

Introducing $\bar{\underline{\sigma}}_{n+1} = \bar{\underline{\sigma}}_{n} + \Delta\bar{\underline{\sigma}}_{n+1}$ into Eq. (3.41), yields after some arrangements in:

$$\underline{f}_{1,n+1} = \underline{\sigma}_{\ell,n}^{cr} + \underline{D}_{n+1}^{cr}\Delta\underline{\varepsilon}_{\ell,n+1}^{cr} - \underline{T}_{n+1}^{cr}\bar{\underline{\sigma}}_{n+1} = \underline{0} \tag{3.42}$$

The system of equations proposed for the plasticity model (in section 3.3.3.2) needs also to be modified to include the deformational contribution of the sets of active smeared cracks ($\Delta\underline{\varepsilon}^{cr}$). By considering $\bar{\underline{\sigma}}_{n+1} = \bar{\underline{\sigma}}_{n} + \Delta\bar{\underline{\sigma}}_{n+1}$ and introducing Eqs. (2.32) and (3.16) into Eq. (3.12), yields after some arrangements in:

$$\underline{f}_{2,n+1} = \left(\bar{\underline{\sigma}}_{n+1} - \left[\bar{\underline{\sigma}}_{n} + \underline{D}^{e}(\Delta\underline{\varepsilon}_{n+1} - \left[\underline{T}_{n+1}^{cr}\right]^{T}\Delta\underline{\varepsilon}_{\ell,n+1}^{cr})\right]\right) + \Delta\lambda_{n+1}\underline{D}^{e}\left(\frac{\partial f}{\partial\bar{\underline{\sigma}}}\right)_{n+1} = \underline{0} \tag{3.43}$$

The equations describing the yield function (Eq. (3.32c)) and the evolution law for hardening variable (Eq. (3.32b)), still hold in the form deduced in section 3.3.3.2, since these equations are not affected by $\Delta\underline{\varepsilon}^{cr}$. In this section these two equations are designated as the followings:

$$f_{3,n+1} = -\tilde{\epsilon}_{c,n+1} + \tilde{\epsilon}_c - \Delta\lambda_{n+1}\frac{\partial f_{n+1}}{\partial\bar{\sigma}_{c,n+1}} = 0 \qquad (3.44)$$

$$f_{4,n+1} = f_{n+1}\left(\underline{\bar{\sigma}}_{n+1},\bar{\sigma}_{c,n+1}\right) = 0 \qquad (3.45)$$

The system of equations includes the Eqs. (3.42)-(3.45) which should be solved for set of the unknowns, namely, the effective stress vector, $\underline{\bar{\sigma}}_{n+1}$, the incremental local crack strain vector, $\Delta\underline{\varepsilon}^{cr}_{\ell,n+1}$, the plastic multiplier, $\Delta\lambda_{n+1}$, and the hardening parameter, $\tilde{\epsilon}_{c,n+1}$, all of them at the $n+1$ loading increment. An iterative local Newton-Raphson method is used to solve this system of equations, according to the following equation:

$$J_{n+1}^{(k)}\begin{bmatrix} d\underline{\varepsilon}^{cr,(k+1)}_{\ell,n+1} \\ d\underline{\bar{\sigma}}^{(k+1)}_{n+1} \\ d\tilde{\epsilon}^{(k+1)}_{c,n+1} \\ d\lambda^{(k+1)}_{n+1} \end{bmatrix} = \begin{bmatrix} -\underline{r}^{(k)}_{1,n+1} \\ -\underline{r}^{(k)}_{2,n+1} \\ -r^{(k)}_{3,n+1} \\ -r^{(k)}_{4,n+1} \end{bmatrix} \qquad (3.46)$$

where the residues are:

$$\underline{r}^{(k)}_{1,n+1} = \underline{\sigma}^{cr,(k)}_{\ell,n} + \underline{D}^{cr,(k)}_{n+1}\Delta\underline{\varepsilon}^{cr,(k)}_{\ell,n+1} - \underline{T}^{cr,(k)}_{n+1}\underline{\bar{\sigma}}_{n+1} \qquad (3.47a)$$

$$\underline{r}^{(k)}_{2,n+1} = \left(\underline{D}^e\right)^{-1}\left[\underline{\bar{\sigma}}^{(k)}_{n+1} - \underline{\bar{\sigma}}_n - \underline{D}^e\left(\Delta\underline{\varepsilon}^{(k)}_{n+1} - \left[\underline{T}^{cr,(k)}_{n+1}\right]^T\Delta\underline{\varepsilon}^{cr,(k)}_{\ell,n+1}\right)\right] + \Delta\lambda^{(k)}_{n+1}\frac{\partial f^{(k)}_{n+1}}{\partial\underline{\bar{\sigma}}^{(k)}_{n+1}} \qquad (3.47b)$$

$$r^{(k)}_{3,n+1} = -\tilde{\epsilon}^{(k)}_{c,n+1} + \tilde{\epsilon}_{c,n} - \Delta\lambda^{(k)}_{n+1}\frac{\partial f^{(k)}_{n+1}}{\partial\bar{\sigma}^{(k)}_{c,n+1}} \qquad (3.47c)$$

$$r^{(k)}_{4,n+1} = f^{(k)}_{n+1}\left(\underline{\bar{\sigma}}^{(k)}_{n+1},\bar{\sigma}^{(k)}_{c,n+1}\right) \qquad (3.47d)$$

The Jacobian matrix ($J_{n+1}^{(k)}$) used in the iterative local Newton-Raphson method is given:

$$
J_{n+1}^{(k)} =
\begin{bmatrix}
\dfrac{\partial \underline{f}_{1,n+1}}{\partial \underline{\varepsilon}_{\ell,n+1}^{cr}} & \dfrac{\partial \underline{f}_{1,n+1}}{\partial \underline{\overline{\sigma}}_{n+1}} & \dfrac{\partial \underline{f}_{1,n+1}}{\partial \tilde{\epsilon}_{c,n+1}} & \dfrac{\partial \underline{f}_{1,n+1}}{\partial \lambda_{n+1}} \\[3mm]
\dfrac{\underline{f}_{2,n+1}}{\partial \underline{\varepsilon}_{\ell,n+1}^{cr}} & \dfrac{\underline{f}_{2,n+1}}{\partial \underline{\overline{\sigma}}_{n+1}} & \dfrac{\underline{f}_{2,n+1}}{\partial \tilde{\epsilon}_{c,n+1}} & \dfrac{\underline{f}_{2,n+1}}{\partial \lambda_{n+1}} \\[3mm]
\dfrac{\partial f_{3,n+1}}{\partial \underline{\varepsilon}_{\ell,n+1}^{cr}} & \dfrac{\partial f_{3,n+1}}{\partial \underline{\overline{\sigma}}_{n+1}} & \dfrac{\partial f_{3,n+1}}{\partial \tilde{\epsilon}_{c,n+1}} & \dfrac{\partial f_{3,n+1}}{\partial \lambda_{n+1}} \\[3mm]
\dfrac{\partial f_{4,n+1}}{\partial \underline{\varepsilon}_{\ell,n+1}^{cr}} & \dfrac{\partial f_{4,n+1}}{\partial \underline{\overline{\sigma}}_{n+1}} & \dfrac{\partial f_{4,n+1}}{\partial \tilde{\epsilon}_{c,n+1}} & \dfrac{\partial f_{4,n+1}}{\partial \lambda_{n+1}}
\end{bmatrix}^{(k)}
\tag{3.48}
$$

where the components of the Jacobian matrix, Eq. (3.52), are as follows:

$$
\frac{\partial \underline{f}_{1,n+1}}{\partial \underline{\varepsilon}_{\ell,n+1}^{cr}} = \underline{D}_{n+1}^{cr}
$$

$$
\frac{\partial \underline{f}_{1,n+1}}{\partial \underline{\overline{\sigma}}_{n+1}} = -\underline{T}_{n+1}^{cr}
$$

$$
\frac{\partial \underline{f}_{1,n+1}}{\partial \tilde{\epsilon}_{c,n+1}} = 0
\tag{3.49}
$$

$$
\frac{\partial \underline{f}_{1,n+1}}{\partial \lambda_{n+1}} = 0
$$

$$
\frac{\partial \underline{f}_{2,n+1}}{\partial \underline{\varepsilon}_{\ell,n+1}^{cr}} = \left[\underline{T}_{n+1}^{cr} \right]^T
$$

$$
\frac{\partial \underline{f}_{2,n+1}}{\partial \underline{\overline{\sigma}}_{n+1}} = \left(\underline{D}^e \right)^{-1} + \Delta \lambda_{n+1} \frac{\partial^2 f_{n+1}}{\left(\partial \underline{\overline{\sigma}}_{n+1} \right)^2}
$$

$$
\frac{\partial \underline{f}_{2,n+1}}{\partial \tilde{\epsilon}_{c,n+1}} = \Delta \lambda_{n+1} \frac{\partial \overline{\sigma}_{c,n+1}}{\partial \tilde{\epsilon}_{c,n+1}} \frac{\partial^2 f_{n+1}}{\partial \overline{\sigma}_{c,n+1} \partial \underline{\overline{\sigma}}_{n+1}}
\tag{3.50}
$$

$$
\frac{\partial \underline{f}_{2,n+1}}{\partial \lambda_{n+1}} = \frac{\partial f_{n+1}}{\partial \underline{\overline{\sigma}}_{n+1}}
$$

$$\frac{\partial f_{3,n+1}}{\partial \underline{\varepsilon}_{\ell,n+1}^{cr}} = \underline{0}$$

$$\frac{\partial f_{3,n+1}}{\partial \overline{\underline{\sigma}}_{n+1}} = -\Delta\lambda_{n+1} \frac{\partial^2 f_{n+1}}{\partial \overline{\underline{\sigma}}_{n+1} \partial \overline{\sigma}_{c,n+1}}$$

$$\frac{\partial f_{3,n+1}}{\partial \tilde{\epsilon}_{c,n+1}} = -\Delta\lambda_{n+1} \frac{\partial \overline{\sigma}_{c,n+1}}{\partial \tilde{\epsilon}_{c,n+1}} \frac{\partial^2 f_{n+1}}{\left(\partial \overline{\sigma}_{c,n+1}\right)^2} - 1 \tag{3.51}$$

$$\frac{\partial f_{3,n+1}}{\partial \lambda_{n+1}} = -\frac{\partial f_{n+1}}{\partial \overline{\sigma}_{c,n+1}}$$

$$\frac{\partial f_{4,n+1}}{\partial \underline{\varepsilon}_{\ell,n+1}^{cr}} = \underline{0}$$

$$\frac{\partial f_{4,n+1}}{\partial \overline{\underline{\sigma}}_{n+1}} = \frac{\partial f_{n+1}}{\partial \overline{\underline{\sigma}}_{n+1}}$$

$$\frac{\partial f_{4,n+1}}{\partial \tilde{\epsilon}_{c,n+1}} = \frac{\partial \overline{\sigma}_{c,n+1}}{\partial \tilde{\epsilon}_{c,n+1}} \frac{\partial f_{n+1}}{\partial \overline{\sigma}_{c,n+1}} \tag{3.52}$$

$$\frac{\partial f_{4,n+1}}{\partial \lambda_{n+1}} = 0$$

Finally, once the convergence is obtained, i.e. the residues of the system of equations are less than an assumed tolerance, the unknowns can be obtained by summation of the increments calculated in each iteration (*i=1 to k*), such as:

$$\overline{\underline{\sigma}}_{n+1}^{(k)} = \overline{\underline{\sigma}}_n + \sum_{i=1}^{k} d\overline{\underline{\sigma}}_{n+1}^{(i)}$$

$$\tilde{\epsilon}_{c,n+1}^{(k)} = \tilde{\epsilon}_{c,n} + \sum_{i=1}^{k} d\tilde{\epsilon}_{c,n+1}^{(i)}$$

$$\Delta\lambda_{n+1}^{(k)} = \sum_{i=1}^{k} d\lambda_{n+1}^{(i)} \tag{3.53}$$

$$\Delta\underline{\varepsilon}_{\ell,n+1}^{cr,(k)} = \sum_{i=1}^{k} d\underline{\varepsilon}_{\ell,n+1}^{cr,(i)}$$

3.3.5 – Isotropic damage law

The stress vector ($\bar{\underline{\sigma}}_{n+1}$) obtained by solving the system of equations presented in the sections 3.3.3.2 and 3.3.4 is in the effective stress space, and must be transferred to the nominal stress space ($\underline{\sigma}_{n+1}$). For the damage models based on the isotropic damage mechanics, the evaluation of the nominal stress is performed by a damage-corrector step (Eq. (3.11)) without an iterative calculation process. The present model adopts a damage-corrector process according to the Eq. (3.14), which considers the compressive damage scalar (d_c) only for negative (compressive) part of effective stress vector. The evaluation of the compressive damage scalar (d_c) during loading history is obtained according to the approach proposed by Gernay et al. (2013):

$$d_c(\tilde{\epsilon}_d) = 1 - \exp(-a_c\tilde{\epsilon}_d) \tag{3.54}$$

where $\tilde{\epsilon}_d$ is a scalar parameter known as damage internal variable.

Accordingly, the damage internal variable, $\tilde{\epsilon}_d$, can be evaluated as a function of the plasticity hardening variable, $\tilde{\epsilon}_c$, which is available at the end of plasticity analysis. As indicated in section 3.3.3.1, damage initiates at the plastic deformation corresponding to $\tilde{\epsilon}_{c1}$, then the damage internal variable, $\tilde{\epsilon}_d$, can be defined as:

$$\tilde{\epsilon}_d = \begin{cases} 0 & if\ \tilde{\epsilon}_c \leq \tilde{\epsilon}_{c1} \\ \tilde{\epsilon}_c - \tilde{\epsilon}_{c1} & if\ \tilde{\epsilon}_c > \tilde{\epsilon}_{c1} \end{cases} \tag{3.55}$$

The non-dimensional parameter a_c indicates the rate of damage with the variation of $\tilde{\epsilon}_d$, obtained from:

$$a_c = 2.3 / (\tilde{\epsilon}_{c,u} - \tilde{\epsilon}_{c1}) \tag{3.56}$$

being $\tilde{\epsilon}_{c,u}$ the ultimate hardening parameter that is related to the compressive fracture energy, $G_{f,c}$, the characteristic length for compression, l_c, the compressive strength, f_c, and $\tilde{\epsilon}_{c1}$ according to the following equation:

$$\tilde{\epsilon}_{c,u} = \frac{3.1\,G_{f,c}}{l_c f_c} - \frac{11}{48}\tilde{\epsilon}_{c1} \tag{3.57}$$

The characteristic lengths in tension (crack bandwidth) and compression (l_c) are usually considered the same (Feenstra, 1993; Lee and Fenves, 2001; Gernay et al., 2013), then in the present approach $l_c = l_b$ was assumed. The parameters E, α_0, f_c, ε_{c1}, $G_{f,c}$, which simulate the response of the material under compression, can be obtained by executing uniaxial compression tests carried out in high stiff rigs, under displacement control, with specimens of slenderness capable of assuring a central zone considered in uniaxial stress field (it is assumed the same E in compression and tension). The instruction to derive the parameter $G_{f,c}$, from the uniaxial compressive tests, independent of geometry of specimens is represented in Annex E, but the detailed exposition can be found elsewhere (Jansen and Shah, 1997; Vasconcelos et al., 2009).

3.4 SIMULATION AT THE MATERIAL LEVEL

The stress-strain histories at the material (single element with one IP), loaded on some different scenarios are simulated by the proposed PDSC model. The loading procedure of the tests consists of imposing prescribed displacement increments and the crack bandwidth (l_b) was assumed equal to 100 mm. Since the concrete properties in each test were different, the corresponding values are indicated in the caption of the figures.

- *Monotonic and cyclic uniaxial compressive tests (Fig. 3.7 and Fig. 3.8):* A monotonic uniaxial compressive test of Kupfer et al. (1969), and a cyclic uniaxial compressive test of Karsan and Jirsa (1969) are simulated, and the predictive performance of the proposed model is appraised by comparing the numerical and experimental results. Fig. 3.7 shows that the hardening and softening stress-strain branches registered experimentally by Kupfer et al. (1969) are properly fitted by

the nominal response of the proposed model. For comparison, Fig. 3.7 also represents the response of the model in effective stress space. As can be seen the stress-strain response in both effective and nominal stress spaces are identical for the domain before attaining the peak ($\tilde{\epsilon}_c \leq \tilde{\epsilon}_{c1}$), whereas for higher deformations ($\tilde{\epsilon}_c > \tilde{\epsilon}_{c1}$) the two responses starts diverging because of the damage initiation process ($d_c > 0$). Under the cyclic uniaxial compression the model (nominal stress response) accurately simulate the stress-strain envelope response registered experimentally, but overestimates the plastic deformation of the material when unloading occurs (Fig. 3.8), since the assumption of perfect-plastic behaviour ($\bar{\sigma}_c(\tilde{\epsilon}_c) = f_c$) for the post peak stage (domain $\tilde{\epsilon}_c > \tilde{\epsilon}_{c1}$) of the $\bar{\sigma}_c - \tilde{\epsilon}_c$ law is a simplified approach to reduce the number of parameters required in the plasticity model.
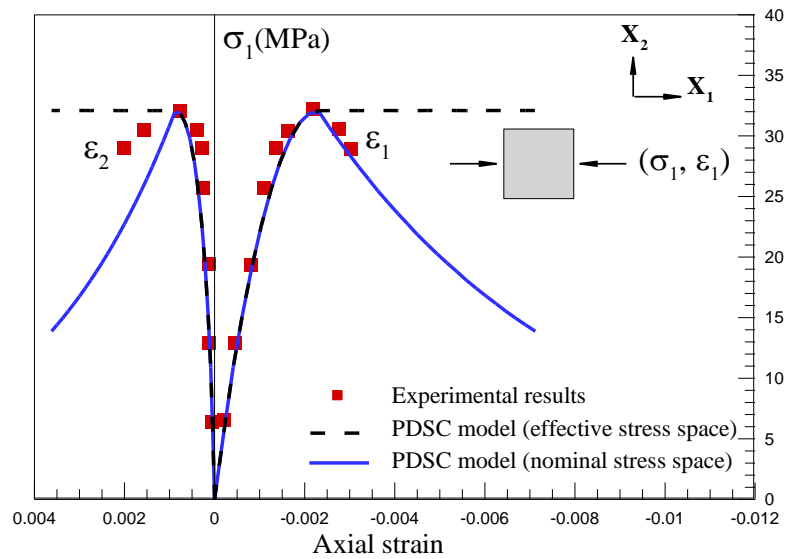
Fig. 3.7 – Experimental (Kupfer et al., 1969) vs. predicted stress-strain response of concrete under monotonic uniaxial compressive test: (Values for the parameters of the constitutive model: poison's ratio, ν =0.2; young's modulus, E=27 GPa; compressive strength, f_c =32 MPa; strain at compression peak stress ε_{c1} =0.0023; parameter to define elastic limit state α_0 =0.3; compressive fracture energy, $G_{f,c}$ =15.1 N/mm).

In Annex D the adopted $\bar{\sigma}_c - \tilde{\epsilon}_c$ law for the domain $\tilde{\epsilon}_c > \tilde{\epsilon}_{c1}$ is replaced by a more elaborated equation which gives better approximation in simulation of the

unloading phase. Another alternative to better predict the residual strain in unloading phases is to follow a more sophisticated diagram, like the one proposed by Barros et al. (2008) but this approach it too demanding in terms of computer time consuming when integrated in a PDSC model, and when the final goal is using this model for the analysis of structures of relatively large dimensions.
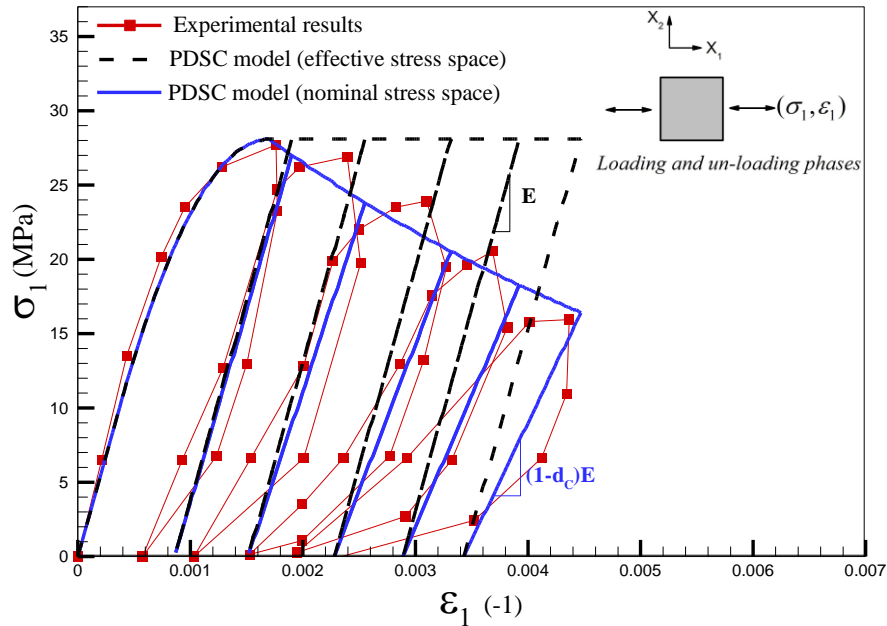
Fig. 3.8 – Experimental (Karsan and Jirsa, 1969) vs. predicted stress-strain response of concrete under cyclic uniaxial compressive test: (Values for the parameters of the constitutive model: ν =0.2; E=27 GPa; α_0 =0.3; ε_{c1} =0.0017; f_c =28 MPa; $G_{f,c}$ =11.5 N/mm).

- *Simulation of closing a crack developed in one direction, by imposing compressive load in the orthogonal direction (Fig. 3.9):* The element is initially subjected to the uniaxial tension in the direction of X_1 (Step 1). Then a crack is formed with the orientation of $\theta = 0^o$, and further propagated up to a stage that the crack does not be able to transfer more tensile stresses (fully opened crack status). At this stage the displacement in the direction of X_1 is fixed (Step 2), and the element is loaded by compressive displacements in the X_2 direction up to end of the analysis (Step 3).

Due to applied compressive displacements, uniaxial compressive stresses are induced in the material in the X_2 direction. Consequently, expansion of the material in the X_1 direction imposes the crack be gradually closing. When the

material is in the compression softening phase, in X_2 direction, the crack will be completely closed. When the crack closes, the state of stress is changed to biaxial compression, and a second hardening-softening response is reproduced corresponding to the appropriate biaxial state of stress. The above-described loading path was successfully simulated by the proposed model, and the prediction agrees well with the solution of Cervenka and Papanikolaou (2008).
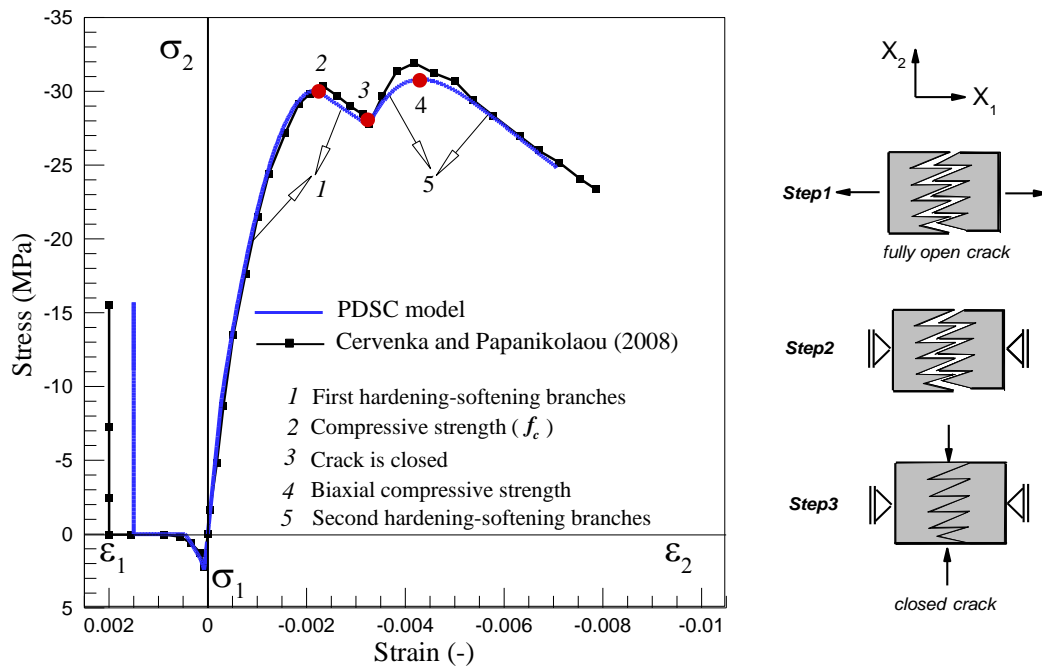
Fig. 3.9 – Prediction of the PDSC model for closing a crack developed in one direction, by imposing compressive load in the orthogonal direction (Values for the parameters of the constitutive model: ν =0.2; E=36 GPa; f_c =30 MPa; $G_{f,c}$ =30 N/mm; ε_{c1} =0.0022; α_0 =0.3; f_{ct} =2.45 MPa; G_f^I =0.05 N/mm; ξ_1 =0.2; α_1 =0.7; ξ_2 =0.75; α_2 =0.2.

3.5 CONCLUSIONS

This Chapter describes a two dimensional (plane stress) plastic-damage multidirectional fixed smeared cracking (PDSC) model to simulate the failure process of concrete and reinforced concrete (RC) structures subjected to different loading paths. The model proposes a unified approach combining a multidirectional fixed smeared crack model to simulate the crack initiation and propagation with a plastic-damage model to account for the inelastic compressive behaviour of concrete between cracks. The smeared crack model

considers the possibility of forming several cracks in the same integration point during the cracking process. The plasticity part accounts for the development of irreversible strains and volumetric strain in compression, whereas the strain softening and stiffness degradation of the material under compression are controlled by an isotropic strain base damage model. The model appraisal is performed by simulating several tests at the material level (single element with one IP). Monotonic and cyclic uniaxial compressive tests were simulated at first, followed by a sophisticated biaxial tension-compression numerical test which is intended to demonstrate the interaction between cracking and plasticity-damage parts of the model. The results of the simulated examples are in close agreement with the experimental data or the results reported by the other authors.

It should be noted that the applications of the proposed model in structural analysis are described in the next chapter (chapter 4).

CHAPTER 4

APPLICATION OF TWO DIMENSIONAL PDSC MODEL IN STRUCTURAL ANALYSIS

4.1 INTRODUCTION

In this chapter, the structural performance of the proposed model is assessed. For this purpose, PDSC constitutive model, described in chapter 3, was implemented into FEMIX 4.0 computer program (Sena-Cruz et al., 2007) as a new approach to simulate the nonlinear behaviour of cement based structures. FEMIX 4.0 is a computer code whose purpose is the analysis of structures by the Finite Element Method (FEM). This code is based on the displacement method, being a large library of types of finite elements available, e.g., 3D frames and trusses, plane stress elements, flat or curved elements for shells, and 3D solid elements. Linear elements may have two or three nodes, plane stress and shell elements may be 4, 8 or 9-noded and 8 or 20 noded hexahedra may be used in 3D solid analyses. This element library is complemented with a set of point, line and surface springs that model elastic contact with the supports, and also several types of interface elements to model inter-element contact. Embedded line elements can be added to other types of elements to model reinforcement bars. All these types of elements can be simultaneously included in the same analysis, with the exception of some incompatible combinations. The analysis may be static or dynamic and the material behaviour may be linear or nonlinear. Data input is facilitated by the possibility of importing CAD models.

Post processing is performed with a general purpose scientific visualization program named *drawmesh,* or more recently by using GID.

In the same nonlinear analysis several nonlinear models may be simultaneously considered, allowing, for instance, the combination of reinforced concrete with strengthening components, which exhibit distinct nonlinear constitutive laws. Interface elements with appropriate friction laws and nonlinear springs may also be simultaneously considered. The global response history is recorded in all the sampling points for selected post-processing. Advanced numerical techniques are available, such as the Newton-Raphson method combined with arc-length techniques and path dependent or independent algorithms. When the size of the systems of linear equations is very large, a preconditioned conjugate gradient method can be advantageously used.

The set of experimental tests simulated in this chapter, has covered a wide range of geometry of specimens, concrete type, loading configurations, and reinforcement conditions in order to demonstrate the robustness of the developed model. Moreover, the simulated structural elements are of particular interest for the assessment of the reliability of the proposed model, since in these examples the failure mechanism involved simultaneous occurrence of cracking and inelastic deformation in compression. In this type of simulations the concrete of a large number of IP is submitted to cracking and inelastic compressive deformations. This situation can be considered as a complex loading scenario, since both smeared cracking and plastic-damage parts of the model are active over a large region of the simulated structure.

4.2 STRUCTURAL EXAMPLES

4.2.1 Shear RC walls

To highlight the efficiency of the proposed constitutive model, the shear wall panels, tested by Maier and Thürlimann (1985), were simulated. The analysed specimens are registered at the experiment as S1, S2, S3, S4, S9, and S10. The experimental loading procedure introduces an initial vertical compressive force, F_v, and then a horizontal force, F_h, that was increased up to the failure of the wall. These shear walls had a

relatively thick beam at their bottom and top edges for fixing the walls to the foundation, and for applying F_h and F_v, respectively, as depicted in Fig. 4.1. The analysed shear walls differ in geometry, reinforcement ratio, and initial vertical load (F_v).
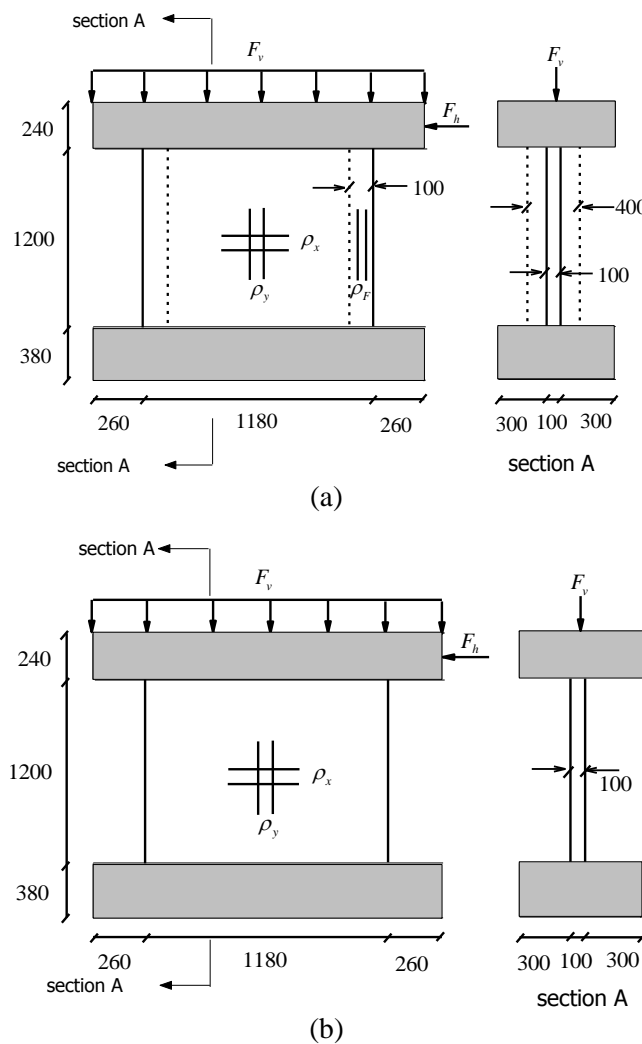
Fig. 4.1 – Geometry and loading configurations of the shear walls tested by Maier and Thürlimann (1985) (dimensions in mm): (a) the walls in *group A* (with vertical flange); (b) the walls in *group B* (without vertical flange).

These walls can be categorized considering geometry of the walls in two groups: *group A*, which includes walls with vertical flanges at their lateral edges; *group B*, which contains the walls with uniform rectangular cross section (without vertical flanges). All the walls are reinforced in both vertical and horizontal directions with the reinforcement ratios

designated as ρ_x and ρ_y. For the walls at the *group A* (specimens with vertical flanges), ρ_F indicates the reinforcement ratio of the vertical flanges. Table 4.1 includes the details corresponding to geometry, reinforcement ratios, and initial vertical force for each shear wall analysed in this section.

Table 4.1 – Details for the shear wall panels.

Specimen ID	geometry	ρ_x (%)	ρ_y (%)	ρ_F (%)	F_v (kN)	$F_{h,u}^{exp}$ (kN)	$F_{h,u}^{num}$ (kN)	$\left|F_{h,u}^{exp} - F_{h,u}^{num}\right|\big/F_{h,u}^{exp}$ (%)
S1	*group A*	1.03	1.16	1.16	433	680	721	6.0
S2	*group A*	1.03	1.16	1.16	1653	928	958	3.3
S3	*group A*	1.03	2.46	2.46	424	977	991	1.4
S4	*group B*	1.03	1.05	1.05	262	392	364	7.1
S9	*group B*	0.0	0.99	0.99	260	342	310	9.3
S10	*group B*	0.98	1.0	5.71	262	670	656	2
							average	4.85

FEM modelling of the walls and top beams were performed using 8-noded serendipity plane stress finite elements with 3×3 Gauss-Legendre IP scheme. Fig. 4.2a presents, as an example, the finite element mesh used for analysis of the wall S4. Instead of modelling the foundation, the bottom nodes of the panels are fixed in vertical and horizontal directions. The vertical and horizontal loads are uniformly distributed over the edges of the top beam, as schematically represented in Fig. 4.2a. Elements of the top beam are assumed to exhibit linear elastic behaviour during the analysis, since no damage is reported for these elements in the original papers. For modelling the behaviour of the steel bars, the stress-strain relationship represented in Fig. 4.3 was adopted (Sena-Cruz, 2004). The reinforcement is meshed using 2-noded perfect bonded embedded cables with two IPs. The values of parameters used to define the constitutive models of steel and concrete are included in Table 4.2 and Table 4.3, respectively. The effect of tension-stiffening was indirectly simulated using the trilinear tension-softening diagram.

The experimental relationship between the applied horizontal force and the horizontal displacement of the top beam, F_h-U_h, for the wall S4 is represented in Fig. 4.2b. This figure also includes the predicted F_h-U_h response obtained by both PDSC and SC models.

(a)

(b)

(c)

(d)

(e)
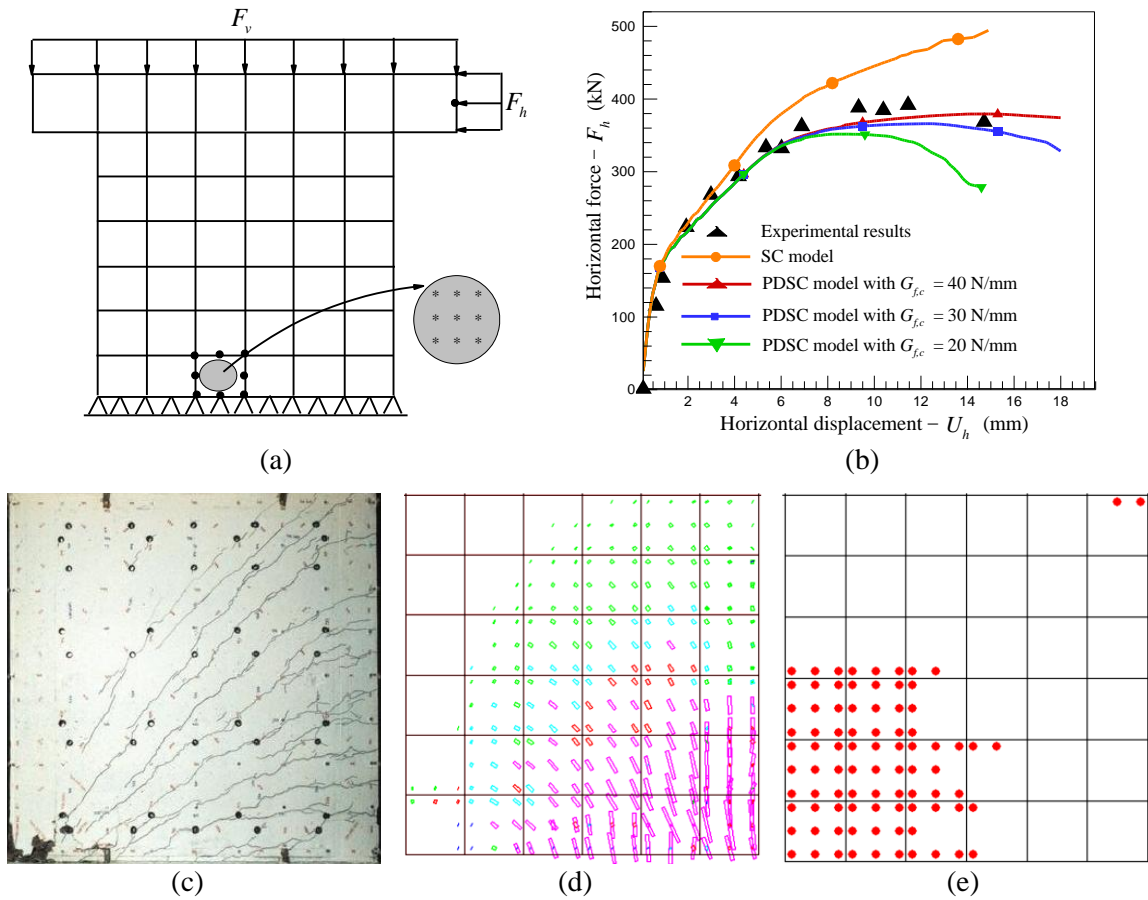
Fig. 4.2 – Simulation of the S4 shear wall tested by Maier and Thürlimann (1985): (a) finite element mesh used for the analysis; (b) horizontal load vs. horizontal displacement diagram, F_h-U_h; (c) experimentally observed crack pattern (Maier and Thürlimann, 1985); (d) crack pattern and (e) plastic zone (results of (d) and (e) correspond to $U_h \approx 18\,mm$, the final converged step, for the simulation using $G_{f,c} = 30$ N/mm) (Notes: (1) - In pink color: crack completely open; in red color: crack in the opening process; in cyan color: crack in the reopening process; in green color: crack in the closing process; in blue color: closed crack; in red circle: the plastic zone; (2) - The crack pattern and plastic zone are represented over the finite element mesh adopted for the concrete).

Table 4.2 – Values of the parameters of the steel constitutive model for the shear walls tests.

	ε_{sy} (%)	σ_{sy} (N/mm^2)	ε_{sh} (%)	σ_{sh} (N/mm^2)	ε_{su} (%)	σ_{su} (N/mm^2)	Third branch exponent
$\phi 8$	0.287	574	0.287	574	2.46	764	1
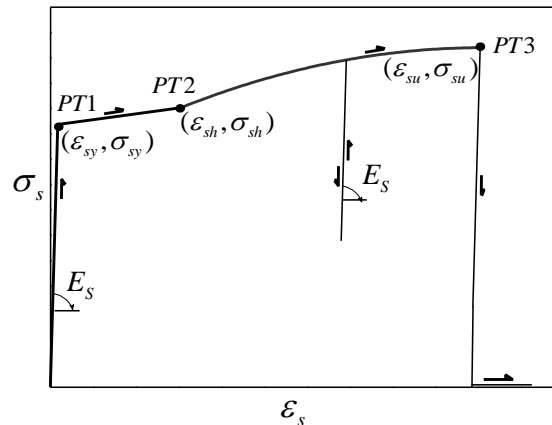
Fig. 4.3 – Uniaxial constitutive model (for both tension and
compression) for the steel bars (Sena-Cruz, 2004).

Table 4.3 – Values of the parameters of the concrete constitutive model for shear wall test.

Property	Value
Poisson's ratio	0.2
Young's modulus	$E = 26000 \ N/mm^2$
Parameters defining the plastic-damage part of the model	$\alpha_0 = 0.4$; $f_c = 30.0$ N/mm²; $\varepsilon_{c1} = 0.0035$; $G_{f,c} = 20, 30, 40$ N/mm for the wall S4; $G_{f,c} = 30$ N/mm for other walls
Trilinear tension softening diagram (Fig. 3.1a)	$f_{ct} = 2.2$ N/mm²; $G_f^1 = 0.14$ N/mm; $\xi_1 = 0.15$; $\alpha_1 = 0.3$; $\xi_2 = 0.575$; $\alpha_2 = 0.15$
Parameter defining the mode I fracture energy available to the new crack (Sena-Cruz, 2004)	2
Type of shear retention factor law	$P_1 = 2$
Crack bandwidth	Square root of the area of Gauss integration point
Threshold angle (Sena-Cruz, 2004)	30 degree
Maximum number of cracks per integration point (Sena-Cruz, 2004)	2

According to the experimental observations, the wall S4 exhibits a ductile F_h-U_h response after attaining the peak load, and the failure was governed by crushing of concrete at the bottom left side of the panel. Predictions of the PDSC model are obtained for three levels of compressive fracture energy ($G_{f,c} = 20, 30, 40 \ N/mm$) to evident the effect of different rate of compressive softening on behaviour of the simulated wall. At $U_h \approx 4 \ mm$ the IP closest to the left bottom side of the wall enters to the compressive softening phase ($d_c > 0$). After $U_h \approx 7 \ mm$ the load carrying capacity and ductility of the

simulated F_h-U_h responses are significantly affected by changing the compressive fracture energy; the load carrying capacity and ductility increase with $G_{f,c}$. Ductility of the wall is underestimated for the simulation with $G_{f,c}$=20 N/mm, and overestimated when using $G_{f,c}$=40 N/mm. A proper fit of the experimentally observed ductility and softening response after peak load was obtained for $G_{f,c}$=30 N/mm. This value is close to the upper limit of the interval values obtained by Vonk (1992). Fig. 4.2d and Fig. 4.2e present, respectively, the numerical crack pattern and the plastic zone, i.e. the area indicating those IPs under inelastic compressive deformation ($\tilde{\epsilon}_c > 0$), for the simulation using $G_{f,c}$ =30 N/mm, at the deformation corresponding to $U_h \approx 18\,mm$ (final converged step). A general analysis of Fig. 4.2d and Fig. 4.2e demonstrate the cracks with fully opened status are spread over the right lower side of the panel (tensile zone) while the plastic zones are concentrated at the bottom left corner of the panel. This numerical prediction correlates well with the experimental observations (see Fig. 4.2c).

The F_h-U_h prediction of the SC model is similar to those of the PDSC model only in the beginning stage (up to $U_h \approx 1\,mm$) when inelastic deformation due to compression is negligible, but for higher displacements the two models start diverging significantly. The SC model does not consider the inelastic behaviour of concrete under compression that justifies the significant overestimation of the predicted load carrying capacity of the simulated panel.

Size of the finite element mesh used for the analysis of the wall S4 is refined with a factor of four in order to show that the structural response predicted by the PDSC model is not dependent of the adopted mesh refinement. Fig. 4.4a shows the refined mesh adopted for this analysis. Eight-noded serendipity plane stress finite elements with 3×3 Gauss–Legendre IP scheme are adopted. The F_h-U_h relationship predicted by the analysis with the refined mesh is compared in Fig. 4.4b with that of the analysis with the coarse mesh (the one already obtained in Fig.4.2b using $G_{f,c}$=30 N/mm). From this figure it is verified that sensitivity of the structural response of the PDSC model to the applied mesh schemes is negligible. Both meshes show similar cracking patterns (see Fig. 4.2d and Fig. 4.4c).

(a)

(b)

(c)
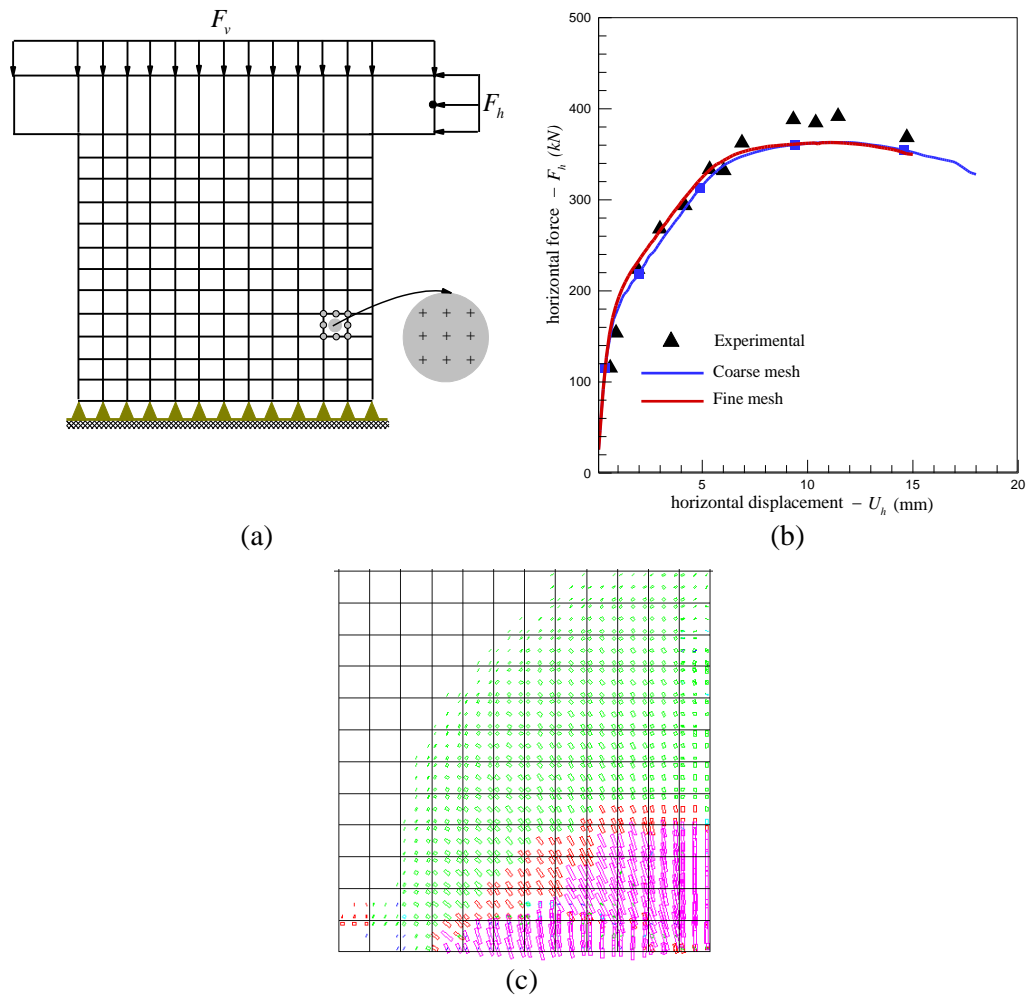
Fig. 4.4 – Sensitivity of the analysis of the panel S4 respect to the size of finite element mesh: (a) refined finite element mesh used for analysis; (b) F_h-U_h relationship; (c) Numerical crack pattern obtained at final converged step of the analysis. Note: the crack pattern is represented over the finite element mesh adopted for the concrete.

Results of the analysis for the other shear walls are represented in Fig. 4.5 in terms of F_h-U_h relationship and crack pattern. As can be seen in this figure the PDSC model assuming $G_{f,c}$=30 N/mm was able to accurately predict the overall experimental F_h-U_h behaviour and the experimental crack patterns of these walls.
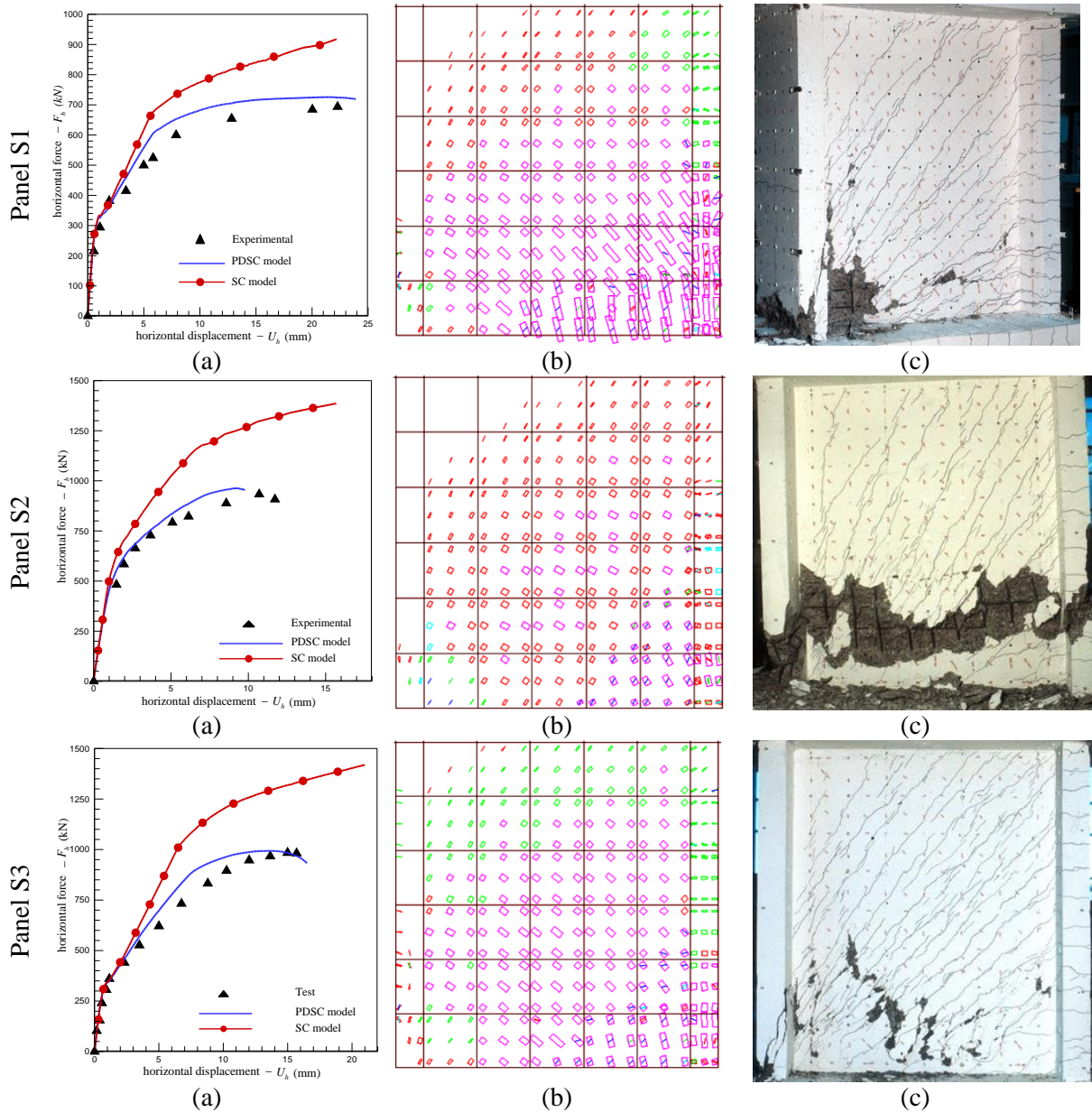
Fig. 4.5 – Simulation of the shear walls S1, S2, S3, S9, S10 tested by Maier and Thürlimann (1985): (a) horizontal load vs. horizontal displacement relationship, F_h-U_h; (b) numerical crack pattern predicted by PDSC model and corresponding to the final converged step; (c) experimentally observed crack pattern (Maier and Thürlimann, 1985). Note: the crack pattern is represented over the finite element mesh adopted for the concrete.

In Table 4.1, the numerical peak load, $F_{h,u}^{num}$, predicted by the PDSC model are compared with the experimental ones, $F_{h,u}^{exp}$, for all the 6 shear walls. The information provided at Table 4.1 verifies that the peak loads of all shear walls are precisely simulated with the

average error of 4.85%. Comparing the F_h-U_h responses obtained by both PDSC and SC models reveals the major influence of simulating compressive nonlinearity on the predicted deformational behaviour and failure mechanism of these shear walls. If nonlinear compressive behaviour is neglected in these analyses, as the approach adopted in SC model, the ductility and load carrying capacity are significantly overestimated.
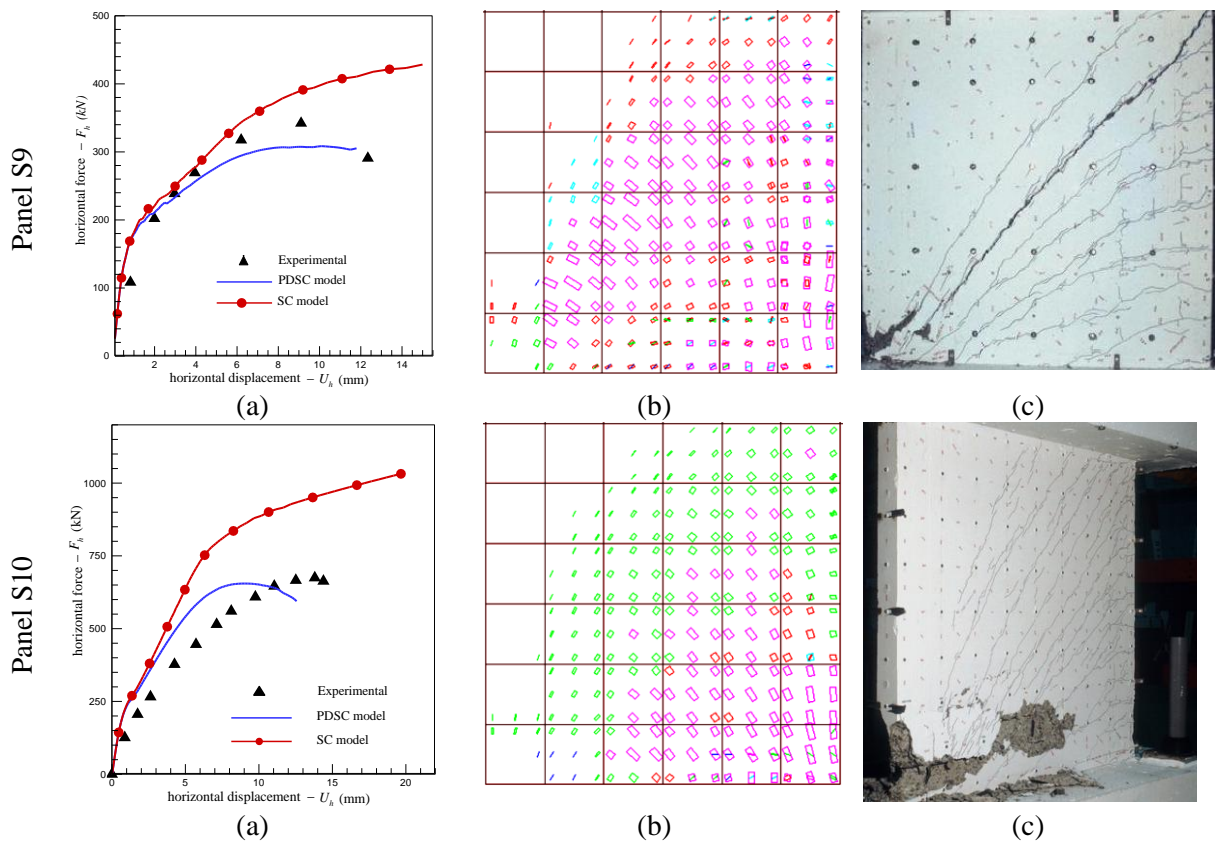
Fig. 4.5 – (Continued)

4.2.2 RC deep beams with openings

Application of the proposed model for simulating reinforced concrete deep beams with openings, tested by El-Maaddawy and Sherif (2009), is considered in this section. A total of six beams (NS-200-B, NS-250-B, NS-200-T, NS-250-T, NS-200-C, NS-250-C) are analysed which have the same shear span over dept ratio, thickness, and reinforcement layout. All the beams include two square openings, one in each shear span, while the differences between these beams are restricted to the location and size of the openings. These beams can be categorized considering the location of the openings within shear

span in three groups: *group C* which includes the beams whose openings are installed at the middle points of the shear spans; *group B*, and *group T*, which contain the beams that their openings are located, respectively, at bottom of shear spans near loading points, and at top of the shear spans near supports. The opening size for each beam was either 200×200 mm^2 or 250×250 mm^2 giving the opening height over the dept (*a/h*) ratios of 0.4 and 0.5 respectively. More details corresponding to the geometry and loading configuration of these beams are provided at Fig. 4.6, and Table 4.4.

Table 4.4 – Details for the deep beam tests.

specimen ID	geometry	opening size (mm^2)	a/h [4] ratio	P_u^{exp} (kN)	P_u^{num} (kN)	$\left\lvert P_u^{exp} - P_u^{num} \right\rvert / P_u^{exp}$ (%)
NS-200-B	*group B* [1]	200×200	0.4	210.7	212	0.61
NS-250-B	*group B*	250×250	0.5	137.9	143.15	3.8
NS-200-C	*group C* [2]	200×200	0.4	163	183	12.2
NS-250-C	*group C*	250×250	0.5	106.6	108.9	2.1
NS-200-T	*group T* [3]	200×200	0.4	220	236	7.2
NS-250-T	*group T*	250×250	0.5	127.6	128.6	0.78
					average	4.45

(1) Opening is located at bottom of shear span near loading point.
(2) Opening is located at middle of the shear span.
(3) Opening is located at top of shear span near support.
(4) *a*: height of openings; *h*: dept of the beam.

The tensile reinforcement consists of 4 steel bars of 14 mm diameter, with the cross-sectional area of 153.9 mm^2 for each bar, while two steel bar of 8 mm diameter, with the cross-section area of 50.3 mm^2 for each bar, are applied as the compressive reinforcement. The web reinforcements are applied with the steel bar of 6 mm diameter, with the cross-section area of 28.3 mm^2, spaced at 150 mm in both vertical and horizontal directions (see Fig. 4.6). The web reinforcement intersecting the opening spaces is cut prior to casting the corresponding specimen (El-Maaddawy and Sherif, 2009).

Due to symmetry of the beams about the vertical axis at the center of the beam, only half beam was modelled. Horizontal displacements of all the nodes on the symmetry axis of the beam are fixed, by applying roller support, to impose the symmetry condition.
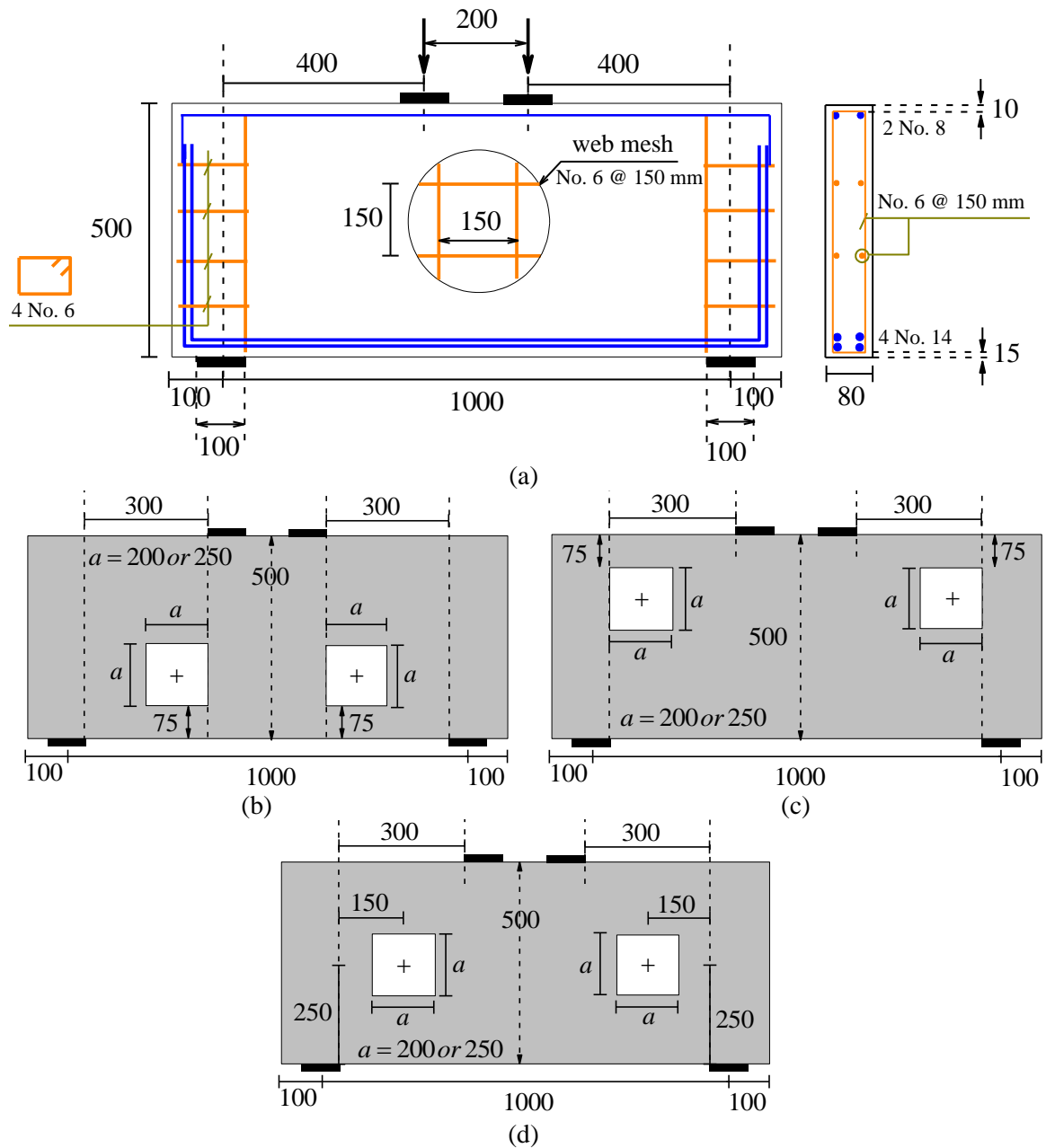
Fig. 4.6 – Deep beams with openings tested by El-Maaddawy and Sherif (2009): (a) details of the reinforcement system, common for all the beams in the experimental program; (b) geometry of the beams at *group B*, NS-200-B and NS-250-B; (c) geometry of the beams at *group T*, NS-200-T and NS-250-T; (d) geometry of the beams at *group C*, NS-200-C and NS-250-C.

Eight-noded serendipity plane stress finite elements with 3×3 Gauss–Legendre IP scheme were used for modelling the beams, supports and loading plates. In Fig. 4.7 is represented, as an example, the finite element mesh used for the simulation of the beam NS-200-C.
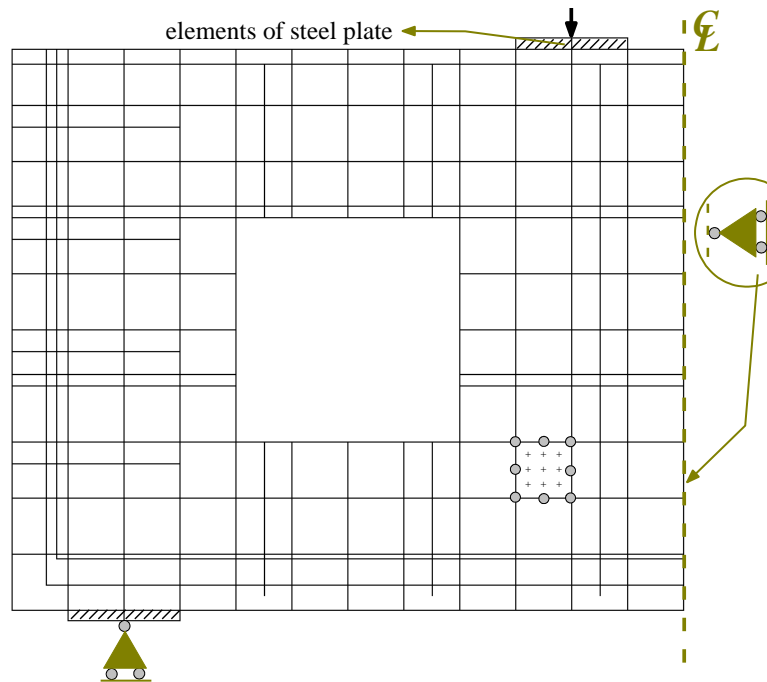
Fig. 4.7 – Finite element mesh, load and support conditions used for analysis of the beam NS-200-C.

The steel reinforcement is meshed using 2-noded perfect bonded embedded cables with two IPs. For modelling the behaviour of the steel bar elements, the stress-strain relationship represented in Fig. 4.3 was adopted. The values of parameters used to define the stress-strain diagram indicated in Fig. 4.3 are included in Table 4.5. Support and loading plates are modeled as a linear-elastic material with Poisson's coefficient of 0.3 and elasticity modulus of 200 GPa. Properties of concrete are taken from Hawileh et al. (2012), and the values of the parameters to define the PDSC model are, accordingly, included in Table 4.6.

Table 4.5 – Values of the parameters of the steel constitutive model for deep beams tests.

	ε_{sy} (%)	σ_{sy} (N/mm^2)	ε_{sh} (%)	σ_{sh} (N/mm^2)	ε_{su} (%)	σ_{su} (N/mm^2)	Third branch exponent
$\phi 14$	0.21	420	1.4	430	4.4	540	1
$\phi 8$	0.21	420	1.4	430	4.4	540	1
$\phi 6$	0.15	300	1.4	330	4.4	440	1

Table 4.6 – Values of the parameters of the concrete constitutive model for the deep beam (with openings) test.

Property	Value
Poisson's ratio	0.2
Young's modulus	$E = 20000 \ N/mm^2$
Parameters defining the plastic-damage part of the model	$\alpha_0 = 0.4$; $f_c = 20.0$ N/mm^2; $\varepsilon_{c1} = 0.0035$; $G_{f,c} = 8 \ N/mm$
Trilinear tension softening diagram (Fig. 3.1a)	$f_{ct} = 1.1 \ N/mm^2$; $G_f^I = 0.04 \ N/mm$; $\xi_1 = 0.0022$; $\alpha_1 = 0.3$; $\xi_2 = 0.1$; $\alpha_2 = 0.15$
Parameter defining the mode I fracture energy available to the new crack (Sena-Cruz, 2004)	2
Type of shear retention factor law	$P_1 = 2$
Crack bandwidth	Square root of the area of Gauss integration point
Threshold angle (Sena-Cruz, 2004)	30 degree
Maximum number of cracks per integration point (Sena-Cruz, 2004)	2

Fig. 4.8 shows the experimental load vs. mid-span deflection ($P - U$ relationship) for the beams in analysis and the respective numerical predictions with the SC and PDSC models. Table 4.4 gives the failure loads of the beams obtained in the experimental program ($P_u^{\exp}$) and in the numerical simulations (P_u^{num}). Amongst the beams with the opening size of 200×200 mm^2 (NS-200-B, NS-200-T, NS-200-C), i.e. the beams having the *a/h* ratio of 0.4, the beam NS-200-T has the maximum experimental failure load (see Fig. 4.8 and Table 4.4). The failure load of the beam NS-200-T is close to that of the beam NS-200-B (the load corresponding to the beam NS-200-T is 4.4% larger than that of NS-200-B), and is 35% higher than that of the beam NS-200-C. The beam NS-200-C has the minimum failure load among these three beams, since its openings, located at the center of the shear spans, significantly interrupts the loading path which is a line connecting loading to the support plates. In case of the beams NS-200-B and NS-200-T whose openings are located at the corners of the shear spans, the loading paths are less interrupted and higher load carrying capacities are obtained at the experimental program. A close inspection of Table 4.4 also reveals that the PDSC model was able to simulate this experimental observation, since the numerical failure load (P_u^{num}) predicted for the beam NS-200-B is higher than that of NS-200-C and is lower than the value calculated for the beam NS-200-T.
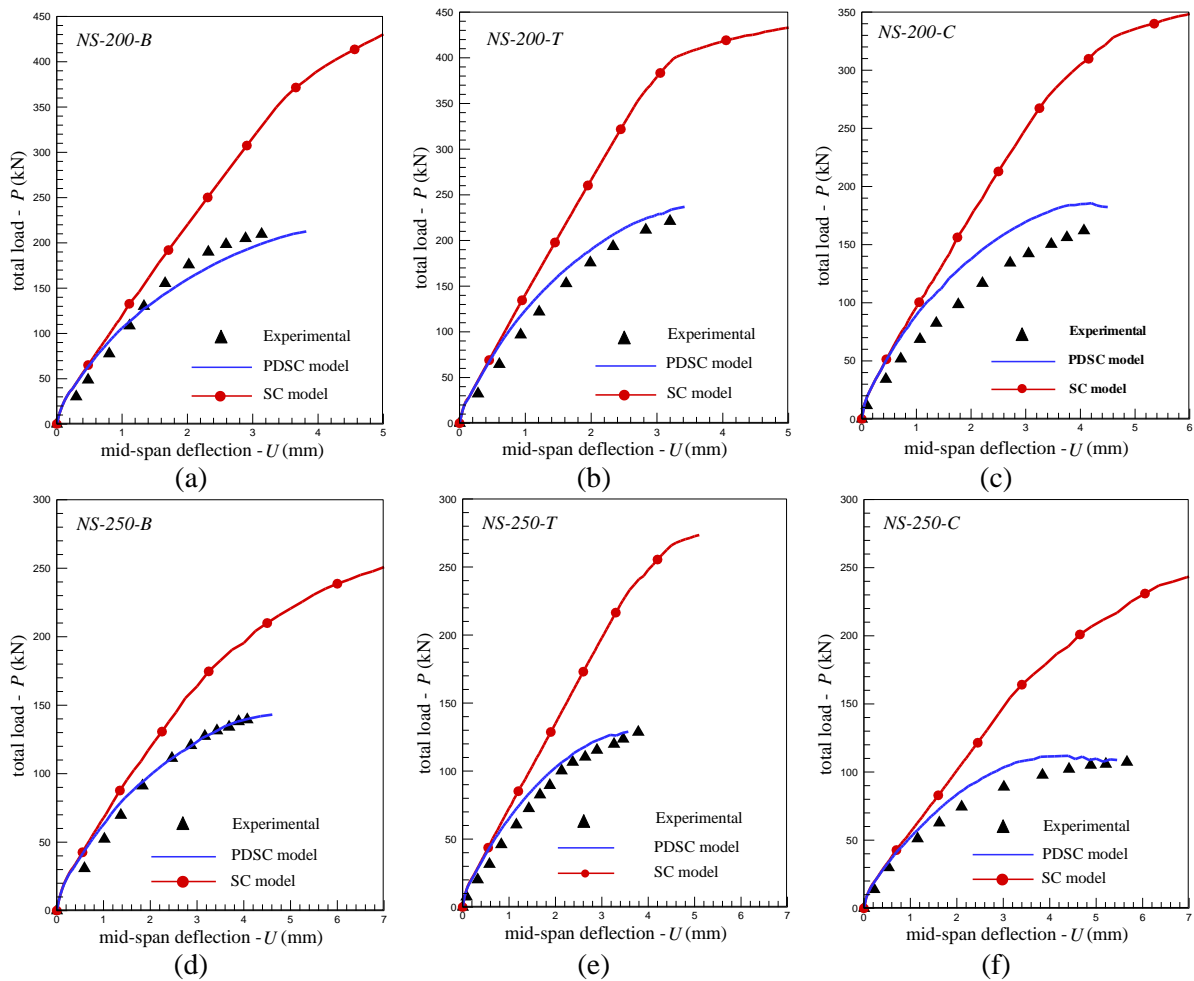
Fig. 4.8 – Experimental load vs. mid-span deflection (El-Maaddawy and Sherif, 2009) in compare with the predictions of the PDSC and SC models for the beams: (a) NS-200-B; (b) NS-200-T; (c) NS-200-C; (d) NS-250-B; (e) NS-250-T; (f) NS-250-C.

By comparing the experimental failure loads of the beams in the same geometry group (*group B*, *group C*, or *group T*) but with the different opening sizes (different *a/h* ratios of 0.4 or 0.5), e.g. compare the failure load of the beam NS-200-T with that of the beam NS-250-T, it can be concluded as the opening size increases, the loading path of the beam is more interrupted, and the failure load decreases. From Fig. 4.8 and Table 4.4, it is evident that PDSC model was able to simulate the reduction of the load carrying capacity as the *a/h* ratio of the beams increases from 0.4 to 0.5.

Fig. 4.8 also shows that the PDSC model fit with high accuracy the experimental $P-U$ curves at all stages of loading till failure. The failure loads were predicted with the average error of 4.45% (see Table 4.4).

(a)

(b)

(c)

(d)

(e)
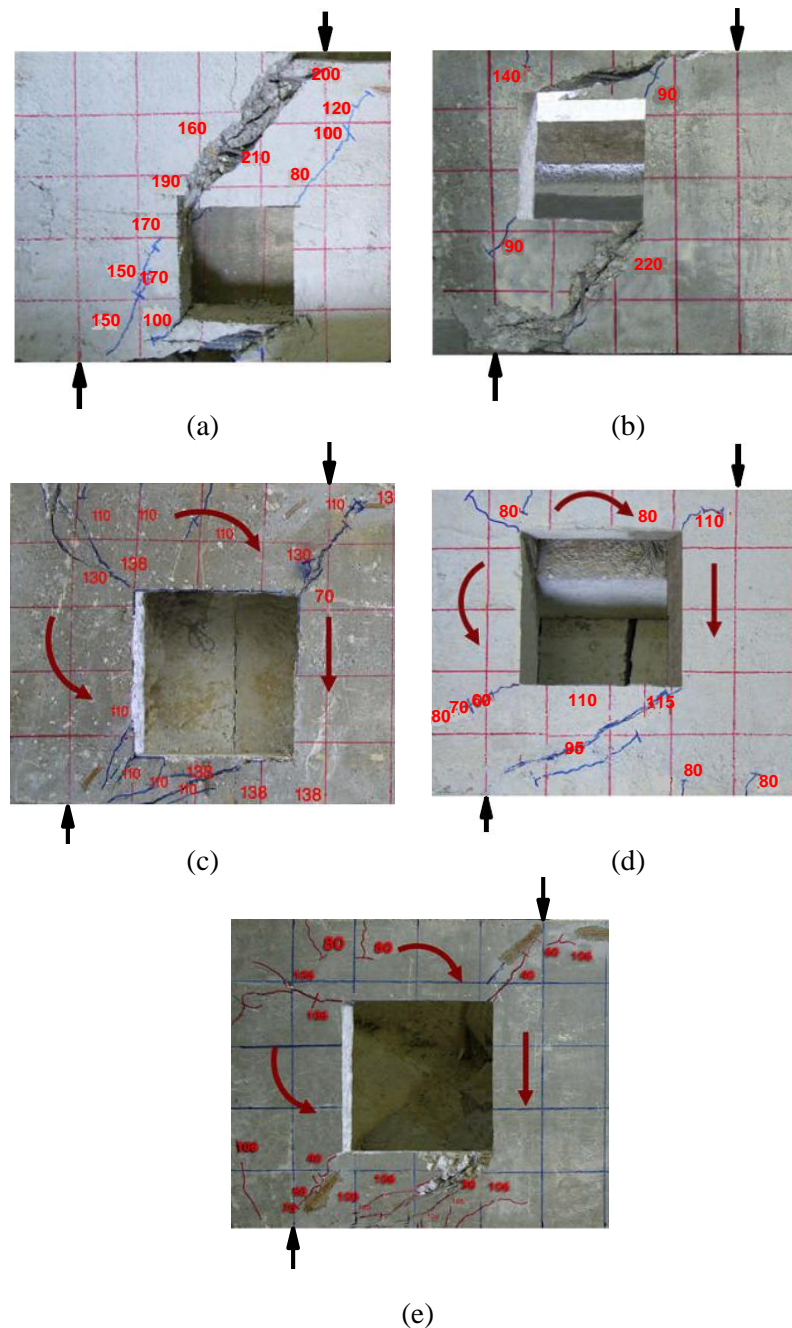
Fig. 4.9 – Experimental crack patterns (El-Maaddawy and Sherif, 2009) for the beams: (a) NS-200-B; (b) NS-200-T; (c) NS-250-B; (d) NS-250-T; (e) NS-250-C.

If SC approach is taken into account to simulate these beams, the predicted $P-U$ responses consider the stiffness degradation only due to cracking of concrete and yielding of steel reinforcements. Since the SC model assumes a linear behaviour for the concrete in compression, the stiffness and ultimate load is overestimated for all the beams, and the final failure mode is incorrectly predicted as yielding of reinforcement (see Fig. 4.8).

The experimental cracking patterns of all the beams at the failure stage demonstrated two critical diagonal cracks in the above and below of one of the openings, see Fig. 4.9. As can be seen in Fig. 4.10, the crack patterns predicted by PDSC model demonstrate flexural cracks with insignificant opening status in middle of the beams, whereas more propagated diagonal cracks (cracks with the orientation of $\theta \approx 45^{\circ}$) can be observed along the line connecting the support and loading plates.
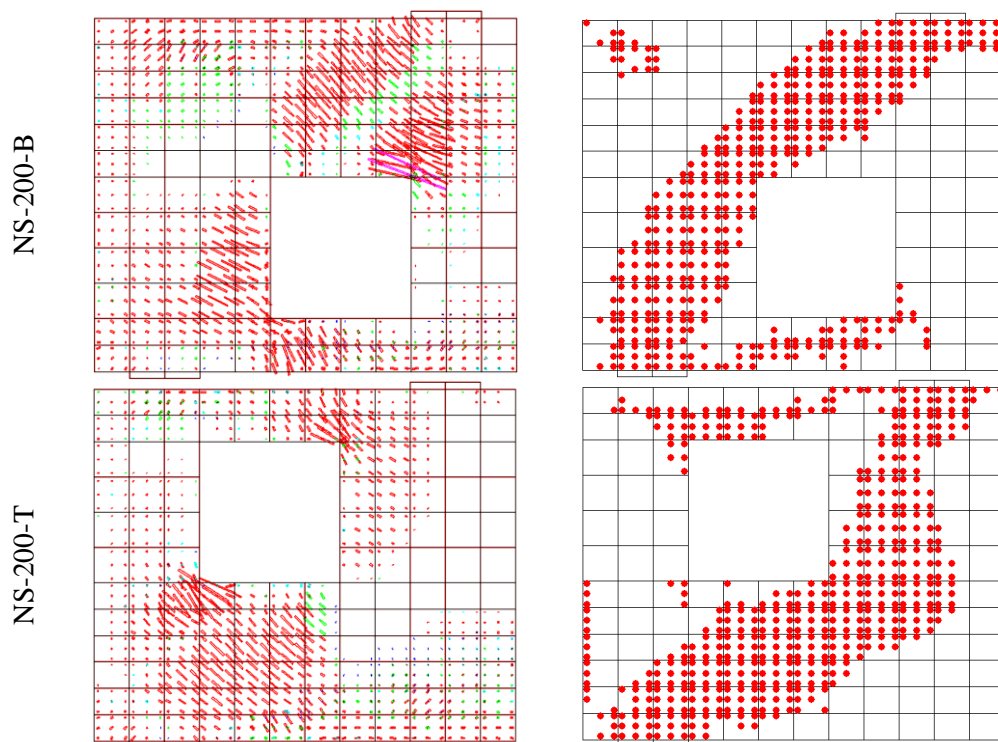
Fig. 4.10 – Numerical crack patterns (left) and plastic zones (right) predicted by PDSC model for the beams in analysis (the results correspond to the final converged step). Note: the crack pattern and plastic zone are represented over the finite element mesh adopted for the concrete.
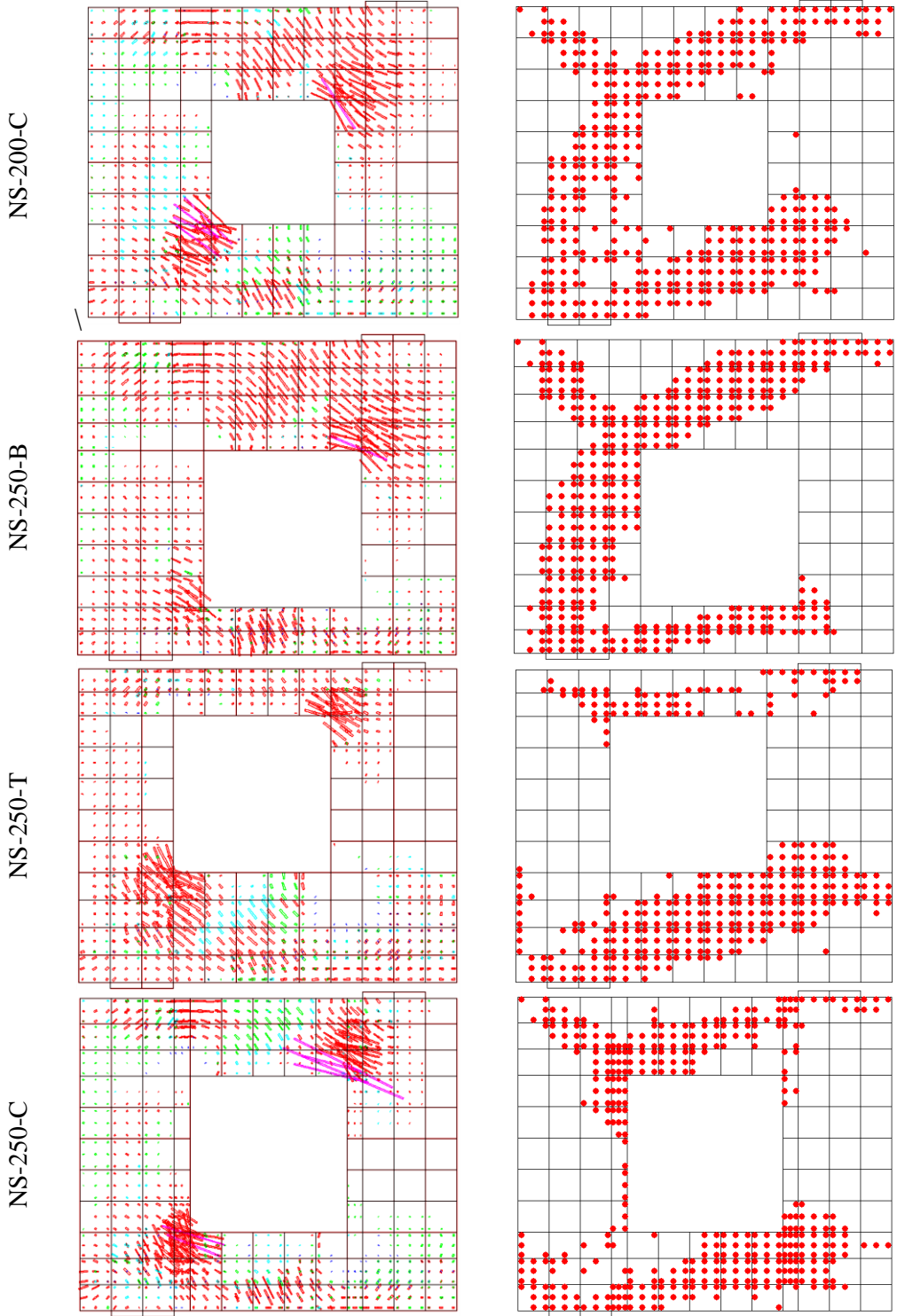
Fig. 4.10 – (Continued)

It seems clear that the PDSC model was able to simulate with high accuracy the
experimentally observed crack patterns of the beams in analysis. The simulated plastic

zones for these beams, see Fig. 4.10, evidence formation of the compressive struts connecting the loading points and supports.

4.2.3 Indirect (splitting) tensile test

Splitting tensile tests are frequently executed as the indirect method for determining the tensile strength of cement based materials. In this section the model ability to predict the concrete behaviour under the splitting tensile test is investigated. The model is applied to simulate the test executed in the work of Abrishambaf et al. (2013), and the model predictions are compared with the results reported at the experimental program. The specimen is a cylinder with a diameter of 150 mm and length of 60 mm made by a steel fibre reinforced self-compacting concrete, SFRSCC, of 60 kg per m^3 steel fibers. To localize the crack plane, the specimen includes two 5 mm notches cut on each opposite face of the specimen. Fig. 4.11 shows the specimen geometry, loading configuration and experimental crack pattern observed at the failure stage.

| (a) | (b) | (c) |
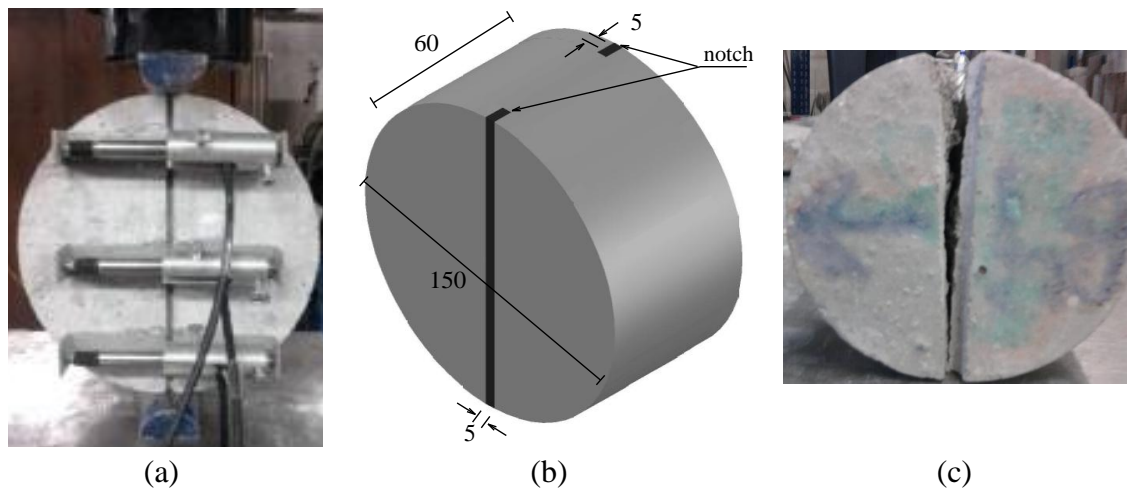
Fig. 4.11 – Details of the splitting tensile test: (a) setup of the test (Abrishambaf et al., 2015); (b) geometry of the specimen, dimensions are in mm; (c) experimental crack pattern at the failure stage (Abrishambaf, 2015).

Only a quarter of the specimen is modelled, due to the double symmetry condition. Roller supports were imposed at all the nodes on the both axes of symmetry to fix the displacements perpendicular to the axes of symmetry (see Fig. 4.12). The finite element mesh of 8-noded plane stress finite elements with 3×3 Gauss-Legendre IP scheme was

adopted for the specimen and the loading plate, see Fig. 4.12. Elements of the loading plate are assumed to exhibit linear elastic behaviour with the elastic modulus and Poisson's ratio corresponding to $E = 200$ GPa, and $v = 0.3$.
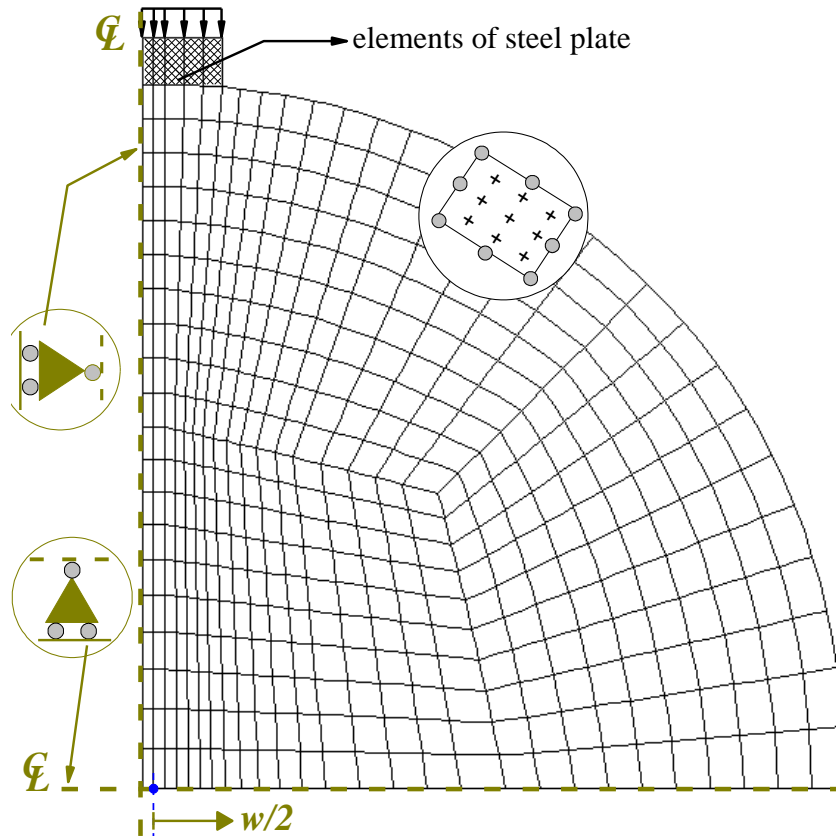
Fig. 4.12 − Finite element mesh, load and support conditions used for analysis of the splitting tensile test.

The applied load is uniformly distributed over the edges of the elements of the loading plate, under the displacement control by the arc-length method. The properties of concrete are taken from Abrishambaf et al. (2013), and the values of the parameters to define the constitutive law for concrete are included in Table 4.7.

Fig. 4.13 shows the relationship between the applied load vs. crack opening mouth displacement ($F - W$) obtained at the experiment in comparison to the predictions of both SC and PDSC constitutive models. The good predictive performance of the PDSC model is further demonstrated by providing the numerical crack pattern and the plastic

zone obtained at the final converged loading step of the calculation process (see Fig. 4.14).

Table 4.7 – Values of the parameters of the concrete constitutive model for the test of cylinder splitting specimen made of SFRSCC.

Property	Value
Poisson's ratio	0.2
Young's modulus	$E = 36000 \ N/mm^2$
Parameters defining the plastic-damage part of the model	$\alpha_0 = 0.4$; $f_c = 48.0 \ N/mm^2$; $\varepsilon_{c1} = 0.0035$; $G_{f,c} = 35 \ N/mm$
Trilinear tension softening diagram (Fig. 3.1a)	$f_{ct} = 3.5 \ N/mm^2$; $G_f^1 = 3.0 \ N/mm$; $\xi_1 = 0.007$; $\alpha_1 = 0.5$; $\xi_2 = 0.15$; $\alpha_2 = 0.55$
Parameter defining the mode I fracture energy available to the new crack (Sena-Cruz, 2004)	2
Type of shear retention factor law	$P_1 = 2$
Crack bandwidth	Square root of the area of Gauss integration point
Threshold angle (Sena-Cruz, 2004)	30 degree
Maximum number of cracks per integration point (Sena-Cruz, 2004)	2

Fig. 4.13 – Experimental load vs. crack mouth opening displacement relationship (Abrishambaf et al., 2013) in comparison with the predictions of the PDSC and SC models.

The analysis executed by SC model reveals at the load corresponding to ≈ 45 kN that the splitting cracks are initiated (see Fig. 4.13). These cracks have an orientation of $\theta = 0^o$ and have formed in IPs in the vicinity of the vertical symmetry axis of the cylinder. Once these cracks start to propagate ($W > 0$), the stiffness of $F - W$ response slightly

decreases, but the predicted load carrying capacity continuously increases without the occurrence of a failure load, since this model (SC model) assumes an elastic behaviour for the concrete in compression. However according to the to the PDSC response, after the initiation of the splitting cracks ($W > 0$), the predicted load increases and attains a hardening branch followed by a softening stage that is mainly governed by the nonlinear inelastic behaviour of concrete under compression. From Fig. 4.13 it is evident that there is a close correlation between the experimental $F - W$ response and the one predicted by the PDSC model. Fig. 14a demonstrates that the cracks with highly propagated opening status are spread along the vertical symmetry axis of the specimen, while Fig. 4.14b shows the plastic zone is concentrated at the region under the loading plate. These observations imply the final failure mechanism of this test (see Fig. 4.11c) is a combination of the tensile splitting crack and the compressive failure modes.

(a)   (b)
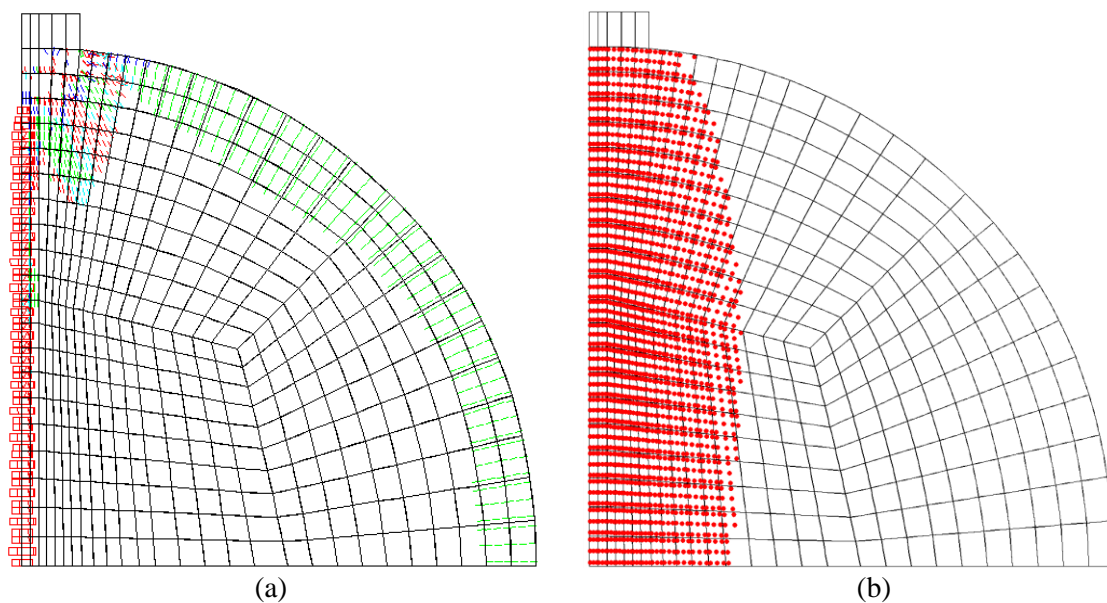
Fig. 4.14 – Predictions of PDSC model for the splitting tensile test: (a) numerical crack pattern; (b) numerical plastic zone (results of (a) and (b) correspond to $W \approx 1.9\,\text{mm}$, the final converged loading step).

It should be aware that in the approach followed in the current work for modelling the behaviour of SFRSCC, this material is considered to be homogeneous. However SFRSCC can be regarded as a heterogeneous medium, like the approach proposed by Cunha et al. (2012). Within their numerical model, SFRSCC was modeled as a material composed of

two phases: matrix and discrete steel fibres. The matrix phase is simulated with a 3D multidirectional fixed smeared crack model, while the stress transfer between crack planes due to the reinforcing mechanisms of fibres bridging active cracks is modeled with 3D embedded elements. This approach is, however, too demanding in terms of computer time consuming when applied to elements of structural scale, which is the type of structures aimed to be analyzed in the present chapter.

Another splitting tensile test, which was simulated in the work of Feenstra and de Borst (1996) is here presented. The specimen is a cube with a side dimension of 150 mm made by a concrete with the compressive strength of 35 MPa. Fig. 4.15 summarizes the specimen geometry and loading configuration of the test. A quarter of the specimen is modelled, due to double symmetry condition, with two different mesh schemes (coarse and fine mesh sizes) in order to demonstrate that the structural response of the model is mesh independent. For both meshes, 8-noded plane stress finite element with 3×3 Gauss–Legendre IP scheme were used. The applied load for each mesh discretization is uniformly distributed over the edges of those elements at the left top corner according to Fig. 4.15. The properties of concrete are taken from Feenstra and de Borst (1996), and the values of the parameters to define the constitutive law for concrete are included in Table 4.8.

Table 4.8 – Values of the parameters of the concrete constitutive model for the test of cube splitting specimen made of plain concrete.

Property	Value
Poisson's ratio	0.2
Young's modulus	E=27000 N/mm^2
Parameters defining the plastic-damage part of the model	α_0 =0.4; f_c =35.0 N/mm^2; ε_{c1} =0.0022; $G_{f,c}$ =4.5 N/mm
Trilinear tension softening diagram (Fig. 3.1a)	$f_{ct} = 2.7$ N/mm^2; G_f^1 =0.06 N/mm; ξ_1 =0.01; $\alpha_1 = 0.3$; ξ_2 =0.25; $\alpha_2 = 0.2$
Parameter defining the mode I fracture energy available to the new crack (Sena-Cruz, 2004)	2
Type of shear retention factor law	$P_1 = 2$
Crack bandwidth	Square root of the area of Gauss integration point
Threshold angle (Sena-Cruz, 2004)	30 degree
Maximum number of cracks per integration point (Sena-Cruz, 2004)	2

Fig. 4.16 shows that the mesh refinement has small influence on the relationships between the applied stress (applied vertical load over the area the load is distributed, 21.4×150 mm^2) vs. the vertical displacement under the load ($f_v - U_v$ relationship) when the PDSC model is used. This figure also includes the $f_v - U_v$ relationships predicted by Feenstra and de Borst (1996), as well as the response obtained with the SC model. The predictive performance of the model is further demonstrated by providing the numerical crack pattern and the plastic zone obtained at the final converged loading step of the calculation process (see Fig. 4.17 and Fig. 4.18). Fig. 4.17 and Fig. 4.18 show that the final failure mode of the test is a combination of the splitting cracks in middle of the cube cross section area, and inelastic compressive deformations in the region under the loading platen.
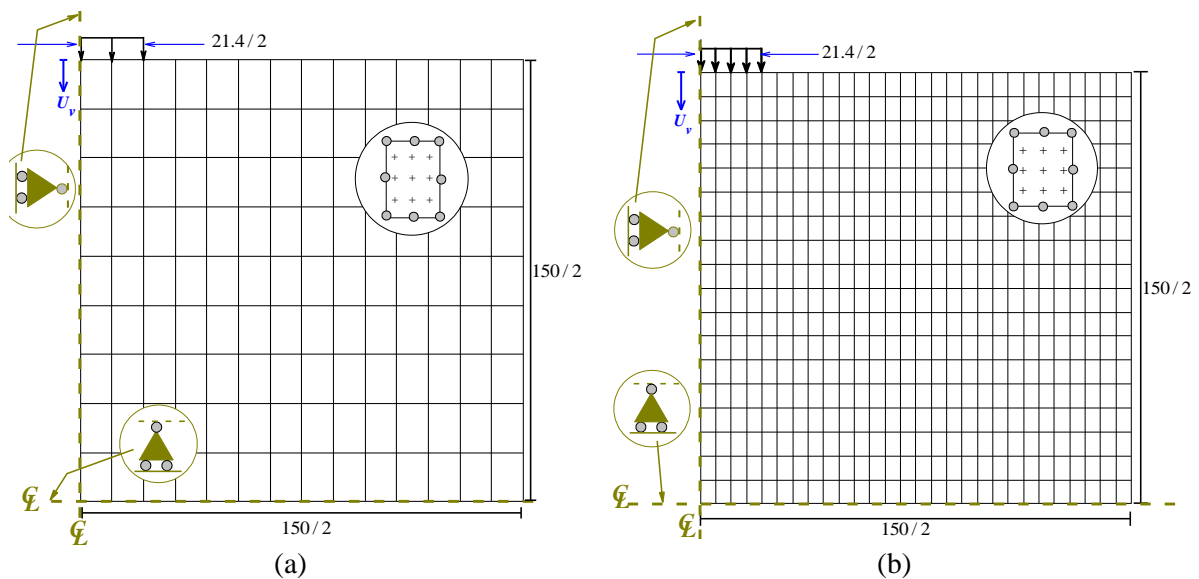
Fig. 4.15 – Cube splitting tensile test: (a) coarse mesh; (b) fine mesh (dimensions in mm).
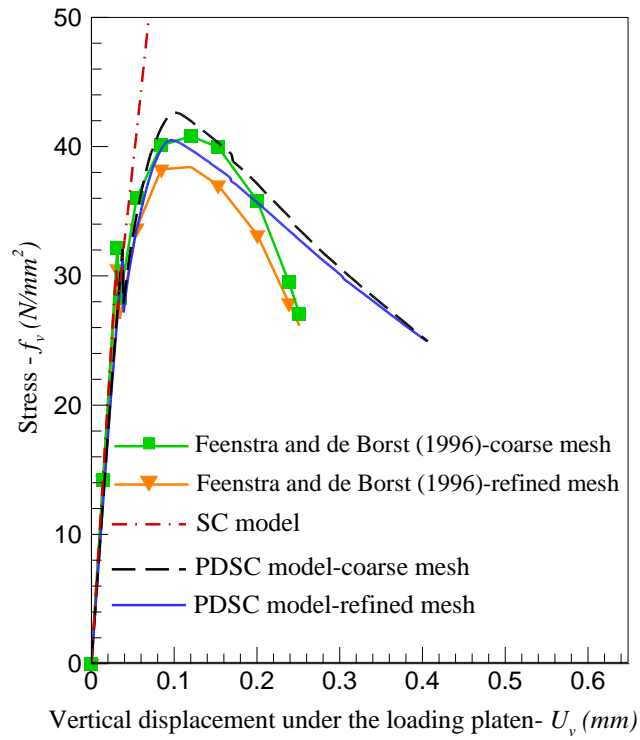
Fig. 4.16 – Stress vs. vertical displacement under the load for the cube splitting tensile test.

(a)   (b)
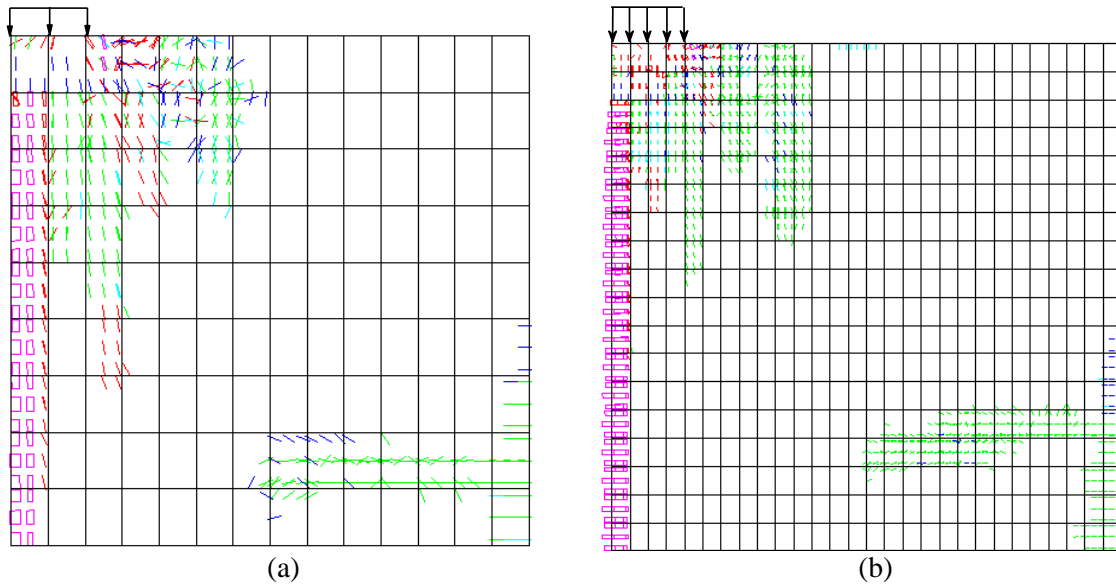
Fig. 4.17 – Numerical crack pattern obtained by PDSC model for cube splitting tensile test: (a) coarse mesh; (b) fine mesh (results correspond to the final converged loading step).

(a)   (b)
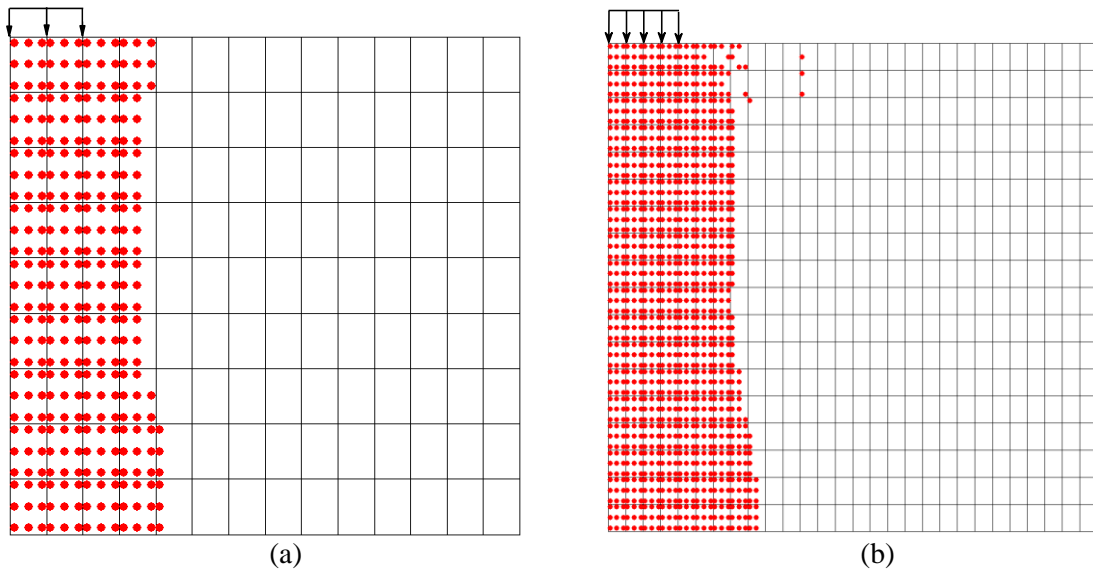
Fig. 4.18 – Numerical plastic zone obtained by PDSC model for cube splitting tensile test: (a) coarse mesh; (b) fine mesh (results correspond to the final converged loading step).

4.2.4 RC short span beams

The experimental program (Soltanzadeh et al., 2016a) is composed of six beams of a span length, L, of 1050 mm and a rectangular cross section of 150 mm wide, b, and 300 mm height, h. Two longitudinal steel bars of 12 mm diameter, $\phi 12$, and one of 10 mm diameter, $\phi 10$, positioned at a depth of 230 mm, d_s, and a ribbed GFRP rebar of 12 mm diameter, $\phi 12$, with a depth of 270 mm, d_{GFRP}, were used for the flexural reinforcement. The general configuration of the beams and the arrangement of the reinforcements are represented in Fig. 4.19.
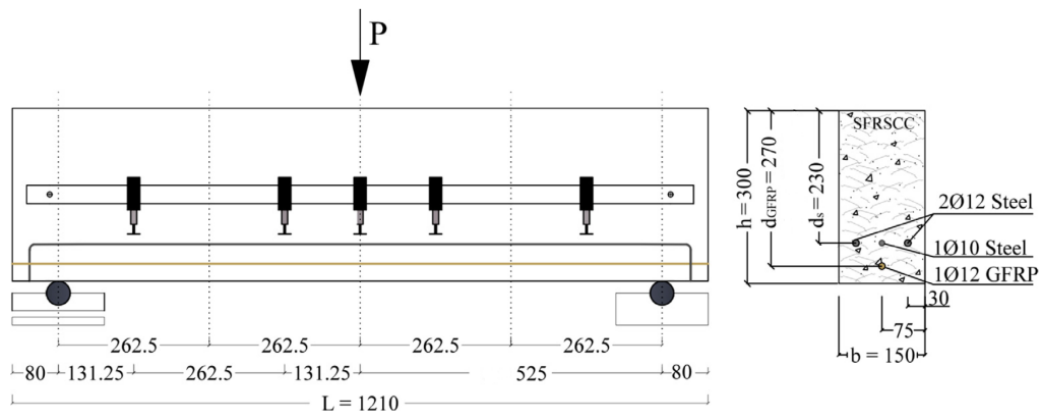
Fig. 4.19 - Beam configuration and test setup (dimensions in mm) (Soltanzadeh et al., 2016a).

The prestress levels of 0% (control beam), 20% and 30% of GFRP ultimate tensile strength ($f_{GFRP,u}$ =1350 MPa) were adopted for the experimental program. Table 4.9 presents the details of each series of fabricated beams, introduced by the label "Bi-Pj", where "i" identifies the number of the tested beams in each series (two beams were tested per each series) and "j" is the percentage of prestress applied to the GFRP bar. The three-point bending test setup adopted in the present study is illustrated in Fig. 4.19. All the beams are developed by a steel fibre reinforced self-compacting concrete, SFRSCC, of 90 kg per m^3 steel fibers.

Table 4.9- General information about the simulation of the prestress load by means of temperature variation.

	Prestress percentage (%)	Stress applied to GFRP corresponding to prestress level σ_t [a] (MPa)	Coefficient of thermal expansion $\alpha(mm/(mm^o c))$	Temperature variation $\Delta T(^o c)$
Bi-P0 (i=1, 2)	0	-	-	-
Bi-P20 (i=1, 2)	20	270	1×10^{-5}	-482
Bi-P30 (i=1, 2)	30	405	1×10^{-5}	-723

[a] σ_t = prestress percentage $\times f_{GFRP,u}$; $f_{GFRP,u}$ =1350 MPa.

Note: the thermal strain and corresponding stress are calculated from: $\varepsilon_t = \alpha \, \Delta T$; $\sigma_t = E_{GFRP} \, \varepsilon_t$.

The finite element mesh of 8-noded plane stress finite elements with 3×3 Gauss-Legendre IP scheme, represented in Fig. 4.20, was adopted for the beams (the differences between beams in different series are limited to the prestress load applied to the GFRP bar). The GFRP bar was modeled using 2-noded truss elements (one degree-of-freedom per each node) with two IPs. The longitudinal steel bars are meshed using 2-noded embedded cables with two IPs. Perfect bond was assumed between the reinforcement bars and the surrounding concrete. For modeling the behavior of the steel bars, the stress-strain relationship represented in Fig. 4.3 was adopted.
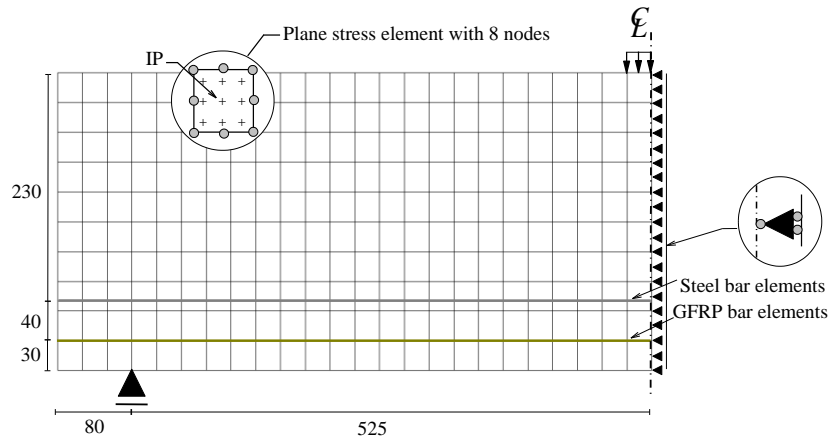
Fig. 4.20 - Finite element mesh used for the simulated beams (dimensions in mm).

The behavior of GFRP bar was modeled using a linear-elastic stress-strain relationship
defined by the values indicated in Table 4.10. The prestress load was simulated by means
of temperature variation applied to the truss elements modeling the GFRP bar. Table 4.9
represents the values of the temperature variation applied to each simulated beam. The
values of parameters used to define the constitutive models of steel and concrete
(FRSCC) are included in Table 4.11 and Table 4.12, respectively.

To simulate the shear crack initiation and the degradation of crack shear stress transfer,
the shear softening diagram represented in Fig. 3.2 is assumed. To define this diagram the
values of the corresponding parameters, included in Table 4.12, were obtained by
simulating the experimental results of the reference beams (Bi-P0) as best as possible.
Then the same values of the parameters of the constitutive model were adopted for the
prestressed beams (Bi-P20, and Bi-P30).

Table 4.10–Mechanical properties of the GFRP bar.

Diameter (mm)	Density (gr/cm^3)	E_{GFRP} [a] (GPa)	$f_{GFRP,u}$ [b] (N/mm2)
12	2.23	56	1350

[a] E_{GFRP} Modulus of elasticity.

[b] $f_{GFRP,u}$ Ultimate tensile strength.

Table 4.11 – Values of the parameters of the steel constitutive model for short beams tests.

Diameter (mm)	ε_{sy} (%)	σ_{sy} (N/mm^2)	ε_{sh} (%)	σ_{sh} (N/mm^2)	ε_{su} (%)	σ_{su} (N/mm^2)	Third branch exponent
10, 12	0.28	500	0.28	500	10.0	591	1

Table 4.12 – Values of the parameters of the concrete constitutive model for the test of short span beams

Property	Value
Poisson's ratio	0.2
Young's modulus	$E = 34000 \ N/mm^2$
Parameters defining the plastic-damage part of the model	$\alpha_0 = 0.4$; $f_c = 65.0 \ N/mm^2$; $\varepsilon_{c1} = 0.004$; $G_{f,c} = 65 \ N/mm$
Quadrilinear tension softening diagram (Fig. 3.1b)	$f_{ct} = 3.25 \ N/mm^2$; $G_f^1 = 6 \ N/mm$; $\xi_1 = 0.0005$; $\alpha_1 = 0.75$; $\xi_2 = 0.0025$; $\alpha_2 = 0.1$; $\xi_3 = 0.1$; $\alpha_3 = 0.6$
Parameter defining the mode I fracture energy available to the new crack (Sena-Cruz, 2004)	2
Parameters defining the crack shear stress-crack shear strain softening diagram (Fig. 3.2)	$\tau_{t,p}^{cr} = 1.75 \ N/mm^2$; $\beta = 0.2$; $G_{f,s} = 1.0 \ N/mm$
Crack bandwidth	Square root of the area of Gauss integration point
Threshold angle (Sena-Cruz, 2004)	30 degree
Maximum number of cracks per integration point (Sena-Cruz, 2004)	2

The experimental and the numerical relationships between the applied load and the deflection at the mid-span for all the beam series are compared in Fig. 4.21.
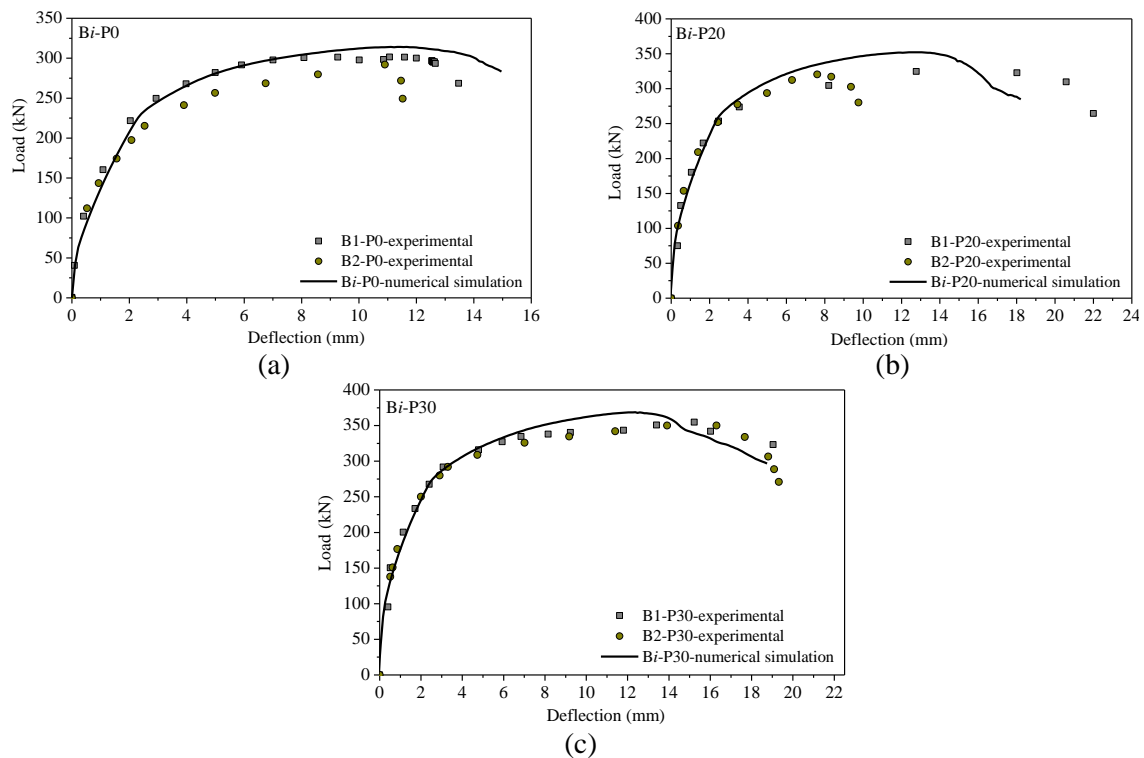
Fig. 4.21 - Numerical prediction of the applied load vs. mid-span deflection in comparison with the corresponding experimental results of the beam series: (a) B*i*-P0; (b) B*i*-P20; (c) B*i*-P30.

In Fig. 4.22 the numerical crack patterns of these beam series at the end of the analysis (at the end of the last converged load increment) are compared with the obtained experimental crack patterns. These two figures show that the numerical model is able to capture with good accuracy the deformational response of the beams and captured profile of the failure crack.

(a)   (b)
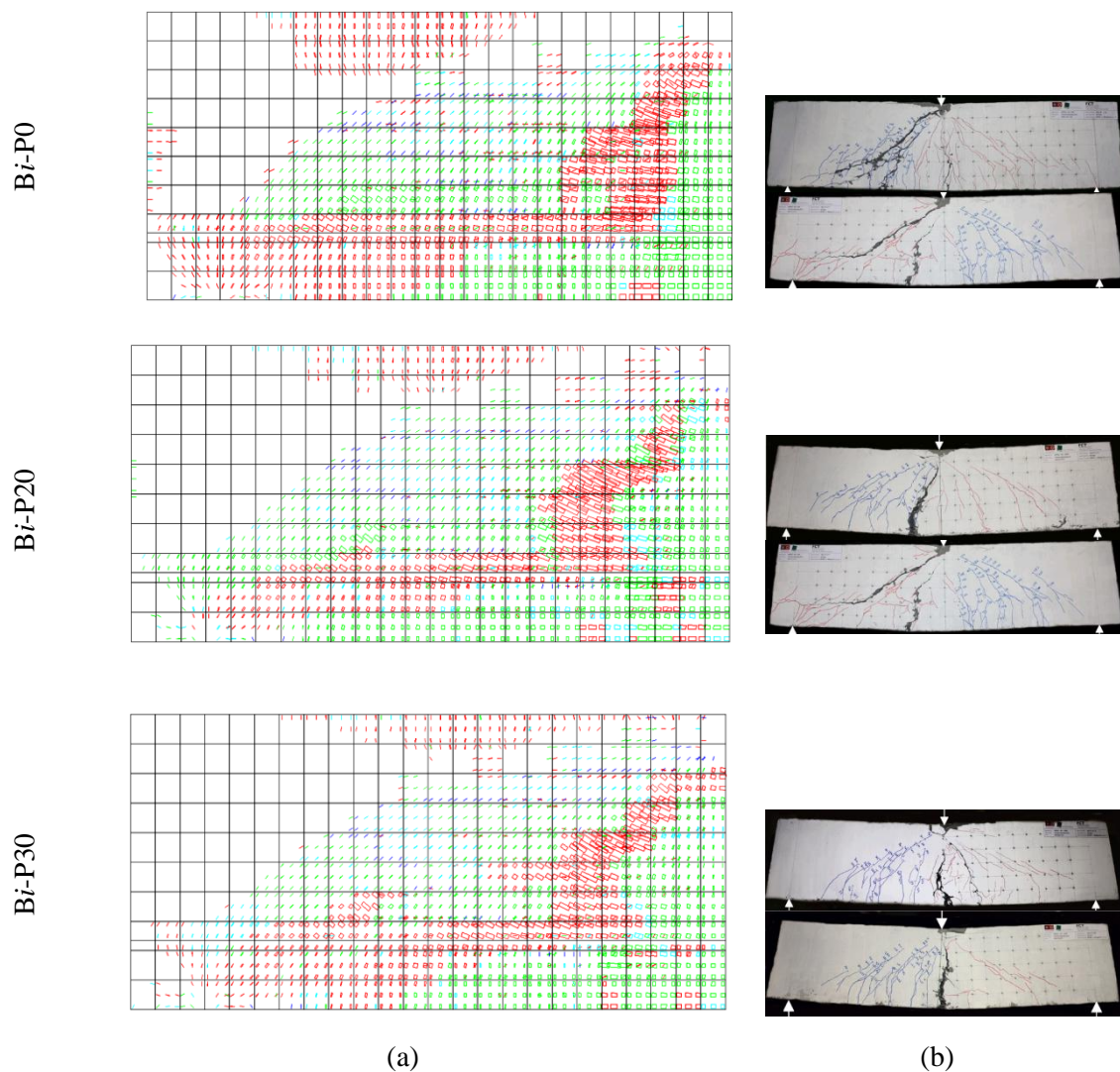
Fig. 4.22 - Crack patterns predicted by the model (a) and crack patterns obtained in the experimental tests (b) for the beam series: B*i*-P0; B*i*-P20; B*i*-P30.

The predicted strain in steel reinforcement (at the closest IP of the symmetric axis of the beams) versus mid-span displacement corresponding to each simulation is represented in Fig. 4.23. These curves shows that at a deflection of about 2.3 *mm* the longitudinal steel

reinforcements of the reference beam (Bi-P0) started yielding, which indicates that the reinforcing mechanisms of the adopted content of steel fibres (90 kg per m^3) were sufficient to assure yield initiation of longitudinal reinforcement before the occurrence of the reference beam's shear failure.
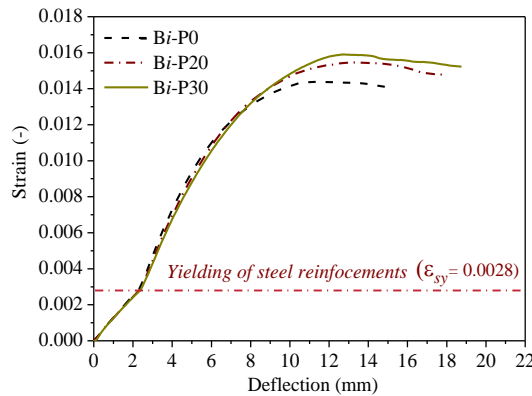
Fig. 4.23 – Strain in steel reinforcement (obtained at the closest IP to the symmetric axis of the beam) vs. mid-span deflection predicted by the numerical simulations.

The numerically predicted relationship between the applied load and the deflection at the mid-span for all the beam series are gathered in Fig. 4.24. The points at crack initiation and at yield initiation of the steel reinforcement are also represented in this figure by using markers, demonstrating that by both the load at crack initiation and at yield initiation of steel reinforcements increase with the prestress level.
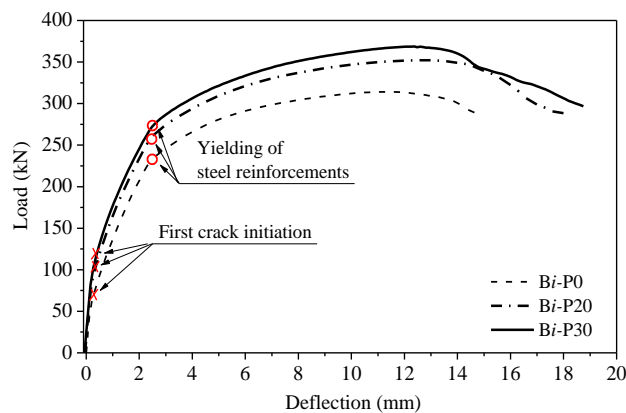
Fig. 4.24 – The predicted load-deformation behavior for all the beam series.

4.2.5 Shear strengthened RC beams

4.2.5.1 Beam prototypes

The experimental program (Barros and Dias, 2013) is composed of a reference beam (Fig. 4.25) and four NSM shear strengthened beams (Fig. 4.26). Fig. 4.25 represents the T cross section geometry and the steel reinforcement detailing for the series of beams, as well as the loading configuration and support conditions. The adopted reinforcement systems were designed to assure shear failure mode for all the tested beams. All the tested beams had a percentage of longitudinal tensile steel bars (ρ_{sl}) of 2%. To localize the shear failure in only the monitored shear spans, a_{sp}, a three point loading configuration with a distinct length for the beam shear spans was selected, as shown in Fig. 4.25. Steel stirrups of 6 mm diameter at a spacing of 112 mm ($\phi6@112mm$) were applied in the b_{sp} beam span to avoid shear failure.
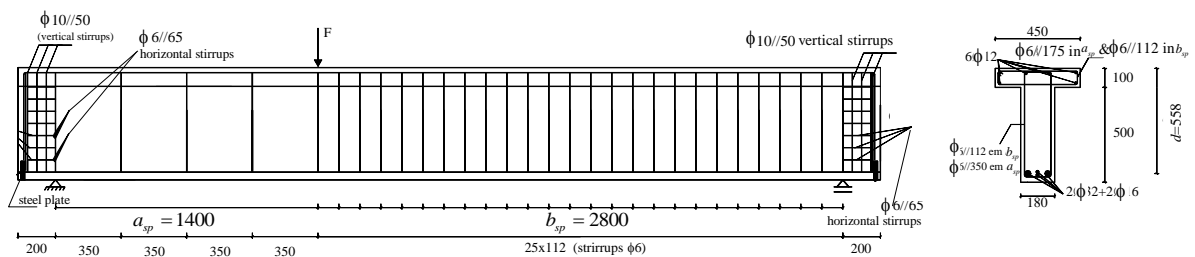
Fig. 4. 25 - Geometry of the reference beam (3S-R), steel reinforcements common to all beams, support and load conditions (dimensions in mm) (Barros and Dias, 2013).

The differences between the tested beams are restricted to the shear reinforcement systems applied in the a_{sp} beam span. The reference beam is designated as 3S-R (three steel stirrups in the a_{sp} shear span, 3S, leading a steel shear reinforcing ratio, ρ_{sw}, of 0.09%), while the following different NSM strengthening configurations were adopted for the other four beams that also include 3 steel stirrups in the a_{sp} shear span (Fig. 4.26 and Table 4.13):
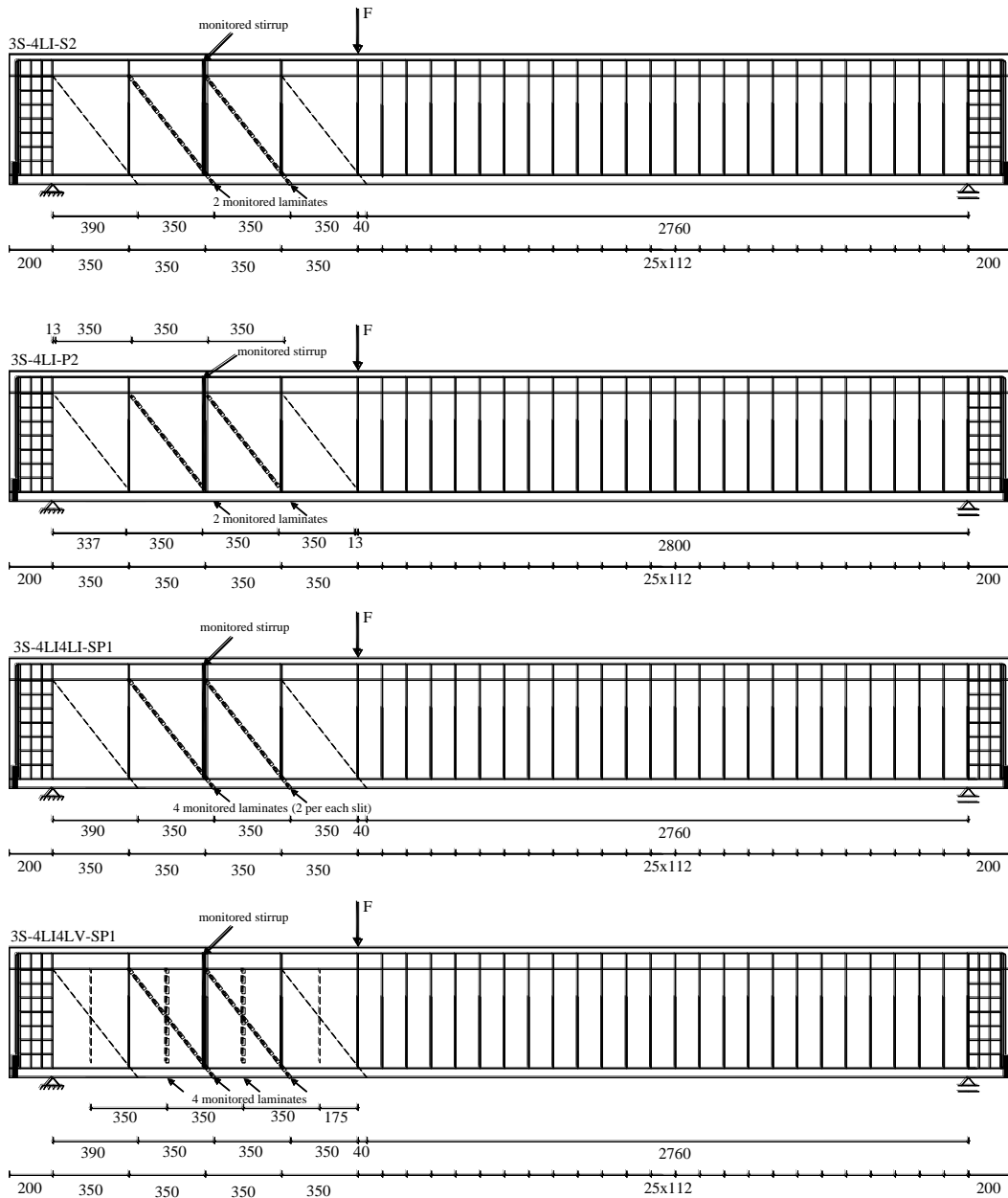
Fig. 4.26 – NSM shear strengthening configurations (CFRP laminates at dashed lines; dimensions in mm) (Barros and Dias, 2013).

3S-4LI-S2 - four CFRP laminates of type 2 (with a cross section of 1.4×20 mm^2) per face, inclined at 52 degrees with respect to the longitudinal axis of the beam ($\theta_f = 52°$), and installed from the bottom surface of the flange to the bottom tensile surface of the beam's web, i.e., bridging the total lateral surfaces of the beam's web; each CFRP laminate was installed in the outer part of a slit of a depth of 21 mm executed on the beam's web lateral surfaces. The length of each laminate was 634 mm;

3S-4LI-P2 - four CFRP laminates of type 2 (with a cross section of 1.4×20 mm^2) per face, inclined at 52 degrees with respect to the longitudinal axis of the beam (θ_f = 52º), and installed from the bottom surface of the flange up to 10 mm above the top surface of the longitudinal tensile steel reinforcement. Each CFRP laminate was installed in the deeper part of a slit of a depth of 35 mm from the surface of the beam's web lateral surfaces. The length of each laminate was 527 mm;

3S-4LI4LI-SP1 - eight CFRP laminates of type 1 (with a cross section of 1.4×10 mm^2) per face, inclined at 52 degrees with respect to the longitudinal axis of the beam (θ_f = 52º). The configuration of the slits executed in this section combines the configurations of the beams 3S-4LI-P2 and 3S-4LI-S2. In each slit, with a depth of 35mm, was installed one laminate as deeper as possible and one laminate as superficial as possible.

3S-4LI4LV-SP1 - eight CFRP laminates of type 1 (with a cross section of 1.4×10 mm^2) per face, four of them inclined at 52 degrees with respect to the longitudinal axis of the beam (θ_f = 52º) and bridging the total lateral surfaces of the beam's web (the length of each inclined laminate was 634 mm), while the other four laminates were installed in vertical slits executed from the bottom surface of the web up to 10 mm above the top surface of the longitudinal tensile steel reinforcement (the length of each vertical laminate was 432 mm). The vertical laminates were installed as deeper as possible into a slit of a depth of 35 mm from the surface of the beam's web lateral surfaces. The inclined laminates were installed as outer as possible into a slit of a depth of 15 mm executed on the beam's web lateral surfaces.

4.2.5.2 Material properties

All the NSM shear strengthened beams were executed with a concrete that presented an average compressive strength (f_c) of 40.1 MPa. For the reference beam 3S-R the value of f_c was 36.4 MPa. The average value of the yield stress of the steel bars of 6, 12, 16 and 32 mm diameter was 556.1, 566.6, 560.8 and 654.5 MPa, respectively, while average value of the ultimate stress for these corresponding bars was: 682.6, 661.6, 675.0 and 781.9 MPa. The constitutive law for the steel bars follows the stress-strain relationship represented in Fig. 4.3, and values for its definition are those indicated in Table 4.14. The

CFRP laminates presented a linear-elastic stress-strain response with a tensile strength of 3009 MPa and an elasticity modulus of 169 GPa and 166 GPa for the laminate type 1 and 2, respectively. The complementary discussion on the characterization of the CFRP laminates and epoxy adhesive can be found in Barros and Dias (2013).

Table 4.13 - CFRP shear strengthening configurations of the tested beams.

Beam	Shear reinforcement system in the shear span a_{sp}				
	Material	Quantity	Percentage (%)	Spacing (mm)	Angle (º)
3S-4LI-S2	Steel stirrups	3ϕ6	0.09	350	90
	NSM CFRP laminates	2×4 laminates (1.4×20 mm^2)	0.113	350	52
3S-4LI-P2	Steel stirrups	3ϕ6	0.09	350	90
	NSM CFRP laminates	2×4 laminates (1.4×20 mm^2)	0.113	350	52
3S-4LI4LI-SP1	Steel stirrups	3ϕ6	0.09	350	90
	NSM CFRP laminates	2×(4×2) laminates (1.4×10 mm^2)	0.113	350	52
3S-4LI4LV-SP1	Steel stirrups	3ϕ6	0.09	350	90
	NSM CFRP laminates	2×4 laminates (1.4×10 mm^2)	0.056	350	90
	NSM CFRP laminates	2×4 laminates (1.4×10 mm^2)	0.044	350	52

4.2.5.3 Finite element modelling and constitutive laws for the materials

The finite element mesh of 8-noded plane stress finite element with 2×2 Gauss-Legendre IP scheme, represented in Fig. 4.27, was adopted (corresponds to the 3S-4LI-S2 beam, but the differences for the other beams are limited to the CFRP strengthening configurations).
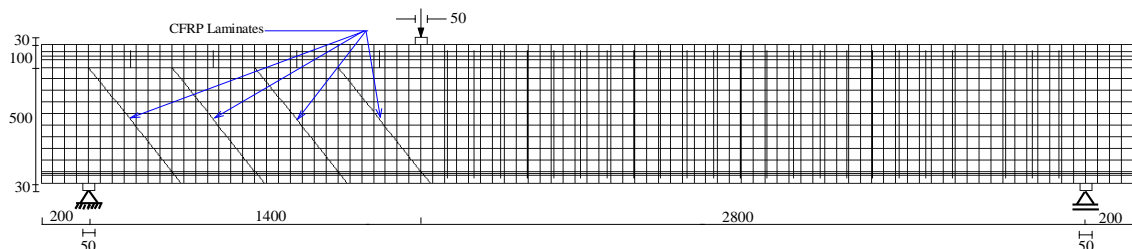
Fig. 4.27 – Finite element mesh used for the beam 3S-4LI-S2 (dimensions are in mm).

To avoid local crushing of the concrete, the load and support conditions were applied through steel plates that are modeled as a linear-elastic material with Poisson's coefficient of 0.3 and elasticity modulus of 200 *GPa*. The longitudinal steel bars, stirrups and CFRP laminates were modelled using 2-noded embedded cables (one degree-of-freedom per each node) with two IPs. Perfect bond was assumed between the reinforcement and the surrounding concrete. The behaviour of CFRP laminates was modeled using a linear-elastic stress-strain relationship. The values correspondent to the parameters of the constitutive model for concrete is gathered in Table 4.15. These values are obtained from the experimental program for the characterization of the relevant properties of the intervening materials.

Table 4.14 – Values of the parameters of the steel constitutive model for test of the shear strengthened RC beams.

Property	$\phi 6$	$\phi 10$	$\phi 12$	$\phi 16$	$\phi 32$
$\varepsilon_{sy}(\%)$	0.27805	0.2833	0.2833	0.2804	0.32725
$\sigma_{sy}(N/mm^2)$	556.1	566.6	566.6	560.8	654.5
$\varepsilon_{sh}(\%)$	1	1	1	1	1
$\sigma_{sh}(N/mm^2)$	583.905	594.93	594.93	588.8	687.2
$\varepsilon_{su}(\%)$	10	10	10	10	10
$\sigma_{su}(N/mm^2)$	682.6	661.6	661.6	675.0	781.9
Third branch exponent	1	1	1	1	1

To simulate the shear crack initiation and the degradation of crack shear stress transfer, the shear softening diagram represented in Fig. 3.2 is assumed, and the values of the parameters to define this diagram are included in Table 4.15.

4.2.5.4 Results and discussions

For the shear strengthened beams (3S-4LI-S2; 3S-4LI-P2; 3S-4LI4LI-SP1; 3S-4LI4LV-SP1), the transversal reinforcement (CFRP laminates and steel stirrups) provides additional confinement effect on the surrounding concrete bulk. This confinement enhances the aggregate interlock effect in the shear cracks crossed by these shear reinforcements.

Table 4.15 – Values of the parameters of the concrete constitutive model for the test of the shear strengthened RC beams.

Property	Value
Poisson's ratio	0.15
Young's modulus	E=32000 N/mm^2
Parameters defining the plastic-damage part of the model	α_0 =0.4; ε_{c1} =0.0035; $G_{f,c}$ =20 N/mm ; for strengthened beams f_c =40.1 N/mm^2; for the reference beam (3S_R) f_c =36.4 N/mm^2
Trilinear tension softening diagram (Fig. 3.1a)	$f_{ct} = 2.5\ N/mm^2$; $G_f^1 = 0.1\ N/mm$; $\xi_1 = 0.008$; $\alpha_1 = 0.25$; $\xi_2 = 0.4$; $\alpha_2 = 0.05$
Parameter defining the mode I fracture energy available to the new crack (Sena-Cruz, 2004)	2
Parameters defining the crack shear stress-crack shear strain softening diagram (Fig. 3.2)	$\tau_{t,p}^{cr}$ =1.6 N/mm^2; $\beta = 0.03$; for strengthened beams $G_{f,s}$ =0.3 N/mm; for the reference beam $G_{f,s}$ =0.04 N/mm
Crack bandwidth	Square root of the area of Gauss integration point
Threshold angle (Sena-Cruz, 2004)	30 degree
Maximum number of cracks per integration point (Sena-Cruz, 2004)	2

For these beams, even though the CFRP laminates and steel stirrups are separately modelled with embedded cable elements, their favourable effect in terms of aggregate interlock was considered by adopting different values of shear fracture energy ($G_{f,s}$) for the reference and strengthened beams.

Since the equivalent shear reinforcement ratio (CFRP laminates and steel stirrups) was not too different amongst the strengthened beams, the same value of $G_{f,s}$ =0.3 N/mm was adopted in the constitutive model, while in the reference beam a $G_{f,s}$ =0.04 N/mm was assumed, see Table 4.15. In fact, by increasing $G_{f,s}$ the beam's stiffness and load carrying capacity also increase, which indirectly simulates the favorable effect of the shear reinforcements on the aggregate interlock.

Predictions of the PDSC model in terms of the applied load versus displacement at the loaded section for all the beams of the experimental program are represented at Fig. 4.28. The good predictive performance was not only in terms of the load-deformation responses, but also in regards of the crack patterns (Figs. 4.29 and 4.30). The plastic zone

for each beam is also represented in Fig. 4.30 that shows the formation of the compressive strut in this type of shear tests.
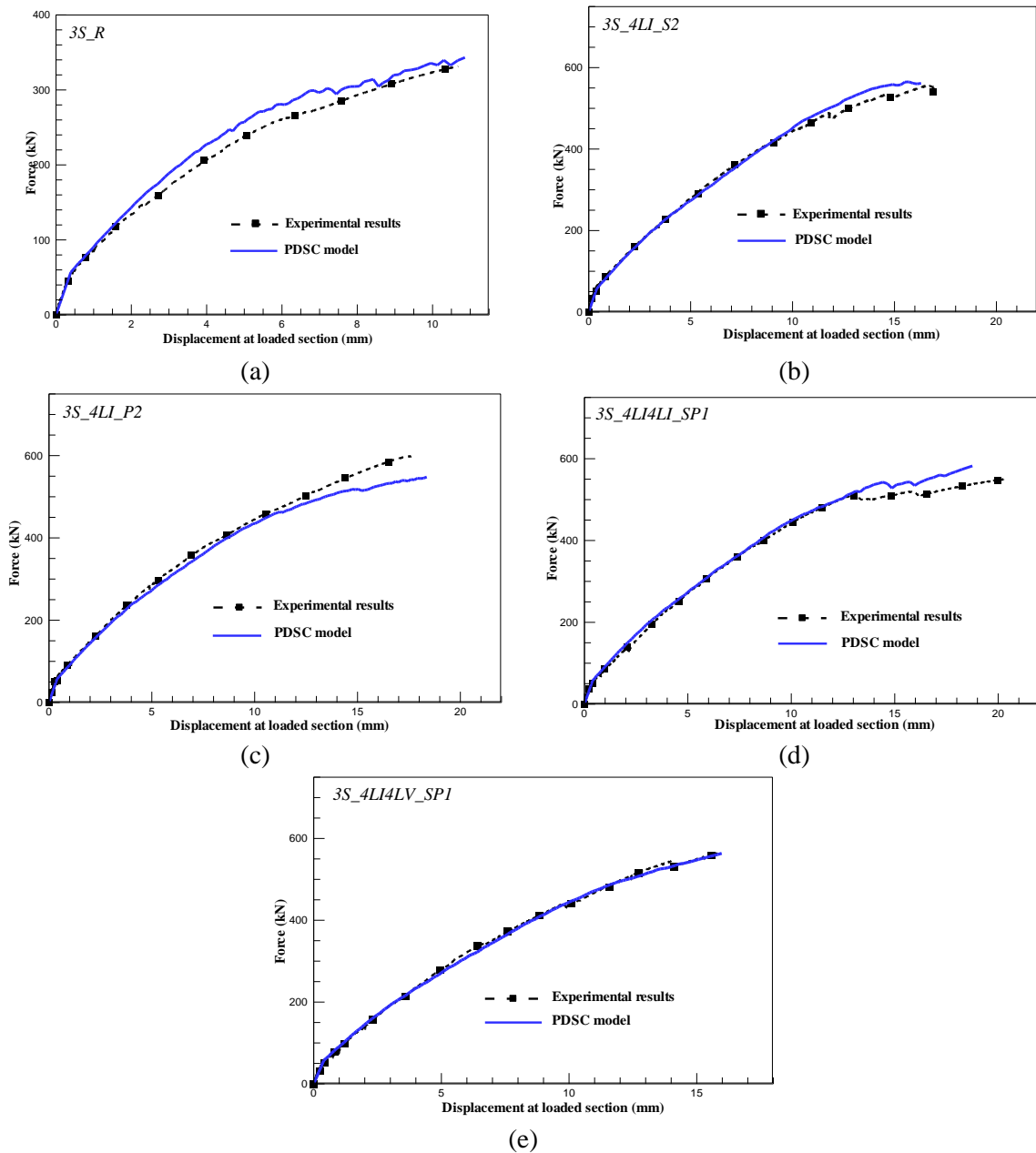
Fig. 4.28 – Experimental (Barros and Dias, 2013) and numerical load vs. the deflection at loaded deflection: (a) 3S-R; (b) 3S-4LI-S2; (c) 3S-4LI-P2; (d) 3S-4LI4LI-SP1; (e) 3S-4LI4LV-SP1.

Fig. 4.31 represents the strain development in the stirrups and CFRP laminates measured through the test of the beam 3S-4LI-S2 in compare to those of the proposed model. The results demonstrate the reasonable level of accuracy for this beam, but this conclusion can

be generalizes for all the simulated beams. Therefore it is believed the assumption of the perfect bond between the transverse shear reinforcement and concrete bulk did not significantly influence the resolution of the numerical predictions.

(a) 3S-R

(b) 3S_4LI_S2

(c) 3S_4LI_P2

(d) 3S_4LI4LI_SP1
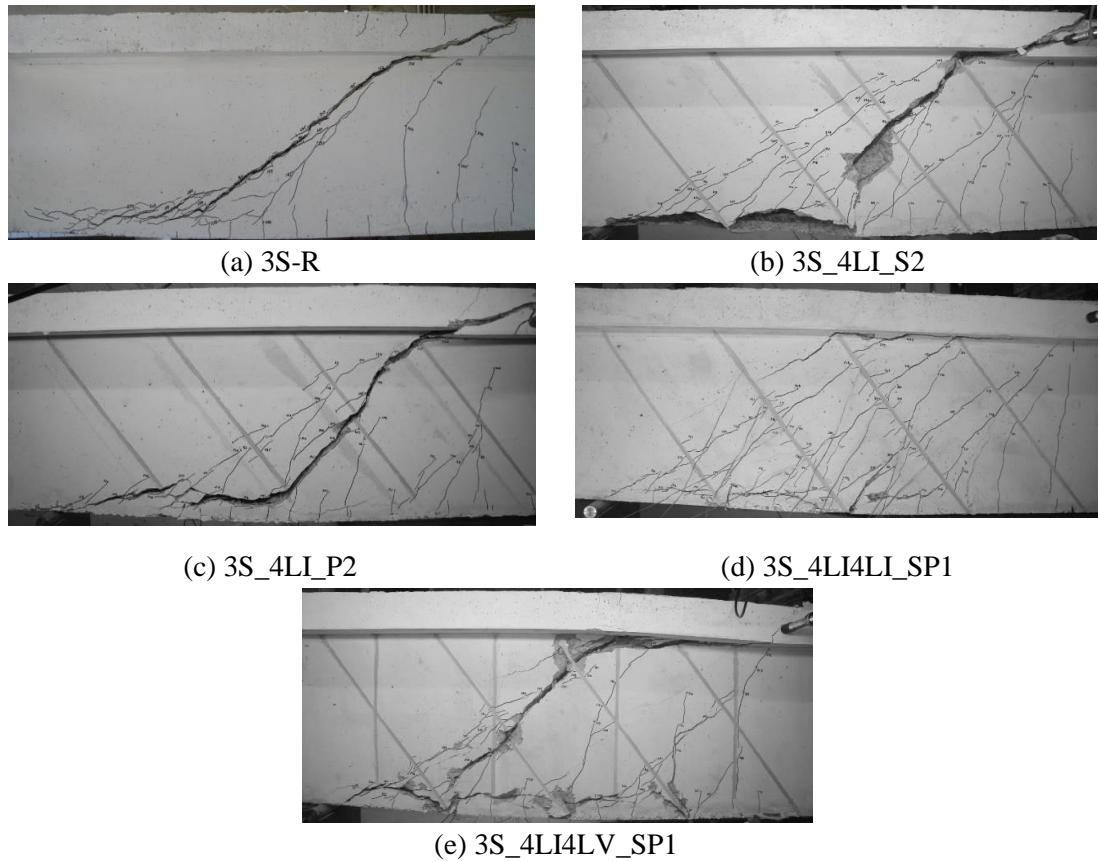
(e) 3S_4LI4LV_SP1

Fig. 4.29 – Crack patterns of the tested beams at failure (Barros and Dias, 2013).

crack pattern
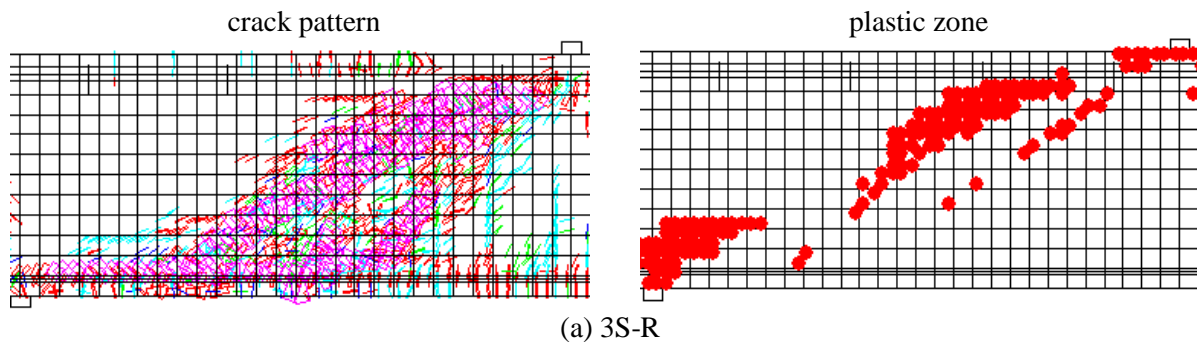
plastic zone

(a) 3S-R

Fig. 4.30 –Crack patterns and plastic zones predicted by PDSC model for the beams: (a) 3S-R; (b) 3S-4LI-S2; (c) 3S-4LI-P2; (d) 3S-4LI4LI-SP1; (e) 3S-4LI4LV-SP1 (the results are correspondent to the final converged step)

crack pattern   plastic zone

(b) 3S-4LI-S2

(c) 3S-4LI-P2

(d) 3S-4LI4LI-SP1

(e) 3S-4LI4LV-SP1
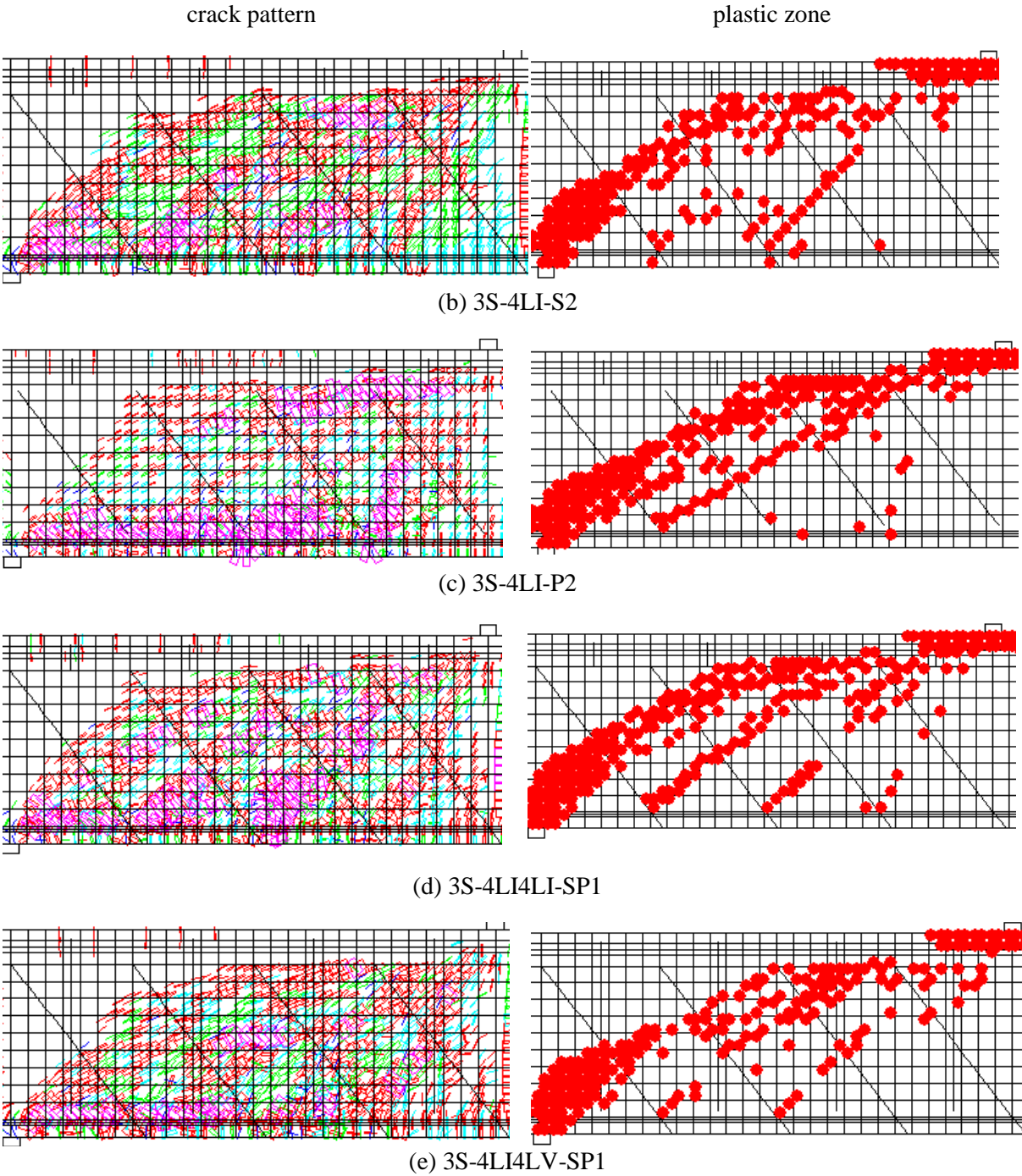
Fig. 4.30 – (Continued)
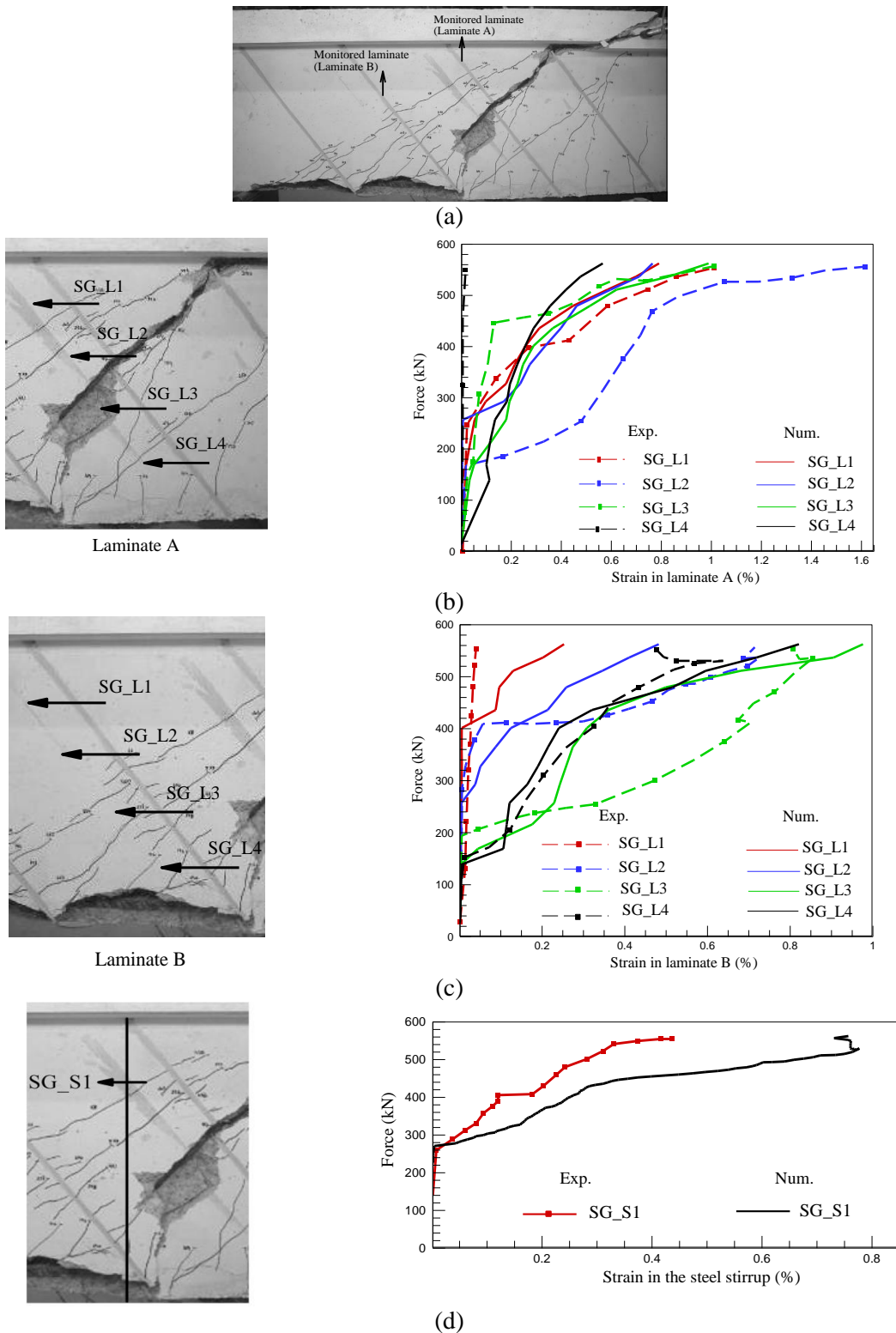
Fig. 4.31 – Experimental and numerical presentations of load-strain diagram for the beam 3S-4LI-S2: (a) monitored laminates; (b) NSM laminate A; (c) NSM laminate B; (d) monitored still stirrup.

4.2.6 Effect of fiber dosage and prestress level on shear behavior of RC beams

The experimental program (Soltanzadeh et al., 2016b) is composed of seven real-scale I cross section beams of 4000 mm total length, L, and 500 mm cross section height, h. These beams are categorized in two groups with, respectively, three and four members. The cross sectional dimensions and arrangement of the reinforcements of the beams in both, the first and second group, is illustrated in Fig. 4.32. The members of both groups shared the same configuration and geometry, but featured different level of prestress (in the first group of beams with three members) and fiber volume fraction (in the second group of beams with four members). Two different shear spans, of 1475 mm and 1650 mm, were also adopted, respectively, for the beams of first and second group, as shown in Fig. 4.32.
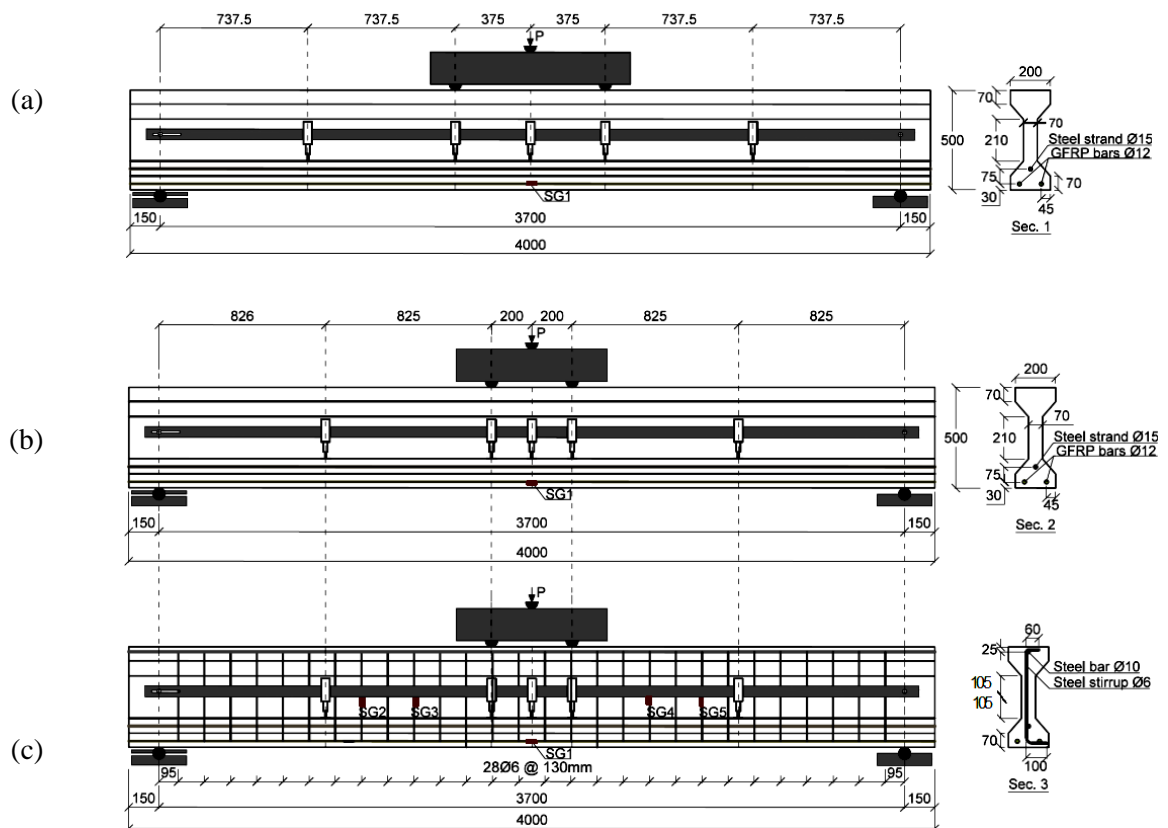
Fig. 4.32 - Geometry, reinforcement and test setup of the beams of (a) group 1 (G1-F1.1-S0; G1-F1.1-S23; G1-F1.1-S46), (b) group 2 except G2-F0-ST, (c) G2-F0-ST (dimensions in mm) (Soltanzadeh et al., 2016b).

The influence of prestressing the steel longitudinal reinforcements on the shear behavior of the beams was studied by testing the three beams of the first group, while the four beams of second group were tested to investigate the effect of fiber dosage on improving the shear resistance of the developed elements. The beams in both groups were longitudinally reinforced with one steel strand (15.2 mm diameter with a nominal cross section of 140 mm^2) of seven wires (of 5 mm diameter each, $\phi 5$), and 2 GFRP rebars of 12 mm diameter, $\phi 12$, with ribbed surface. For the GFRP rebars elasticity modulus of 56 GPa (E_{GFRP}=56 GPa), and tensile strength of 1350 ($f_{GFRP,u}$=1350 MPa) was reported at the experimental program (Soltanzadeh et al., 2016b).

In the beams of the first group the level of prestress, solely applied to the steel strand, was the main variable investigated. These beams were developed without conventional steel stirrups by using the concrete composition SCC-F1.1 that includes 90 kg/m^3 steel fibers (equal to 1.1% of the concrete volume). The beams of the second group were developed with constant level of prestress and different dosage of steel fibers, namely: 0%, 1.1% and 1.5% in volume (or respectively 0, 90, 120 kg/m^3 steel fibers in weight). The concretes with 0% and 1.5% steel fibers are designated as SCC-F0 and SCC-F1.5, respectively. Both the steel and GFRP reinforcements of this group (group 2) of the beams were prestressed, the steel strand at 56% of its tensile strength (974 MPa, since the tensile strength of the strand is 1740 MPa), while the two GFRP bars were prestressed at 30% of its tensile strength (405 MPa, since $f_{GFRP,u}$=1350 MPa). These beams of the second group were developed without conventional steel stirrups except the beam G2-F0-ST. The beam G2-F0-ST was reinforced with steel stirrup of 6 mm diameter, $\phi 6$, with spacing of 130 mm. The steel stirrups had the elastic modulus of 200 GPa and yield, and ultimate tensile strength of respectively 556 MPa and 682 MPa. Table 4.16 presents the relevant characteristics of the beams of the first and second groups.

Eight-noded serendipity plane stress finite elements with 3×3 Gauss–Legendre IP scheme were used for modeling the beams of both groups 1 and 2. In Fig. 4.33 is represented, as an example, the finite element mesh used for the simulation of the beam G1-F1.1-S0. The longitudinal steel strand and GFRP bars were modeled using 2-noded cable elements (one degree-of-freedom per each node) with two IPs. The compressive reinforcement and steel

stirrups installed in the beam G2-F0-ST are meshed using 2-noded embedded cables with two IPs. Perfect bond was assumed between the reinforcement bars/strand and the surrounding concrete. For modeling the behavior of the steel reinforcement, the stress-strain relationship represented in Fig. 4.3 was adopted. The values of the parameters that define the stress-strain law (Fig. 4.3) for the steel strand, stirrups, and compressive reinforcement are included in Table 4.17. The behavior of GFRP bar was modeled using a linear-elastic stress-strain relationship. The prestress load was simulated by means of temperature variation applied to the cable elements modeling the GFRP bars and steel strand. Table 4.18 includes the values of the temperature variation applied for each simulated beam. The values of the parameters used to define the constitutive law for concretes SCC-F0, SCC-F1.1 and SCC-F1.5 are indicated in Table 4.19.

Table-4.16 Details of the beams in first and second group.

Specimen ID		Concrete type	Prestress level		V_f (%)	Stirrup
			Steel strand (% of f_{sy}; stress level in MPa)	GFRP (% of $f_{GFRP,u}$; stress level in MPa)		
Group 1	G1-F1.1-S0	SCC-F1.1	0; 0	0	1.1	NO
	G1-F1.1-S23	SCC-F1.1	23; 400	0	1.1	NO
	G1-F1.1-S46	SCC-F1.1	46; 800	0	1.1	NO
Group 2	G2-F0	SCC-F0	56; 974	30; 405	0	NO
	G2-F0-ST	SCC-F0	56; 974	30; 405	0	YES
	G2-F1.1	SCC-F1.1	56; 974	30; 405	1.1	NO
	G2-F1.5	SCC-F1.5	56; 974	30; 405	1.5	NO
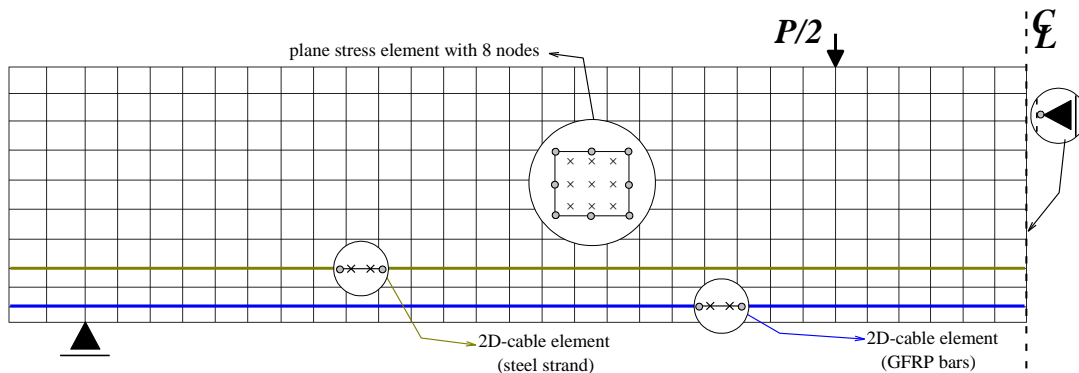
Fig. 4.33 - Finite element mesh, load and support conditions used for analysis of the beam G1-F1.1-S0.

Table-4.17 Values of the parameters of the steel constitutive model.

Diameter (mm)	ε_{sy} (%)	σ_{sy} (N/mm²)	ε_{sh} (%)	σ_{sh} (N/mm²)	ε_{su} (%)	σ_{su} (N/mm²)	Third branch exponent
[a] 15.2	0.87	1740	0.87	1740	20.0	1917	1
[b] 10	0.28	566	1	594	10.0	661	1
[c] 6	0.278	556	1	583	10.0	682	1

[a] steel strand; [b] compressive reinforcement; [c] stirrups.

Table-4.18 General information about the simulation of the prestress load by means of temperature variation.

Specimen ID	[a] $\sigma_{t,S}$ (MPa)	[b] $\sigma_{t,GFRP}$ (MPa)	[c] α $(mm/(mm\,^oC))$	[d] ΔT_S (^oC)	[e] ΔT_{GFRP} (^oC)
G1-F1.1-S0	-	-	-	-	-
G1-F1.1-S23	400	-	1×10^{-5}	-200	-
G1-F1.1-S46	800	-	1×10^{-5}	-400	-
G2-F0	974	405	1×10^{-5}	-487	-723
G2-F0-ST	974	405	1×10^{-5}	-487	-723
G2-F1.1	974	405	1×10^{-5}	-487	-723
G2-F1.5	974	405	1×10^{-5}	-487	-723

[a] $\sigma_{t,s}$ thermal stress applied to the steel strand; [b] $\sigma_{t,GFRP}$ thermal stress applied to the GFRP bars; [c] α coefficient of thermal expansion; [d] ΔT_S (^oC) temperature variation applied to the steel strand; [e] ΔT_{GFRP} (^oC) temperature variation applied to the GFRP bars.

Note: the thermal strain and corresponding stress for the steel strand are calculated from: $\varepsilon_{t,S} = \alpha\,\Delta T_S$; $\sigma_{t,S} = E_S\,\varepsilon_{t,S}$. For the GFRP bars the following equations are taken: $\varepsilon_{t,GFRP} = \alpha\,\Delta T_{GFRP}$; $\sigma_{t,GFRP} = E_{GFRP}\,\varepsilon_{t,GFRP}$.

To simulate the shear crack initiation and the degradation of crack shear stress transfer, the shear softening diagram represented in Fig. 3.2 is assumed, and the values of the parameters to define this diagram for each concrete are included in Table 4.19. For the concretes SCC-F1.1 and SCC-F1.5 the same crack shear strength was used ($\tau_{t,p}^{cr}$ =1.75 MPa), while for the concrete SCC-F0 the value 1.2 MPa was adopted for $\tau_{t,p}^{cr}$. The shear fracture energy for the concrete without steel fiber (concrete SCC-F0) was adopted as $G_{f,s}$ =0.08 *N/mm*. For the concretes including the steel fibers (concretes SCC-F1.1 and SCC-F1.5) higher values of $G_{f,s}$ are adopted, as indicated in Table 4.19, to simulate the effect of fiber reinforcement in resisting the degradation of shear stress transfer between the faces of the cracks during the cracking process.

Table 4.19 – Values of the parameters of the concrete constitutive model for concretes SCC-F0, SCC-F1.1, and SCC-F1.5.

Property	Value
Poisson's ratio	0.2
Young's modulus	for SCC-F0 E=32100 N/mm^2; for SCC-F1.1 E=33230 N/mm^2; for SCC-F1.5 E=30580 N/mm^2
Parameters defining the plastic-damage part of the model	for SCC-F0: f_c=66.45 N/mm^2; $G_{f,c}$=25 N/mm; ε_{c1}=0.0035; α_0=0.4; for SCC-F1.1: f_c=67.05 N/mm^2; $G_{f,c}$=55 N/mm; ε_{c1}=0.004; α_0=0.4; for SCC-F1.5: f_c=60.03 N/mm^2; $G_{f,c}$=65 N/mm; ε_{c1}=0.004; α_0=0.4
Quadrilinear tension softening diagram (Fig. 3.1b)	for SCC-F0: f_{ct}=3.25 N/mm^2; G_f^1=0.08 N/mm; ξ_1=0.007; α_1=0.3; ξ_2=0.1; α_2=0.15; ξ_3=0.15; α_3=0.05; for SCC-F1.1: f_{ct}=3.25 N/mm^2; G_f^1=6.0 N/mm; ξ_1=0.0005; α_1=0.75; ξ_2=0.0025; α_2=1.0; ξ_3=0.1; α_3=0.6; for SCC-F1.5: f_{ct}=3.25 N/mm^2; G_f^1=7.5 N/mm; ξ_1=0.0005; α_1=0.75; ξ_2=0.0025; α_2=1.0; ξ_3=0.1; α_3=0.6
Parameter defining the mode I fracture energy available to the new crack (Sena-Cruz, 2004)	2

Parameters defining the crack shear stress-crack shear strain softening diagram (Fig. 3.2)	for SCC-F0: $\tau_{t,p}^{cr}$=1.2 N/mm^2; β=0.4;
	 $G_{f,s}$=0.08 N/mm;
	 for SCC-F1.1: $\tau_{t,p}^{cr}$=1.75 N/mm^2; β=0.2;
	 $G_{f,s}$=1.5 N/mm;
	 for SCC-F1.5: $\tau_{t,p}^{cr}$=1.75 N/mm^2; β=0.2;
	 $G_{f,s}$=2.0 N/mm

Crack bandwidth	Square root of the area of Gauss integration point
Threshold angle (Sena-Cruz, 2004)	30 degree
Maximum number of cracks per integration point (Sena-Cruz, 2004)	2

Fig. 4.34 and Fig. 4.35 compare the numerical and the experimental load vs. mid-span deflection for the beams of first and second groups, respectively. Fig. 4.36 represents the experimental crack pattern of all the beams in both groups at the failure stage.
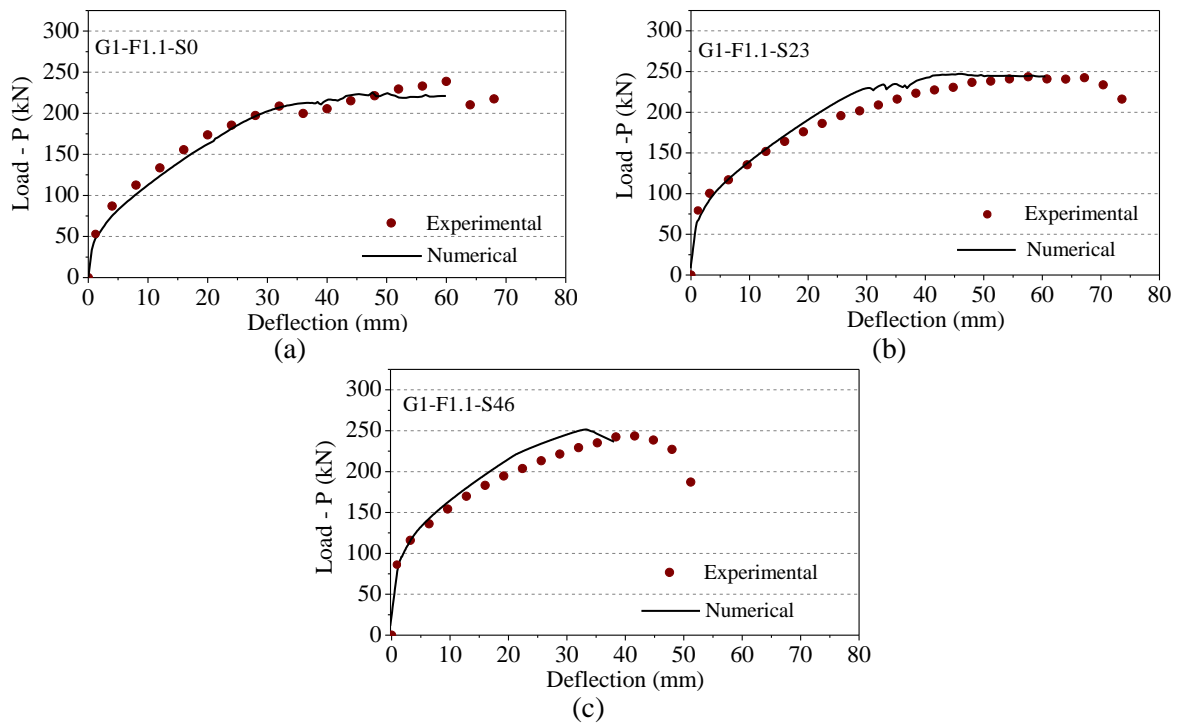
Fig. 4.34 - Experimental and numerical load *vs.* mid-span deflection of the beams of the first group: (a) G1- F1.1-S0; (b) G1- F1.1-S23; (c) G1- F1.1-S46.

In Fig. 4.37 is represented, as an example, the numerical crack pattern for the simulation of the beams G2-F1.5 at the end of the analysis (at the end of the last converged loading step). The figures 4.34 to 4.37 show that the numerical model is able to capture with good accuracy the deformational response of the beams and the experimentally observed profile of the failure crack. For all the beams the numerical peak load, $F_{\max}^{Num}$, predicted by the model are compared with the experimental ones, $F_{\max}$, in Table 4.20. The information provided in Table 4.20 shows that the peak loads of all beams are closely simulated with the average error of 6.07%.

(a)   (b)

(c)   (d)
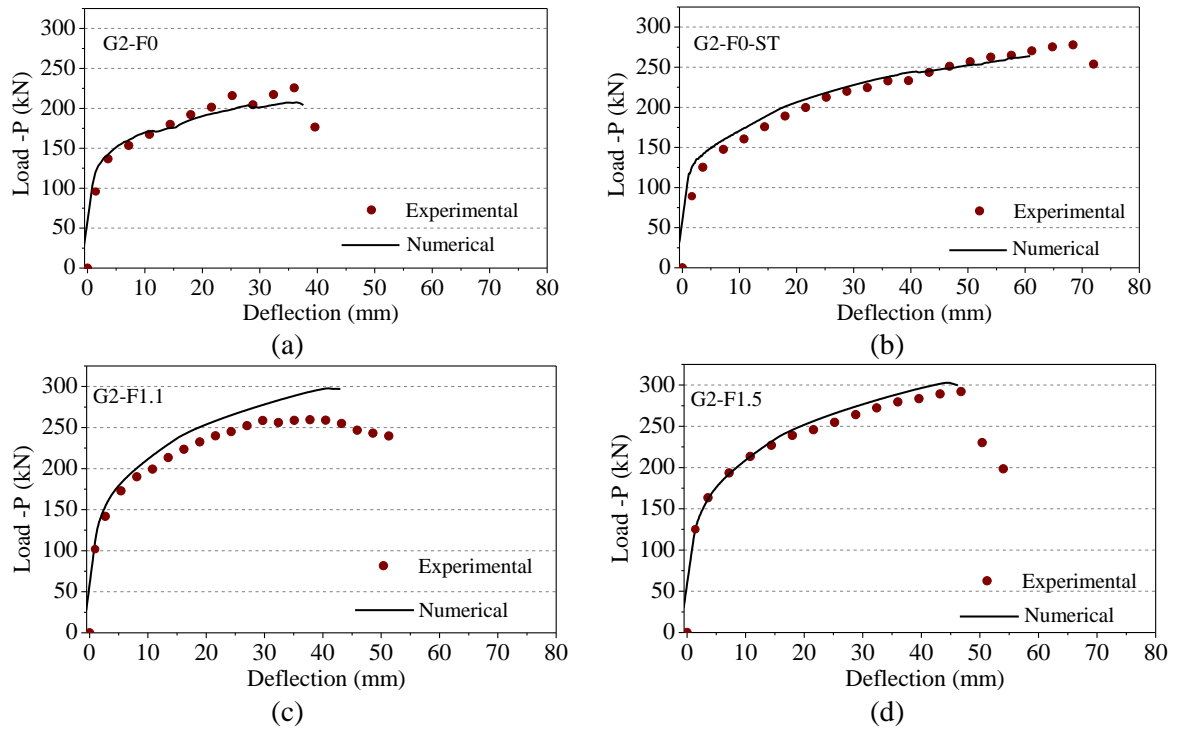
Fig. 4.35 - Experimental and numerical load *vs.* mid-span deflection of the beams of the second
group: (a) G2- F0; (b) G2- F0-ST; (c) G2- F1.1; (d) G2-F1.5.

G1-F1.1-S0 (Reference)   G1-F1.1-S23

G1-F1.1-S46

G2-F0 (Reference)   G2-F0-ST

G2-F1.1   G2-F1.5
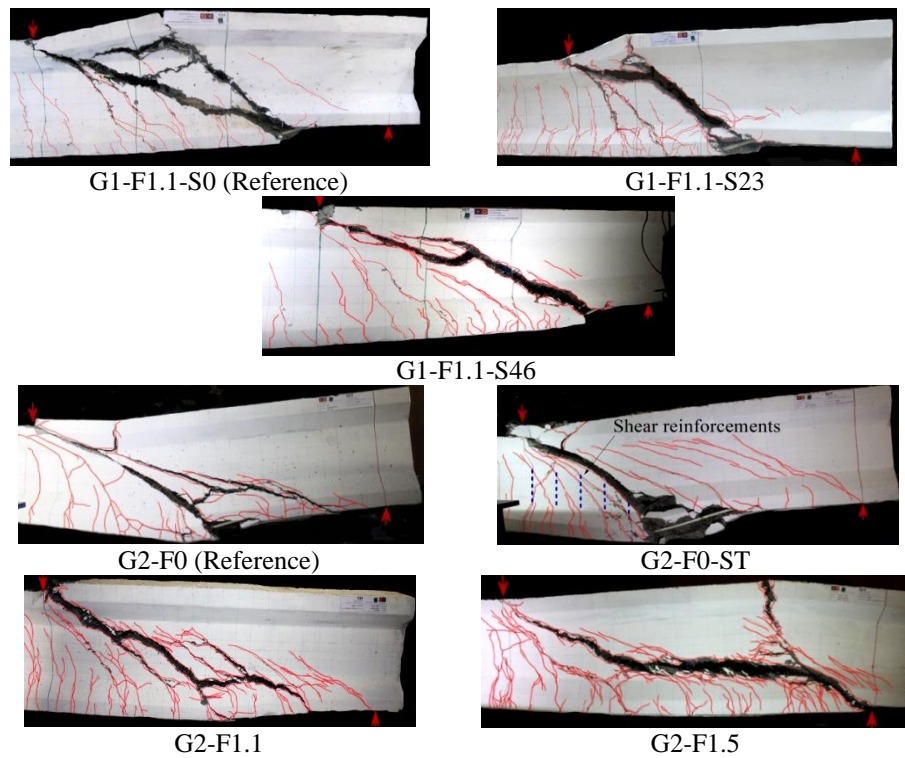
Fig. 4.36 – Crack pattern at failure of the first and second group of beams
(Soltanzadeh et al., 2016b).
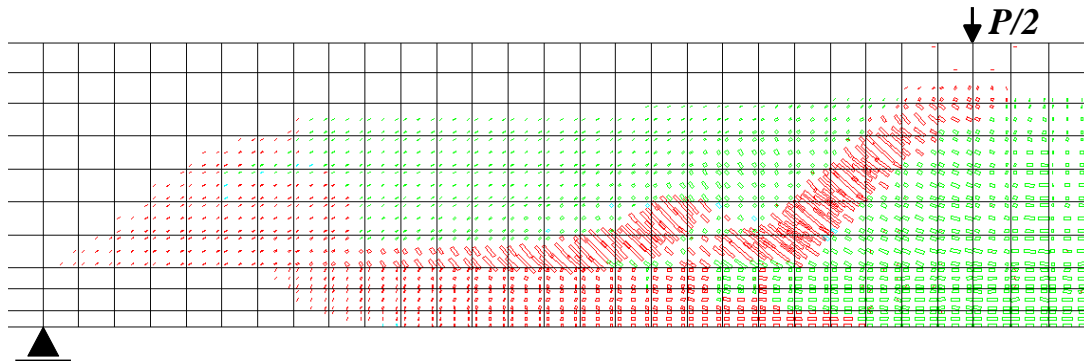
Fig. 4.37 - Numerical crack pattern predicted by PDSC model for the beam G2- F1.5 (The results correspond to the final converged step).

Fig. 4.38 compares the numerical and the experimental load vs. strain ($P - \varepsilon_{STIRRUP}$) relationship, where strain was registered in the location where the strain gauges SG4 and SG5 were installed in the stirrups of the beam G2-F0-ST (see Fig. 4.32). This figure indicates the both stirrups are already yielded at the failure stage of the beam G2-F0-ST, which was also observed in the experimental program.
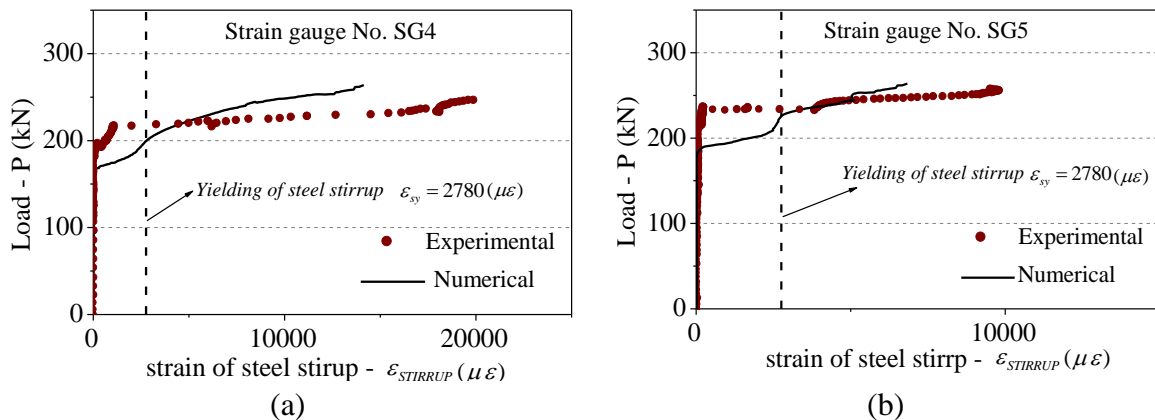
Fig. 4.38 - Experimental and numerical load vs. strain in steel stirrups of beam G2-F0-ST.

The predicted $P - \varepsilon_{GFRP}$ relationships (load versus strain obtained in the IP closest to the mid-span of the beam) for all the beams, except for the G1-F1.1-S46 beam (due to malfunctioning of the corresponding strain gauge), are compared with those of experiments in Fig. 4.39.

Fig. 4.38 and Fig. 4.39 show the numerical simulations, in general, predict with good accuracy the strain measured in the stirrups and GFRP bars, which means the assumption of perfect bond between the steel stirrups and GFRP bars and surrounding concrete adopted in these simulations, is acceptable. It should be aware that strains recorded by strain gauges are quite dependent on their distance to the cracks crossing the reinforcements where they are installed.

Table 4.20 – Details of the experimental results and the numerical analysis.

Specimen ID	F_{max} (kN)	F_{max}^{Num} (kN)	$\left| F_{max} - F_{max}^{Num} \right| / F_{max}$ (%)
G1-F1.1-S0	240.12	221.04	7.9
G1-F1.1-S23	244.80	249.08	1.74
G1-F1.1-S46	245.6	251.53	2.41
G2-F0	229.52	207.63	9.53
G2-F0-ST	277.98	263.88	5.0
G2-F1.1	263	296.91	12.89
G2-F1.5	293.75	302.78	3.07
		Average	6.07
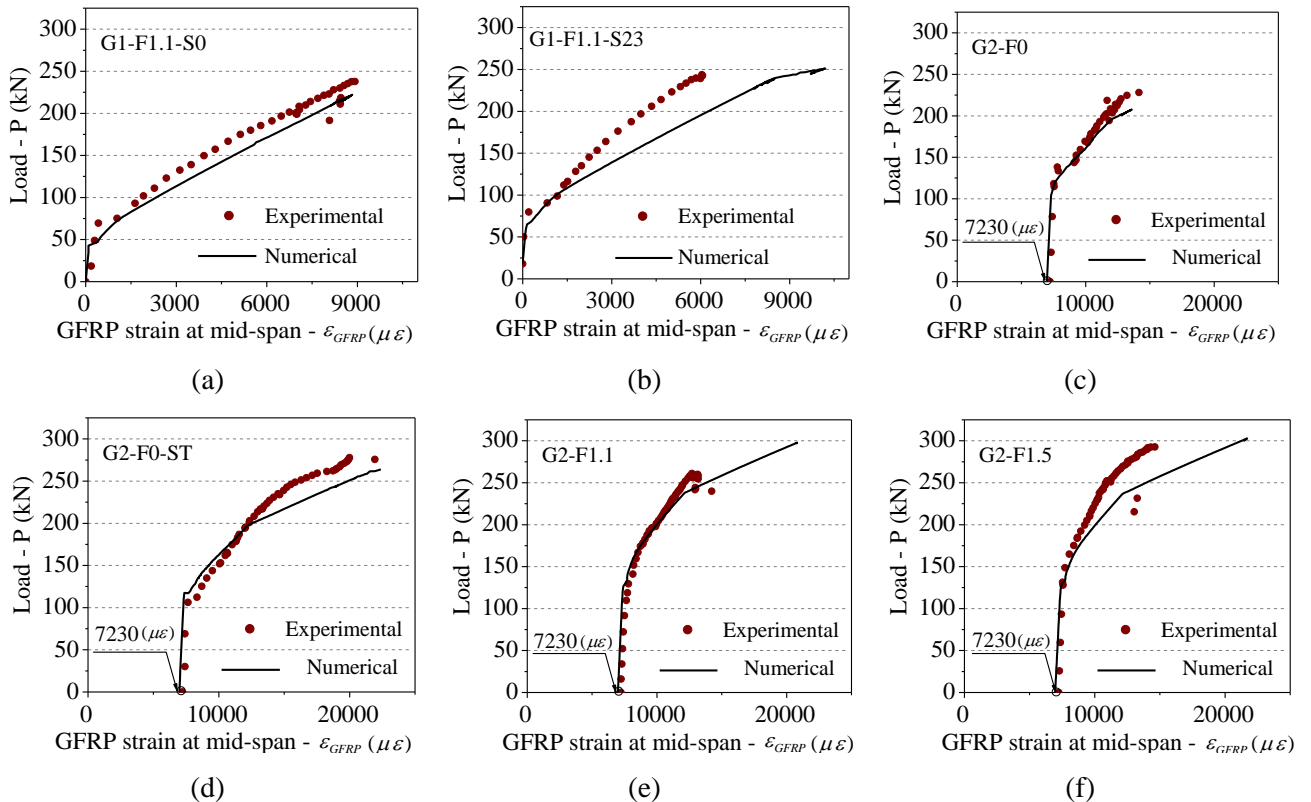
Fig. 4.39 - Experimental and numerical load vs. GFRP strain at mid-span of the beams.

The numerical relationships of the load vs. strain of steel strand at the beam's mid-span ($P - \varepsilon_{STRAND}$) for all the developed beams are represented in Fig. 4.40 (the strain is obtained at the IP closest to the mid-span of the beam). Fig. 4.40 shows that the steel strand is not yielded in the control beam of the group 1 (the beam G1-F1.1-S0), while in the beams G1-F1.1-S23 and G1-F1.1-S46 (the beams in group 1 and with prestress applied to the steel strand) the steel strand has yielded at the loads about 230 kN.
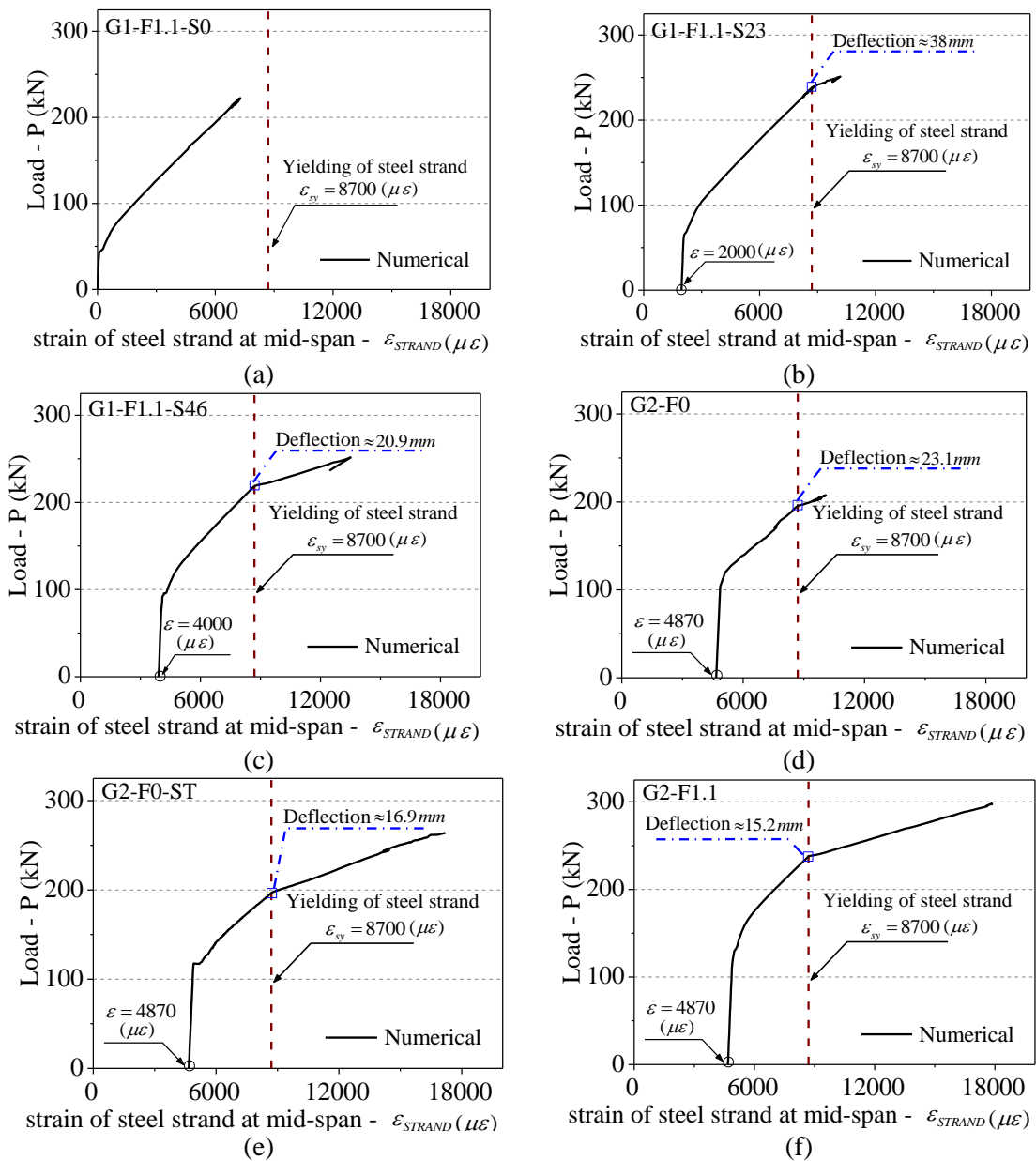
Fig. 4.40 - Numerical load vs. strain of strand in mid-span of the beams relationships.
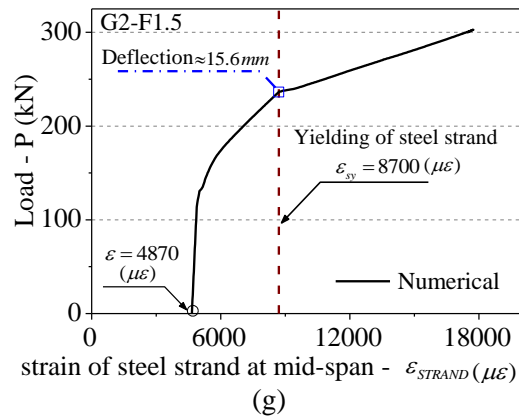
Fig. 4.40 – (Continued)

For the beams G2-F0 and G2-F0-ST, which are in the second group and made by concrete SCC-F0, the steel strands has yielded at the load of about 200 kN. The predicted strain in the strand at failure stage of the beam G2-F0-ST is about 77% higher than that of the G2-F0, which is mainly due to the larger ultimate deflection of the beam G2-F0-ST.

For the beams in the second group and made by SFRSCC (the beams G2-F1.1 and G2-F1.5), the yield initiation of steel strands has occurred at the load of about 240 kN. This load is higher than those predicted for the beams made by concrete SCC-F0 (the beams G2-F0 and G2-F0-ST), since the steel fibers bridging the flexural cracks crossing the steel strand have contributed to decrease the average strain installed in the strand (Mazaheripour et al., 2016).

Taking into account that the steel strand of the G1-F1.1-S0 beam was the unique to have not yielded, the remaining beams can be considered as having failed in flexural-shear, since the formation of a critical shear crack in these beams has occurred after yield initiation of the steel strand and was caused by the strain-hardening character of this type of steel, and the linear behavior and relatively high ultimate tensile strain of GFRP bars.

4.3 CONCLUSIONS

The constitutive model developed in chapter 3, was integrated in plane stress element of the FEMIX computer code, which is a general purpose finite element program. The chapter 4 is mainly dedicated to explore the potentialities of the proposed constitutive model for the analysis of concrete and RC structures. The model is employed to simulate

experimental tests that are governed by nonlinear phenomenon due to simultaneous occurrence of cracking and inelastic deformation in compression. The simulated examples cover a wide range of geometry of specimens, concrete type, loading configurations, and reinforcement conditions.

The numerical simulations have predicted with good accuracy the load carrying capacity ductility, crack pattern, plastic (compressive) zone, and failure modes of all types of structures analysed. The results of these analyses indicate the robustness and accuracy of the proposed model for simulating concrete and RC structures subjected to multi-axial loading configurations.

CHAPTER 5

THREE DIMENSIONAL PDSC MODEL: FORMULATION AND APPLICATION IN STRUCTURAL ANALYSIS

5.1 INTRODUCTION

Three dimensional FEM analyses can be simplified into two dimensional ones when geometry of the structure under analysis and the distribution of loads allow the structure to be treated as bi-dimensional body. In this case the two dimensional analysis can be used to save the computational cost with sufficient accuracy. However in some cases, due to specific geometry of the structure or the distribution of the loads, the two-dimensional analyses are incapable to predict with sufficient accuracy the behaviour of the structures under analysis, therefore three dimensional approaches should be used instead

The present chapter proposes a new three dimensional (3D) constitutive model for cement based materials, based in the generalization of the two dimensional (2D) plastic-damage multidirectional fixed smeared crack model (represented in chapter 3), allowing the possibility of simulating its failure in structures with arbitrary geometry and dimensions. The proposed model simulates the crack opening and shear sliding according to an already existing 3D multidirectional fixed smeared crack model (Ventura-Gouveia et al., 2008; Ventura-Gouveia, 2011). The model simulates the nonlinear compressive

behaviour of concrete between the cracks using a numerical strategy that combines the elasto-plasticity (plasticity) and damage theories.

Later in this chapter the three dimensional PDSC model was included in the 3D solid element of the FEMIX computer code (Sena-Cruz et al., 2007; Ventura-Gouveia et al., 2008), and its performance validated by simulating examples at the material and structural levels. The numerical tool is employed to simulate the experimental tests of RC column subjected to different eccentric loadings, RC beams made by different concrete strength classes, and RC walls subjected to pure torsion. The predicted load carrying capacity, ductility, crack pattern, plastic (compressive) zone, and failure modes of all types of analysed structures are discussed and compared with the experimental data. Finally, a parametric study is executed for highlighting the sensitivity of the numerical simulations to the values adopted for the model parameters.

5.2 MODEL DESCRIPTION

5.2.1 Part of the model corresponding to the cracking process

To derive the constitutive equation of the proposed model, the additive decomposition of the incremental strain vector, $\Delta\underline{\varepsilon}$, into an incremental crack strain vector, $\Delta\underline{\varepsilon}^{cr}$, and an incremental elastic strain vector, $\Delta\underline{\varepsilon}^{e}$, and an incremental plastic strain vector, $\Delta\underline{\varepsilon}^{p}$, is adopted (i.e. $\Delta\underline{\varepsilon} = \Delta\underline{\varepsilon}^{cr} + \Delta\underline{\varepsilon}^{e} + \Delta\underline{\varepsilon}^{p}$). The incremental elastic strain vector is related to the incremental stress vector, $\Delta\underline{\bar{\sigma}}$, according to the following constitutive equation:

$$\Delta\underline{\bar{\sigma}} = \underline{D}^{e} \, (\Delta\underline{\varepsilon} - \Delta\underline{\varepsilon}^{p} - \Delta\underline{\varepsilon}^{cr})$$

(5.1)

Being $\Delta\underline{\bar{\sigma}} = \{\Delta\bar{\sigma}_1, \Delta\bar{\sigma}_2, \Delta\bar{\sigma}_3, \Delta\bar{\tau}_{23}, \Delta\bar{\tau}_{31}, \Delta\bar{\tau}_{12}\}$ the incremental stress vector induced into the material due to $\Delta\underline{\varepsilon} = \{\Delta\varepsilon_1, \Delta\varepsilon_2, \Delta\varepsilon_3, \Delta\gamma_{23}, \Delta\gamma_{31}, \Delta\gamma_{12}\}$ and considering the constitutive matrix of the intact material, $\underline{D}^{e}$.

The $\Delta\underline{\varepsilon}^{cr}$ is obtained from the incremental local crack strain vector, $\Delta\underline{\varepsilon}_{\ell}^{cr}$ according to the Eq. (2.32).

where:

$$\Delta\underline{\varepsilon}_\ell^{cr} = \left[\Delta\varepsilon_n^{cr}, \Delta\gamma_{t_1}^{cr}, \Delta\gamma_{t_2}^{cr}\right]^T \tag{5.2}$$

with the subscripts n, t_1, and t_2 indicating the axes of the local coordinate system of the crack (see Fig. 5.1). The component $\Delta\varepsilon_n^{cr}$ is the mode I incremental crack normal strain, while $\Delta\gamma_{t_1}^{cr}$ and $\Delta\gamma_{t_2}^{cr}$ are the sliding mode incremental crack shear strains in the directions $\hat{t}_1$ and $\hat{t}_2$, respectively.
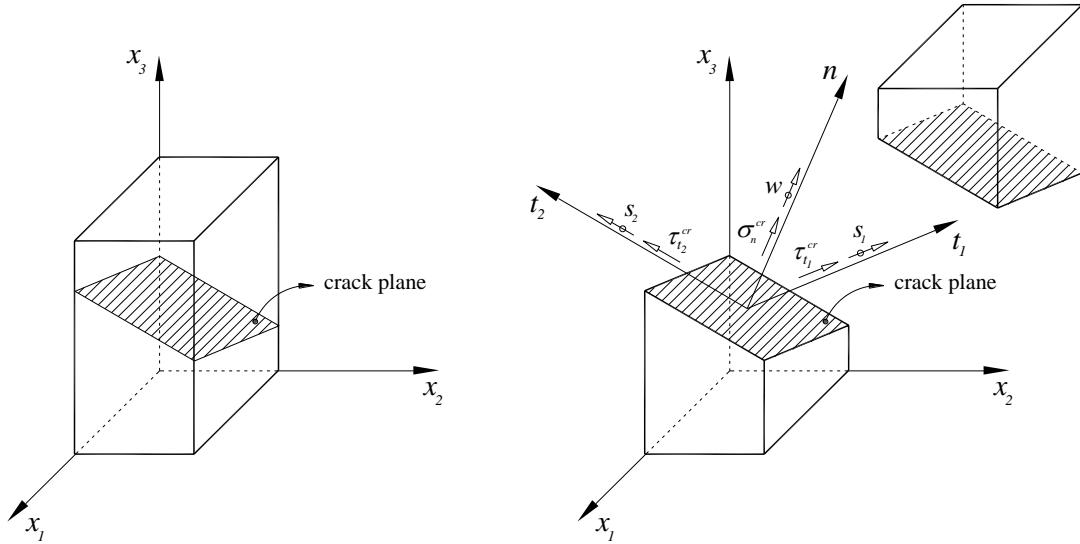
Fig. 5.1 – Crack stress components, displacements and local coordinate system of the crack (Ventura-Gouveia et al., 2008; Ventura-Gouveia, 2011).

At the crack zone of an IP, the opening and sliding process is governed by the following crack constitutive relationship according to Eq. (2.35), (i.e. $\Delta\underline{\sigma}_\ell^{cr} = \underline{D}^{cr}\Delta\underline{\varepsilon}_\ell^{cr}$).

where $\Delta\underline{\sigma}_\ell^{cr}$ is the vector of the incremental crack stress in the crack coordinate system with the contribution of normal, $\Delta\sigma_n^{cr}$, and tangential components, $\Delta\tau_{t_1}^{cr}$, $\Delta\tau_{t_2}^{cr}$:

$$\Delta\underline{\sigma}_\ell^{cr} = \left[\Delta\sigma_n^{cr}, \Delta\tau_{t_1}^{cr}, \Delta\tau_{t_2}^{cr}\right]^T \tag{5.3}$$

Fig. 5.1 represents the components of the crack stress vector (i.e. σ_n^{cr}, $\tau_{t_1}^{cr}$, $\tau_{t_2}^{cr}$) in the local coordinate system of the crack, and the corresponding displacements (i.e. w, s_1, s_2), being w the opening displacement, s_1 the sliding displacement in $\hat{t}_1$ direction, and s_2 sliding displacement in $\hat{t}_2$ direction.

At the IP the equilibrium condition is assured by imposing the Eq. (2.37), (i.e. $\Delta \underline{\sigma}_\ell^{cr} = \underline{T}^{cr} \Delta \underline{\bar{\sigma}}$).

The matrix $\underline{D}^{cr}$ that includes the constitutive law of the active cracks, i.e., the ones not completely closed, is defined as:

$$\underline{D}^{cr} = \begin{bmatrix} D_n^{cr} & 0 & 0 \\ 0 & D_{t_1}^{cr} & 0 \\ 0 & 0 & D_{t_2}^{cr} \end{bmatrix} \tag{5.4}$$

where D_n^{cr}, $D_{t_1}^{cr}$ and $D_{t_2}^{cr}$ represent, respectively, the modulus corresponding to fracture mode I (normal), sliding modulus in the $\hat{t}_1$ direction, and sliding modulus in the $\hat{t}_2$ direction.

The crack normal stress, σ_n^{cr}, and the modulus D_n^{cr} are obtained from a trilinear/quadrilinear diagram i.e. $\sigma_n^{cr} - \varepsilon_n^{cr}$ law, like the one represented in Fig. 3.1.

The sliding modulus $D_{t_1}^{cr}$ and $D_{t_2}^{cr}$ can be simulated as:

$$D_{t_1}^{cr} = D_{t_2}^{cr} = \frac{\beta}{1-\beta} G_c \tag{5.5}$$

where G_c is the concrete elastic shear modulus, while the shear retention factor, β, can be a constant value or, alternatively, obtained by Eq. (3.6).

The $\tau_t^{cr} - \gamma_t^{cr}$ softening law (represented in Fig. 3.2) adopted to simulate more correctly the shear stress transfer during the crack opening process (Ventura-Gouveia, 2011; Baghi

and Barros, 2016; Soltanzadeh et al., 2016b). In this approach the crack shear stress ($\Delta\tau_{t_1}^{cr}$ or $\Delta\tau_{t_2}^{cr}$), and the modulus D_t^{cr} are obtained from the $\tau_t^{cr} - \gamma_t^{cr}$ softening law. The modulus of the first branch, $D_{t,1}^{cr}$ (see Fig. 3.2), is obtained according to Eq. (5.5) and using a constant value in the range $]0,1[$ for β. For each crack shear component, the crack shear strain at peak ($\gamma_{t_1,p}^{cr}$ or $\gamma_{t_2,p}^{cr}$) is obtained using the crack shear strength $\tau_{t,p}^{cr}$ and the crack shear modulus $D_{t,1}^{cr}$ from the following equation (Ventura-Gouveia, 2011):

$$\gamma_{t_1,p}^{cr} = \gamma_{t_2,p}^{cr} = \frac{\tau_{t,p}^{cr}}{D_{t,1}^{cr}} \qquad (5.6)$$

The ultimate crack shear strain in each sliding directions ($\gamma_{t_1,u}^{cr}$ or $\gamma_{t_2,u}^{cr}$) depends on the shear fracture energy, $G_{f,s}$, crack shear strength, $\tau_{t,p}^{cr}$, and the crack bandwidth, l_b, as follows (Ventura-Gouveia, 2011):

$$\gamma_{t_1,u}^{cr} = \gamma_{t_2,u}^{cr} = \frac{2G_{f,s}}{\tau_{t,p}^{cr} l_b} \qquad (5.7)$$

As demonstrated in the previous 2D version of the PDSC model (represented in chapter 3), for accurate predictions of the behavior of RC elements failing in shear, is fundamental the adoption of a crack shear softening approach.

It should be noted the above-described equations are represented for the particular case of only one crack per IP, however, the model is able to consider forming several cracks in the same IP. The details corresponding to this development can be found elsewhere (Ventura-Gouveia et al., 2008; Ventura-Gouveia, 2011).

5.2.2 Part of the model corresponding to the elasto-plasticity

The plastic strain vector, $\Delta\underline{\varepsilon}^p$, which appears in Eq. (5.1), is evaluated by a time-independent plasticity model that is defined by four entities: yield function (yield

surface); flow rule; evolution law for the hardening parameter; and conditions for defining loading-unloading process. The plasticity part of the model is formulated in the effective stress space, and accounts for the development of irreversible strains and inelastic volumetric expansion of material under compression. To define the effective stress space a distinction is made between the stress acting on damaged and undamaged configurations of the material when subjected to a compression stress field. Effective stress means the stress acting in the undamaged configuration of the material, defined as the force divided by the undamaged area. Force divided by the total area (damaged plus undamaged area) is called nominal stress (Edalat-Behbahani et al., 2015; Edalat-Behbahani et al., 2016). Formulation of the plastic response in the effective stress space implies the plasticity model do not account for the damage formed when the material is loaded in compression. In this model, the state of damage in material under compression is simulated in the framework of CDM as will be discussed in section 5.2.3.

For the three dimensional model, the equations describing yield function (Eq. (3.15)), flow rule (Eq. (3.16)), evolution law for the hardening parameter (Eq. (3.17)), and onditions for defining loading-unloading process (Eq. (3.18)) still hold in the form deduced in section 3.3.3.

5.2.3 Part of the model corresponding to the damage process

In this model, the stiffness degradation and softening behaviour of concrete under compression are simulated in the framework of CDM, in which the damage is considered as an isotropic process. In this approach the state of damage in concrete under compression is equally distributed in all directions, and can be represented by a scalar measure, represented by d_c. The scalar damage parameter d_c calculated according to Eq. (3.54). The scalar damage parameter d_c is used to map the effective stress vector ($\bar{\underline{\sigma}}$) into the nominal stress vector ($\underline{\sigma}$) according to Eq. (3.14).

The coupling between the presented parts of the model and the corresponding obtained system of nonlinear equations, that should be solved to update the local variables of the 3D PDSC model at a generic load increment of the incremental/iterative Newton–Raphson algorithm generally adopted in FEM-based material nonlinear analysis, are

similar to the described in the section 3.3.3.2 and 3.3.4 of the chapter 3 for the 2D PDSC model.

5.3 SIMULATIONS AT THE MATERIAL LEVEL

The proposed model is initially validated by executing numerical tests at the material level (single cube-shaped 8-noded solid element with one IP), which are intended as an elementary verification of the basic capabilities of the model. The loading procedure of the tests consists of imposing prescribed displacement increments and assuming the crack bandwidth (l_b) equal to 100 mm. Since the concrete properties in each test were different, the corresponding values are indicated in the caption of the figures.

- *Simulation of cyclic compression-tension loading sequence (Fig. 5.2):* The element is initially loaded in compression, along the direction X_2, up to a stage where the concrete enters in the softening phase ($\tilde{\epsilon}_c > \tilde{\epsilon}_{c1}$). Due to compressive loading beyond the uniaxial compressive strength of the concrete ($f_c = 30$ MPa), damage due to inelastic compressive deformation is developed ($d_c > 0$). Then the element is unloaded to tension and the unloading occurs with the damaged stiffness $(1 - d_c)E$, being E the undamaged stiffness at the plasticity model. By increasing the tensile loading, a crack (with the crack plane orthogonal to the loading direction X_2) initiates and further propagates. The element is then reloaded to compression, which causes the crack to be gradually closed with a secant unloading branch. By increasing compressive loading the crack is completely closed and later the response returns back to the softening stage in compression. The loading procedure is continued for one more cycle of compression-tension-compression, and the similar material response as that of the first cycle was simulated. The response of the proposed model (in nominal stress space) is compared in Fig. 5.2a with the solution reported at the work of Gernay et al. (2013).
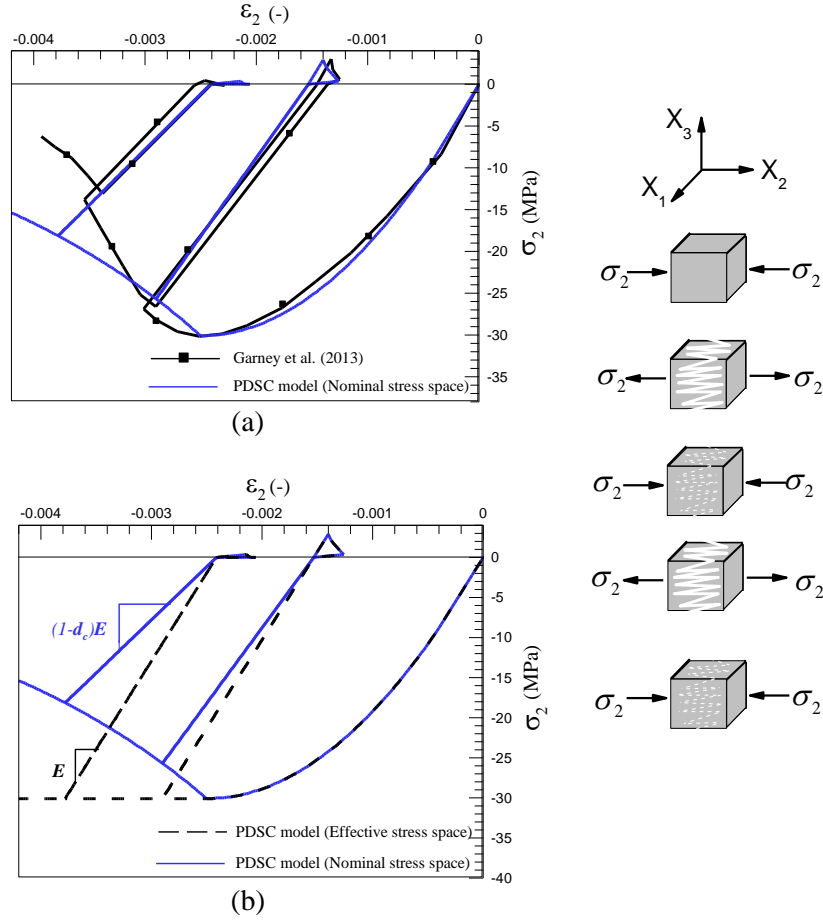
Fig. 5.2 – Simulation of cyclic compression-tension load sequence at the material level (values for the parameters of the constitutive model: ν =0.2; E =22 GPa; f_c =30 MPa; $G_{f,c}$ =7 N/mm; f_{ct} =3 MPa; ε_{c1} =0.0025; α_0 =0.3; G_f^1 =0.04 N/mm; ξ_1 =0.2; α_1 =0.7; ξ_2 =0.75; α_2 =0.2).

For comparison, Fig. 5.2b represents the response of the proposed model in nominal stress space (represented at Fig. 5.2a) and the one in effective stress space. In compression zone ($\sigma_2 < 0$), the stress-strain responses in both effective and nominal stress spaces are identical for the domain before attaining the peak ($\tilde{\epsilon}_c \leq \tilde{\epsilon}_{c1}$), whereas for higher deformations ($\tilde{\epsilon}_c > \tilde{\epsilon}_{c1}$) the two responses starts diverging because of the damage evolution process ($d_c > 0$). In tension zone, the simulated responses in both effective and nominal stress spaces are also identical, since the compressive damage

scalar (d_c) only affects the negative (compressive) part of effective stress vector ($\bar{\underline{\sigma}}^-$), (see Eq. (5.14)).

- *Simulation of closing a crack developed in one direction, by imposing compressive load in the orthogonal direction (Fig. 5.3):* The element is initially subjected to the uniaxial tension in the direction of X_2 (Step 1).
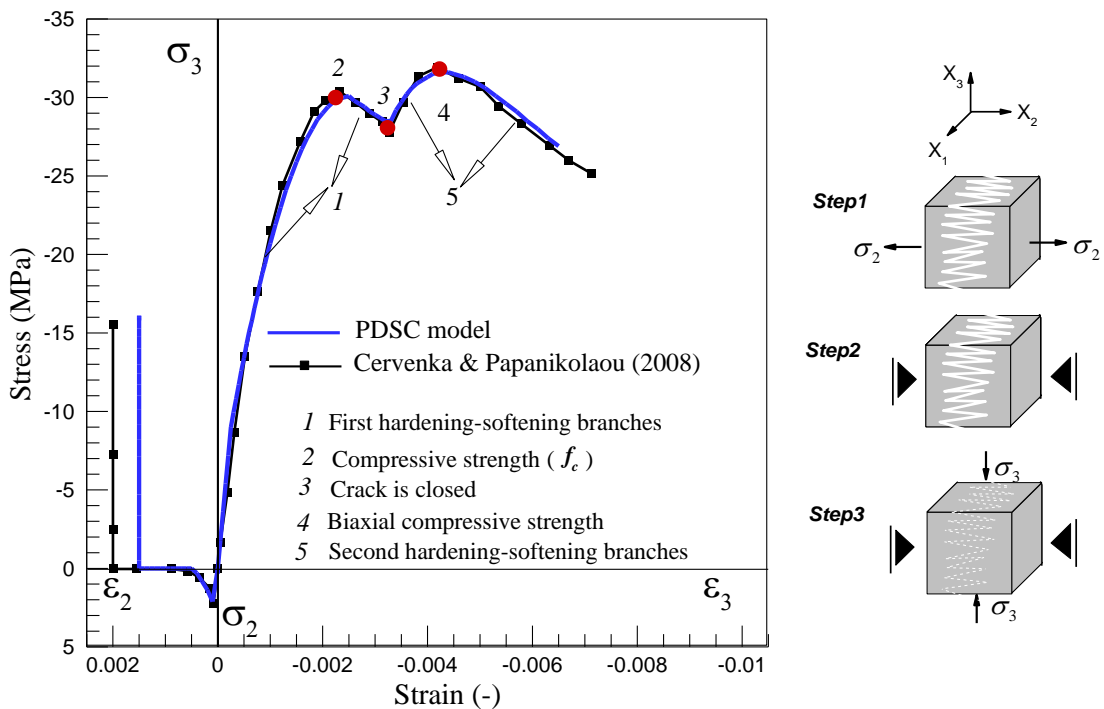
Fig. 5.3 – Prediction of the PDSC model for closing a crack developed in one direction, by imposing compressive load in the orthogonal direction (values for the parameters of the constitutive model: ν =0.2; E =36 GPa; f_c =30 MPa; $G_{f,c}$ =30 N/mm; f_{ct} =2.45 MPa; ε_{c1} =0.0025; α_0 =0.3; G_f^1 =0.05 N/mm; ξ_1=0.2; α_1=0.7; ξ_2=0.75; α_2=0.2).

Then a crack is formed with the orientation of $\theta = 0°$, and further propagated up to a stage that the crack does not be able to transfer more tensile stresses (fully opened crack status). At this stage the displacement in the direction of X_2 is fixed (Step 2), and the element is loaded by compressive displacements in the X_3 direction up to end of the analysis (Step 3).

Due to applied compressive displacements, uniaxial compressive stresses are induced in the material in the X_3 direction. Consequently, expansion of the material in the X_2 direction imposes the crack be gradually closing. When the material is in the compression softening phase, in X_3 direction, the crack will be completely closed. When the crack closes, the state of stress is changed to biaxial compression, and a second hardening-softening response is reproduced corresponding to the appropriate biaxial state of stress. The above-described loading path was successfully simulated by the proposed model (see Fig. 5.3), and the prediction agrees well with the solution of Cervenka and Papanikolaou (2008).

- *Simulation of closing two cracks developed along two orthogonal directions, by imposing compressive load in the third orthogonal direction (Fig. 5.4)*: The element is initially subjected to equal tensile displacements along orthogonal directions X_1 and X_2, therefore, two orthogonal cracks are developed (Step 1 in Fig. 5.4). The tensile displacements are increased up to the stage that the two orthogonal cracks attain the fully opened crack status.

At this stage the displacements of the elements in directions X_1 and X_2 are fixed (Step 2 in Fig. 5.4) and, simultaneously, compressive displacements are imposed in direction X_3 up to end of the analysis (Step 3 in Fig. 5.4). Due to compressive contraction in direction X_3, the material expands along X_1 and X_2 directions, consequently the both existing cracks are gradually closing. When the material is in compressive softening stage (in direction X_3), both cracks become completely closed, and the state of stress in direction X_3 changes from uniaxial compression to triaxial compressive state. Fig. 5.4 presents the simulated loading path, and its comparison to the solution reported by Cervenka and Papanikolaou (2008). A good agreement can be observed.
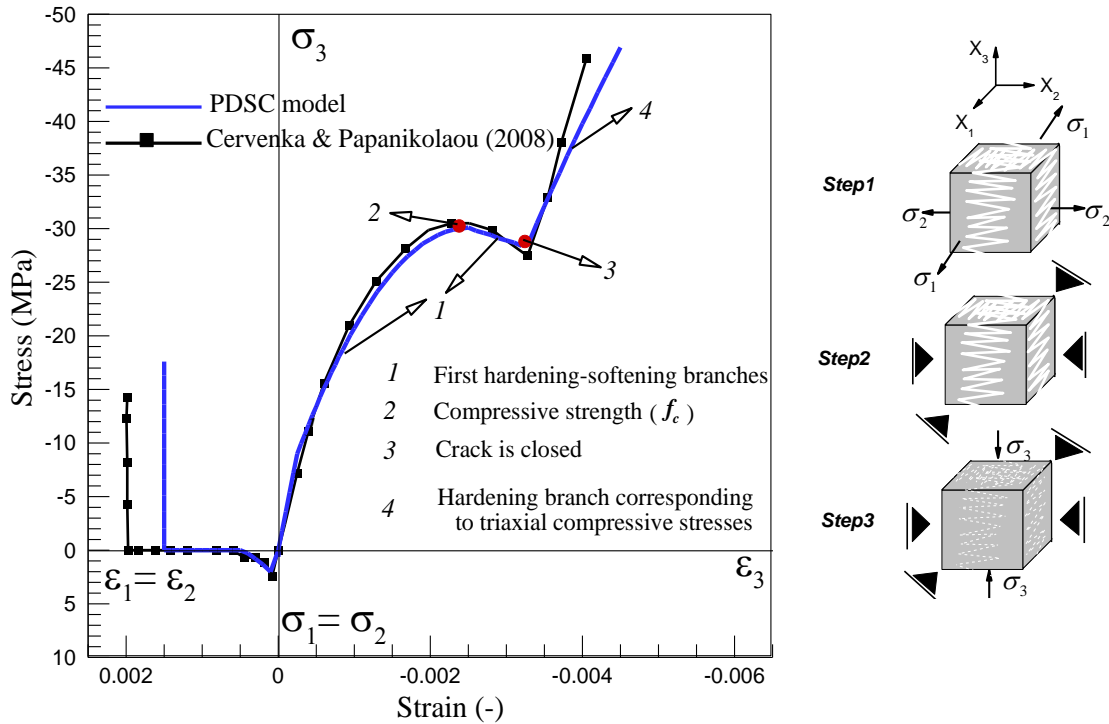
Fig. 5.4 – Prediction of the PDSC model for closing two cracks developed along two orthogonal directions, by imposing compressive load in the third orthogonal direction (values for the parameters of the constitutive model adopted the same as those mentioned in Fig. 5.3).

5.4 SIMULATIONS AT THE STRUCTURAL LEVEL

5.4.1 RC columns subjected to different eccentric loadings

To highlight the efficiency of the proposed model, three RC columns, here designated as C-e0.3, C-e0.57, and C-e0.86 tested by El-Maaddawy (2009), were simulated. All the specimens have the same geometry and reinforcement layout as represented in Fig. 5.5. The test setup used for the execution of these tests is represented in Fig. 5.6. The test specimen includes two end corbels, with the cross sections of 250×250 mm and length of 350 mm, to transfer the load to the central region of the specimen, designated by "test region", which has the cross section of 125×125 mm and length of 500 mm. The flexural and shear reinforcement adopted for the end corbels are designed to ensure the damage only occurs in the "test region" (El-Maaddawy, 2009). The differences between the specimens C-e0.3, C-e0.57, and C-e0.86 are restricted only to the length of the

eccentricity (e) of the load applied to each specimen. The value of "e" for the C-e0.3, C-e0.57, and C-e0.86 is, respectively, 37.5, 71, and 107.5 mm that correspond to an eccentricity length over the section height (e/h) ratios of 0.3, 0.57, and 0.86 ($h=125$ *mm*). The longitudinal steel reinforcement in the "test region" consists of 4 steel bars of 10 mm diameter while 6 mm diameter hoops are applied as the shear reinforcement. More details about the geometry, reinforcing system and support conditions are indicated in Fig. 5.5 and Fig. 5.6.
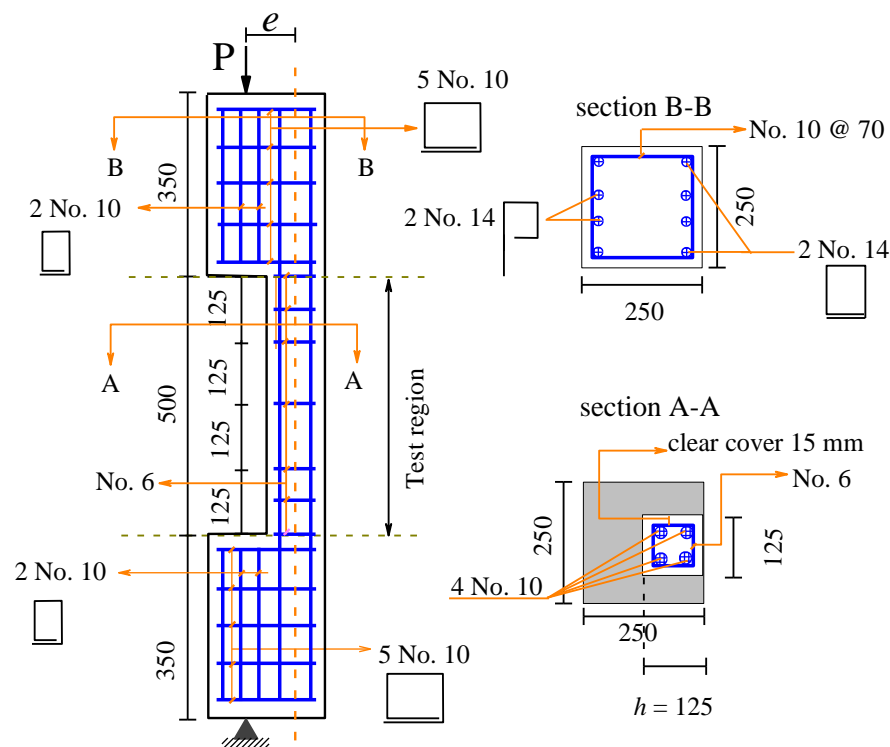
Fig. 5.5 – Details of the test specimen (El-Maaddawy, 2009) (dimensions in mm).

FEM modelling of the concrete, and the loading steel plates are performed using twenty-noded solid elements with 2×2×2 Gauss–Legendre integration scheme. The loading steel plates are modeled as a linear-elastic material with Poisson's coefficient of 0.3 and elasticity modulus of 200 GPa. Fig. 5.7 represents, as an example, the finite element mesh used for the simulation of the column C-e0.86 (the differences between each column test are limited to the length of eccentricity for the load application). The longitudinal steel bars and steel hoops are modeled with 3D embedded cables of 2 nodes (one degree-of-

freedom per node), by using a 2 Gauss-Legendre integration scheme, and assuming perfect bond to the surrounding medium.
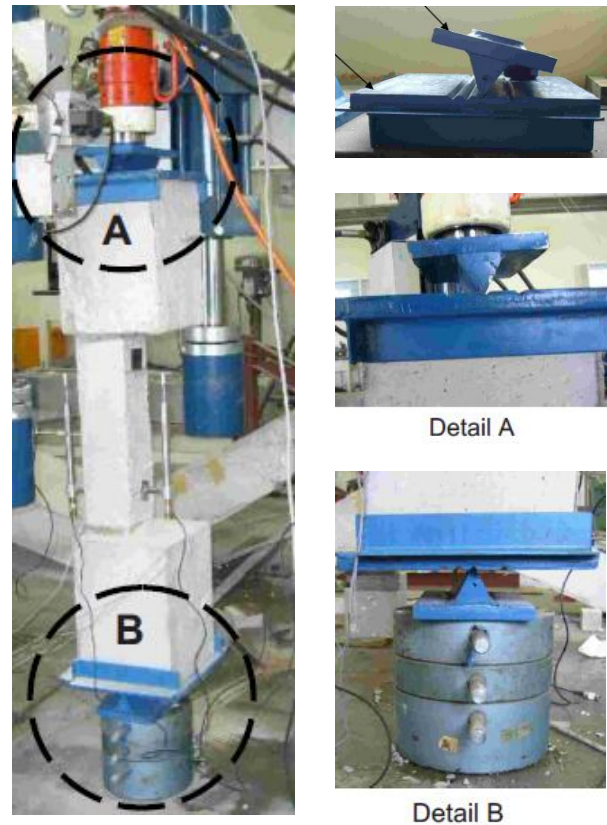
Fig. 5.6 – Test set up (El-Maaddawy, 2009).

For modelling the behaviour of the steel bar elements, the stress-strain relationship represented in Fig. 4.3 was adopted, and the values of parameters used to define this diagram are included in Table 5.1. Properties of concrete are taken from (El-Maaddawy, 2009), and the values of the parameters to define the PDSC model are, accordingly, included in Table 5.2. Elements of the top and bottom corbels are assumed exhibiting linear elastic behaviour during the analysis, since no damage is reported for these elements in the original papers. The applied load is uniformly distributed over the appropriate edges of those elements of the top steel plate (see Detail A of Fig. 5.6), and the simulation is performed under the displacement control by the arc-length method considering the horizontal X_2 translational degree of freedom of a point located at the mid-height of tensile zone of the column.

Table 5.1 – Values of the parameters of the steel constitutive model for the tests with RC column subjected to eccentric loading.

	ε_{sy} (%)	σ_{sy} (N/mm^2)	ε_{sh} (%)	σ_{sh} (N/mm^2)	ε_{su} (%)	σ_{su} (N/mm^2)	Third branch exponent
$\phi 6$, $\phi 10$	0.26	550	0.26	550	10	725	1

Table 5.2 – Values of the parameters of the concrete constitutive model for the tests with RC column subjected to eccentric loading.

Property	Value
Poisson's ratio	0.2
Young's modulus	$E = 20000\ N/mm^2$
Parameters defining the plastic-damage part of the model	$\alpha_0 = 0.4$; $f_c = 26\ N/mm^2$; $\varepsilon_{c1} = 0.003$; $G_{f,c} = 10\ N/mm$
Trilinear tension softening diagram (Fig. 3.1a)	$f_{ct} = 1.8\ N/mm^2$; $G_f^I = 0.08\ N/mm$; $\xi_1 = 0.004$; $\alpha_1 = 0.4$; $\xi_2 = 0.1$; $\alpha_2 = 0.15$
Parameter defining the mode I fracture energy available to the new crack (Sena-Cruz, 2004)	2
Type of shear retention factor law	$P_1 = 2$
Crack bandwidth	Cube root of the volume of Gauss integration point
Threshold angle (Sena-Cruz, 2004)	30 degree
Maximum number of cracks per integration point (Sena-Cruz, 2004)	2

(a)   (b)

Fig. 5.7 – Finite element mesh used for the simulation of the column C-e0.86: (a) concrete and steel plates; (b) reinforcements.

The experimental relationship between the applied load versus the lateral mid-height displacement ($P-U_h$) of the column C-e0.3 is represented in Fig. 5.8a. This figure includes the predicted $P-U_h$ responses obtained by PDSC model and the SC model. The SC model includes the same 3D multidirectional fixed smeared crack approach (Ventura-Gouveia et al., 2008; Ventura-Gouveia, 2011) to account for cracking, but considers the linear elastic behaviour for the material under compressive deformations.

(a)

(b)

(c)
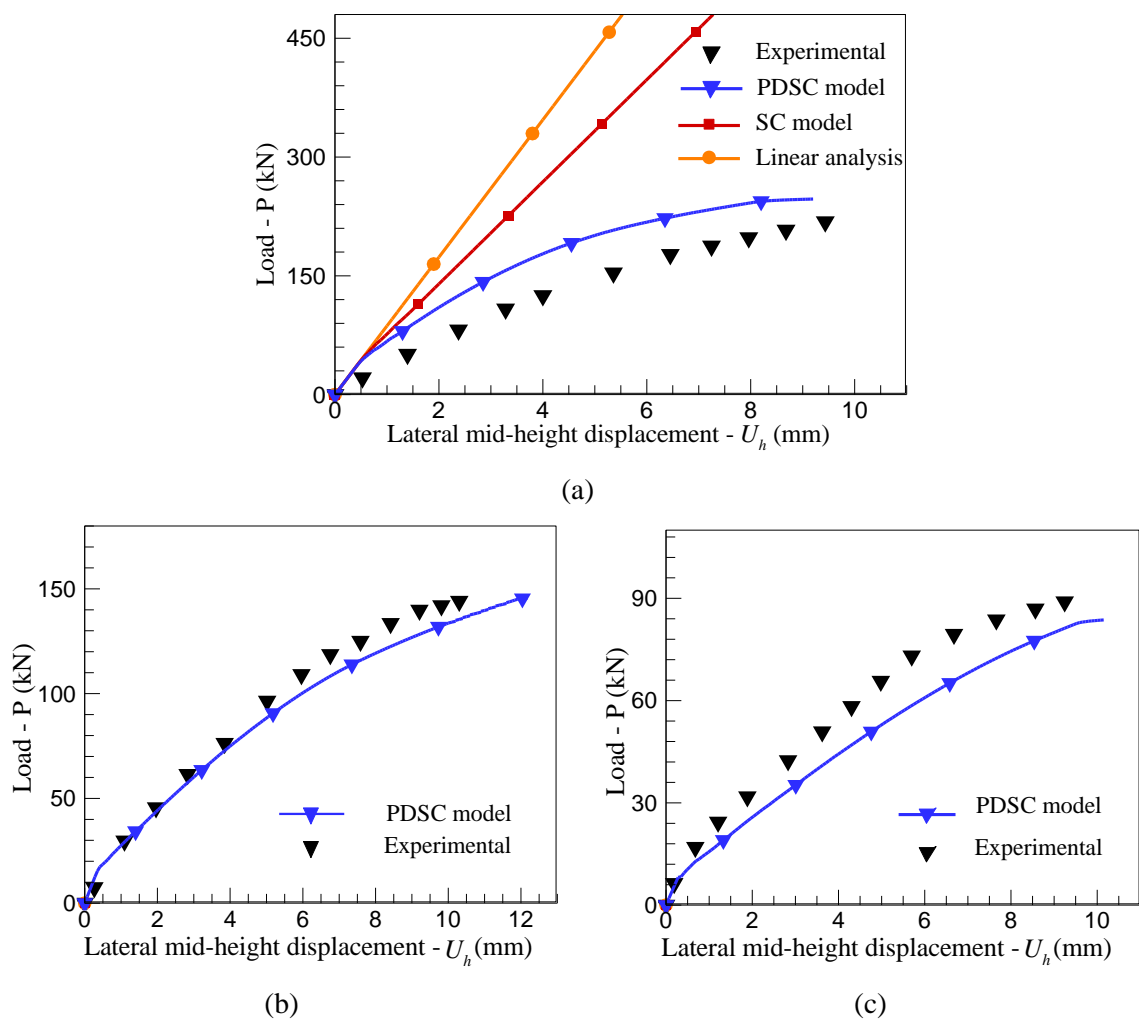
Fig. 5.8 – Experimental *vs.* numerical *P-U_h* responses (El-Maaddawy, 2009) for the specimen: (a) C-e0.3; (b) C-e0.57; (c) C-e0.86.

According to the experimental observations, the column C-e0.3 exhibits a ductile $P-U_h$ response, and its failure was governed mainly by crushing of concrete at the compression

side of the column, without yielding of the longitudinal steel in the tensile side of the specimen.

The experimental load vs. strain ($P - \varepsilon_{r,t}$) relationships, where strain was recorded in mid-height of the longitudinal steel reinforcement located at tensile zone, corresponding to the column C-e0.3 is provided at Fig. 5.9a. This figure, Fig. 5.9a, indicates that the strain in the reinforcement at failure stage is about $\varepsilon_{r,t} \approx 0.0008$, which is less than the strain corresponding to the yield initiation of steel bar ($\varepsilon_{r,t} \approx 0.0026$).
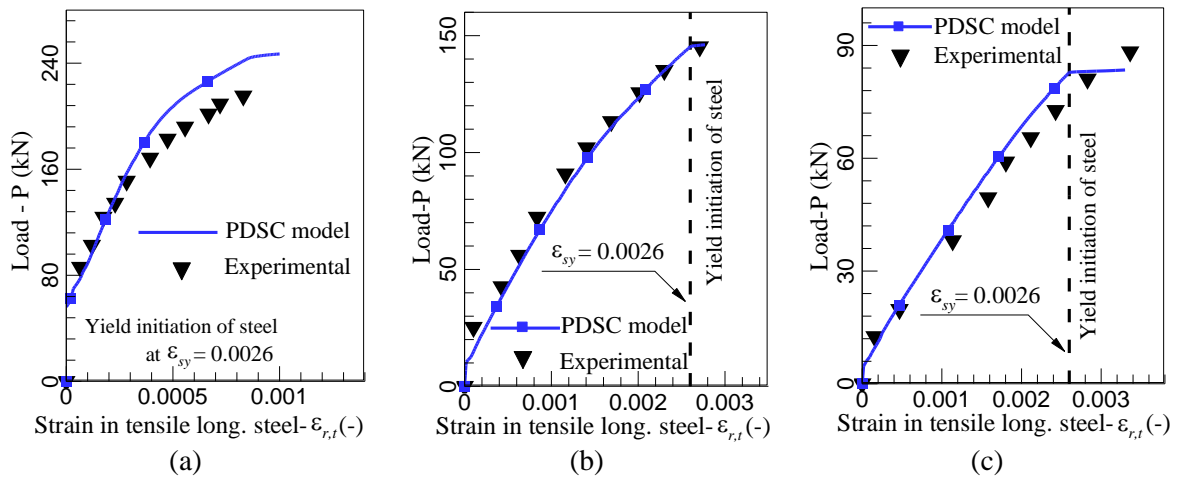
Fig. 5.9 – Experimental vs. numerical $P - \varepsilon_{r,t}$ responses (El-Maaddawy, 2009) for the specimen: (a) C-e0.3; (b) C-e0.57; (c) C-e0.86.

The numerical analysis using the SC model reveals that at the load corresponding to ≈ 40 kN the cracks in the tension-side of the column C-e0.3 are initiated (see Fig. 5.8a). Once these cracks start to propagate, the stiffness of $P - U_h$ response slightly decreases, but the predicted load carrying capacity continuously increases without the occurrence of a failure load, since the SC model assumes an elastic behaviour for the concrete in compression. However, according to the PDSC response, after the initiation of the cracks in the tension-side of the column, the $P - U_h$ response is mainly governed by the nonlinear compressive behaviour of concrete at compression side of the column.

Fig. 5.10b and 5.10c present, respectively, the numerical crack pattern and the plastic zone, at the deformation corresponding to $U_h \approx 9.2$ mm (last converged step). As can be

seen in Fig. 5.10b, the cracks with large opening status are spread at the tension-side of the column, while Fig. 5.10c shows the plastic zone is concentrated at the compression side of the column. This numerical prediction correlates well with the experimental observations (see Fig. 5.10a). The $P - \varepsilon_{r,t}$ response predicted by PDSC model, also, confirms the longitudinal steel bars located in the tensile side of the column have not yielded at the failure stage (see Fig. 5.9a).

<div align="center">(a)   (b)   (c)</div>
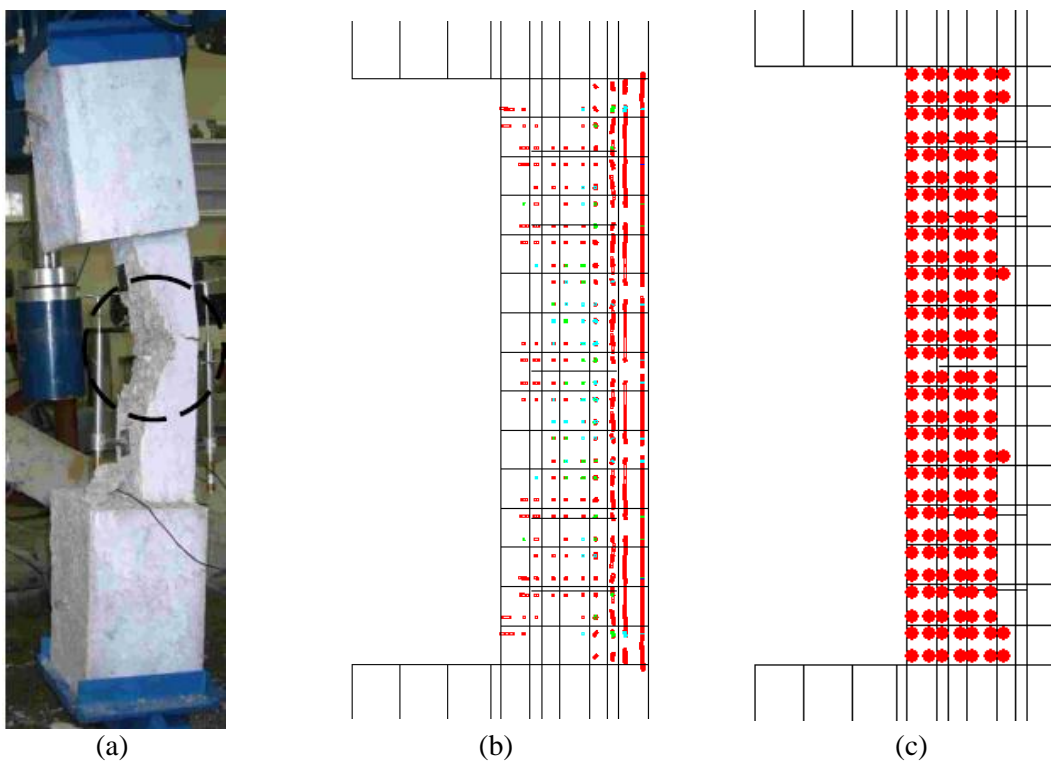
Fig. 5.10 – Results of the specimen C-e0.3: (a) experimentally observed damage (El-Maaddawy, 2009); (b) numerical crack pattern and (c) plastic zone (results of (b) and (c) correspond to the last converged step ($U_h \approx 9.2\,mm$).

According to the experimental program, the columns C-e0.57 and C-e0.86 have failed by yielding of longitudinal tension steel and crushing of concrete at compression side of the specimen (El-Maaddawy, 2009). Predictions of PDSC model for the columns C-e0.57 and C-e0.86 are represented in Fig. 5.8 and Fig. 5.9 in terms of $P - U_h$ and $P - \varepsilon_{r,t}$ relationships, respectively. As can be in seen in these two figures the PDSC model was able to predict with good accuracy the overall experimental $P - U_h$ and $P - \varepsilon_{r,t}$

responses of the columns C-e0.57 and C-e0.86. The predicted $P - \varepsilon_{r,t}$ relationships for both columns confirm the tensile longitudinal steel bars are already yielded at their failure stages. By comparing the experimental $P - U_h$ and $P - \varepsilon_{r,t}$ responses of the three columns, it can be concluded that by increasing the *e/h* ratio the failure load decreases whereas the strains in tensile longitudinal reinforcement bars increase. This experimental observation was successfully simulated by the PDSC model as revealed in Fig. 5.8 and Fig. 5.9.

5.4.2 RC beams made by different concrete strength classes

The proposed model is applied in this section on the simulation of RC beams made by different concrete strength classes, tested by Yang et al. (2003). The six beams analysed: L-60, L-75, L-100, H-60, H-75, H-100, have the same shear span over cross-section depth ratio (*a/h*) and thickness (*b*). Fig. 5.11 and Table 5.3 provide the relevant information about these beams. The tensile longitudinal reinforcement ratio for all the beams is about 1.0%, applied in one or two layers, while no shear reinforcement at the shear spans is adopted for these beams. The tensile reinforcement consists of steel bars of 19 mm diameter and 22 mm diameter, with a total cross sectional area represented by A_{st} in Table 5.3.
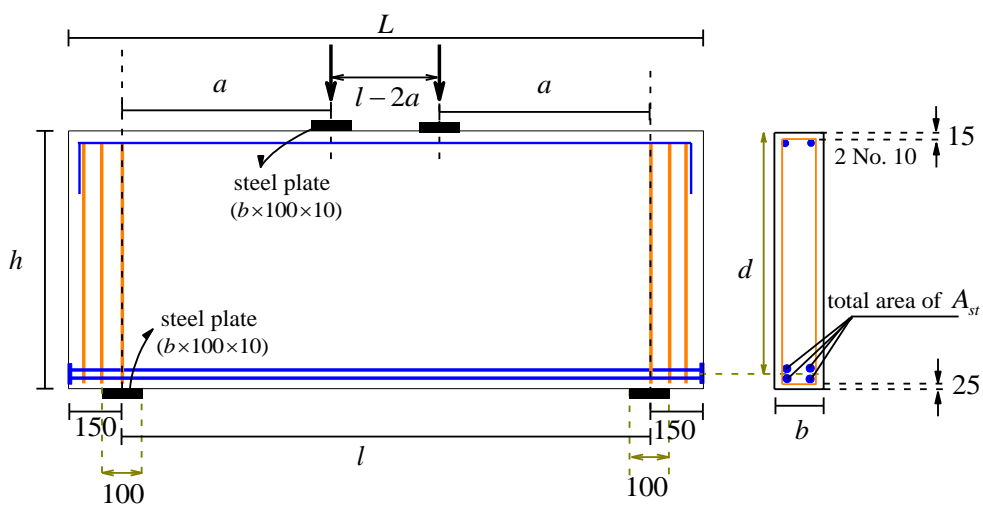
Fig. 5.11 – Geometry and reinforcement layout for the beams tested by Yang et al. (2003) (dimensions in mm).

Table 5.3 – Details of the beams tested by Yang et al. (2003).

ID	group	f_c (MPa)	h (mm)	a (mm)	d (mm)	L (mm)	l (mm)	A_{st} [a] (mm^2)	Web Reinf.	a/h (-)	b (mm)
L-60	L	31.4	600	300	555	2400	2100	861			160
H-60	H	78.5	600	300	555	2400	2100	861			160
L-75	L	31.4	750	375	685	1650	1350	1148	No	0.5	160
H-75	H	78.5	750	375	685	1650	1350	1148			160
L-100	L	31.4	1000	500	935	1900	1600	1348			160
H-100	H	78.5	1000	500	935	1900	1600	1348			160

[a] A_{st}: 861 (= 3 No. 19); 1148 (= 4 No. 19); 1348 (= 2 No. 19 + 2 No. 22)

In order to prevent flexural failure by the yielding of tension bars prior to shear failure, some of the bars (namely those of 19 mm diameter) were of high tensile strength. Two steel bars of 10 mm diameter were used as compressive reinforcements for all the beams. The properties of the steel bars are indicated in Table 5.4. The beams can be assembled in two groups according to the concrete strength level: *L group* that contains the beams of concrete strength of 31.4 MPa (f_c =31.4 MPa); and *H group* formed by the beams made by high strength concrete (f_c =78.5 MPa). Each group (*L* or *H*) contains three beams that differ on the overall depth of the cross section (*h*=600, 750, or 1000 mm), while all the beams have the same *a/h* ratio equal to 0.5.

Twenty-noded solid elements with 3×3×3 Gauss–Legendre integration scheme were used for modelling the beams, supports and loading plates. Fig. 5.12 presents, as an example, the finite element mesh used for the simulation of the beam L-75. The steel reinforcement is modelled by 2-noded perfect bonded embedded cables with two IPs. For modelling the behaviour of the steel bar elements, the stress-strain relationship represented in Fig. 4.3 was adopted, whose defining values are included in Table 5.4.

Support and loading plates are modeled as a linear-elastic material with Poisson's coefficient of 0.3 and elasticity modulus of 200 GPa. Properties of both regular and high strength concrete (f_c =31.4 MPa, f_c =78.5 MPa) are taken from Yang et al. (2003), and the values of the parameters to define the PDSC model are, accordingly, included in Table 5.5.
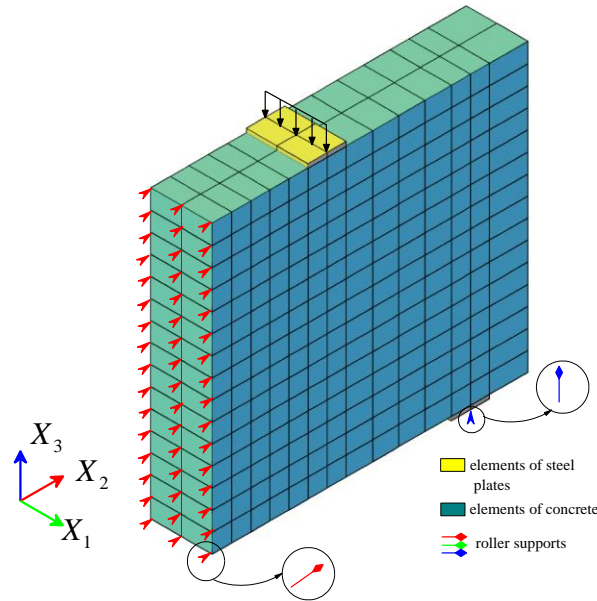
Fig. 5.12 – Finite element mesh used for the simulation of the beam L-75 (due to symmetry conditions only half beam was modelled).

For the concrete with f_c =31.4 MPa the value of $G_{f,c}$ = 10 N/mm was considered, which is the lower limit of the interval values proposed by Vonk (1992). For the high strength concrete the average value of the interval proposed by Vonk (1992) was assumed ($G_{f,c}$ = 15 N/mm). To simulate the shear crack initiation and the degradation of crack shear stress transfer, the shear softening diagram represented in Fig. 3.2 is assumed, and the values of the parameters to define this diagram are included in Table 5.5. Due to lack of reliable experimental evidences to characterise this diagram, the adopted values were estimated taking into account the results obtained in previous simulations with RC beams failing in shear, as well as the influence of the concrete strength class in the values of these parameters (Barros et al., 2016; Baghi and Barros, 2016; Edalat-Behbahani et al., 2015).

Table 5.4 – Values of the parameters of the steel constitutive model for modelling the beams tested by Yang et al. (2003).

Bar diameter	ε_{sy} (%)	σ_{sy} (N/mm^2)	ε_{sh} (%)	σ_{sh} (N/mm^2)	ε_{su} (%)	σ_{su} (N/mm^2)	Third branch exponent
ϕ22	0.21	407	2.5	420	10	553	1
ϕ19	0.413	804	1.3	808	10	890	1
ϕ10	0.209	408	1.42	412	4.4	549	1

Table 5.5 – Values of the parameters of the concrete constitutive model for simulating the beams
tested by Yang et al. (2003).

Property	Group	Value
Poisson's ratio	L, H	ν =0.15
Young's modulus	L	E =27000 N/mm^2
	H	E =39000 N/mm^2
Parameters defining the plastic-damage part of the model	L	α_0 =0.4; f_c =31.4 N/mm^2; ε_{c1} =0.0025; $G_{f,c}$ =10 N/mm
	H	α_0 =0.4; f_c =78.5 N/mm^2; ε_{c1} =0.0035; $G_{f,c}$ =15 N/mm
Trilinear tension softening diagram (Fig. 3.1a)	L	f_{ct} =1.8 N/mm^2; G_f^1 =0.07 N/mm; ξ_1 =0.005; α_1 = 0.3; ξ_2 =0.1; α_2 = 0.15
	H	f_{ct} =2.0 N/mm^2; G_f^1 =0.08 N/mm; ξ_1 =0.005; α_1 = 0.3; ξ_2 =0.1; α_2 = 0.15
Parameter defining the mode I fracture energy available to the new crack (Sena-Cruz, 2004)	L, H	2
Parameters defining the crack shear stress-crack shear strain softening diagram (Fig. 3.2)	L, H	$\tau_{t,p}^{cr}$ =1.2 N/mm^2; β =0.1 ; $G_{f,s}$ =0.08 N/mm
Crack bandwidth	L, H	Cube root of the volume of Gauss integration point
Threshold angle (Sena-Cruz, 2004)	L, H	30 degree
Maximum number of cracks per integration point (Sena-Cruz, 2004)	L, H	2

The relationships between the applied force and the mid-span displacement, *F-U*, for all
the beams, registered experimentally and obtained numerically with the PDSC model, are
represented in Fig. 5.13.

According to the experimental observations, all the beams exhibited large load carrying
capacity after the formation of the first diagonal crack, due to the resisting mechanism
ensured by the compressive strut connecting the loading points and the supports. The
experimental cracking patterns of all beams at the failure stage demonstrated the
formation of flexural cracks with very small crack width in middle of the beam, whereas
highly propagated diagonal cracks were observed along the line connecting the support
and loading plates. All beams failed by crushing of concrete compressive strut in brittle

and sudden manner (Yang et al., 2003). In Fig. 5.14 is represented, as an example, the experimental cracking patterns of the beams H-60 at its failure stage, while the same pattern was observed for the other beams at the test (Yang et al., 2003).
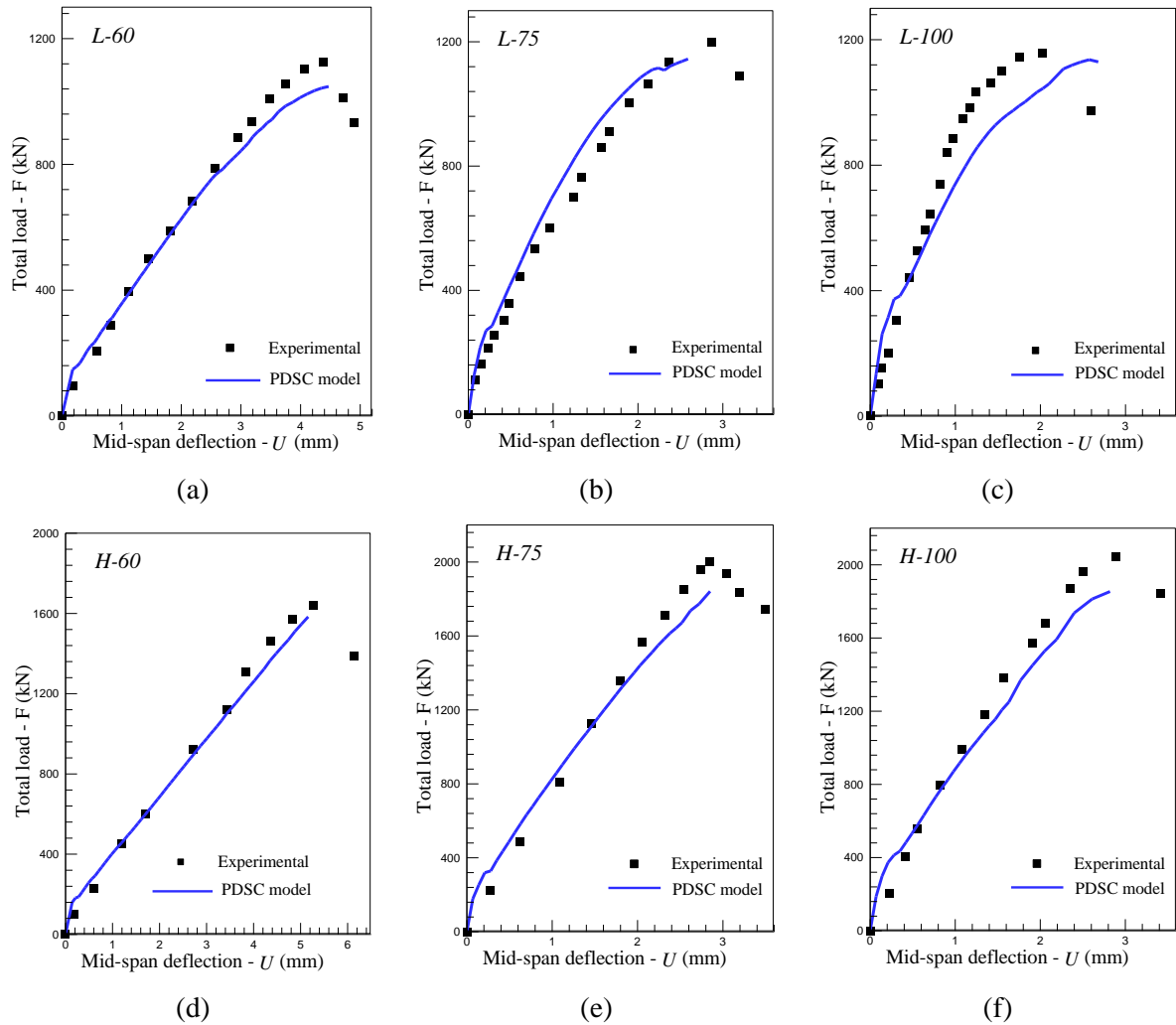
Fig. 5.13 – Experimental (Yang et al., 2003) and numerical load vs. mid-span deflection for the beams: (a) L-60; (b) L-75; (c) L-100; (d) H-60; (e) H-75; (f) H-100.

Table 5.6 gives the failure loads of the beams obtained in the experimental program (F^{exp}) and in the numerical simulations (F^{num}), where it is verified that PDSC model was able to simulate, with high accuracy, the experimental failure loads with an average error of 5.13% (see Table 5.6).

(a)   (b)

(c)
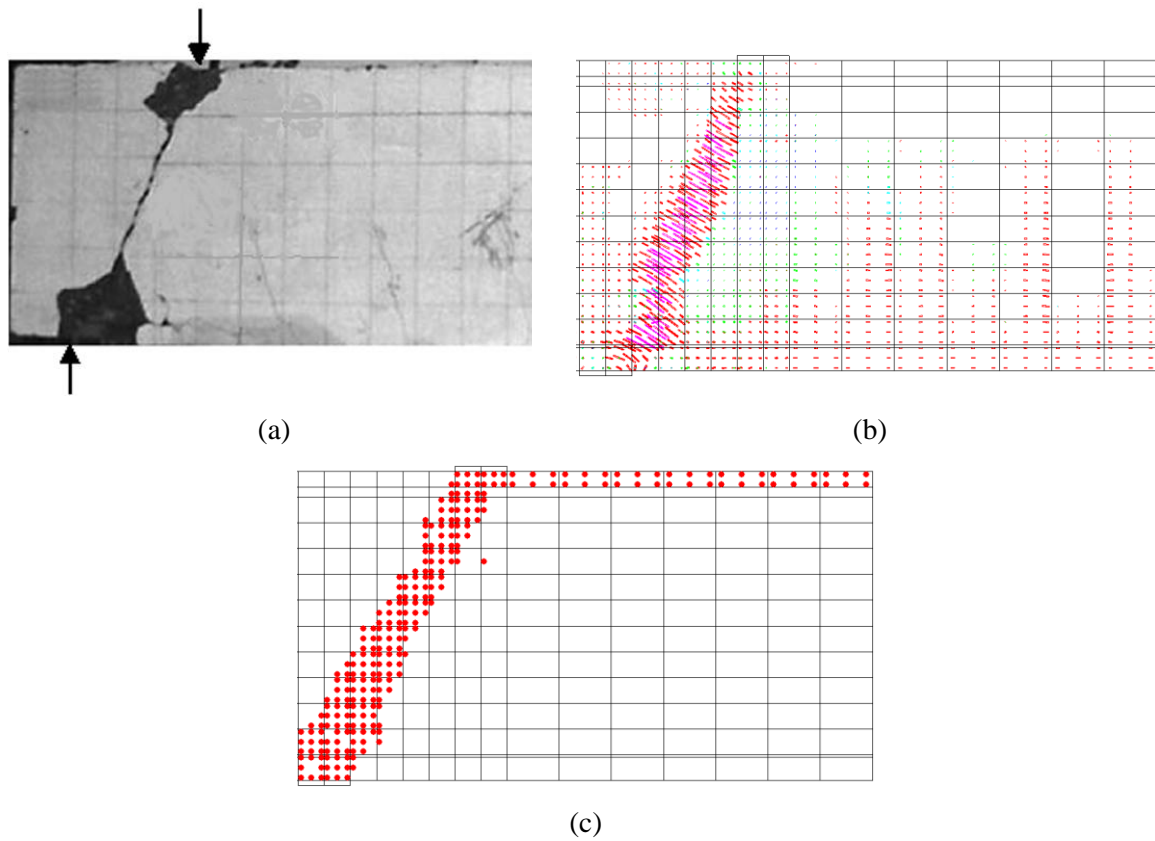
Fig. 5.14 – Results of the beam H-60: (a) experimental crack patterns; (b) numerical crack pattern; (c) plastic zone (for (b) and (c) the damage stages are obtained at the last converged step).

By comparing F^{exp} of the beams with the same cross section depth but of different concrete compressive strength, it can be concluded the increase of f_c from 31.4 to 78.5 MPa resulted in an average increase of 66% in the failure loads. This experimental observation was successfully captured by the PDSC model, as shown in Table 5.6 and Fig. 5.13. This figure also shows that the PDSC model fit with high accuracy the experimental $F-U$ curves at all stages of loading till failure. Fig. 5.14b shows that the diagonal cracks at the last converged step of the analysis are in the full opening status (cracks in pink colour), which means that the cracks are not capable of transferring any type of stresses, while the simulated plastic zone for this beam (Fig. 5.14c) evidences the formation of the compressive struts connecting the loading points and supports.

Table 5.6 – Experimental and numerical failure loads of the beams.

ID	group	F^{exp} (kN)	F^{num} (kN)	$\dfrac{\left\|F^{exp} - F^{num}\right\|}{F^{exp}}$ (%)
L-60	L	1070.2	1047.8	2.09
H-60	H	1646.4	1583.6	3.81
L-75	L	1193.6	1140.7	4.43
H-75	H	2020.8	1841.6	8.86
L-100	L	1164.2	1144.3	1.7
H-100	H	2058.0	1854.1	9.9
			average	5.13

5.4.3 RC wall subjected to pure torsion

In this section the PDSC model is used for simulating reinforced concrete walls under pure torsion loading configuration, tested by Peng and Wong (2011). The walls that were designated by S8, S10 in the experimental program were selected for the numerical simulations. The experimental loading procedure introduces the horizontal-pushing forces F1 and F2 (the force F2 acts in the opposite direction of F1) to produce a torque on the wall specimens. The magnitude of the forces F1 and F2 at the experimental program was almost identical varying in the range of ± 1 kN (Peng and Wong 2011). The distance between the two pushing forces was 500 mm. These walls had relatively thick slabs (with the dimension of 1250 mm $\times$750 mm $\times$200 mm) at their bottom and top edges for fixing the walls to the foundation, and for applying the forces (F1 and F2), respectively (see Fig. 5.15).

The walls are reinforced in both vertical and horizontal directions with the reinforcement ratios designated as ρ_v and ρ_h, respectively (see Table 5.7). Both walls have the same thickness, t_w, and height, h_w, as indicated in Table 5.7, and are made of a concrete with a compressive strength of 29.5 MPa. Details corresponding to the reinforcement applied in horizontal and vertical directions are included in Table 5.7. The primary variable of these two walls is the length of the wall (l_w): the l_w of S8 and S10 is, respectively, 800 mm and 1000 mm.
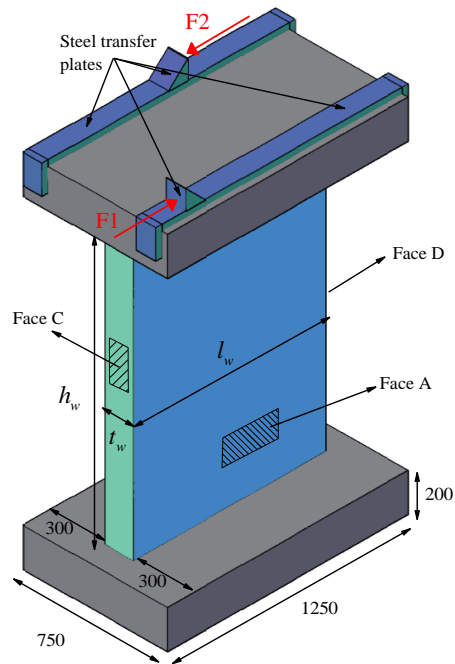
Fig. 5.15 – General arrangement of the wall specimens tested by Peng and Wong (2011)
(dimensions in mm)..

Table 5.7 – Details of the RC walls submitted to torsion.

| ID | t_w (mm) | h_w (mm) | l_w (mm) | [1]Vertical reinforcement | | | [5]Horizontal reinforcement | | |
				[2]N	[3]D (mm)	[4]ρ_v (%)	[6]D (mm)	[7]S_h (mm)	[8]ρ_h (%)
S8	150	1500	800	9	10	1.18	8	125	0.57
S10	150	1500	1000	8	12	1.2	10	200	0.55

(1) vertical reinforcement is applied in two layers; (2) number of bars applied in each layer of
vertical reinforcement; (3) diameter of each bar in vertical reinforcement; (4) vertical
reinforcement ratio; (5) horizontal reinforcement was applied in the form of the rectangular
hoop; (6) diameter of one leg of each stirrup; (7) spacing of the stirrups; (8) horizontal
reinforcement ratio.

The test setup used for execution these tests is represented in Fig. 5.16a. Figs. 5.16b and
16c indicate the arrangement of linear variable displacement transducers (LVDTs) used to
measure the twist angle per unit length (θ) of these walls. As can be seen in these figures,
four LVDTs (designated by L_{3i}, L_{3j}, L_{2i}, L_{2j}) are installed at two height levels (here is
called "level 2" and "level 3") of each wall. The twist angle per unit length (θ) was

calculated at the experimental program by using the measured data of these four LVDTs
according to the following equation:

$$\theta = \left[\arctan(\frac{\left|L_{3i}\right| + \left|L_{3j}\right|}{d_l}) - \arctan(\frac{\left|L_{2i}\right| + \left|L_{2j}\right|}{d_l}) \right] / d_h \qquad (6.1)$$

where the values of d_h and d_l are defined in Fig. 5.16c.

Face D

(a)   (b)

For the wall S8 d_l=720 mm
For the wall S10 d_l=920 mm
For both walls d_h=750 mm

Distance between
two LVDTs (d_l)

Measurment length (d_h)

Level 3

Level 2

L_{3i} L_{3j}

represents LVDT

L_{2i} L_{2j}

Face A   Face B

(c)
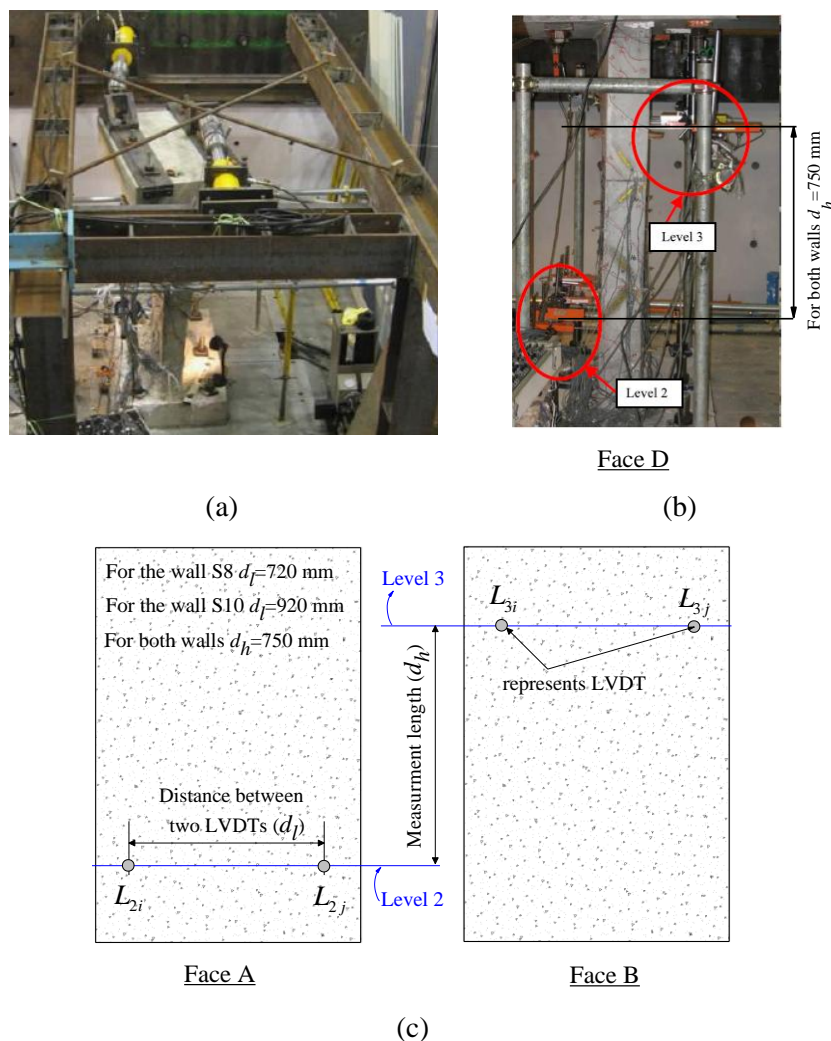
Fig. 5.16 – Setup for the test of shear walls subjected to torsion (Peng and
Wong, 2011).

FEM modelling of the walls, top slabs and steel plates were performed using twenty-noded solid finite elements with 3×3×3 Gauss-Legendre IP scheme. Fig. 5.17 presents, as an example, the finite element mesh used for analysis of the wall S10. Instead of modelling the foundation, all the degrees-of-freedom of the bottom nodes of the walls are considered fixed. The loads F1 and F2 are uniformly distributed over the appropriate faces of the steel plate elements, as schematically represented in Fig. 5.17. The loading steel plates are modeled as a linear-elastic material with Poisson's coefficient of 0.3 and elasticity modulus of 200 GPa. Elements of the top slab are assumed to exhibit linear elastic behaviour during the analysis, since no damage is reported for this RC Slab in the original paper. For modelling the behaviour of the steel bars, the stress-strain relationship represented in Fig. 4.3 was adopted. The reinforcement is meshed using 2-noded perfect bonded embedded cables with two IPs.
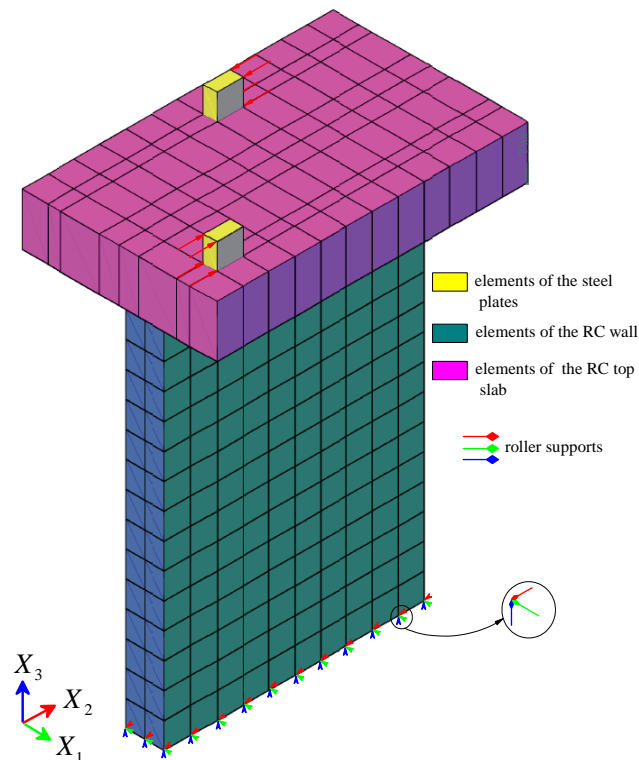
Fig. 5.17 – Finite element mesh used for the simulation of the wall S10.

The values of parameters used to define the constitutive models of steel and concrete are included in Table 5.8 and Table 5.9, respectively. For modelling the shear stress transfer

during the crack opening process, the crack shear softening law (Fig. 3.2) was adopted, whose defining values are included in Table 5.9. Fig. 5.18 shows the experimental torque vs. twist angle per length $(T - \theta)$ relationships for both walls and the respective numerical predictions with the PDSC model. According to the experimental observations, these walls exhibit ductile $T - \theta$ responses after the crack initiation, and their failure were governed by the formation of diagonal cracks inclined about 45° to the vertical axis. Fig. 5.19 represents, as an example, the experimental crack pattern of the S8 wall at its failure stage and the respective numerical prediction. For both walls the ductility and the torque carrying capacity are predicted by the PDSC model with good accuracy, although a slight higher torque was obtained numerically, mainly in the Wall S10. The numerical crack pattern shows that the inclined cracks with highly propagated opening status are spread over all faces of the wall which is in agreement with the experimental observation.

Table 5.8 – Values of the parameters of the steel constitutive model for the test of RC walls.

	ε_{sy} (%)	σ_{sy} (N/mm²)	ε_{sh} (%)	σ_{sh} (N/mm²)	ε_{su} (%)	σ_{su} (N/mm²)	Third branch exponent
$\phi 8$	0.228	422	0.2284	422	10	574	1
$\phi 10$	0.253	450	0.253	450	10	576	1
$\phi 12$	0.261	481	0.261	481	10	600	1

Table 5.9 – Values of the parameters of the concrete constitutive model for the test of RC walls.

Property	Value
Poisson's ratio	0.2
Young's modulus	$E = 26000$ N/mm²
Parameters defining the plastic-damage part of the model	$\alpha_0 = 0.4$; $\varepsilon_{c1} = 0.003$; $G_{f,c} = 10$ N/mm ; $f_c = 29.5$ N/mm²
Trilinear tension softening diagram (Fig. 3.1a)	$f_{ct} = 2.0$ N/mm²; $G_f^1 = 0.07$ N/mm; $\xi_1 = 0.006$; $\alpha_1 = 0.3$; $\xi_2 = 0.2$; $\alpha_2 = 0.1$
Parameter defining the mode I fracture energy available to the new crack (Sena-Cruz, 2004)	2
Parameters defining the crack shear stress-crack shear strain softening diagram (Fig. 3.2)	$\tau_{t,p}^{cr} = 1.2$ N/mm²; $\beta = 0.3$; $G_{f,s} = 0.07$ N/mm
Crack bandwidth	Cube root of the volume of Gauss integration point
Threshold angle (Sena-Cruz, 2004)	30 degree
Maximum number of cracks per integration point (Sena-Cruz, 2004)	2

(a)   (b)

Fig. 5.18 – Experimental (Peng and Wong, 2011) and numerical torque-twist angle per length for: (a) the wall S8; (b) the wall S10.

(a)   (b)
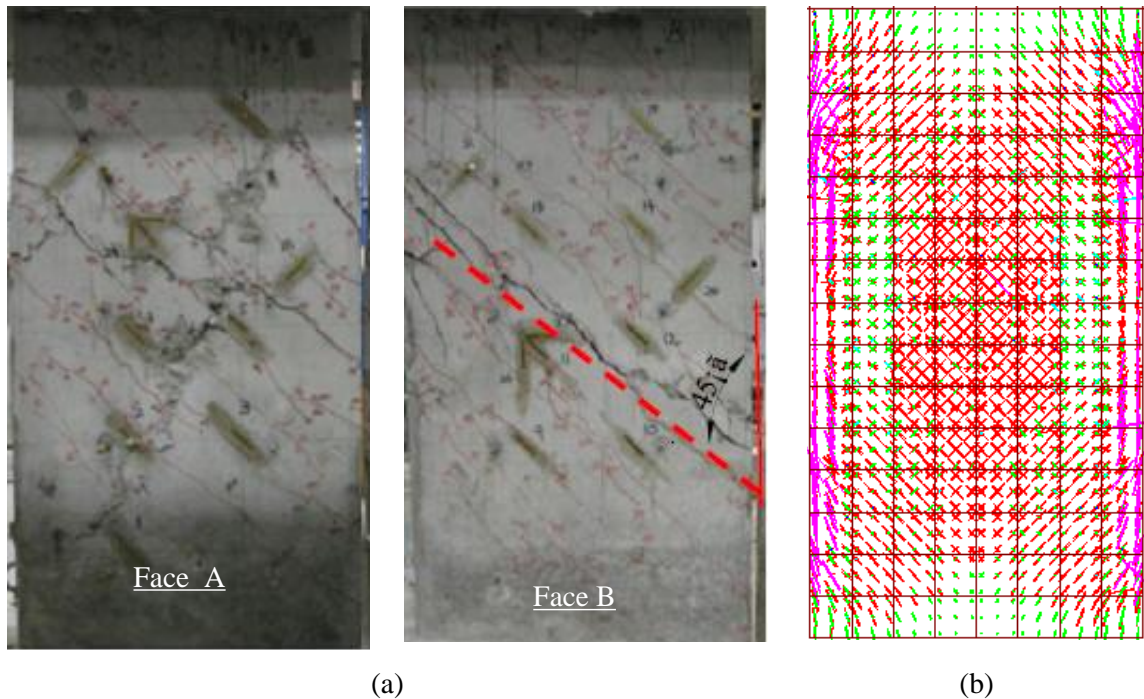
Fig. 5.19 – Results of the S8 wall: (a) experimentally observed crack pattern (Peng and Wong, 2011); (b) numerically predicted crack pattern, obtained at the last converged step. Note: the numerical crack pattern is represented over the finite element mesh adopted for concrete, i.e., the finite element mesh adopted for the reinforcement is hidden.

5.5 PARAMETRIC STUDY FOR THE MODEL PARAMETERS

A parametric study is performed to assess the influence of the values of the model parameters on the simulated behaviour of the structures analyzed in the previous section (section 5.4). The parameters under consideration are those simulating the nonlinear behaviour of concrete under compression ($f_c, G_{f,c}, \varepsilon_{c1}$), and those used to define the crack shear softening diagram ($\tau_{t,p}^{cr}, G_{f,s}, \beta$). To assess the influence of the parameters f_c, $G_{f,c}$ and ε_{c1} the RC beam L-75 was chosen since its failure behavior is governed mainly by crushing of the compressive strut. The RC wall S10 was selected to study the influence of the parameters $\tau_{t,p}^{cr}$, $G_{f,s}$, β, because the influence of the crack shear softening diagram, which simulate the degradation of the shear stress transfer between the faces of the crack, is significant to predict correctly the deformational and cracking behaviour of this wall.

5.5.1 Influence of f_c

Three different values for f_c were adopted, 20, 31.4 and 40 N/mm^2 in the simulations of the L-75 beam, the first one is lower than the value considered in the analysis of Section 5.4.2 (f_c =31.4 N/mm^2), while the third is higher.

Fig. 5.20a indicates that the beam's stiffness and the load carrying capacity increase with f_c. As expected, the SC model predicts a much higher ultimate load since the concrete in compression is assumed having a linear behaviour.

The stages where the effect of inelastic compressive deformation becomes relevant on the force-deflection responses of the beam in analysis are indicated in Fig. 5.20a using markers. It is verified that these markers are localized in the force-deflection response of this beam when predictions with the PDSC model start diverging from that of SC model. The higher is the concrete compressive strength the larger is the load carrying capacity of the beam corresponding to the marker, which is justified by the adoption of a constant value for the α_0 parameter, which defines the initiation of the inelastic deformation of concrete in compression ($f_{c0} = \alpha_0 f_c$). Since experimental research demonstrates (Hassan

et al., 2012) the amplitude of the initial linear-elastic branch of the uniaxial compressive behaviour increases with the concrete compressive strength (and consequently α_0 increases with f_c), the initiation of the influence of the concrete inelastic compressive deformation in the response of the beam will be postponed for larger deflection.
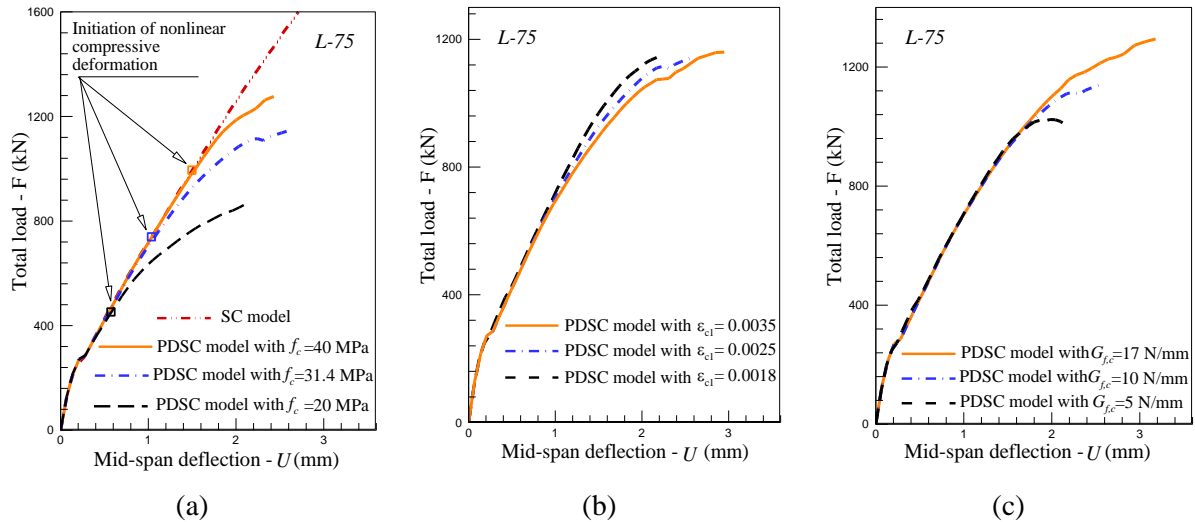
Fig. 5.20 – Sensitivity of the analysis of the beam L-75 with respect to the values of the parameters: (a) f_c; (b) ε_{c1}; (c) $G_{f,c}$.

5.5.2 Influence of ε_{c1}

To assess the influence of the parameter ε_{c1} on the response of the beam in analysis, three values were considered, 0.0018, 0.0025 and 0.0035, the first one is lower than the value considered in the analysis executed in Section 5.4.2 (ε_{c1} =0.0025), while the third value is higher. The parameter ε_{c1} influences both plasticity and damage parts of the PDSC model. Within the plasticity part, the value of the hardening parameter at compressive strength, $\tilde{\epsilon}_{c1}$, is calculated according to Eq. (3.19) by attributing a certain value to ε_{c1}. According to this equation $\tilde{\epsilon}_{c1}$ follows the tendency of ε_{c1}, therefore the pre-peak branch (hardening phase) of the $\bar{\sigma}_c - \tilde{\epsilon}_{c1}$ diagram is as stiffer as smaller is ε_{c1}, as shown in Fig. 3.6a. According to the PDSC model, the damage threshold is assumed to be related to $\tilde{\epsilon}_{c1}$: when $\tilde{\epsilon}_c \le \tilde{\epsilon}_{c1}$, $d_c = 0$, while for $\tilde{\epsilon}_c > \tilde{\epsilon}_{c1}$ the scalar damage parameter is

$d_c > 0$. Since $\tilde{\epsilon}_{c1}$ increases with ε_{c1}, the occurrence of damage (i.e. $d_c > 0$, which characterize the entrance of concrete in its compressive strain softening stage), initiates at higher compressive deformation. These effects are reflected in the deformational behaviour of the beam, since its stiffness in the initial force-deflection stage has decreased with the increase of ε_{c1} (Fig. 5.20b). However, the entrance in the post-peak concrete compressive softening stage is postponed with the increase of ε_{c1}, resulting a increase of the beam's ductility and load carrying capacity at the ultimate stage. This means that by increasing ε_{c1} the stiffness of the load vs. deflection response decreases, but the ultimate load, and its deflection increase, with benefits in terms of the ductility response and load capacity of the beam.

5.5.3 Influence of $G_{f,c}$

The parameter of compressive fracture energy ($G_{f,c}$) controls the rate of strain softening in compression, i.e. the level of stress decrease with the increase of compressive strain (see Fig. 3.6c). As larger is $G_{f,c}$ as smoother is this stress decay, which is a characteristic of very ductile materials like fibre reinforced concrete (Barros and Sena-Cruz, 2001). Fig. 5.20c compares the force-deflection responses obtained for three different values of the $G_{f,c}$, 5, 10 and 17 N/mm, the first one is lower than the value considered in the analysis of Section 5.4.2 ($G_{f,c}$=10 *N/mm*), while the third is higher. Fig. 5.20c shows that the parameter $G_{f,c}$ influences the force-deflection response of the beam only after the deflection of 1.7 mm, which corresponds to the deflection stage above that the effect of strain softening behaviour of concrete under compression becomes relevant. By increasing $G_{f,c}$ the ultimate load capacity and deflection performance are increased.

5.5.4 Influence of $\tau_{t,p}^{cr}$

Fig. 5.21a represents the influence of the parameter $\tau_{t,p}^{cr}$ on the torque vs. twist angle per length ($T - \theta$) relationship of the S10 wall. Three different values for $\tau_{t,p}^{cr}$ were chosen,

0.5, 1.2 and 3.0 N/mm^2, the first one is lower while the last one is higher than the value considered in the analysis of Section 5.4.3 ($\tau_{t,p}^{cr}$ =1.2 N/mm^2).
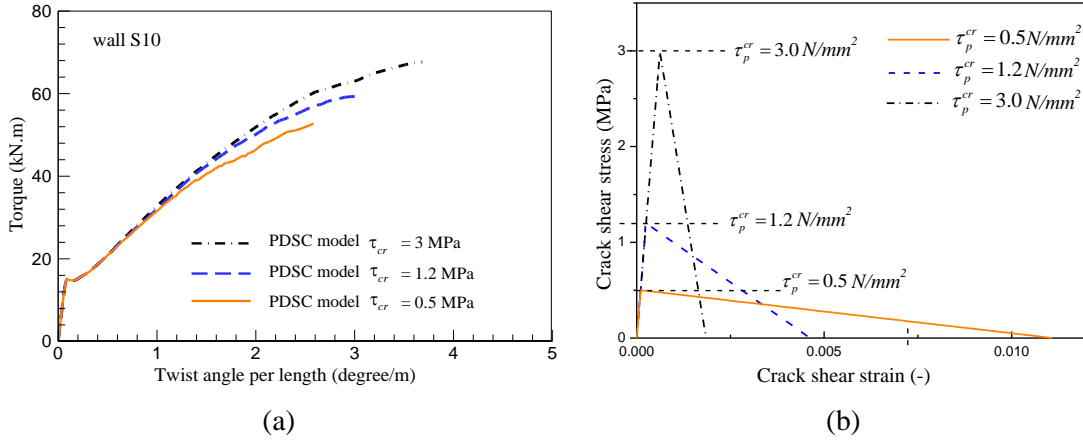
Fig. 5.21 – Sensitivity of the analysis of the S10 wall with respect to the value of the parameter $\tau_{t,p}^{cr}$.

As expected, increasing $\tau_{t,p}^{cr}$ leads to higher torque carrying and deformation capacity at structural level. This is justified by the crack shear stress-shear strain diagrams represented in Fig. 5.21b, since for the simulation with higher $\tau_{t,p}^{cr}$, the entrance of the shear cracks in their softening stage is postponed for larger crack shear deformations, conducting to higher torque carrying capacity for the simulated wall.

5.5.5 Influence of β

The parameter β is used to define the crack shear stress variation in the pre-peak stage, $D_{t,1}^{cr}$, of the $\tau_t^{cr} - \gamma_t^{cr}$ diagram, see Eq. (5.5). The value of crack shear strain at peak, $\gamma_{t,p}^{cr}$, is then evaluated in accordance to the calculated $D_{t,1}^{cr}$. To better understand the influence of β, the S10 wall was simulated by adopting three distinct values for β: β =0.05, β =0.3, β =0.85. The $T - \theta$ curves corresponding to these simulations are depicted in Fig. 5.22a, where it is visible that the stiffness in the initial cracking stage of the wall's response increases with β, while the wall maximum torque capacity increases with the decrease of β. The stiffness of the pre-peak branch of the $\tau_t^{cr} - \gamma_t^{cr}$ diagram increases

with β (see Fig. 5.22b), which justifies the first observation. However, by decreasing β, the entrance of the critical shear cracks in the shear softening phase is postponed for larger deflection levels of the beam, providing an increase on its torque carrying capacity at ultimate stage.
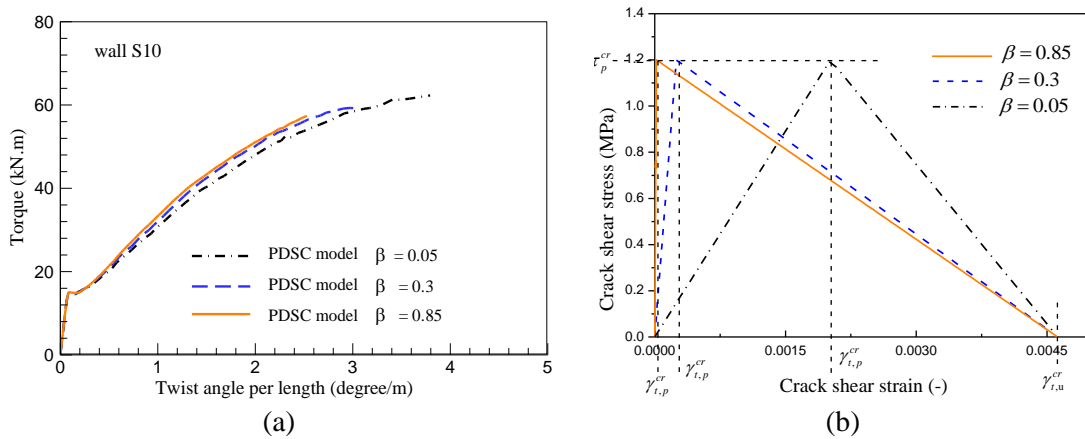
Fig. 5.22 – Sensitivity of the analysis of the S10 wall with respect to the value of the parameter β.

5.5.6 Influence of $G_{f,s}$

Fig. 5.23a compares the predicted $T - \theta$ responses for the three levels of shear fracture energy corresponding to 0.03, 0.07, and 1.0 N/mm. The first value ($G_{f,s}$=0.03 *N/mm*) is lower than the value considered in analysis of section 5.4.3 ($G_{f,s}$=0.07 *N/mm*), while the third is higher.

By increasing $G_{f,s}$ the crack shear stress decay in the softening stage is smaller, which means that the material has more ductile shear behavior at the crack level (see Fig. 5.23b). As Figure 5.23a demonstrates, this effect leads to a higher torque carrying and deformation capacity at structural level.
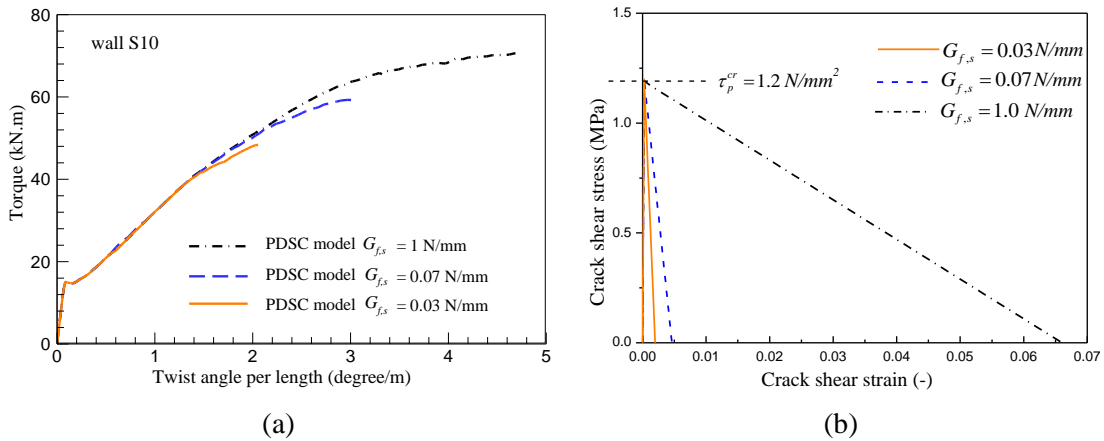
Fig. 5.23 – Sensitivity of the analysis of the S10 wall with respect to the value of the parameter $G_{f,s}$.

5.6 CONCLUSION

This chapter propose a 3D constitutive model for cement based materials, based in the generalization of a 2D plastic-damage multidirectional fixed smeared crack model. The proposed model was then included in the 3D solid element of the FEMIX computer code, and its valdation was executed at the material and structural levels. Cyclic tension-compression test were simulated at first, followed by sophisticated biaxial and triaxial tension-compression numerical tests. In these numerical tests the interaction between cracking and plasticity-damage parts of the model were discussed. It was shown that the stress-strain predictions of the model for these numerical tests were in a very good agreement with the solution reported by another author.

A wide range of experimental data from literature including RC column under combined axial and flexural loading condition, RC beams made by different concrete strength classes, and RC walls subjected to torsion, are simulated to highlight the capability of the model to predict with good accuracy the deformation and cracking behaviour of these types of structures. According to these simulations, the following results can be drawn:

- Results of the experimental program executed by El-Maaddawy (2009) reveals that by increasing length of the eccentricity (*e*) of the load applied to each column, the failure load decreases whereas the strains in tensile longitudinal reinforcement

bars increase. This experimental observation was successfully simulated by the PDSC model.

- In the experimental program of Yang et al. (2003), the primary variable of the test is the compressive strength of concrete. The specimens are categorized into two groups: L group which includes the specimens with f_c =31.4 MPa, and H group which includes the specimens having the compressive strength of 78.5 MPa. The PDSC model was able to simulate with high accuracy the deformational and cracking behavior of the beams in both groups L and H.

- Two walls subjected to torsion loading configuration are simulated by the proposed model. Predicted torque carrying capacity, ductility, crack pattern for these walls are in reasonable agreement with the experimental observations.

In this chapter a parametric study is also executed, to acess the sensitivity of the simulations to the values of the model parameters. In general, for the structure failing in shear the effect of the model parameters $G_{f,s}$, $\tau_{t,p}^{cr}$, β can be summarized as the following:

- By increasing $G_{f,s}$ the crack shear stress decay in the softening stage of $\tau_t^{cr} - \gamma_t^{cr}$ diagram is smaller, which leads to a higher load carrying and deformation capacity at structural level.

- By increasing $\tau_{t,p}^{cr}$ the entrance of the shear cracks in their softening stage is postponed for larger crack shear deformations, conducting to higher load carrying and deformation capacity at structural level.

- By decreasing β the entrance of the critical shear cracks in the shear softening phase is postponed for larger deflection levels of the beam, providing an increase on its load carrying capacity at ultimate stage.

For the structures whose failures are governed by inelastic compressive behaviour of the concrete, the effects of the model parameters f_c, ε_{c1}, $G_{f,c}$ can be summarized as the following:

- The higher is the concrete compressive strength (f_c), the higher is the value of peak stress at $\bar{\sigma}_c - \tilde{\epsilon}_c$ diagram (i.e. f_c is the stress at peak of $\bar{\sigma}_c - \tilde{\epsilon}_c$ diagram), and the larger is the load carrying capacity of the structure.

- By increasing ε_{c1} the stiffness in the initial force-deflection behaviour of the structure decreases, but ductility and load carrying capacity at the ultimate stage of force-deflection behaviour increase.

- By increasing $G_{f,c}$ a more ductile strain softening stage in compression is simulated, which leads to a higher load carrying and deformation capacity at structural level.

CHAPTER 6

CONCLUSIONS AND FUTURE PERSPECTIVES

6.1 GENERAL CONCLUSIONS

A two dimensional (2D) constitutive model was developed for predicting the failure behaviour of structures made by cement based materials when submitted to different loading paths. The proposed model incorporates a multidirectional fixed smeared crack approach to simulate crack initiation and propagation, whereas the inelastic behaviour of material between cracks is treated by a numerical strategy that combines plasticity and damage theories. The smeared crack model considers the possibility of forming several fixed cracks in the same integration point during the cracking process. The crack initiation occurs when the maximum principal tensile stress in an IP attains the concrete tensile strength under an assumed tolerance. After crack initiation, the relationship between normal stress and normal strain in the crack coordinate system is simulated via a trilinear or a quadrilinear diagrams. Two methods are available to simulate the crack shear stress transfer: one based on the concept of shear retention factor, and the other on a shear softening diagram that requires some information about fracture mode II propagation.

The plasticity model is formulated in effective stress space and is defined by four entities: yield function (yield surface); flow rule; evolution law for the hardening variable; and

condition for defining loading–unloading process. The yield function was derived from the Willam–Warnke failure criterion, and its evolution during the plastic flow is governed by a single hardening parameter (for compression). The plasticity part is responsible for simulating irreversible strains and volumetric strain in compression, whereas the strain softening and stiffness degradation of the material under compression are simulated in the framework of continuum damage mechanics, in which the damage is considered as an isotropic process. In this approach the state of damage in concrete under compression is equally distributed in all directions, and can be represented by a scalar measure that is evaluated as a function of the concrete plastic strain.

The model was implemented into the plane stress state element of the FEMIX 4.0 computer program as a new approache to simulate the nonlinear behaviour of concrete structures. The model is initially validated by simulating stress-strain histories of the materials loaded on some different scenarios. Monotonic and cyclic uniaxial compressive tests were simulated at first, followed by a biaxial tension-compression numerical test that is intended to demonstrate the interaction between cracking and plasticity-damage parts of the model. The results of the simulated example under uniaxial compressive load demonstrate the accuracy of the model in capturing the uniaxial behavior of concrete under compression. Under the cyclic uniaxial compression, the model (nominal stress response) accurately simulated the stress–strain envelope response registered experimentally, but overestimates the plastic deformation of the material when unloading occurs. Under the biaxial tension-compression test the model succeeded to simulate closing a crack developed in one direction, by imposing compressive load in the orthogonal direction. The stress-strain prediction of the model for this numerical test was in a very good agreement with the solution reported by another author.

Subsequently, the model appraisal is performed by simulating experimental tests with structural reinforced concrete (RC) elements. For this propose, a wide range of experimental tests was simulated to demonstrate the robustness of the developed model (two dimensional PDSC model). The numerical simulations have predicted with good accuracy the load carrying capacity, deformation, crack pattern, and plastic (compressive) zones of all types of tests analyzed. The results of these analyses demonstrate the

applicability of the proposed model for simulating structures made by cement based materials subjected to multi-axial loading configurations.

The previous model (2D-PDSC) was extended in order to be capable of simulating RC structures modelled by solid finite elements (those where is important to consider a 3D stress field). This model (3D-PDSC) was implemented in the FEMIX computer code and its predictive performance was initially validated by executing some numerical tests at the material level, which were intended as an elementary verification of the basic capabilities of the model. Next the model appraisal was performed at the structural level. Experimental tests, from literature, including RC column subjected to different eccentric loadings, RC beams made by different concrete strength classes, and RC walls subjected to torsion, are simulated to highlight the capability of the model to predict with good accuracy the deformation and cracking behaviour of these types of structures. Results of these analysis indicates the robustness and accuracy of the proposed model for simulating the structures made by cement based material as subjected to different loading paths.

At the end, a feedback can be presented to the objectives already defined in the Introduction section (see section 1.2). It can be concluded that all of these objectives are achieved in this thesis, based on the following justifications: The numerical simulations, represented in the chapters 3, 4, and 5 shows the proposed models are stable and numerically effective in the entire loading regime until failure; Experimental tests from literature, covering a wide range of geometry of specimens, concrete type, loading configurations, and reinforcement conditions, are simulated to demonstrate the applicability of the model for simulating the structures subjected to different loading paths; A parametric study for the model parameters is executed. Through the parametric study it was explained how changing each model parameter can affect the predictive performance of the model; Results of the analysis obtained by the proposed model were compared also with those of another constitutive model (available in FEMIX) that includes the same multidirectional fixed smeared crack, to simulate cracking, but considers the linear elastic behavior for the material between the cracks. In general, and considering the type of structures analysed, this comparison clearly demonstrated the advantages of the proposed model for simulating the experimental behaviour of cement

based material, mainly when relatively large volume of concrete can enter in the compression softening stage.

6.2 RECOMMENDATIONS FOR FUTURE RESEARCH

6.2.1 Creep model

The constitutive models developed in this study (two and three dimensional PDSC models), can simulate time dependent irreversible deformations of the material under load (creep phenomenon). In the current version of the models the incremental concrete strain vector, $\Delta\underline{\varepsilon}^{co}$, (which characterize the deformation of the intact material between the cracks) is decomposed into its elastic ($\Delta\underline{\varepsilon}^{e}$) and plastic parts ($\Delta\underline{\varepsilon}^{p}$), ($\Delta\underline{\varepsilon}^{co} = \Delta\underline{\varepsilon}^{e} + \Delta\underline{\varepsilon}^{p}$). This strain decomposition concept can be extended in order to integrate the parcel due to creep, $\Delta\underline{\varepsilon}^{crp}$, (i.e. $\Delta\underline{\varepsilon}^{co} = \Delta\underline{\varepsilon}^{e} + \Delta\underline{\varepsilon}^{p} + \Delta\underline{\varepsilon}^{crp}$). Thereby the incremental constitutive relation of the new model is obtained as: $\Delta\underline{\bar{\sigma}} = \underline{D}^{e}(\Delta\underline{\varepsilon} - \Delta\underline{\varepsilon}^{p} - \Delta\underline{\varepsilon}^{cr} - \Delta\underline{\varepsilon}^{crp})$. The definition of $\Delta\underline{\bar{\sigma}}$, $\underline{D}^{e}$, $\Delta\underline{\varepsilon}$, $\Delta\underline{\varepsilon}^{cr}$ are the same as those introduced in Chapter 3.

Due to this additional term ($\Delta\underline{\varepsilon}^{crp}$) the flow rule and isotropically hardening of the yield surface are remained as before. Stress update process must be augmented by stress components due to time dependent deformations. Based on the stress update, internal nodal forces will be calculated and compared by the external one to satisfy the equilibrium equation.

6.2.2 Numerical simulation of fire condition

Another phenomenon that can be captured by the concept of strain decomposition is the dependence of the material properties to the temperature. In this way another term of $\Delta\underline{\varepsilon}^{T}$ related to the thermal variation must be introduced into the constitutive equation of the plastic-damage multidirectional fixed smeared crack model. Such constitutive equation can be written as $\Delta\underline{\bar{\sigma}} = \underline{D}^{e}(\Delta\underline{\varepsilon} - \Delta\underline{\varepsilon}^{p} - \Delta\underline{\varepsilon}^{cr} - \Delta\underline{\varepsilon}^{T})$.

In a previous work (Ventura-Gouveia, 2011) a general thermal model was developed and introduced in the FEMIX computer code. Steady-state and transient thermal analysis are

available, including early-age heat generation during the hardening phase of concrete. Furthermore, the multidirectional fixed 3D smeared crack model was adapted to incorporate the incremental strain decomposition and a thermo-mechanical model obtained.

In future developments, the model can be adapted to incorporate the possibility of simulating structures under high temperatures, like fire condition. A possible application of the numerical tool can be mentioned in simulating behavior of ECC/FRP panel strengthening system subjected to the high temperatures. This composite system has been designed to show considerable residual strength after exposure to fire condition

REFERENCES

Abrishambaf, A. (2015), "Creep behaviour of cracked steel fibre reinforced self-compacting concrete laminar structures", PhD thesis, Department of Civil Engineering, University of Minho.

Abrishambaf, A., Barros, J.A.O., Cunha, V.M.C.F. (2013), "Relation between fibre distribution and post-cracking behaviour in steel fibre reinforced self-compacting concrete panels", Cement and Concrete Research, 51, 57–66.

Abrishambaf, A., Barros, J.A.O., Cunha, V.M.F.C. (2015), "Tensile stress-crack width law for steel fibre reinforced self-compacting concrete obtained from indirect (splitting) tensile tests", Cement and Concrete Composites, 57, 153–165.

Abu Al-Rub, R.K., Kim, S.M. (2010), "Computational applications of a coupled plasticity–damage constitutive model for simulating plain concrete fracture", Engineering Fracture Mechanics, 77 (10), 1577–1603.

Alfano, G., Crisfield, M.A. (2001), "Finite element interface models for delamination analysis of laminated composites: mechanical and computational issues", International Journal for Numerical Methods in Engineering, 50:1701-1736.

Ayatollahi, M.R., Aliha, M.R.M. (2005), "Cracked Brazilian disc specimen subjected to mode II deformation", Engineering Fracture Mechanics, 72, 493-503.

Baghi, H., Barros, J.A.O. (2016), "Shear strengthening of reinforced concrete T beams with Hybrid Composite Plate", Composites for Construction Journal, 20 (6).

Ghiassi, B., Marcari, G., Oliveira, D.V., Lourenço, P.B. (2012)," Numerical analysis of bond behavior between masonry bricks and composite materials", Engineering Structures, 43, 210-220.

Barros, J.A.O., Dias, S.J.E., Baghi, H., Ventura-Gouveia, A. (2016), "Exploring new potentialities of NSM CFRP laminates for the shear strengthening of RC beams", ACI Structural Journal, 111 (3), 1275-1287.

Barros, J.A.O., Costa, I.G., Ventura-Gouveia, A. (2011), "CFRP flexural and shear strengthening technique for RC beams: experimental and numerical research", Advances in Structural Engineering Journal, 14 (3), 559–81.

Barros, J.A.O., Dias, S. (2013), "Assessment of the effectiveness of the NSM shear strengthening technique for deep T cross section RC beams", FRPRCS11, Guimaraes, Portugal.

Barros, J.A.O., Sena-Cruz, J.M. (2001), "Fracture energy of steel fibre reinforced concrete", Journal of Mechanics of Composite Materials and Structures, 8 (1), 29-45.

Barros, J.A.O., Varma, R.K., Sena-Cruz, J.M., Azevedo, A.F.M. (2008), "Near surface mounted CFRP strips for the flexural strengthening of RC columns - experimental and numerical research", Engineering Structures Journal, 30 (12), 3412-3425.

Bazant, Z.P., Oh, B.H. (1983), "Crack band theory for fracture of concrete", Materials and Structures, 16 (3), 155-177.

Bazant, Z.P., Caner, F.C., Carol, I., Adley, M.D., Akers, S.A. (2000), "Microplane model M4 for concrete: I Formulation with work-conjugate deviatoric stress", Journal of Engineering Mechanics, 126 (9), 944-953.

Camacho, G.T., Ortiz M. (1996), "Computational modeling of impact damage in brittle materials", International Journal of Solids and Structures, 33, 2899-2938.

Carrazedo, R., Mirmiran, A., Hanai, J.B. (2013), "Plasticity based stress–strain model for concrete confinement", Engineering Structures, 48, 645–657.

Carol, I., Rizzi, E., William, K.J. (2001), "On the formulation of anisotropic elastic degradation.: II. Generalized pseudo-Rankine model for tensile damage", International Journal Solids and Structures, 38, 519–46.

CEB-FIP. Model Code 2010 (2010), Tomas Telford, Lausanne, Switzerland.

Cervenka, J., Papanikolaou, V. (2008), "Three dimensional combined fracture–plastic material model for concrete", International Journal of Plasticity, 24:2192–2220.

Cerfontaine, B., Dieudonné, A.C., Radu, J.P., Collin, F., Charlier, R. (2015), "3D zero-thickness coupled interface finite element: Formulation and application", Computers and Geotechnics, 69, 124-140.

Cervenka, J., Bažant, Z.P., Wierer, M. (2005), "Equivalent localization element for crack band approach to mesh sensitivity in microplane model", International Journal for Numerical Methods in Engineering, 62 (5), 700–726.

Chen, W.F., Han, D.J., (1988), "Plasticity for structural engineers", Springer, New York.

Cicekli, U., Voyiadjis, G.Z., Abu Al-Rub R.K. (2007), "A plastic and anisotropic damage model for plain concrete", International Journal of Plasticity, 23, 1874–900.

Coutinho, A.L.G.A., Martins, M.A.D., Sydenstricker, R.M., Alves, J.L.D., Landau, L. (2003), "Simple zero thickness kinematically consistent interface elements", Computers and Geotechnics, 30 (5), 347–374.

Cunha, V.M.C.F. (2010), "Steel fibre reinforced self-compacting concrete-from micromechanics to composite behaviour", University of Minho, Guimaraes, Portugal, (PhD thesis).

Cunha, V.M.C.F., Barros, J.A.O., Sena-Cruz, J.M. (2012), "A finite element model with discrete embedded elements for fibre reinforced composites", Computers and Structures, 94-95, 22-33.

de Borst, R., Remmers, J.J.C., Needleman, A., Abellan, M. A. (2004), "Discrete vs smeared crack models for concrete fracture: bridging the gap", International Journal for Numerical and Analytical Methods in Geomechanics, 28, 583-607.

de Borst, R., Nauta, P. (1985), "Non-orthogonal cracks in a smeared finite element model", Engineering Computations, 2, 35-46.

de Borst, R. (1986), "Computational aspects of smeared crack analysis", In: Hinton, E., Owen, D.R.J. (Eds.), Computational Modelling of Reinforced Concrete. Pineridge Press, Swansea, 44–83.

Dias-da-Costa, D.A.S.G. (2010), "Strong discontinuities in the scope of the discrete crack approach", PhD thesis, Department of Civil Engineering, University of Coimbra.

Dunne, F., Petrinic, N. (2005), "Introduction to computational plasticity", Oxford University Press.

Edalat-Behbahani, A., Barros, J.A.O., Ventura-Gouveia, A. (2015), "Plastic-damage smeared crack model to simulate the behaviour of structures made by cement based materials", International Journal of Solids Structures, 73-74, 20-40.

Edalat-Behbahani, A., Barros, J.A.O., Ventura-Gouveia, A. (2016), "Application of plastic-damage multidirectional fixed smeared crack model in analysis of RC structures", Engineering Structures, 125, 374-391.

El-Maaddawy, T. (2009), "Strengthening of eccentrically loaded reinforced concrete columns with fiber-reinforced polymer wrapping system: experimental investigation and analytical modeling", Journal of Composites for Construction, 13 (1), 13-24.

El-Maaddawy, T.A, Sherif, S. (2009), "FRP composites for shear strengthening of reinforced concrete deep beams with openings", Composite Structures, 89, 60–69.

Faria, R. Oliver, J. Cervera, M. (1998), "A strain-based plastic viscous-damage model for massive concrete structures", International Journal Solids and Structures, 35 (14), 1533-1558.

Feenstra, P.H. (1993), "Computational aspect of biaxial stress in plain and reinforced concrete" PhD thesis, Department of Civil Engineering, Delft University of Technology.

Feenstra, P.H., de Borst, R. (1996), "A composite plasticity model for concrete", International Journal of Solids and Structures, 33 (5), 707-730.

Ferrara, L., di Prisco, M. (2001), "Mode I fracture behavior in concrete: nonlocal damage modeling", Journal of Engineering Mechanics, 127 (7), 678-692.

Gernay, T. (2012), "A multiaxial constitutive model for concrete in the fire situation including transient creep and cooling down phases", PhD Thesis, University of Liege, Belgium.

Gernay, T., Millard, A., Franssen, J. (2013), "A multiaxial constitutive model for concrete in the fire situation: Theoretical formulation", International Journal of Solids Structures, 50, 3659-3673.

Grassl, P., Jirasek, M. (2006), "Damage–plastic model for concrete failure", International Journal of Solids and Structures, 43, 7166–7196.

Grassl, P., Lundgren, K., Gylltoft. K. (2002), "Concrete in compression: a plasticity theory with a novel hardening law", International Journal of Solids and Structures, 39, 5205–5223.

Grassl, P., Xenos, D., Nystrom, U., Rempling, R., Gylltoft, K. (2013), "CDPM2: A damage-plasticity approach to modelling the failure of concrete", International Journal of Solids and Structures, 50, 3805–3816.

Hansen, E., William, K., Carol, I. (2001), "A two-surface anisotropic damage/plasticity model for plain concrete", In: de Borst R., Mazars J., Pijaudier-Cabot G., van Mier J.G.M., editors. Fracture mechanics of concrete structures, Lisse: Balkema, 549–556.

Hassan, A.M.T., Jones, S.W., Mahmud, G.H. (2012), "Experimental test methods to determine the uniaxial tensile and compressive behaviour of ultra high performance fibre reinforced concrete (UHPFRC)", Construction and Building Materials, 37, 874–882.

Hawileh, R.A. (2012), "Nonlinear finite element modeling of RC beams strengthened with NSM FRP rods", Construction and Building Materials, 27, 461–471.

Hawileh, R.A, El-Maaddawy, T.A, Naser, M.Z. (2012), "Nonlinear finite element modelling of concrete deep beams with openings strengthened with externally-bonded composites", Materials and Design, 42, 378-387.

Hillerborg, A., Modéer, M., Petersson, P.E. (1976), "Analysis of crack formation and crack growth in concrete by means of fracture mechanics and finite elements", Cement and Concrete Research, 6 (6), 773-781.

Hisabe, N., Yoshitake, I., Tanaka, H., Hamada, S. (2006), "Mechanical behaviour of fiber reinforced concrete element subjected to pure shearing stress", International RILEM

workshop on high performance finer reinforced cementitious composites in structural applications, RILEM Publication SARL, 375-381.

Hugues, B.P., Chapman, G.P. (1966), "The deformation of concrete and micro-concrete in compression and tension with particular reference to aggregate size", Magazine of Concrete Research, 18 (54), 19-24.

Jason, L., Huerta, A., Pijaudier-Cabot, G., Ghavamian, S. (2006), "An elastic plastic damage formulation for concrete: Application to elementary tests and comparison with an isotropic damage model", Computer Methods in Applied Mechanics and Engineering, 195 (52), 7077-7092.

Jefferson, A.D. (2003), "Craft—a plastic damage contact model for concrete - I. Model theory and thermodynamic considerations", International Journal of Solids Structures, 40, 5973-5999.

Jirásek, M. (2004), "Non-local damage mechanics with application to concrete", RFGC–8/2004. Failure, Degradation and Instabilities, 683-707.

JSCE-G 553-1999. (2005), "Test method for shear strength of steel fiber reinforced concrete, Standard specification for concrete structures, Test method and specification", JSCE.

Ju, J.W. (1989), "On energy-based coupled elasto-plastic damage theories: constitutive modeling and computational aspects", International Journal of Solids and Structures, 25 (7), 803-833.

Kachonov, L.M. (1958), "On the creep fracture time", Izv. Akad. Nauk USSR Otd. Tech, 8:26–31 [in Russian].

Kaliakin, V.N., Li, J. (1995), "Insight into deficiencies associated with commonly used zero-thickness interface elements", Computers and Geotechnics, 17 (2), 225–252.

Karsan, I.D., Jirsa, J.O. (1969), "Behaviour of concrete under compressive loadings" Journal of Structure Division, ASCE, 95 (12), 2535–2563.

Kim Y.H., Hueste, M.B.D., Trejo, D., Cline, D.B.H. (2010), "Shear characteristics and design for high strength self-consolidating concrete", Journal of Structural Engineering, 136 (8), 989-1000.

Kozar, I., Ozbolt, J. (2010), "Some aspects of load-rate sensitivity in visco-elastic microplane material model", Computers and Concrete, 7 (4), 317–329.

Krätzig, W.B., Pölling, R. (2004), "An elasto-plastic damage model for reinforced concrete with minimum number of material parameters", Computers and Structures, 82 (15-16), 1201-1215.

Kupfer, H., Hilsdorf, H.K., Rusch, H. (1969), "Behaviour of concrete under biaxial states of stress", American Concrete Institute journal, 66 (8), 656–666.

Lee, J., Fenves, G.L. (1998), "Plastic-damage model for cyclic loading of concrete structures", Journal of Engineering Mechanics Division, ASCE, 124, 892–900.

Lee, J., Fenves, G.L. (2001), "A return-mapping algorithm for plastic-damage models: 3-D and plane stress formulation", International Journal of Numerical Methods in Engineering, 50, 487-506.

Lu, D., Du, X., Wang, G., Zhou, A, Li, A. (2016), "A three-dimensional elastoplastic constitutive model for concrete", Computers and Structures, 163, 41-55.

Lubliner, J., Oliver, J., Oller, S., Oñate, E. (1989), "A plastic-damage model for concrete", International Journal of Solids and Structures, 25 (3), 299-326.

Luccioni, B.M., Rougier, V.C. (2005), "A plastic damage approach for confined concrete", Computers & Structures, 83 (27), 2238-2256.

Maier, J., Thürlimann, B. (1985), "Bruchversuche an Stahlbetonscheiben", IBK Bericht 8003-1, ETH Zürich, Institut für Baustatik und Konstruktion (IBK), Zürich.

Malvern, L.E., (1969), "Introduction to the mechanics of a continuous medium", Prentice-Hall International, Englewood Cliffs, New Jersey.

Marfia, S., Rinaldi, Z., Sacco, E., (2004), "Softening behavior of reinforced concrete beams under cyclic loading", International Journal Solids and Structures, 41 (11-12), 3293-3316.

May, S., de Borst, R., Vignollet, J. (2016) "Powell–Sabin B-splines for smeared and discrete approaches to fracture in quasi-brittle materials", Computer Methods in Applied Mechanics and Engineering, 307, 193-214.

Mazaheripour, H., Barros, J.A.O., Sena-Cruz, J.M. (2016), "Tension-stiffening model for FRC reinforced by hybrid FRP and steel bars", Composites Part B: Engineering, 88, 162-181.

Mazars, J., Pijaudier-Cabot, G. (1989), "Continuum damage theory - application to concrete". J. Eng. Mech., 115 (2), 345-365.

Meschke, G., Lackner, R., Mang, H.A. (1998), "An anisotropic elastoplastic-damage model for plain concrete", International Journal of Numerical Methods in Engineering, 42, 703–727.

Moës, N., Belytschko, T. (2002), "Extended finite element method for cohesive crack growth", Engineering Fracture Mechanics, 69 (7), 813-833.

Nechnech, W., Meftah, F., Reynouard, J.M. (2002), "An elasto-plastic damage model for plain concrete subjected to high temperatures", Journal of Engineering Structures, 24 (5), 597-611.

Omidi, O., Valliappan, S., Lotfi, V. (2013), "Seismic cracking of concrete gravity dams by plastic-damage model using different damping mechanisms", Finite Element in Analysis and Design, 63, 80-97.

Omidi, O., Lotfi, V. (2013), "Continuum large cracking in a rate-dependent plastic–damage model for cyclic-loaded concrete structures", International Journal for Numerical and Analytical Methods in Geomechanics, 37, 1363–1390.

Oliver, J.A. (1989), "Consistent characteristic length for smeared cracking models", International Journal Numerical Methods in Engineering, 28, 461–474.

Oliver, J., Linero, D.L., Huespe, A.E., Manzoli, O.L. (2008), "Two-dimensional modeling of material failure in reinforced concrete by means of a continuum strong discontinuity approach", Computer Methods in Applied Mechanics and Engineering, 197, 332-348.

Ortiz, M. (1985), "A constitutive theory for inelastic behaviour of concrete", Mechanics of Materials, 4, 67–93.

Ortiz, M., Pandolfi, A. (1999), "Finite-deformation irreversible cohesive elements for three-dimensional crack-propagation analysis, International Journal for Numerical Methods in Engineering, 44, 1267-1282.

Papanikolaou, V.K., Kappos, A.J. (2007), "Confinement-sensitive plasticity constitutive model for concrete in triaxial compression", International Journal of Solids and Structures, 44 (21), 7021–7048.

Park, H., Kim, J.Y. (2005), "Plasticity model using multiple failure criteria for concrete in compression", International Journal of Solids and Structures, 42 (8), 2303-2322, 2005.

Pereira, E.B. (2012), "Processes of cracking in strain hardening in cementitious composites", PhD Thesis, University of Minho, Portugal.

Petrova,V.E., Sadowski, T. (2012), "Theoretical analysis of Mode II cracks in a compact shear specimen", Computational Materials Science, 64, 248-252.

Poltronieri, F., Piccolroaz, A., Bigoni, D., Romero Baivier, S. (2014), "A simple and robust elastoplastic constitutive model for concrete", Engineering Structures, 60, 81–84.

Peng, X.N., Wong, Y.L. (2011), "Behavior of reinforced concrete walls subjected to monotonic pure torsion-an experimental study", Engineering structures, 33, 2495-2508.

Reinhardt, H.W. (1984), "Fracture mechanics of an elastic softening material like concrete", Heron, 29 (2), 1-42.

Ristinmaa, M., Wallin, M., Ottosen, N.S. (2007), "Termodynamic format and heat generation of isotropic hardening plasticity", Acta Mechanica.

Rao, G.A., Rao, A.S. (2009), "Toughness indices of steel fiber reinforced concrete under mode II loading", Materials and Structures, 42, 1173–1184.

Rots, G.J., de Borst, R. (1987), "Analysis of mixed mode fracture in concrete", Journal of Engineering Mechanics, 113 (11), 1739-1758.

Rots, J.G. (1988), "Computational modeling of concrete structures", PhD Thesis, Delft University of Technology.

Sagaseta, J., Vollum, R.L. (2011), "Shear design of short-span beams". Magazine of Concrete Research, 62, 4, 267-282.

Schellekens, J.C.J. (1990), Interface elements in finite element analysis", Report25.2-90-2-17, Delft University of Technology, Delft.

Seguarado, J., LLorca, J. (2004), "A new three-dimensional interface finite element to simulate fracture in composites", International Journal of Solids and Structures, 41:2977-2993.

Sena-Cruz, J.M. (2004), "Strengthening of concrete structures with near-surface mounted CFRP laminate strips", PhD thesis, Department of Civil Engineering, University of Minho.

Sena-Cruz, J.M., Barros, J.A.O., Azevedo, A.F.M., Ventura-Gouveia, A. (2007), "Numerical simulation of the nonlinear behaviour of RC beams strengthened with NSM CFRP strips", Proceedings of CMNE/CILAMCE Congress, FEUP, Porto, Portugal.

Soltanzadeh, F., Edalat-Behbahani, A., Mazaheripour, H., Barros, J.A.O. (2016a) "Shear resistance of SFRSCC short-span beams without transversal reinforcements, Composites Structures, 139, 42-61.

Soltanzadeh, F., Edalat-Behbahani, A., Barros, J.A.O., Mazaheripour, H. (2016b), "Effect of fiber dosage and prestress level on shear behavior of hybrid GFRP-steel reinforced concrete I-shape beams without stirrups", Composites Part B: Engineering, 102, 57-77.

Simone, A. (2007), "Continuous-discontinuous modelling of failure", Rev Eur Génie Civil, 11(7–8), 1069–1085, http://dx.doi.org/10.1080/17747120.2007.9692977.

Simo, J.C., Hughes, T.J.R. (1998), "Computational inelasticity", Springer.

Sinha, B.P., Gerstle, K.H., Tulin, L.G. (1964), "Stress-strain relations for concrete under uniaxial loading", ACI Structural Journal, 61(2), 195-211.

Schellekens, J.C.J., de Borst, R. (1993), "On the numerical integration of interface elements", International Journal for Numerical Methods in Engineering, 36 (1), 43–66.

Shah, S.P., Swartz, S.E., Ouyang, C. (1995), "Fracture Mechanics of Concrete: Applications of Fracture Mechanics to Concrete, Rock and Other Quasi-Brittle Materials", John Wiley & Sons, Inc.

Suidan, M., Schnobrich, W.C. (1973), "Finite element analysis of reinforced concrete", Journal of Structural Division, ASCE, 99 (10), 2109-2122.

Suryanto B., Nagai K, Maekawa K. (2010), "Modeling and analysis of shear-critical ECC members with anisotropic stress and strain fields", Journal of Advanced Concrete Technology, 8 (2), 239–258.

Swaddiwudhipong, S., Seow, P.E.C. (2006), "Modelling of steel fiber-reinforced concrete under multi-axial loads", Cement and Concrete Research, 36, 1354–1361.

Tao, X., Phillips, D.V. (2005), "A simplified isotropic damage model for concrete under bi-axial stress states", Cement and Concrete Composites, 27 (6), 716-726.

Taqieddin, Z.N. (2008) "Elasto-plastic and damage modelling of reinforced concrete", PhD thesis, Department of Civil and Environmental Engineering, Louisiana State University.

Taqieddin, Z., Voyiadjis, G.Z., Almasri, A.H. (2012), "Formulation and verification of a concrete model with strong coupling between isotropic damage and elastoplasticity and comparison to a weak coupling model", Journal of Engineering Mechanics ASCE, 138, 530–541.

Thanoon, W.A., Alwathaf, A.H., Noorzaei, J., Jaafar, M.S., Abdulkadir, M.R. (2008), "Nonlinear finite element analysis of grouted and ungrouted hollow interlocking mortarless block masonry system", Engineering Structures, 30, 1560-1572.

Tijssens, M.G.A., Sluys B.L.J., Van der Giessen, E. (2000), "Numerical simulation of quasi-brittle fracture using damaging cohesive surfaces", European Journal of Mechanics - A/Solids, 19 (5), 761-779.

Teixeira, M.D.E., Barros, J.A.O., Cunha, V.M.C.F., Moraes-Neto, B.N., Ventura-Gouveia A. (2015), "Numerical simulation of the punching shear behaviour of self-compacting fibre reinforced flat slabs" Construction and Building Material, 74, 25-36.

van Mier, J.G.M. (1984), "Strain-softening of concrete under multiaxial loading conditions", PhD thesis, Technical University of Eindhoven.

Ventura-Gouveia, A. (2011), "Constitutive models for the material nonlinear analysis of concrete structures including time dependent effects", PhD thesis, Department of Civil Engineering, University of Minho.

Ventura-Gouveia, A., Barros, J.A.O., Azevedo, A.F.M., Sena-Cruz, J.M. (2008), "Multifixed smeared 3D crack model to simulate the behaviour of fiber reinforced concrete structures", Challenges for Civil Construction International Conference (CCC2008), Porto, Portugal, 16-18.

Vonk, R.A. (1992), "Softening of concrete loaded in compression", PhD thesis, Eindhoven University of Technology, The Netherlands.

Voyiadjis, G.Z., Kattan, P.I. (2006), "Advances in Damage Mechanics: Metals and Metal Matrix Composites, with an Introduction to Fabric Tensors", Second Edition, Elsevier, Oxford.

Voyiadjis, G.Z., Taqieddin, Z.N., Kattan, P.I. (2008), "Anisotropic Damage-Plasticity Model for Concrete", International Journal of Plasticity, 24 (10), 1946-1965.

Wang, C.H. (1996), "Introduction to fracture mechanics", *DSTO-GD-0103*, Airframes and Engines Division Aeronautical and Maritime Research Laboratory.

Wells, G.N., Sluys, L.J. (2001), "A new method for modelling cohesive cracks using finite elements", International Journal of Numerical Methods in Engineering, 50, 2667–2682.

Willam, K., Rhee, I., Beylkin, G. (2001), "Multiresolution analysis of elastic degradation in heterogeneous materials", Meccanica, 36 (1), 131-150.

Willam, K., Rhee, I., Xi, Y. (2003), "Thermal degradation of heterogeneous concrete materials", Special issue on Durability, Journal of Materials in Civil Engineering, ASCE, 17 (3), 276-285.

Willam, K.J., Warnke, E.P. (1974), "Constitutive model for the triaxial behaviour of concrete in Concrete Structures Subjected to Triaxial Stresses.", volume 19 of IABSE Report, International Association of Bridge and Structural Engineers, Zurich, 1-30,

Wischers, G. (1978), "Application of Effects of Compressive Loads on Concrete," Betontech., Berlin, Nos. 2 and 3, Düsseldorf.

Wu, J.U., Li J., Faria, R. (2006), "An energy release rate-based plastic-damage model for concrete", International Journal of Solids and Structures, 43, 583–612.

Wu, H.Q., Gilbert, R.I. (2009), "Modeling short-term tension stiffening in reinforced concrete prisms using a continuum-based finite element model", Engineering Structures, 31, 2380-2391.

Xenos, D., Grassl, P. (2016), "Modelling the failure of reinforced concrete with nonlocal and crack band approaches using the damage-plasticity model CDPM2", Finite Elements in Analysis and Design, 117-118, 11-20.

Xu, S., Reinhardt, H.W. (2005), "Shear fracture on the basis of fracture mechanics", Otto-Graf Journal, 16, 21-78.

Yang, K.H., Chung, H.S., Lee, E.T, Eun, H.C. (2003), "Shear characteristics of high-strength concrete deep beams without shear reinforcements", Engineering Structures, 25, 1343–1352.

Zhang, J., Li, J. (2012), "Investigation into Lubliner yield criterion of concrete for 3D simulation", Engineering Structures, 44, 122–127.

Zhang, J., Li, J., Woody-Ju, J. (2016), "3D elastoplastic damage model for concrete based on novel decomposition of stress", International Journal of Solids and Structures, 94-95, 125-137.

Salehian, H., Barros, J.A.O. (2015), "Assessment of the performance of steel fibre reinforced self-compacting concrete in elevated slabs", Cement and Concrete Composites, 55, 268-280.

GEOMETRIC REPRESENTAION OF STRESS INVARIANTS

Fig. A.1 represents a three dimensional orthogonal coordinate system aligned in the directions of the principal stresses ($\bar{\sigma}_1$, $\bar{\sigma}_2$, $\bar{\sigma}_3$), which is known as Haigh- Westergaard coordinate system. An additional axis, called Hydrostatic axis, is also defined in this figure, which is aligned in the direction of the bisector $\bar{\sigma}_1 = \bar{\sigma}_2 = \bar{\sigma}_3$. The state of stress for every point on the hydrostatic axis is $\bar{\sigma}_1 = \bar{\sigma}_2 = \bar{\sigma}_3$. Any plane perpendicular to Hydrostatic axis is called deviatoric plane.

Consider a generic state of stress represented by point P with the coordinates ($\bar{\sigma}_1$, $\bar{\sigma}_2$, $\bar{\sigma}_3$) in Haigh-Westergaard stress space. Assuming the stress point O is the origin, the stress vector $\overrightarrow{OP}$ can be decomposed into two components: the component $\overrightarrow{ON}$ in the direction of hydrostatic axis and the component $\overrightarrow{NP}$ perpendicular to $\overrightarrow{ON}$ (the vector $\overrightarrow{NP}$ is the projection of $\overrightarrow{OP}$ on the deviatoric plane). The vector $\overrightarrow{NP}$ has the magnitude of $\bar{\rho} = \sqrt{2\bar{J}_2}$, while the magnitude of the vector $\overrightarrow{ON}$ is $\bar{\xi} = \bar{I}_1 / \sqrt{3}$ (Chen and Han, 1988).

To trace the exact location of the stress point P in the deviatoric plane, the stress invariant $\bar{J}_3$ (third invariant of the effective deviatoric stress tensor) is also required. If the triplet axes $\bar{\sigma}_1$, $\bar{\sigma}_2$, $\bar{\sigma}_3$ are projected on the deviatoric plane, and the axis $\bar{\sigma}_1$ is taken as the

vertical one, the orientation of the vector $\overrightarrow{NP}$ in the deviatoric plane is defined by the angle of similarity ($\bar{\theta}$) according to the following equation (Chen and Han, 1988):

$$\bar{\theta} = \frac{1}{3} cos^{-1}\left(\frac{3\sqrt{3}}{2} \frac{\bar{J}_3}{\bar{J}_2^{3/2}} \right) \qquad (A.1)$$

where $\bar{J}_2$ is second invariant of the effective deviatoric stress tensor.
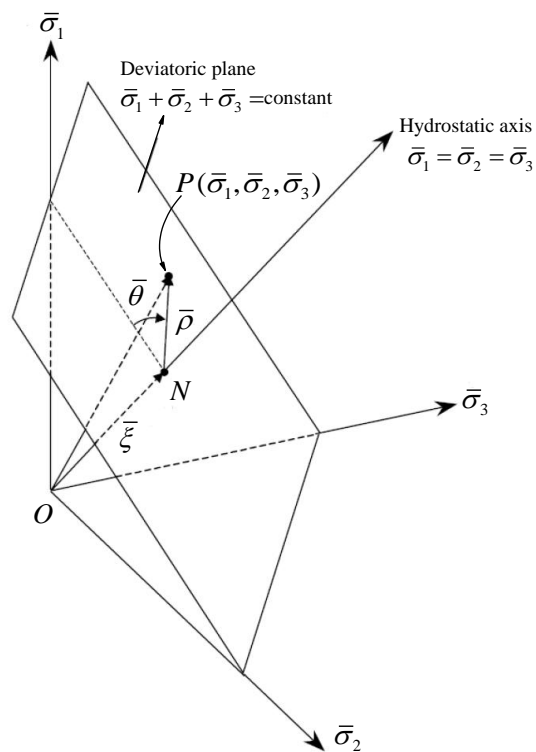
Fig. A.1 – Haigh-Westergaard stress space (Grassl et al., 2002).

EXTRACTING YIELD FUNCTION FROM FAILURE CRITERION

According to the Willam-Warnke failure criterion, two extreme meridians and an elliptical function, used to interpolate the current failure meridian between the two extreme meridians, can represent the entire failure surface. The extreme meridians are called the tensile meridian where angle of similarity is zero ($\bar{\theta} = 0°$), and the compressive meridian where $\bar{\theta} = 60°$ (see Fig. B.1).

(a)   (b)
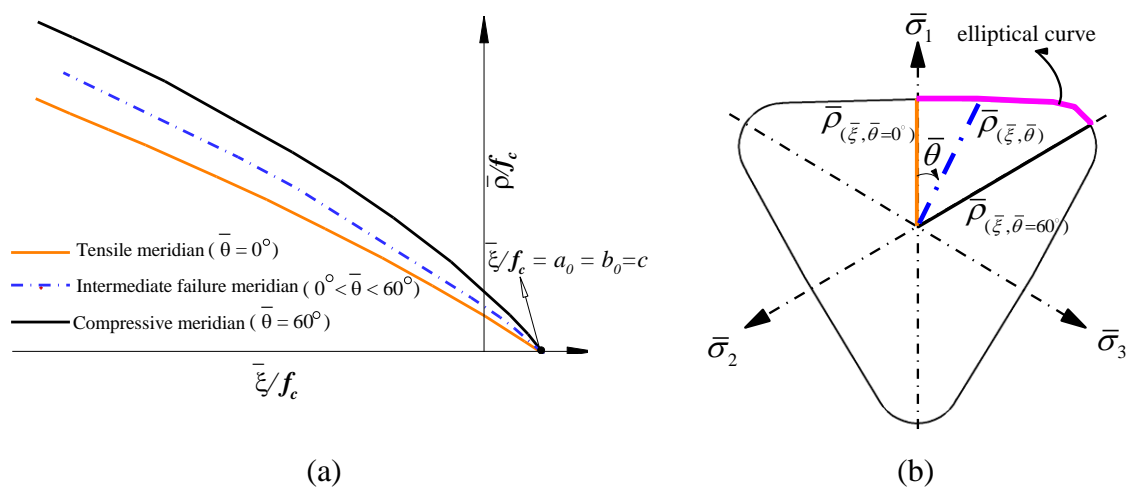
Fig. B.1 – Willam-Warnke failure surface represented in (a) meridian plane; (b) deviatoric plane ($\bar{\sigma}_1, \bar{\sigma}_2, \bar{\sigma}_3$ are the principle effective stresses).

The equations for the tensile and compressive meridians in ($\bar{\xi}$, $\bar{\rho}$, $\bar{\theta}$) coordinate system are given by the following quadratic parabolas (Swaddiwudhipong and Seow, 2006):

$$\frac{\bar{\xi}}{f_c} = a_2 \left(\frac{\bar{\rho}_{(\bar{\xi},\bar{\theta}=0^\circ)}}{f_c} \right)^2 + a_1 \left(\frac{\bar{\rho}_{(\bar{\xi},\bar{\theta}=0^\circ)}}{f_c} \right) + a_0 \qquad (B.1)$$

$$\frac{\bar{\xi}}{f_c} = b_2 \left(\frac{\bar{\rho}_{(\bar{\xi},\bar{\theta}=60^\circ)}}{f_c} \right)^2 + b_1 \left(\frac{\bar{\rho}_{(\bar{\xi},\bar{\theta}=60^\circ)}}{f_c} \right) + b_0 \qquad (B.2)$$

being $\bar{\xi}$ the hydrostatic stress invariant defined as $\bar{\xi} = \bar{I}_1 / \sqrt{3}$, and $\bar{\rho}$ the deviatoric stress invariants also defined as $\bar{\rho} = \sqrt{2\bar{J}_2}$. The term $\bar{\rho}_{(\bar{\xi},\bar{\theta})}$ implies the deviatoric stress invariant ($\bar{\rho}$) that is corresponds to any set of $\bar{\xi}$ and $\bar{\theta}$. For the tensile meridian (where $\bar{\theta} = 0^\circ$) and compressive meridian (where $\bar{\theta} = 60^\circ$), the deviatoric stress invariant ($\bar{\rho}$) are denoted, respectively, by $\bar{\rho}_{(\bar{\xi},\bar{\theta}=0^\circ)}$ and $\bar{\rho}_{(\bar{\xi},\bar{\theta}=60^\circ)}$.

It is assumed that the tensile and compressive parabolas (meridians) intersect each other at the hydrostatic axis, $\bar{\rho} = \sqrt{2\bar{J}_2} = 0$, therefore $a_0 = b_0$ (Willam and Warnke, 1974; Swaddiwudhipong and Seow, 2006).

The constants a_0, a_1, a_2, b_1, and b_2 are the five constants of the W-W failure surface, and the procedure used in their determination is discussed in the following. To obtain the unknowns a_0, a_1, a_2 (which are the coefficients of the tensile meridian) it is sufficient to choose three known failure states lying on the tensile meridian (Eq. B.1), such that:

1. Uniaxial tensile strength, (f_{ct}).

2. Biaxial compressive strength, ($f_{cc} = 1.15 f_c$), (Kupfer et al., 1969).

3. An experimental data corresponding to confined biaxial compression with the coordinate, ($\bar{\xi}/f_c$, $\bar{\rho}/f_c$)=(-6.754, 3.461) (Kupfer et al., 1969).

These three failure points, expressed in $(\bar{\xi}, \bar{\rho}, \bar{\theta})$ coordinate system, are represented in Table B.1.

Table B.1 – Experimental failure points to determine the constants of tensile meridian

Test	Failure points		
	$(\bar{\xi}/f_c)$	$(\bar{\rho}/f_c)$	$(\bar{\theta})$
Uniaxial tension	$\dfrac{1}{\sqrt{3}}\dfrac{f_{ct}}{f_c}$	$\sqrt{\dfrac{2}{3}}\dfrac{f_{ct}}{f_c}$	0
Biaxial compression	$-\dfrac{2}{\sqrt{3}}(1.15)$	$\sqrt{\dfrac{2}{3}}(1.15)$	0
Confined biaxial compression	-6.754	3.461	0

Including these three failure point, represented in Table B.1, into Eq. (B.1), yields after some arrangement the following system of equations:

$$\begin{bmatrix} 1 & \sqrt{\dfrac{2}{3}}\mu & \dfrac{2}{3}\mu^2 \\ 1 & \sqrt{\dfrac{2}{3}}1.15 & \dfrac{2}{3}(1.15)^2 \\ 1 & 3.461 & (3.461)^2 \end{bmatrix} \begin{bmatrix} a_0 \\ a_1 \\ a_2 \end{bmatrix} = \begin{bmatrix} \dfrac{1}{\sqrt{3}}\mu \\ -\dfrac{2}{\sqrt{3}}(1.15) \\ -6.754 \end{bmatrix} \tag{B.3}$$

being μ a non-dimensional parameter defined as $\mu = f_{ct}/f_c$. According to the approach adopted in the PDSC model, the tensile crack opening is initiated based on the Rankine tensile criterion (i.e. a crack occurs when the maximum principal tensile stress in a IP attains f_{ct}), so the plasticity part does not required to account for the tensile cracking behavior of concrete. Therefore to determine the parameter μ for the plasticity model, the value of concrete tensile strength, f_{ct}, was replaced by f_c (i.e. $\mu = f_c/f_c = 1$), which is a higher value adopted to prevent the crack opening based on the plasticity failure criterion.

The coefficients of the tensile meridian (a_0, a_1, a_2), which are the unknowns of the equation B.3, can be deduced as:

$$a_0 = \frac{\sqrt{3}(7.4241\mu + 0.6737\mu^2)}{8.197 - 9.0605\mu + 1.6814\mu^2} \tag{B.4a}$$

$$a_1 = \frac{\sqrt{3}(-5.7392 - 3.694\mu - 2.091\mu^2)}{8.197 - 9.0605\mu + 1.6814\mu^2} \tag{B.4b}$$

$$a_2 = \frac{\sqrt{3}(-1.0098 + 3.3911\mu)}{8.197 - 9.0605\mu + 1.6814\mu^2} \tag{B.4c}$$

The same procedure is repeated for the unknown coefficients of the compressive meridians (b_1, b_2). Two failure states (failure points) lying on the compressive meridian ($\bar{\theta} = 60°$) are used as:

1. Uniaxial compressive strength, (f_c), ($\bar{\xi}/f_c$, $\bar{\rho}/f_c$)=($-1/\sqrt{3}$, $\sqrt{2/3}$).
2. An experimental data corresponding to confined biaxial compression with the coordinate, ($\bar{\xi}/f_c$, $\bar{\rho}/f_c$)=(-3.3774, 2.77), (Kupfer et al., 1969).

By substituting the coordinates of these two failure points into equation of compressive meridian (Eq. B.2), the following system of equations is obtained:

$$\begin{bmatrix} \sqrt{\dfrac{2}{3}} & \dfrac{2}{3} \\ 2.77 & (2.77)^2 \end{bmatrix} \begin{bmatrix} b_1 \\ b_2 \end{bmatrix} = \begin{bmatrix} (-1/\sqrt{3}) - b_0 \\ -3.3774 - b_0 \end{bmatrix} \tag{B.5}$$

By taking into account $b_0 = a_0$, the coefficients b_1 and b_2 are obtained by solving Eq. (B.5). These coefficients in the final form are as the following:

$$b_1 = \frac{\sqrt{3}(-2.3328 - 9.169\mu - 1.5469\mu^2)}{8.197 - 9.0605\mu + 1.6814\mu^2} \tag{B.6d}$$

$$b_2 = \frac{\sqrt{3}(-1.2437 + 4.6489\mu + 0.04254\mu^2)}{8.197 - 9.0605\mu + 1.6814\mu^2} \tag{B.6e}$$

The W-W failure criterion uses the following elliptical equation to interpolate current failure meridian, or the intermediate failure meridians, between the two extremes (tensile and compressive meridians) (Willam and Warnke, 1974; Swaddiwudhipong and Seow, 2006):

$$\bar{\rho}_{(\bar{\xi},\bar{\theta})} = \frac{s}{t} \tag{B.7a}$$

where

$$s = 2\bar{\rho}_{(\bar{\xi},\bar{\theta}=60^\circ)}(\bar{\rho}^2_{(\bar{\xi},\bar{\theta}=60^\circ)} - \bar{\rho}^2_{(\bar{\xi},\bar{\theta}=0^\circ)})\cos\bar{\theta} + \bar{\rho}_{(\bar{\xi},\bar{\theta}=60^\circ)}(2\bar{\rho}_{(\bar{\xi},\bar{\theta}=0^\circ)} - \bar{\rho}_{(\bar{\xi},\bar{\theta}=60^\circ)})$$
$$\times \left[4(\bar{\rho}^2_{(\bar{\xi},\bar{\theta}=60^\circ)} - \bar{\rho}^2_{(\bar{\xi},\bar{\theta}=0^\circ)})\cos^2\bar{\theta} + 5\bar{\rho}^2_{(\bar{\xi},\bar{\theta}=0^\circ)} - 4\bar{\rho}_{(\bar{\xi},\bar{\theta}=0^\circ)}\bar{\rho}_{(\bar{\xi},\bar{\theta}=60^\circ)} \right]^{1/2} \tag{B.7b}$$

and

$$t = 4(\bar{\rho}^2_{(\bar{\xi},\bar{\theta}=60^\circ)} - \bar{\rho}^2_{(\bar{\xi},\bar{\theta}=0^\circ)})\cos^2\bar{\theta} + (\bar{\rho}_{(\bar{\xi},\bar{\theta}=60^\circ)} - 2\bar{\rho}_{(\bar{\xi},\bar{\theta}=0^\circ)})^2 \tag{B.7c}$$

being $\bar{\rho}_{(\bar{\xi},\bar{\theta})}$ is the deviatoric stress invariant of current failure meridian (see Fig. B.1b that demonstrates the deviatoric plane of W-W). As Fig. B.1b shows, Eq. (B.7) ensures convexity and smoothness of the surface anywhere. Eqs. (B.1), (B.2) and (B.7) describe one sixth of the failure cone lying between $0 \le \bar{\theta} \le 60$, then due to six fold symmetry, these equations are sufficient to present the entire failure surface.

The intermediate failure meridians are also quadratic parabola in a form (Swaddiwudhipong and Seow, 2006):

$$\frac{\bar{\xi}}{f_c} = a\left(\frac{\bar{\rho}_{(\bar{\xi},\bar{\theta})}}{f_c}\right)^2 + b\left(\frac{\bar{\rho}_{(\bar{\xi},\bar{\theta})}}{f_c}\right) + c \tag{B.8}$$

The intermediate meridian must also meet the hydrostatic axis at the same location that tensile and compressive meridians already intersected, such a requirement implies that (Swaddiwudhipong and Seow, 2006):

$$c = a_0 = b_0 \tag{B.9}$$

The two unknowns a and b are determined by solving Eq. (B.8) in two known failure points laying on the intermediate failure meridian. Based on the current state of effective stress vector ($\bar{\sigma}$) the angle of similarity is calculated from Eq. (A.1) (see Annex A). The arbitrary control points of $\bar{\xi}/f_c = \bar{\xi}_{CP1} = -0.5$ and $\bar{\xi}/f_c = \bar{\xi}_{CP2} = -0.6$ can be chosen, then the corresponding failure points of $\bar{\rho}_{(\bar{\xi}=\bar{\xi}_{CP1},\bar{\theta})}$, and $\bar{\rho}_{(\bar{\xi}=\bar{\xi}_{CP2},\bar{\theta})}$ were interpolated from Eq. (B.7). The coefficients a and b can then be obtained from:

$$a = \frac{(\bar{\xi}_{CP2} - a_0) - b\left(\dfrac{\bar{\rho}_{(\bar{\xi}=\bar{\xi}_{CP2},\bar{\theta})}}{f_c}\right)}{\left(\dfrac{\bar{\rho}_{(\bar{\xi}=\bar{\xi}_{CP2},\bar{\theta})}}{f_c}\right)^2} \tag{B.10}$$

$$b = \frac{(-\bar{\xi}_{CP2} + a_0)\left(\dfrac{\bar{\rho}_{(\bar{\xi}=\bar{\xi}_{CP1},\bar{\theta})}}{f_c}\right)^2 + (\bar{\xi}_{CP1} - a_0)\left(\dfrac{\bar{\rho}_{(\bar{\xi}=\bar{\xi}_{CP2},\bar{\theta})}}{f_c}\right)^2}{\left(\dfrac{\bar{\rho}_{(\bar{\xi}=\bar{\xi}_{CP2},\bar{\theta})}}{f_c}\right)\left[\left(\dfrac{\bar{\rho}_{(\bar{\xi}=\bar{\xi}_{CP1},\bar{\theta})}}{f_c}\right)\left(\dfrac{\bar{\rho}_{(\bar{\xi}=\bar{\xi}_{CP2},\bar{\theta})}}{f_c}\right) - \left(\dfrac{\bar{\rho}_{(\bar{\xi}=\bar{\xi}_{CP1},\bar{\theta})}}{f_c}\right)^2\right]} \tag{B.11}$$

Including $\bar{\xi} = \bar{I}_1/\sqrt{3}$ and $\bar{\rho}_{(\bar{\xi},\bar{\theta})} = \sqrt{2\bar{J}_2}$ into Eq. (B.8) and replacing f_c with the current uniaxial compressive stress, i.e. the hardening function denoted by $\bar{\sigma}_c$, the equation of yield function is obtained in the form of Eq. (3.15).

SIMULATION OF CYCLIC UNIAXIAL COMPRESSIVE TEST

The adopted $\bar{\sigma}_c - \tilde{\epsilon}_c$ law for the domain $\tilde{\epsilon}_c > \tilde{\epsilon}_{c1}$ ($\bar{\sigma}_c = f_c$) can be replaced by the following equation which includes the parameter κ controlling the slop of the post-peak branch:

$$\bar{\sigma}_c(\tilde{\epsilon}_c) = \frac{f_c}{\kappa - \tilde{\epsilon}_{c1}}(\tilde{\epsilon}_c - \tilde{\epsilon}_{c1}) + f_c \tag{C.1}$$

where κ is calculated as $\kappa = l_0 \, \tilde{\epsilon}_{c1}$, and the non-dimensional coefficient l_0 can take the values as $1 < l_0 < \infty$. For $l_0 = \infty$ Eq. (C.1) gives $\bar{\sigma}_c(\tilde{\epsilon}_c) = f_c$ that corresponds to ideal plastic behaviour (slop of $\bar{\sigma}_c - \tilde{\epsilon}_c$ law for the domain $\tilde{\epsilon}_c > \tilde{\epsilon}_{c1}$ becomes zero).

Using the values of the parameters of the constitutive model in the simulation of cyclic test of Karsan and Jirsa (1969), Fig. C.1a represents the Eq. (C.1) for two distinct values of $l_0 = 4.5$ and $l_0 = 9$. As can be seen in this figure, by increasing the value of l_0 the inclination of the $\bar{\sigma}_c - \tilde{\epsilon}_c$ law is decreased. The appropriate value for the parameter l_0 is usually obtained using an inverse analysis whereas such inverse method is described in the contribution Abu Al-Rub and Kim (2010). For the case $l_0 = 4.5$ (assuming all the other parameters have the same values as described in Fig. 3.8) the cyclic stress-strain response

of the model for the test of Karsan and Jirsa (1969) is represented in Fig. C.1b which demonstrates a close approximation of the residual plastic deformations when compared to those registered in the experimental test.
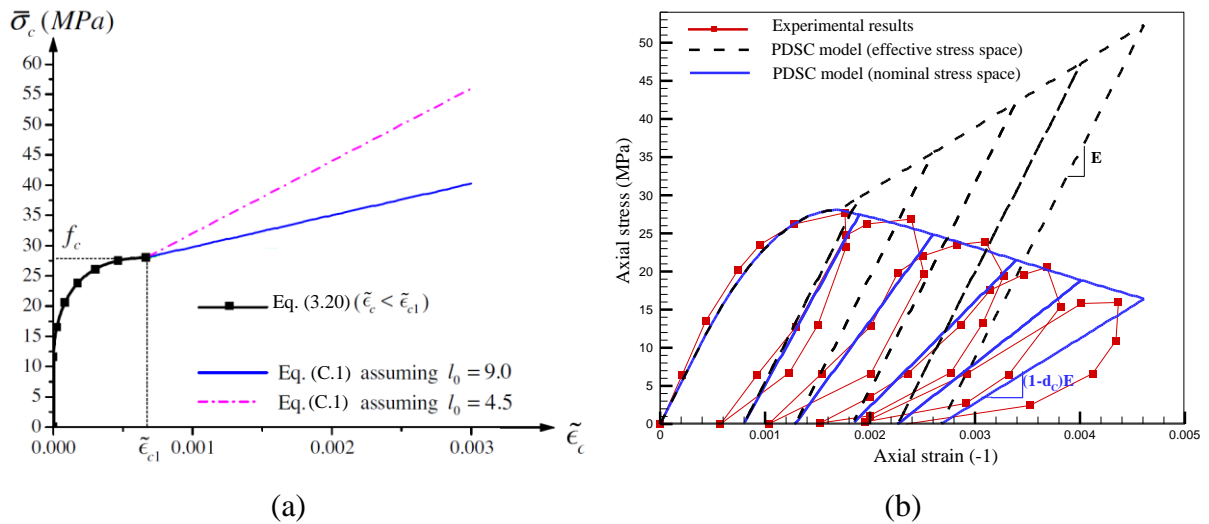
Fig. C.1 – Cyclic uniaxial compressive test of Karsan and Jirsa (1969) ; (a) the $\bar{\sigma}_c - \tilde{\epsilon}_c$ law of the model, (b) Experimental (Karsan and Jirsa, 1969) vs. predicted stress-strain response (assuming l_0 =4.5).

FIRST AND SECOND ORDER DERIVATIVES

D.1 Derivative of the stress invariants with respect to the components of the effective stress vector

For a general case of three dimensional problem, the effective stress tensor is written in the vector format as:

$$\bar{\underline{\sigma}}_i = \bar{\underline{\sigma}}_j = \bar{\underline{\sigma}} = \begin{bmatrix} \sigma_x & \sigma_y & \sigma_z & \tau_{yz} & \tau_{xz} & \tau_{xy} \end{bmatrix}^T \tag{D.1}$$

The first order derivatives of the stress invariants $\bar{I}_1$, $\bar{J}_2$, and $\bar{J}_3$ with respect to components of the effective stress vector ($\bar{\underline{\sigma}}_i$) are defined as the following:

$$\frac{\partial \bar{I}_1}{\partial \sigma_x} = \frac{\partial \bar{I}_1}{\partial \sigma_y} = \frac{\partial \bar{I}_1}{\partial \sigma_z} = 1; \qquad \frac{\partial \bar{I}_1}{\partial \tau_{yz}} = \frac{\partial \bar{I}_1}{\partial \tau_{xz}} = \frac{\partial \bar{I}_1}{\partial \tau_{xy}} = 0 \tag{D.2}$$

$$\frac{\partial \bar{J}_2}{\partial \sigma_x} = \frac{1}{3}\left(2\sigma_x - \sigma_y - \sigma_z\right), \quad \frac{\partial \bar{J}_2}{\partial \tau_{yz}} = 2\tau_{yz} \tag{D.3a}$$

$$\frac{\partial \bar{J}_2}{\partial \sigma_y} = \frac{1}{3}\left(2\sigma_y - \sigma_x - \sigma_z\right), \quad \frac{\partial \bar{J}_2}{\partial \tau_{xz}} = 2\tau_{xz} \tag{D.3b}$$

$$\frac{\partial \bar{J}_2}{\partial \sigma_z} = \frac{1}{3}\left(2\sigma_z - \sigma_x - \sigma_y\right), \quad \frac{\partial \bar{J}_2}{\partial \tau_{xy}} = 2\tau_{xy} \tag{D.3c}$$

$$\frac{\partial \bar{J}_3}{\partial \sigma_x} = \frac{1}{9}\left(2\sigma_x^2 - \sigma_y^2 - \sigma_z^2 - 2\sigma_x\sigma_y - 2\sigma_x\sigma_z + 4\sigma_y\sigma_z\right) \tag{D.4a}$$

$$+ \frac{1}{3}\left(\tau_{xy}^2 + \tau_{xz}^2 - 2\tau_{yz}^2\right)$$

$$\frac{\partial \bar{J}_3}{\partial \sigma_y} = \frac{1}{9}\left(2\sigma_y^2 - \sigma_x^2 - \sigma_z^2 - 2\sigma_x\sigma_y - 2\sigma_y\sigma_z + 4\sigma_x\sigma_z\right) \tag{D.4b}$$

$$+ \frac{1}{3}\left(\tau_{xy}^2 + \tau_{yz}^2 - 2\tau_{xz}^2\right)$$

$$\frac{\partial \bar{J}_3}{\partial \sigma_z} = \frac{1}{9}\left(2\sigma_z^2 - \sigma_x^2 - \sigma_y^2 - 2\sigma_x\sigma_z - 2\sigma_y\sigma_z + 4\sigma_x\sigma_y\right) \tag{D.4c}$$

$$+ \frac{1}{3}\left(\tau_{xz}^2 + \tau_{yz}^2 - 2\tau_{xy}^2\right)$$

$$\frac{\partial J_3}{\partial \tau_{yz}} = \frac{2}{3}\tau_{yz}\left(\sigma_y + \sigma_z - 2\sigma_x\right) + 2\tau_{xy}\tau_{xz} \tag{D.4d}$$

$$\frac{\partial J_3}{\partial \tau_{xz}} = \frac{2}{3}\tau_{xz}\left(\sigma_x + \sigma_z - 2\sigma_y\right) + 2\tau_{xy}\tau_{yz} \tag{D.4e}$$

$$\frac{\partial J_3}{\partial \tau_{xy}} = \frac{2}{3}\tau_{xy}\left(\sigma_x + \sigma_y - 2\sigma_z\right) + 2\tau_{xz}\tau_{yz} \tag{D.4f}$$

D.2 Derivative of the yield function with respect to the components of the effective stress vector

The first order derivative of the yield function with respect to the components of the effective stress vector ($\bar{\sigma}_i$) is given by:

$$\frac{\partial f\left(\bar{\sigma};\bar{\sigma}_c(\bar{\epsilon}_c)\right)}{\partial\bar{\sigma}_i} = \frac{1}{2}\left[\left(\frac{\bar{I}_1}{\sqrt{3}\,c} - \frac{\sqrt{2}\,b}{c}\,\sqrt{\bar{J}_2}\right)\bar{\sigma}_c - \frac{2\,a}{c}\,\bar{J}_2\right]^{-\frac{1}{2}} \times$$

$$\left[\left\{\frac{1}{\sqrt{3}\,c}\frac{\partial\bar{I}_1}{\partial\bar{\sigma}_i} - \frac{\sqrt{2}}{c}\left(\sqrt{\bar{J}_2}\frac{\partial b}{\partial\bar{\sigma}_i} + \frac{1}{2}\frac{\partial\bar{J}_2}{\partial\bar{\sigma}_i}\,\bar{J}_2^{-0.5}\,b\right)\right\}\bar{\sigma}_c \right.$$

$$\left. - \frac{2}{c}\left(\frac{\partial a}{\partial\bar{\sigma}_i}\,\bar{J}_2 + a\frac{\partial\bar{J}_2}{\partial\bar{\sigma}_i}\right)\right] \qquad (D.5)$$

D.3 Derivative of the coefficients of loading meridian (*a*, *b*) with respect to the components of stress vector

First order derivatives of the coefficient of the loading meridian parabola (coefficients *a*, and *b*) with respect to the components of the effective stress vector ($\bar{\sigma}_i$), are as follows:

$$\frac{\partial b}{\partial\bar{\sigma}_i} = \left[\left(\bar{\xi}_{CP1} - b_0\right)\times 2\bar{\rho}_{(\bar{\xi}=\bar{\xi}_{CP2},\bar{\theta})}\frac{\partial\bar{\rho}_{(\bar{\xi}=\bar{\xi}_{CP2},\bar{\theta})}}{\partial\bar{\sigma}_i} - 2\left(\bar{\xi}_{CP2} - b_0\right)\bar{\rho}_{(\bar{\xi}=\bar{\xi}_{CP1},\bar{\theta})}\frac{\partial\bar{\rho}_{(\bar{\xi}=\bar{\xi}_{CP1},\bar{\theta})}}{\partial\bar{\sigma}_i}\right] \qquad (D.6a)$$

$$\times B^{-1} - B^{-2}\times A\times\left[\frac{\partial\bar{\rho}_{(\bar{\xi}=\bar{\xi}_{CP1},\bar{\theta})}}{\partial\bar{\sigma}_i}\bar{\rho}^2_{(\bar{\xi}=\bar{\xi}_{CP2},\bar{\theta})} + 2\bar{\rho}_{(\bar{\xi}=\bar{\xi}_{CP1},\bar{\theta})}\bar{\rho}_{(\bar{\xi}=\bar{\xi}_{CP2},\bar{\theta})}\frac{\partial\bar{\rho}_{(\bar{\xi}=\bar{\xi}_{CP2},\bar{\theta})}}{\partial\bar{\sigma}_i}\right.$$

$$\left. - 2\bar{\rho}_{(\bar{\xi}=\bar{\xi}_{CP1},\bar{\theta})}\bar{\rho}_{(\bar{\xi}=\bar{\xi}_{CP2},\bar{\theta})}\frac{\partial\bar{\rho}_{(\bar{\xi}=\bar{\xi}_{CP1},\bar{\theta})}}{\partial\bar{\sigma}_i} - \bar{\rho}^2_{(\bar{\xi}=\bar{\xi}_{CP1},\bar{\theta})}\frac{\partial\bar{\rho}_{(\bar{\xi}=\bar{\xi}_{CP2},\bar{\theta})}}{\partial\bar{\sigma}_i}\right]$$

$$\frac{\partial a}{\partial\bar{\sigma}_i} = -\left[\frac{\partial b}{\partial\bar{\sigma}_i}\bar{\rho}_{(\bar{\xi}=\bar{\xi}_{CP2},\bar{\theta})} + b\frac{\partial\bar{\rho}_{(\bar{\xi}=\bar{\xi}_{CP2},\bar{\theta})}}{\partial\bar{\sigma}_i}\right]\times\bar{\rho}^{-2}_{(\bar{\xi}=\bar{\xi}_{CP2},\bar{\theta})} \qquad (D.6b)$$

$$- 2\bar{\rho}^{-3}_{(\bar{\xi}=\bar{\xi}_{CP2},\bar{\theta})}\frac{\partial\bar{\rho}_{(\bar{\xi}=\bar{\xi}_{CP2},\bar{\theta})}}{\partial\bar{\sigma}_i}\left[\left(\bar{\xi}_{CP2} - b_0\right) - b\bar{\rho}_{(\bar{\xi}=\bar{\xi}_{CP2},\bar{\theta})}\right]$$

where the auxiliary variables *A* and *B* are defined as:

$$A = \left[\left(\bar{\xi}_{CP1} - b_0\right)\times\bar{\rho}^2_{(\bar{\xi}=\bar{\xi}_{CP2},\bar{\theta})} - \left(\bar{\xi}_{CP2} - b_0\right)\bar{\rho}^2_{(\bar{\xi}=\bar{\xi}_{CP1},\bar{\theta})}\right] \qquad (D.6c)$$

$$B = \left[\bar{\rho}_{(\bar{\xi}=\bar{\xi}_{CP1},\bar{\theta})}\bar{\rho}^2_{(\bar{\xi}=\bar{\xi}_{CP2},\bar{\theta})} - \bar{\rho}_{(\bar{\xi}=\bar{\xi}_{CP2},\bar{\theta})}\bar{\rho}^2_{(\bar{\xi}=\bar{\xi}_{CP1},\bar{\theta})}\right] \qquad (D.6d)$$

It is also noted that according to Eq. (B.9), the constants a_0 and b_0 have the same value (i.e. $a_0 = b_0$).

D.4 Derivative of the interpolation function $\bar{\rho}_{(\bar{\xi},\bar{\theta})}$ (Eq. (B.7a)) with respect to the components of the effective stress vector

The derivation of the interpolation function respect to the stress vector components ($\bar{\sigma}_i$) is given by:

$$\frac{\partial \bar{\rho}_{(\bar{\xi},\bar{\theta})}}{\partial \bar{\sigma}_i} = D \times B^{-1} + E \times A \tag{D.7a}$$

$$A = 2\bar{\rho}_c \left(\bar{\rho}_c^2 - \bar{\rho}_t^2 \right) \cos \bar{\theta} + \bar{\rho}_c \left(2\bar{\rho}_t - \bar{\rho}_c \right) \left[4\left(\bar{\rho}_c^2 - \bar{\rho}_t^2 \right) \cos^2 \bar{\theta} + 5\bar{\rho}_t^2 - 4\bar{\rho}_t \bar{\rho}_c \right]^{0.5} \tag{D.7b}$$

$$B = 4\left(\bar{\rho}_c^2 - \bar{\rho}_t^2 \right) \cos^2 \bar{\theta} + \left(\bar{\rho}_c - 2\bar{\rho}_t \right)^2 \tag{D.7c}$$

$$E = -B^{-2} \left[4\left(\bar{\rho}_c^2 - \bar{\rho}_t^2 \right) \times 2\left(\cos \bar{\theta} \right)\left(-\sin \bar{\theta} \right) \frac{\partial \bar{\theta}}{\partial \bar{\sigma}_i} \right] \tag{D.7d}$$

$$D = 2\bar{\rho}_c \left(\bar{\rho}_c^2 - \bar{\rho}_t^2 \right)\left(-\sin \bar{\theta} \right) \frac{\partial \bar{\theta}}{\partial \bar{\sigma}_i} + \frac{1}{2} \left[4\left(\bar{\rho}_c^2 - \bar{\rho}_t^2 \right) \cos^2 \bar{\theta} + 5\bar{\rho}_t^2 - 4\bar{\rho}_t \bar{\rho}_c \right]^{-0.5} \tag{D.7e}$$

$$\times \bar{\rho}_c \left(2\bar{\rho}_t - \bar{\rho}_c \right) \times 4\left(\bar{\rho}_c^2 - \bar{\rho}_t^2 \right) \times 2\left(\cos \bar{\theta} \right)\left(-\sin \bar{\theta} \right) \frac{\partial \bar{\theta}}{\partial \bar{\sigma}_i}$$

where the variables $\bar{\rho}_t$ and $\bar{\rho}_c$ are defined as $\bar{\rho}_t = \bar{\rho}_{(\bar{\xi},\bar{\theta}=0°)}$ and $\bar{\rho}_c = \bar{\rho}_{(\bar{\xi},\bar{\theta}=60°)}$, respectively.

D.5 Derivative of angle of similarity ($\bar{\theta}$) with respect to the component of the effective stress vector

The angle of similarity is only dependent on the stress field. So, its first order derivation with respect to the components of the stress vector ($\bar{\sigma}_i$) is:

$$\frac{\partial \bar{\theta}}{\partial \bar{\sigma}_i} = -\frac{1}{\left|\sin(3\bar{\theta})\right|} \frac{\sqrt{3}}{2} \left(\frac{\partial \bar{J}_3}{\partial \bar{\sigma}_i} \bar{J}_2^{-3/2} - \frac{3}{2} \bar{J}_3 \times \bar{J}_2^{-5/2} \times \frac{\partial \bar{J}_2}{\partial \bar{\sigma}_i} \right) \tag{D.8}$$

D.6 Derivative of the yield function with respect to the hardening function

First order derivation of the yield function with respect to the hardening function ($\bar{\sigma}_c$) is given by:

$$\frac{\partial f}{\partial \bar{\sigma}_c} = \frac{1}{2} \left(\frac{\bar{I}_1}{\sqrt{3}\,c} - \frac{\sqrt{2}\,b}{c}\sqrt{\bar{J}_2} \right) \left[\left(\frac{\bar{I}_1}{\sqrt{3}} - \frac{\sqrt{2}\,b}{c}\sqrt{\bar{J}_2} \right) \bar{\sigma}_c - \frac{2a}{c}\bar{J}_2 \right]^{-1/2} - 1 \tag{D.9}$$

D.7 Second order derivative of stress invariants with respect to the components of the effective stress vector

The second order derivative of the first invariant of the effective stress tensor, $\bar{I}_1$, with respect to the effective stress components ($\bar{\sigma}_i$) and ($\bar{\sigma}_j$) is given by:

$$\frac{\partial^2 \bar{I}_1}{\partial \bar{\sigma}_j \partial \bar{\sigma}_i} = \underline{0} \tag{D.10}$$

The second order derivative of of the second invariant of the deviatoric effective stress tensor, $\bar{J}_2$, with respect to the effective stress components ($\bar{\sigma}_i$) and ($\bar{\sigma}_j$) is given by:

$$\frac{\partial}{\partial\sigma_x}\left(\frac{\partial\bar{J}_2}{\partial\sigma_x}\right)=\frac{2}{3} \quad;\frac{\partial}{\partial\sigma_x}\left(\frac{\partial\bar{J}_2}{\partial\sigma_y}\right)=-\frac{1}{3} \quad;\frac{\partial}{\partial\sigma_x}\left(\frac{\partial\bar{J}_2}{\partial\sigma_z}\right)=-\frac{1}{3} \quad;\frac{\partial}{\partial\sigma_x}\left(\frac{\partial\bar{J}_2}{\partial\tau_{yz}}\right)=0 \quad;\frac{\partial}{\partial\sigma_x}\left(\frac{\partial\bar{J}_2}{\partial\tau_{xz}}\right)=0 \quad;\frac{\partial}{\partial\sigma_x}\left(\frac{\partial\bar{J}_2}{\partial\tau_{xy}}\right)=0 \quad \text{(D.11)}$$

$$\frac{\partial}{\partial\sigma_y}\left(\frac{\partial\bar{J}_2}{\partial\sigma_x}\right)=-\frac{1}{3} \quad;\frac{\partial}{\partial\sigma_y}\left(\frac{\partial\bar{J}_2}{\partial\sigma_y}\right)=\frac{2}{3} \quad;\frac{\partial}{\partial\sigma_y}\left(\frac{\partial\bar{J}_2}{\partial\sigma_z}\right)=-\frac{1}{3} \quad;\frac{\partial}{\partial\sigma_y}\left(\frac{\partial\bar{J}_2}{\partial\tau_{yz}}\right)=0 \quad;\frac{\partial}{\partial\sigma_y}\left(\frac{\partial\bar{J}_2}{\partial\tau_{xz}}\right)=0 \quad;\frac{\partial}{\partial\sigma_y}\left(\frac{\partial\bar{J}_2}{\partial\tau_{xy}}\right)=0$$

$$\frac{\partial}{\partial\sigma_z}\left(\frac{\partial\bar{J}_2}{\partial\sigma_x}\right)=-\frac{1}{3} \quad;\frac{\partial}{\partial\sigma_z}\left(\frac{\partial\bar{J}_2}{\partial\sigma_y}\right)=-\frac{1}{3} \quad;\frac{\partial}{\partial\sigma_z}\left(\frac{\partial\bar{J}_2}{\partial\sigma_z}\right)=\frac{2}{3} \quad;\frac{\partial}{\partial\sigma_z}\left(\frac{\partial\bar{J}_2}{\partial\tau_{yz}}\right)=0 \quad;\frac{\partial}{\partial\sigma_z}\left(\frac{\partial\bar{J}_2}{\partial\tau_{xz}}\right)=0 \quad;\frac{\partial}{\partial\sigma_z}\left(\frac{\partial\bar{J}_2}{\partial\tau_{xy}}\right)=0$$

$$\frac{\partial}{\partial\tau_{yz}}\left(\frac{\partial\bar{J}_2}{\partial\sigma_x}\right)=0 \quad;\frac{\partial}{\partial\tau_{yz}}\left(\frac{\partial\bar{J}_2}{\partial\sigma_y}\right)=0 \quad;\frac{\partial}{\partial\tau_{yz}}\left(\frac{\partial\bar{J}_2}{\partial\sigma_z}\right)=0 \quad;\frac{\partial}{\partial\tau_{yz}}\left(\frac{\partial\bar{J}_2}{\partial\tau_{yz}}\right)=2 \quad;\frac{\partial}{\partial\tau_{yz}}\left(\frac{\partial\bar{J}_2}{\partial\tau_{xz}}\right)=0 \quad;\frac{\partial}{\partial\tau_{yz}}\left(\frac{\partial\bar{J}_2}{\partial\tau_{xy}}\right)=0$$

$$\frac{\partial}{\partial\tau_{xz}}\left(\frac{\partial\bar{J}_2}{\partial\sigma_x}\right)=0 \quad;\frac{\partial}{\partial\tau_{xz}}\left(\frac{\partial\bar{J}_2}{\partial\sigma_y}\right)=0 \quad;\frac{\partial}{\partial\tau_{xz}}\left(\frac{\partial\bar{J}_2}{\partial\sigma_z}\right)=0 \quad;\frac{\partial}{\partial\tau_{xz}}\left(\frac{\partial\bar{J}_2}{\partial\tau_{yz}}\right)=0 \quad;\frac{\partial}{\partial\tau_{xz}}\left(\frac{\partial\bar{J}_2}{\partial\tau_{xz}}\right)=2 \quad;\frac{\partial}{\partial\tau_{xz}}\left(\frac{\partial\bar{J}_2}{\partial\tau_{xy}}\right)=0$$

$$\frac{\partial}{\partial\tau_{xy}}\left(\frac{\partial\bar{J}_2}{\partial\sigma_x}\right)=0 \quad;\frac{\partial}{\partial\tau_{xy}}\left(\frac{\partial\bar{J}_2}{\partial\sigma_y}\right)=0 \quad;\frac{\partial}{\partial\tau_{xy}}\left(\frac{\partial\bar{J}_2}{\partial\sigma_z}\right)=0 \quad;\frac{\partial}{\partial\tau_{xy}}\left(\frac{\partial\bar{J}_2}{\partial\tau_{yz}}\right)=0 \quad;\frac{\partial}{\partial\tau_{xy}}\left(\frac{\partial\bar{J}_2}{\partial\tau_{xz}}\right)=0 \quad;\frac{\partial}{\partial\tau_{xy}}\left(\frac{\partial\bar{J}_2}{\partial\tau_{xy}}\right)=2$$

The second order derivative of of the third invariant of the deviatoric effective stress tensor, $\bar{J}_3$, with respect to the effective stress components ($\bar{\sigma}_i$) and ($\bar{\sigma}_j$) is given by:

$$\frac{\partial}{\partial\sigma_x}\left(\frac{\partial\bar{J}_3}{\partial\sigma_x}\right)=\frac{2}{9}(2\sigma_x-\sigma_y-\sigma_z) \quad;\quad \frac{\partial}{\partial\sigma_x}\left(\frac{\partial\bar{J}_3}{\partial\sigma_y}\right)=\frac{2}{9}(2\sigma_z-\sigma_y-\sigma_x) \quad;\quad \frac{\partial}{\partial\sigma_x}\left(\frac{\partial\bar{J}_3}{\partial\sigma_z}\right)=\frac{2}{9}(2\sigma_y-\sigma_x-\sigma_z) \qquad \text{(D.12)}$$

$$\frac{\partial}{\partial\sigma_y}\left(\frac{\partial\bar{J}_3}{\partial\sigma_x}\right)=\frac{2}{9}(2\sigma_z-\sigma_y-\sigma_x) \quad;\frac{\partial}{\partial\sigma_y}\left(\frac{\partial\bar{J}_3}{\partial\sigma_y}\right)=\frac{2}{9}(2\sigma_y-\sigma_x-\sigma_z) \quad;\frac{\partial}{\partial\sigma_y}\left(\frac{\partial\bar{J}_3}{\partial\sigma_z}\right)=\frac{2}{9}(2\sigma_x-\sigma_y-\sigma_z)$$

$$\frac{\partial}{\partial\sigma_z}\left(\frac{\partial\bar{J}_3}{\partial\sigma_x}\right)=\frac{2}{9}(2\sigma_y-\sigma_x-\sigma_z) \quad;\frac{\partial}{\partial\sigma_z}\left(\frac{\partial\bar{J}_3}{\partial\sigma_y}\right)=\frac{2}{9}(2\sigma_x-\sigma_y-\sigma_z) \quad;\frac{\partial}{\partial\sigma_z}\left(\frac{\partial\bar{J}_3}{\partial\sigma_z}\right)=\frac{2}{9}(2\sigma_z-\sigma_y-\sigma_x)$$

$$\frac{\partial}{\partial\tau_{yz}}\left(\frac{\partial\bar{J}_3}{\partial\sigma_x}\right)=-\frac{4}{3}\tau_{yz} \qquad\qquad ;\frac{\partial}{\partial\tau_{yz}}\left(\frac{\partial\bar{J}_3}{\partial\sigma_y}\right)=\frac{2}{3}\tau_{yz} \qquad\qquad ;\frac{\partial}{\partial\tau_{yz}}\left(\frac{\partial\bar{J}_3}{\partial\sigma_z}\right)=\frac{2}{3}\tau_{yz}$$

$$\frac{\partial}{\partial\tau_{xz}}\left(\frac{\partial\bar{J}_3}{\partial\sigma_x}\right)=\frac{2}{3}\tau_{xz} \qquad\qquad ;\frac{\partial}{\partial\tau_{xz}}\left(\frac{\partial\bar{J}_3}{\partial\sigma_y}\right)=-\frac{4}{3}\tau_{xz} \qquad\qquad ;\frac{\partial}{\partial\tau_{xz}}\left(\frac{\partial\bar{J}_3}{\partial\sigma_z}\right)=\frac{2}{3}\tau_{xz}$$

$$\frac{\partial}{\partial\tau_{xy}}\left(\frac{\partial\bar{J}_3}{\partial\sigma_x}\right)=\frac{2}{3}\tau_{xy} \qquad\qquad ;\frac{\partial}{\partial\tau_{xy}}\left(\frac{\partial\bar{J}_3}{\partial\sigma_y}\right)=\frac{2}{3}\tau_{xy} \qquad\qquad ;\frac{\partial}{\partial\tau_{xy}}\left(\frac{\partial\bar{J}_3}{\partial\sigma_z}\right)=-\frac{4}{3}\tau_{xy}$$

$$\frac{\partial}{\partial\sigma_x}\left(\frac{\partial\bar{J}_3}{\partial\tau_{yz}}\right)=-\frac{4}{3}\tau_{yz} \qquad ;\frac{\partial}{\partial\sigma_x}\left(\frac{\partial\bar{J}_3}{\partial\tau_{xz}}\right)=\frac{2}{3}\tau_{xz} \qquad ;\frac{\partial}{\partial\sigma_x}\left(\frac{\partial\bar{J}_3}{\partial\tau_{xy}}\right)=\frac{2}{3}\tau_{xy}$$

$$\frac{\partial}{\partial\sigma_y}\left(\frac{\partial\bar{J}_3}{\partial\tau_{yz}}\right)=\frac{2}{3}\tau_{yz} \qquad ;\frac{\partial}{\partial\sigma_y}\left(\frac{\partial\bar{J}_3}{\partial\tau_{xz}}\right)=-\frac{4}{3}\tau_{xz} \qquad ;\frac{\partial}{\partial\sigma_y}\left(\frac{\partial\bar{J}_3}{\partial\tau_{xy}}\right)=\frac{2}{3}\tau_{xy}$$

$$\frac{\partial}{\partial\sigma_z}\left(\frac{\partial\bar{J}_3}{\partial\tau_{yz}}\right)=\frac{2}{3}\tau_{yz} \qquad ;\frac{\partial}{\partial\sigma_z}\left(\frac{\partial\bar{J}_3}{\partial\tau_{xz}}\right)=\frac{2}{3}\tau_{xz} \qquad ;\frac{\partial}{\partial\sigma_z}\left(\frac{\partial\bar{J}_3}{\partial\tau_{xy}}\right)=-\frac{4}{3}\tau_{xy}$$

$$\frac{\partial}{\partial\tau_{yz}}\left(\frac{\partial\bar{J}_3}{\partial\tau_{yz}}\right)=\frac{2}{3}(\sigma_y+\sigma_z-2\sigma_x) \quad ;\frac{\partial}{\partial\tau_{yz}}\left(\frac{\partial\bar{J}_3}{\partial\tau_{xz}}\right)=2\tau_{xy} \qquad ;\frac{\partial}{\partial\tau_{yz}}\left(\frac{\partial\bar{J}_3}{\partial\tau_{xy}}\right)=2\tau_{xz}$$

$$\frac{\partial}{\partial\tau_{xz}}\left(\frac{\partial\bar{J}_3}{\partial\tau_{yz}}\right)=2\tau_{xy} \qquad ;\frac{\partial}{\partial\tau_{xz}}\left(\frac{\partial\bar{J}_3}{\partial\tau_{xz}}\right)=\frac{2}{3}(\sigma_x+\sigma_z-2\sigma_y) \quad ;\frac{\partial}{\partial\tau_{xz}}\left(\frac{\partial\bar{J}_3}{\partial\tau_{xy}}\right)=2\tau_{yz}$$

$$\frac{\partial}{\partial\tau_{xy}}\left(\frac{\partial\bar{J}_3}{\partial\tau_{yz}}\right)=2\tau_{xz} \qquad ;\frac{\partial}{\partial\tau_{xy}}\left(\frac{\partial\bar{J}_3}{\partial\tau_{xz}}\right)=2\tau_{yz} \qquad ;\frac{\partial}{\partial\tau_{xy}}\left(\frac{\partial\bar{J}_3}{\partial\tau_{xy}}\right)=\frac{2}{3}(\sigma_x+\sigma_y-2\sigma_z)$$

D.8 Second order derivative of the yield function with respect to the effective stress components

The second order derivative of of the yield function with respect to the effective stress components ($\bar{\sigma}_i$) and ($\bar{\sigma}_j$) is given by:

$$\frac{\partial}{\partial\bar{\sigma}_j}\left(\frac{\partial f\left(\bar{\sigma};\bar{\sigma}_c(\tilde{\epsilon}_c)\right)}{\partial\bar{\sigma}_i}\right)=\frac{1}{2}\left[-\frac{1}{2}A^{-3/2}\frac{\partial A}{\partial\bar{\sigma}_j}\times B+A^{-1/2}\frac{\partial B}{\partial\bar{\sigma}_j}\right] \tag{D.13a}$$

where functions *A*, *B* and their derivatives ($\partial A/\partial\bar{\sigma}_j$, $\partial B/\partial\bar{\sigma}_j$) are:

$$A=\left(\frac{\bar{I}_1}{\sqrt{3}c}-\frac{\sqrt{2}b}{c}\sqrt{\bar{J}_2}\right)\bar{\sigma}_c-\frac{2a}{c}\bar{J}_2 \tag{D.13b}$$

$$B=\left\{\frac{1}{\sqrt{3}c}\frac{\partial\bar{I}_1}{\partial\bar{\sigma}_i}-\frac{\sqrt{2}}{c}\left(\sqrt{\bar{J}_2}\frac{\partial b}{\partial\bar{\sigma}_i}+\frac{1}{2}\frac{\partial\bar{J}_2}{\partial\bar{\sigma}_i}\bar{J}_2^{-0.5}b\right)\right\}\bar{\sigma}_c \tag{D.13c}$$
$$-\frac{2}{c}(\frac{\partial a}{\partial\bar{\sigma}_i}\bar{J}_2+a\frac{\partial\bar{J}_2}{\partial\bar{\sigma}_i})$$

$$\frac{\partial A}{\partial\bar{\sigma}_j}=\left(\frac{1}{\sqrt{3}c}\frac{\partial\bar{I}_1}{\partial\bar{\sigma}_j}-\frac{\sqrt{2}}{c}\{\sqrt{\bar{J}_2}\frac{\partial b}{\partial\bar{\sigma}_j}+\frac{1}{2\sqrt{\bar{J}_2}}\frac{\partial\bar{J}_2}{\partial\bar{\sigma}_j}b\}\right)\bar{\sigma}_c-\frac{2}{c}\{\frac{\partial a}{\partial\bar{\sigma}_j}J_2+\frac{\partial\bar{J}_2}{\partial\bar{\sigma}_j}a\} \tag{D.13d}$$

$$\frac{\partial B}{\partial \overline{\underline{\sigma}}_j} = \frac{1}{\sqrt{3}\,c}\frac{\partial}{\partial \overline{\underline{\sigma}}_j}\left(\frac{\partial \overline{I}_1}{\partial \overline{\underline{\sigma}}_i}\right) - \frac{\sqrt{2}}{c}\left[\frac{\partial \overline{J}_2}{\partial \overline{\underline{\sigma}}_j}\frac{\partial b}{\partial \overline{\underline{\sigma}}_i}\overline{J}_2^{-0.5}0.5 + \overline{J}_2^{0.5}\frac{\partial}{\partial \overline{\underline{\sigma}}_j}\left(\frac{\partial b}{\partial \overline{\underline{\sigma}}_i}\right)\right. \tag{D.13d}$$

$$+0.5\left\{b\frac{\partial}{\partial \overline{\underline{\sigma}}_j}\left(\frac{\partial \overline{J}_2}{\partial \overline{\underline{\sigma}}_i}\right)\overline{J}_2^{-0.5} - 0.5\overline{J}_2^{-1.5}\frac{\partial \overline{J}_2}{\partial \overline{\underline{\sigma}}_i}\frac{\partial \overline{J}_2}{\partial \overline{\underline{\sigma}}_j}b + \frac{\partial \overline{J}_2}{\partial \overline{\underline{\sigma}}_i}\overline{J}_2^{-0.5}\frac{\partial b}{\partial \overline{\underline{\sigma}}_j}\right\}\Bigg]\overline{\sigma}_c$$

$$\frac{2}{c}\left(\frac{\partial}{\partial \overline{\underline{\sigma}}_j}\left(\frac{\partial a}{\partial \overline{\underline{\sigma}}_i}\right)J_2 + \frac{\partial \overline{J}_2}{\partial \overline{\underline{\sigma}}_j}\frac{\partial a}{\partial \overline{\underline{\sigma}}_i} + \frac{\partial}{\partial \overline{\underline{\sigma}}_j}\left(\frac{\partial \overline{J}_2}{\partial \overline{\underline{\sigma}}_i}\right)a + \frac{\partial a}{\partial \overline{\underline{\sigma}}_j}\frac{\partial \overline{J}_2}{\partial \overline{\underline{\sigma}}_i}\right)$$

D.9 Second order derivative of the coefficients of the loading meridian (*a*, *b*) with respect to the effective stress components

The second order derivative of coefficient *b* with respect to the effective stress components ($\overline{\underline{\sigma}}_i$) and ($\overline{\underline{\sigma}}_j$) is given by:

$$\frac{\partial}{\partial \overline{\underline{\sigma}}_j}\left(\frac{\partial b}{\partial \overline{\underline{\sigma}}_i}\right) = \left[2(\overline{\xi}_{CP1}-b_0)\{\frac{\partial \overline{\rho}_{(\overline{\xi}=\overline{\xi}_{CP2},\overline{\theta})}}{\partial \overline{\underline{\sigma}}_j}\frac{\partial \overline{\rho}_{(\overline{\xi}=\overline{\xi}_{CP2},\overline{\theta})}}{\partial \overline{\underline{\sigma}}_i}+\overline{\rho}_{(\overline{\xi}=\overline{\xi}_{CP2},\overline{\theta})}\frac{\partial^2 \overline{\rho}_{(\overline{\xi}=\overline{\xi}_{CP2},\overline{\theta})}}{\partial \overline{\underline{\sigma}}_j\partial \overline{\underline{\sigma}}_i}\}\right. \tag{D.14a}$$

$$-2(\overline{\xi}_{CP2}-b_0)\{\frac{\partial \overline{\rho}_{(\overline{\xi}=\overline{\xi}_{CP1},\overline{\theta})}}{\partial \overline{\underline{\sigma}}_j}\frac{\partial \overline{\rho}_{(\overline{\xi}=\overline{\xi}_{CP1},\overline{\theta})}}{\partial \overline{\underline{\sigma}}_i}+\overline{\rho}_{(\overline{\xi}=\overline{\xi}_{CP1},\overline{\theta})}\frac{\partial^2 \overline{\rho}_{(\overline{\xi}=\overline{\xi}_{CP1},\overline{\theta})}}{\partial \overline{\underline{\sigma}}_j\partial \overline{\underline{\sigma}}_i}\}\right]$$

$$\times B^{-1} - B^{-2}\frac{\partial B}{\partial \overline{\underline{\sigma}}_j}F - B^{-2}G\frac{\partial A}{\partial \overline{\underline{\sigma}}_j}+2B^{-3}\frac{\partial B}{\partial \overline{\underline{\sigma}}_j}\times A\times G - B^{-2}\times A\times$$

$$\left[\{\overline{\rho}^2_{(\overline{\xi}=\overline{\xi}_{CP2},\overline{\theta})}\frac{\partial^2 \overline{\rho}_{(\overline{\xi}=-2,\overline{\theta})}}{\partial \overline{\underline{\sigma}}_j\partial \overline{\underline{\sigma}}_i}+2\overline{\rho}_{(\overline{\xi}=\overline{\xi}_{CP2},\overline{\theta})}\frac{\partial \overline{\rho}_{(\overline{\xi}=\overline{\xi}_{CP2},\overline{\theta})}}{\partial \overline{\underline{\sigma}}_j}\frac{\partial \overline{\rho}_{(\overline{\xi}=-2,\overline{\theta})}}{\partial \overline{\underline{\sigma}}_i}\}\right.$$

$$+\{2\overline{\rho}_{(\overline{\xi}=\overline{\xi}_{CP2},\overline{\theta})}\frac{\partial \overline{\rho}_{(\overline{\xi}=\overline{\xi}_{CP1},\overline{\theta})}}{\partial \overline{\underline{\sigma}}_j}\frac{\partial \overline{\rho}_{(\overline{\xi}=\overline{\xi}_{CP2},\overline{\theta})}}{\partial \overline{\underline{\sigma}}_i}+2\overline{\rho}_{(\overline{\xi}=\overline{\xi}_{CP1},\overline{\theta})}\frac{\partial \overline{\rho}_{(\overline{\xi}=\overline{\xi}_{CP2},\overline{\theta})}}{\partial \overline{\underline{\sigma}}_j}$$

$$\frac{\partial \overline{\rho}_{(\overline{\xi}=\overline{\xi}_{CP2},\overline{\theta})}}{\partial \overline{\underline{\sigma}}_i}+2\overline{\rho}_{(\overline{\xi}=\overline{\xi}_{CP1},\overline{\theta})}\overline{\rho}_{(\overline{\xi}=\overline{\xi}_{CP2},\overline{\theta})}\frac{\partial^2 \overline{\rho}_{(\overline{\xi}=\overline{\xi}_{CP2},\overline{\theta})}}{\partial \overline{\underline{\sigma}}_j\partial \overline{\underline{\sigma}}_i}\}-2\{\frac{\partial \overline{\rho}_{(\overline{\xi}=\overline{\xi}_{CP1},\overline{\theta})}}{\partial \overline{\underline{\sigma}}_j}$$

$$\overline{\rho}_{(\overline{\xi}=\overline{\xi}_{CP2},\overline{\theta})}\frac{\partial \overline{\rho}_{(\overline{\xi}=\overline{\xi}_{CP1},\overline{\theta})}}{\partial \overline{\underline{\sigma}}_i}+\overline{\rho}_{(\overline{\xi}=\overline{\xi}_{CP1},\overline{\theta})}\frac{\partial \overline{\rho}_{(\overline{\xi}=\overline{\xi}_{CP2},\overline{\theta})}}{\partial \overline{\underline{\sigma}}_j}\frac{\partial \overline{\rho}_{(\overline{\xi}=\overline{\xi}_{CP1},\overline{\theta})}}{\partial \overline{\underline{\sigma}}_i}$$

$$+\overline{\rho}_{(\overline{\xi}=\overline{\xi}_{CP1},\overline{\theta})}\overline{\rho}_{(\overline{\xi}=\overline{\xi}_{CP2},\overline{\theta})}\frac{\partial^2 \overline{\rho}_{(\overline{\xi}=\overline{\xi}_{CP1},\overline{\theta})}}{\partial \overline{\underline{\sigma}}_j\partial \overline{\underline{\sigma}}_i}\}-$$

$$\{2\overline{\rho}_{(\overline{\xi}=\overline{\xi}_{CP1},\overline{\theta})}\frac{\partial \overline{\rho}_{(\overline{\xi}=\overline{\xi}_{CP1},\overline{\theta})}}{\partial \overline{\underline{\sigma}}_j}\frac{\partial \overline{\rho}_{(\overline{\xi}=\overline{\xi}_{CP2},\overline{\theta})}}{\partial \overline{\underline{\sigma}}_i}+\overline{\rho}^2_{(\overline{\xi}=\overline{\xi}_{CP1},\overline{\theta})}\frac{\partial^2 \overline{\rho}_{(\overline{\xi}=\overline{\xi}_{CP2},\overline{\theta})}}{\partial \overline{\underline{\sigma}}_j\partial \overline{\underline{\sigma}}_i}\}\right]$$

where the auxiliary functions A, B, F, G, and the derivatives $\partial A/\partial\bar{\underline{\sigma}}_j$, $\partial B/\partial\bar{\underline{\sigma}}_j$ are defined as follows:

$$A = \left[\left(\bar{\bar{\xi}}_{CP1} - b_0 \right) \times \bar{\rho}^2_{(\bar{\xi}=\bar{\xi}_{CP2},\,\bar{\theta})} - \left(\bar{\bar{\xi}}_{CP2} - b_0 \right) \bar{\rho}^2_{(\bar{\xi}=\bar{\xi}_{CP1},\,\bar{\theta})} \right] \tag{D.14b}$$

$$B = \left[\bar{\rho}_{(\bar{\xi}=\bar{\xi}_{CP1},\,\bar{\theta})} \bar{\rho}^2_{(\bar{\xi}=\bar{\xi}_{CP2},\,\bar{\theta})} - \bar{\rho}^2_{(\bar{\xi}=\bar{\xi}_{CP1},\,\bar{\theta})} \bar{\rho}_{(\bar{\xi}=\bar{\xi}_{CP2},\,\bar{\theta})} \right] \tag{D.14c}$$

$$F = \left[\left(\bar{\bar{\xi}}_{CP1} - b_0 \right) \times 2\bar{\rho}_{(\bar{\xi}=\bar{\xi}_{CP2},\,\bar{\theta})} \frac{\partial\bar{\rho}_{(\bar{\xi}=\bar{\xi}_{CP2},\,\bar{\theta})}}{\partial\bar{\underline{\sigma}}_i} - 2\left(\bar{\bar{\xi}}_{CP2} - b_0 \right) \bar{\rho}_{(\bar{\xi}=\bar{\xi}_{CP1},\,\bar{\theta})} \frac{\partial\bar{\rho}_{(\bar{\xi}=\bar{\xi}_{CP1},\,\bar{\theta})}}{\partial\bar{\underline{\sigma}}_i} \right] \tag{D.14d}$$

$$G = \frac{\partial\bar{\rho}_{(\bar{\xi}=\bar{\xi}_{CP1},\,\bar{\theta})}}{\partial\bar{\underline{\sigma}}_i} \bar{\rho}^2_{(\bar{\xi}=\bar{\xi}_{CP2},\,\bar{\theta})} + 2\bar{\rho}_{(\bar{\xi}=\bar{\xi}_{CP1},\,\bar{\theta})} \bar{\rho}_{(\bar{\xi}=\bar{\xi}_{CP2},\,\bar{\theta})} \frac{\partial\bar{\rho}_{(\bar{\xi}=\bar{\xi}_{CP2},\,\bar{\theta})}}{\partial\bar{\underline{\sigma}}_i} \times \tag{D.14e}$$
$$-2\bar{\rho}_{(\bar{\xi}=\bar{\xi}_{CP1},\,\bar{\theta})} \bar{\rho}_{(\bar{\xi}=\bar{\xi}_{CP2},\,\bar{\theta})} \frac{\partial\bar{\rho}_{(\bar{\xi}=\bar{\xi}_{CP1},\,\bar{\theta})}}{\partial\bar{\underline{\sigma}}_i} - \bar{\rho}^2_{(\bar{\xi}=\bar{\xi}_{CP1},\,\bar{\theta})} \frac{\partial\bar{\rho}_{(\bar{\xi}=\bar{\xi}_{CP2},\,\bar{\theta})}}{\partial\bar{\underline{\sigma}}_i}$$

$$\frac{\partial B}{\partial\bar{\underline{\sigma}}_j} = \frac{\partial\bar{\rho}_{(\bar{\xi}=\bar{\xi}_{CP1},\,\bar{\theta})}}{\partial\bar{\underline{\sigma}}_j} \bar{\rho}^2_{(\bar{\xi}=\bar{\xi}_{CP2},\,\bar{\theta})} + 2\bar{\rho}_{(\bar{\xi}=\bar{\xi}_{CP1},\,\bar{\theta})} \bar{\rho}_{(\bar{\xi}=\bar{\xi}_{CP2},\,\bar{\theta})} \frac{\partial\bar{\rho}_{(\bar{\xi}=\bar{\xi}_{CP2},\,\bar{\theta})}}{\partial\bar{\underline{\sigma}}_j} \times \tag{D.14f}$$
$$-2\bar{\rho}_{(\bar{\xi}=\bar{\xi}_{CP1},\,\bar{\theta})} \bar{\rho}_{(\bar{\xi}=\bar{\xi}_{CP2},\,\bar{\theta})} \frac{\partial\bar{\rho}_{(\bar{\xi}=\bar{\xi}_{CP1},\,\bar{\theta})}}{\partial\bar{\underline{\sigma}}_j} - \bar{\rho}^2_{(\bar{\xi}=\bar{\xi}_{CP1},\,\bar{\theta})} \frac{\partial\bar{\rho}_{(\bar{\xi}=\bar{\xi}_{CP2},\,\bar{\theta})}}{\partial\bar{\underline{\sigma}}_j}$$

$$\frac{\partial A}{\partial\bar{\underline{\sigma}}_j} = 2(\bar{\bar{\xi}}_{CP1} - b_0)\bar{\rho}_{(\bar{\xi}=\bar{\xi}_{CP2},\,\bar{\theta})} \frac{\partial\bar{\rho}_{(\bar{\xi}=\bar{\xi}_{CP2},\,\bar{\theta})}}{\partial\bar{\underline{\sigma}}_j} - 2(\bar{\bar{\xi}}_{CP2} - b_0)\bar{\rho}_{(\bar{\xi}=\bar{\xi}_{CP1},\,\bar{\theta})} \frac{\partial\bar{\rho}_{(\bar{\xi}=\bar{\xi}_{CP1},\,\bar{\theta})}}{\partial\bar{\underline{\sigma}}_j} \tag{D.14g}$$

The second order derivative of the coefficient a with respect to the effective stress components $(\bar{\underline{\sigma}}_i)$ and $(\bar{\underline{\sigma}}_j)$ is given by:

$$\frac{\partial^2 a}{\partial \underline{\overline{\sigma}}_j \partial \underline{\overline{\sigma}}_i} = -\overline{\rho}_{(\overline{\xi}=\overline{\xi}_{CP2},\overline{\theta})}^2 \left[\frac{\partial^2 b}{\partial \underline{\overline{\sigma}}_j \partial \underline{\overline{\sigma}}_i} \overline{\rho}_{(\overline{\xi}=\overline{\xi}_{CP2},\overline{\theta})} + \frac{\partial b}{\partial \underline{\overline{\sigma}}_i} \frac{\partial \overline{\rho}_{(\overline{\xi}=\overline{\xi}_{CP2},\overline{\theta})}}{\partial \underline{\overline{\sigma}}_j} + \frac{\partial b}{\partial \underline{\overline{\sigma}}_j} \frac{\partial \overline{\rho}_{(\overline{\xi}=\overline{\xi}_{CP2},\overline{\theta})}}{\partial \underline{\overline{\sigma}}_i} \right. \tag{D.15}$$

$$\left. + b \frac{\partial^2 \overline{\rho}_{(\overline{\xi}=\overline{\xi}_{CP2},\overline{\theta})}}{\partial \underline{\overline{\sigma}}_j \partial \underline{\overline{\sigma}}_i} \right] + \left[2\{ \frac{\partial b}{\partial \underline{\overline{\sigma}}_i} \overline{\rho}_{(\overline{\xi}=\overline{\xi}_{CP2},\overline{\theta})} + b \frac{\partial \overline{\rho}_{(\overline{\xi}=\overline{\xi}_{CP2},\overline{\theta})}}{\partial \underline{\overline{\sigma}}_i} \} \times \overline{\rho}_{(\overline{\xi}=\overline{\xi}_{CP2},\overline{\theta})}^{-3} \right.$$

$$\left. \frac{\partial \overline{\rho}_{(\overline{\xi}=\overline{\xi}_{CP2},\overline{\theta})}}{\partial \underline{\overline{\sigma}}_j} \right] - 2 \left[[-3 \frac{\partial \overline{\rho}_{(\overline{\xi}=\overline{\xi}_{CP2},\overline{\theta})}}{\partial \underline{\overline{\sigma}}_j} \frac{\partial \overline{\rho}_{(\overline{\xi}=\overline{\xi}_{CP2},\overline{\theta})}}{\partial \underline{\overline{\sigma}}_i} \overline{\rho}_{(\overline{\xi}=\overline{\xi}_{CP2},\overline{\theta})}^{-4} [(\overline{\overline{\xi}}_{CP2} - b_0) \right.$$

$$\left. - b \overline{\rho}_{(\overline{\xi}=\overline{\xi}_{CP2},\overline{\theta})}]] + \left[\overline{\rho}_{(\overline{\xi}=\overline{\xi}_{CP2},\overline{\theta})}^{-3} \frac{\partial^2 \overline{\rho}_{(\overline{\xi}=\overline{\xi}_{CP2},\overline{\theta})}}{\partial \underline{\overline{\sigma}}_j \partial \underline{\overline{\sigma}}_i} [(\overline{\overline{\xi}}_{CP2} - b_0)` - b \overline{\rho}_{(\overline{\xi}=\overline{\xi}_{CP2},\overline{\theta})}] \right] \right.$$

$$\left. + \left[\overline{\rho}_{(\overline{\xi}=\overline{\xi}_{CP2},\overline{\theta})}^{-3} \frac{\partial \overline{\rho}_{(\overline{\xi}=\overline{\xi}_{CP2},\overline{\theta})}}{\partial \underline{\overline{\sigma}}_i} \{-\frac{\partial b}{\partial \underline{\overline{\sigma}}_j} \overline{\rho}_{(\overline{\xi}=\overline{\xi}_{CP2},\overline{\theta})} - b \frac{\partial \overline{\rho}_{(\overline{\xi}=\overline{\xi}_{CP2},\overline{\theta})}}{\partial \underline{\overline{\sigma}}_j} \} \right] \right]$$

D.10 Second order derivative of the interpolation function $\overline{\rho}_{(\overline{\xi},\overline{\theta})}$ with respect to the effective stress components

The second order derivative of the interpolation function ($\overline{\rho}_{(\overline{\xi},\overline{\theta})}$) with respect to the effective stress components ($\underline{\overline{\sigma}}_i$) and ($\underline{\overline{\sigma}}_j$) is given by:

$$\frac{\partial}{\partial \underline{\overline{\sigma}}_j} \left(\frac{\partial \overline{\rho}_{(\overline{\xi},\overline{\theta})}}{\partial \underline{\overline{\sigma}}_i} \right) = F + G + H \tag{D.16a}$$

where the auxiliary functions *F*, *G*, and *H* are defined as follows:

$$F = 2\overline{\rho}_c \left(\overline{\rho}_c^2 - \overline{\rho}_t^2 \right) \{(-\cos\overline{\theta}) \frac{\partial \overline{\theta}}{\partial \underline{\overline{\sigma}}_j} \frac{\partial \overline{\theta}}{\partial \underline{\overline{\sigma}}_i} + \frac{\partial^2 \overline{\theta}}{\partial \underline{\overline{\sigma}}_j \partial \underline{\overline{\sigma}}_i} (-\sin\overline{\theta})\} \times B^{-1} - B^{-2} \tag{D.16b}$$

$$\{4 \left(\overline{\rho}_c^2 - \overline{\rho}_t^2 \right) \times 2\cos\overline{\theta} \times -\sin\overline{\theta} \frac{\partial \overline{\theta}}{\partial \underline{\overline{\sigma}}_j} \} \times \{2\overline{\rho}_c \left(\overline{\rho}_c^2 - \overline{\rho}_t^2 \right) \times -\sin\theta \frac{\partial \overline{\theta}}{\partial \underline{\overline{\sigma}}_i} \}$$

$$G = \bar{\rho}_c \left(2\bar{\rho}_t - \bar{\rho}_c \right) + \frac{1}{2} \times 4\left(\bar{\rho}_c^2 - \bar{\rho}_t^2 \right) \times 2 \times \left\{ \left(-\frac{1}{2} \times C^{-3/2} \times 4\left(\bar{\rho}_c^2 - \bar{\rho}_t^2 \right) \times 2 \right. \right. \tag{D.16c}$$

$$\cos\bar{\theta}(-\sin\bar{\theta})\frac{\partial\bar{\theta}}{\partial\underline{\bar{\sigma}}_j} \times (\frac{\partial\bar{\theta}}{\partial\underline{\bar{\sigma}}_i}\cos\bar{\theta}(-\sin\bar{\theta})) \times B^{-1} \Big) + \Big(\{ \sin^2\bar{\theta}\frac{\partial\bar{\theta}}{\partial\underline{\bar{\sigma}}_j}\frac{\partial\bar{\theta}}{\partial\underline{\bar{\sigma}}_i}$$

$$-\cos^2\bar{\theta}\frac{\partial\bar{\theta}}{\partial\underline{\bar{\sigma}}_j}\frac{\partial\bar{\theta}}{\partial\underline{\bar{\sigma}}_i} - \sin\bar{\theta}\cos\bar{\theta}\frac{\partial^2\bar{\theta}}{\partial\underline{\bar{\sigma}}_j\partial\underline{\bar{\sigma}}_i} \} \times C^{-1/2} \times B^{-1/2} \Big) + \Big(-B^{-2}\{\frac{\partial\bar{\theta}}{\partial\underline{\bar{\sigma}}_j}$$

$$(-\sin\bar{\theta}) \times 2 \times 4 \times \cos\bar{\theta}\left(\bar{\rho}_c^2 - \bar{\rho}_t^2 \right) \} \times C^{-1/2} \times \cos\bar{\theta}(-\sin\bar{\theta})\frac{\partial\bar{\theta}}{\partial\underline{\bar{\sigma}}_i} \Big) \Big\}$$

$$H = -1 \times \Bigg[\{ -2B^{-3} \times 2 \times 4\left(\bar{\rho}_c^2 - \bar{\rho}_t^2 \right)\cos\bar{\theta}(-\sin\bar{\theta})\frac{\partial\bar{\theta}}{\partial\underline{\bar{\sigma}}_j}(4\left(\bar{\rho}_c^2 - \bar{\rho}_t^2 \right) \times 2D) \times E \} \tag{D.16d}$$

$$+ \{ 4\left(\bar{\rho}_c^2 - \bar{\rho}_t^2 \right) \times 2 \times (\sin^2\bar{\theta}\frac{\partial\bar{\theta}}{\partial\underline{\bar{\sigma}}_j}\frac{\partial\bar{\theta}}{\partial\underline{\bar{\sigma}}_i} - \cos^2\bar{\theta}\frac{\partial\bar{\theta}}{\partial\underline{\bar{\sigma}}_j}\frac{\partial\bar{\theta}}{\partial\underline{\bar{\sigma}}_i} - \cos\bar{\theta}\sin\bar{\theta}$$

$$\frac{\partial^2\bar{\theta}}{\partial\underline{\bar{\sigma}}_j\partial\underline{\bar{\sigma}}_i}) \times B^{-2} \times E \} + \{ 2\bar{\rho}_c\left(\bar{\rho}_c^2 - \bar{\rho}_t^2 \right) - \sin\bar{\theta}\frac{\partial\bar{\theta}}{\partial\underline{\bar{\sigma}}_j} + \bar{\rho}_c(2\bar{\rho}_t - \bar{\rho}_c) \times \frac{1}{2}$$

$$\times 4 \times C^{-1/2} \times 4 \times 2\left(\bar{\rho}_c^2 - \bar{\rho}_t^2 \right)\cos\bar{\theta}(-\sin\bar{\theta})\frac{\partial\bar{\theta}}{\partial\underline{\bar{\sigma}}_i} \} 4\left(\bar{\rho}_c^2 - \bar{\rho}_t^2 \right) \times B^{-2} \times D \Bigg]$$

and:

$$B = 4\left(\bar{\rho}_c^2 - \bar{\rho}_t^2 \right)\cos^2\bar{\theta} + \left(\bar{\rho}_c - 2\bar{\rho}_t \right)^2 \tag{D.16e}$$

$$C = 4\left(\bar{\rho}_c^2 - \bar{\rho}_t^2 \right)\cos^2\bar{\theta} + 5\bar{\rho}_t^2 - 4\bar{\rho}_t\bar{\rho}_c \tag{D.16f}$$

$$D = \left(\cos\bar{\theta} \right)\left(-\sin\bar{\theta} \right)\frac{\partial\bar{\theta}}{\partial\underline{\bar{\sigma}}_i} \tag{D.16g}$$

$$E = 2\bar{\rho}_c\left(\bar{\rho}_c^2 - \bar{\rho}_t^2 \right)\cos\bar{\theta} + \bar{\rho}_c\left(2\bar{\rho}_t - \bar{\rho}_c \right)\left[4\left(\bar{\rho}_c^2 - \bar{\rho}_t^2 \right)\cos^2\bar{\theta} + 5\bar{\rho}_t^2 - 4\bar{\rho}_t\bar{\rho}_c \right]^{0.5} \tag{D.16h}$$

where the variables $\bar{\rho}_t$ and $\bar{\rho}_c$ are defined as $\bar{\rho}_t = \bar{\rho}_{(\bar{\xi}, \bar{\theta}=0°)}$ and $\bar{\rho}_c = \bar{\rho}_{(\bar{\xi}, \bar{\theta}=60°)}$, respectively.

D.11 Second order derivative of the angle of similarity with respect to the effective stress components

The second order derivative of the angle of similarity with respect to the effective stress components $(\bar{\sigma}_i)$ and $(\bar{\sigma}_j)$ is given by:

$$
\frac{\partial}{\partial \bar{\sigma}_j}\left(\frac{\partial \bar{\theta}}{\partial \bar{\sigma}_i}\right) = -\frac{\sqrt{3}}{2}\left[\left(-3 \times \frac{\partial \bar{\theta}}{\partial \bar{\sigma}_i} - \cot g(3\bar{\theta}) \times \cos ec(3\bar{\theta})\right) \times \left(\frac{\partial \bar{J}_3}{\partial \bar{\sigma}_i}\bar{J}_2^{-3/2} + \right.\right.
$$
$$
\left. \bar{J}_3 \times \frac{-3}{2} \times \bar{J}_2^{-5/2} \times \frac{\partial \bar{J}_2}{\partial \bar{\sigma}_i}\right) + \left(\frac{\partial^2 \bar{J}_3}{\partial \bar{\sigma}_j \partial \bar{\sigma}_i}\bar{J}_2^{-3/2} - 1.5\bar{J}_2^{-5/2} \times \frac{\partial \bar{J}_2}{\partial \bar{\sigma}_j}\right.
$$
$$
\frac{\partial \bar{J}_3}{\partial \bar{\sigma}_i} - 1.5\left\{\frac{\partial \bar{J}_3}{\partial \bar{\sigma}_j} \times J_2^{-5/2} \times \frac{\partial \bar{J}_2}{\partial \bar{\sigma}_i} - 2.5\bar{J}_2^{-7/2}\frac{\partial \bar{J}_2}{\partial \bar{\sigma}_j} \times \bar{J}_3 \times \frac{\partial \bar{J}_2}{\partial \bar{\sigma}_i}\right.
$$
$$
\left.\left.\left. + \bar{J}_2^{-5/2} \times \bar{J}_3 \times \frac{\partial^2 \bar{J}_3}{\partial \bar{\sigma}_j \partial \bar{\sigma}_i}\right\}\right) \times \frac{1}{\sin(3\bar{\theta})}\right]
$$

(D.17)

D.12 Second order derivative of the yield function with respect to the hardening function

The second order derivative of the yield function with respect to hardening function $(\bar{\sigma}_c)$ and $(\bar{\sigma}_c)$ is given by:

$$
\frac{\partial}{\partial \bar{\sigma}_c}\left(\frac{\partial f}{\partial \bar{\sigma}_c}\right) = -\frac{1}{4}\left(\frac{\bar{I}_1}{\sqrt{3}} - \frac{\sqrt{2}b}{c}\sqrt{\bar{J}_2}\right)^2\left[\left(\frac{\bar{I}_1}{\sqrt{3}} - \frac{\sqrt{2}b}{c}\sqrt{\bar{J}_2}\right)\bar{\sigma}_c - \frac{2a}{c}\bar{J}_2\right]^{-3/2}
$$

(D.18)

D.13 Second order derivative of the yield function with respect to the hardening function and to components of stress vector

The second order derivative of the yield function with respect to the hardening function ($\bar{\sigma}_c$) and to the components of the effective stress vector $(\bar{\sigma}_i)$ is given by:

$$
\begin{aligned}
\frac{\partial}{\partial \underline{\bar{\sigma}}_i}\left(\frac{\partial f}{\partial \bar{\sigma}_c}\right) = \frac{1}{2}\Bigg\{ & \left[\left(\frac{\bar{I}_1}{\sqrt{3}} - \frac{\sqrt{2}\,b}{c}\sqrt{\bar{J}_2}\right)\bar{\sigma}_c - \frac{2a}{c}\bar{J}_2\right]^{-1/2} \times \\
& \left[\frac{1}{\sqrt{3}\,c}\frac{\partial \bar{I}_1}{\partial \underline{\bar{\sigma}}_i} - \frac{\sqrt{2}}{c}(\sqrt{\bar{J}_2}\frac{\partial b}{\partial \underline{\bar{\sigma}}_i} + \frac{1}{2}\frac{\partial \bar{J}_2}{\partial \underline{\bar{\sigma}}_i}\frac{b}{\sqrt{\bar{J}_2}})\right] \\
& -\frac{1}{2}\left[\left(\frac{\bar{I}_1}{\sqrt{3}} - \frac{\sqrt{2}\,b}{c}\sqrt{\bar{J}_2}\right)\bar{\sigma}_c - \frac{2a}{c}\bar{J}_2\right]^{-3/2} \times \left(\frac{\bar{I}_1}{\sqrt{3}} - \frac{\sqrt{2}\,b}{c}\sqrt{\bar{J}_2}\right) \\
& \times\left(\frac{1}{\sqrt{3}\,c}\frac{\partial \bar{I}_1}{\partial \underline{\bar{\sigma}}_i} - \frac{\sqrt{2}}{c}(\sqrt{\bar{J}_2}\frac{\partial b}{\partial \underline{\bar{\sigma}}_i} + \frac{1}{2}\frac{\partial \bar{J}_2}{\partial \underline{\bar{\sigma}}_i}\frac{b}{\sqrt{\bar{J}_2}}) - \frac{2a}{c}(\frac{\partial a}{\partial \underline{\bar{\sigma}}_i}\bar{J}_2 + \frac{\partial \bar{J}_2}{\partial \underline{\bar{\sigma}}_i}a)\right)\Bigg\}
\end{aligned}
\tag{D.19}
$$

METHODOLOGY TO DERIVE COMPRESSIVE FRACTURE ENERGY FROM EXPERIMENTAL DATA

To determine the compressive fracture energy of a generic intervening material, uniaxial compression test with the set-up like the one represented in Fig. E.1 is recommended.
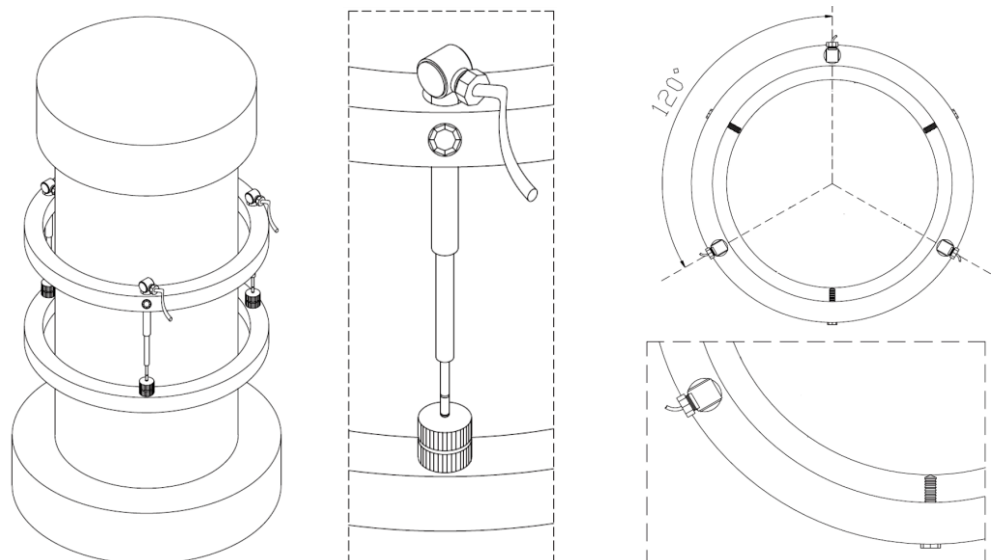

Fig. E.1 – Set up of uniaxial compression test (Cunha, 2010).

In general, two cones of confined concrete are formed at the top and bottom extremities of the specimen due to the friction between the steel plates of the test setup and the

specimen's top and bottom ends. The more concrete is confined, in the contact region of the sample and the steel plates, the higher strength measurement is likely to be. To avoid the effect of confinement on the measured strength of the specimens the following treatments are recommended:

- Application of intermediate layers of teflon between the specimen's top and bottom ends and the steel plates to reduce the friction between the two surfaces.
- If a cylinder specimen is adopted, the height of the specimen should be higher than, at least, two times of the cylinder diameter. Only the central region of the cylinder specimen is monitored, since the state of stress in this region is more likely to be uniaxial (i.e. the confined concrete cones at the top and bottom extremities have minimum effect on the state of stress in the central region of the specimen).

As can be seen in Fig. E.1, the two ring devices were positioned at top and bottom of the central region of the specimen (here is called "test region"). The axial displacement of the specimen at the "test region", δ_s, was measured using three linear voltage displacement transducers, LVDTs, placed in such a way as depicted in Fig. E.1.

Considering σ denotes stress measured at the test, the compressive fracture energy can be determined by the area under the post-peak branch of $\sigma - \delta_{inel}$ diagram, see Fig. E.2 (Jansen and Shah 1997; Vasconcelos et al., 2009). Inelastic displacement, δ_{inel}, is calculated from the following equation:

$$\delta_{inel} = \delta_s - \frac{\sigma}{k_0} \qquad (E.1)$$

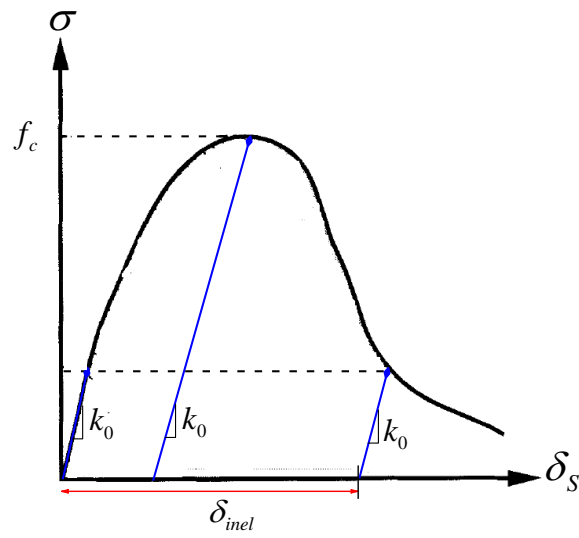where k_0 is the initial stiffness of $\sigma - \delta_{inel}$ response (see Fig. E.2).

Fig. E.2 – Model for determination of δ_{inel}.